CRANFIELD UNIVERSITY

Rémy STEENBAKKER

PHOSPHOR THERMOMETRY IN AN EB-PVD TBC

SCHOOL OF APPLIED SCIENCES

Ph.D. THESIS

CRANFIELD UNIVERSITY

SCHOOL OF APPLIED SCIENCES

Ph.D. THESIS

Academic Year 2004-2007

Rémy STEENBAKKER

PHOSPHOR THERMOMETRY IN AN EB-PVD TBC

Supervisors: **Prof. John R. Nicholls**
Dr. Richard G. Wellman

January 2008

**This thesis is submitted in partial fulfilment of the requirements
for the degree of Doctor of Philosophy**

ABSTRACT

Thermal Barrier Coatings (TBCs) are used to reduce the actual working temperature of the high pressure turbine blade surface. Knowing the temperature across a TBC and at the interface with the thermally grown oxide (TGO) under realistic conditions is highly desirable. As the major life-controlling factors for TBC systems are linked with temperature, this would provide useful data for a better understanding of these phenomena and to assess the remnant life-time of the TBC. This would also enable the design of advanced cooling strategies in the most efficient way using a minimum amount of air. Further the integration of a sensor coating into an on-line temperature detection system will enable the full potential of TBCs to be realised due to improved precision in temperature measurement and early warning of degradation. This in turn will increase fuel efficiency and reduce CO_2 emissions.

The concept of sensing TBCs was patented by *Choy et al.* [114] in 1998 and consists of locally modifying the composition of the TBC so that it acts as a thermographic phosphor. As a result, the temperature dependence of the lifetime of the laser induced phosphorescence process can be used for temperature measurements.

The purpose of this work was to develop a multilayer sensing TBC deposited by electron beam physical vapour deposition (EB-PVD) which could be used to remotely measure the temperature at different depths in the coating. In this study, the reader is introduced to the theory of luminescence sensing and its TBC application. Several yttria partially stabilised zirconia TBCs, co-doped with rare earth oxides (YSZ:RE) phosphors, were studied and it was shown that dysprosia doped YSZ has the highest temperature sensitivity. The influence of dopant concentration, layering and high temperature aging on the phosphorescence process were also researched. During the project, a novel, non-destructive, method to monitor the high temperature degradation of the TBC using phosphorescence measurements was found. Alternative phosphor compositions, based on yttrium aluminium garnet (YAG) material, were successfully deposited by EB-PVD and it was shown that doped YAG TBC compositions could further improve the maximum temperature measurement capability of current sensing TBCs. A multilayer EB-PVD coating comprising of two different phosphor layers was deposited and tested in order to demonstrate that such systems could be used to remotely measure the temperature at two different depths in the TBC simultaneously and therefore to monitor the thermal gradient in the coating, permitting the direct measurement of heat flux under thermal gradient conditions, for example in service.

ACKNOWLEDGEMENTS

-Peter (*DooDoo*), my "*bounce*" partner…Stop pretending you can aim!

-Laura for the collaboration at the beginning and this last *Pt* deposition (and yes you can cook lasagne in 30 min).

-Everybody in Building 57, staff, students, FREDs, they all contributed to the friendly working environment.

-Security for not having clamped my car.

Finally, this thesis is dedicated to my parents and my little brother (*mon p'tit Vomitou*).

CONTENTS

LIST OF SYMBOLS

APS	Air Plasma Spraying
AU	Arbitrary Unit
c	Cubic phase
c/a	Tetragonality
CMAS	Calcium-Magnesium Alumino Silicate
CTS	Charge Transfer State
D/t	Ratio between Column diameter and the coating thickness
DS	Directionally Solidified
EB-PVD	Electron Beam Physical Vapour Deposition
EDX	Energy Dispersive X-ray
E-SEM	Environmental Scanning Electron Microscope
FOD	Foreign Object Damage
IGT	Industrial Gas Turbine
LTD	LifeTime Decay
m	Monoclinic phase
PX96	Alumina polycrystal substrate, 96% purity

PX99	Alumina polycrystal substrate, 99% purity
SEM	Scanning Electron Microscope
SFC	Specific Fuel Consumption
SX	Single crystal
SX99	Alumina single crystal substarte, 99.99% purity
t	Tetragonal phase
t'	Metastable tetragonal phase
t''	Yttria rich metastable tetragonal phase
τ	Phosphorescence lifetime
TBC	Thermal Barrier Coating
TGO	Thermally Grown Oxide
T_m	Melting point of the coating material
VIA	Vapour Incident Angle
XRD	X-Ray Diffraction
YAG	Yttrium Aluminium Garnet
YAG:RE	Yttrium Aluminium Garnet doped with Rare Earth oxide
YAG:Dy	Yttrium Aluminium Garnet doped with dysprosia
YAM	Yttrium Aluminium Monoclinic
YAP	Yttrium Aluminium Perovskite
YSZ	Yttria partially Stabilised Zirconia
YSZ:RE	Yttria partially Stabilised Zirconia co-doped with Rare Earth oxide
YSZ:Dy	Yttria partially stabilised zirconia co-doped with dysprosia

LIST OF FIGURES

*L*IST OF TABLES

INTRODUCTION

The gas turbine is a power plant which generates a considerable amount of energy for its size and weight. It produces energy from a flow of hot gas resulting from the combustion of a wide variety of fuels like natural gas, biomass gas, diesel fuel, naphtha and crude oil. Since its first successful application less than a century ago, the gas turbine has played an increasingly important role in the power generation and aerospace industries throughout the world.

The increasing consumption of energy, airline traffic, environmental concerns and the expected shortage of fossil fuel have driven the need to develop highly efficient turbines. This "quest" is closely related to the gas temperature at the entrance of the turbine section: the higher the turbine entry temperature, the higher the thermal

efficiency and the lower the emission of pollutants. Therefore advances in high temperature materials and coating technology are crucial for future developments.

In today's engine, Thermal Barrier Coatings (TBCs) protect internally cooled turbine components by reducing the metal surface temperature and allow those parts to operate at temperatures above their melting point. A TBC system consists of a metallic bond coat, a thermally grown oxide (TGO) and a ceramic top coat which is typically applied by Air Plasma Spraying (APS) or Electron Beam Physical Vapour Deposition (EB-PVD). A thermal gradient up to 150°C can be achieved with current TBC systems. It is believed that TBCs have not reached their full potential and their properties can be further improved for even better material protection.

The principal objective of this work is to design a multilayer "sensing" EB-PVD TBC with sensing capabilities using the temperature dependence of the phosphorescence process. A detailed description of the concept of sensing TBCs will be given in the chapter entitled "**Sensing TBCs**". The main idea is to deposit two phosphor layers, one at the TGO/ceramic interface and one at the top surface of the TBC, this will enable simultaneous remote temperature measurements at two different depths in the coating and the determination of the thermal gradient across the thickness of the TBC.

The development of a sensing TBC is stimulated by numerous factors, as it has been said before, the improvement in the efficiency in a gas turbine is achieved by increasing turbine entry temperatures but also by reducing the amount of air used to cool the turbine blades. Thus knowing the surface metal temperature under realistic conditions

would enable the design of an advanced cooling strategy in the most efficient way using a minimum amount of air. This, in turn, will increase fuel efficiency and reduce CO_2 emissions of gas turbine engines.

Moreover, the major life-controlling factor for TBC systems is believed to be linked with the temperature at the bond coat/top coat interface therefore it is desirable to monitor this temperature in-situ. Other failure mechanisms which are also temperature dependent like creep, ceramic sintering or phase transformation are of great importance in assessing the lifetime of a TBC. Therefore, accurate temperature measurement within a TBC would provide useful data to further the understanding of such damage mechanisms. Furthermore, since the temperature can be monitored at different depths in the coating, thermographic phosphors could enable accurate temperature gradient measurement within the TBC under realistic conditions.

Failure, in the form of spallation or delamination of the coating or erosion, will cause a local reduction of the coating thickness, if a sensing TBC was used, the resulting increase in metal surface temperature could be monitored, hence, providing an excellent means to assess the "*health*" of the TBC. Finally, sensing TBCs could provide structural information because the wavelength, relative intensity and line width of the emission lines are sensitive to the material phase, therefore, it could give information about the degradation processes in the zirconia layer. Consequently, an accurate temperature measurement in the TBC would result in the development of better TBC systems with longer lifetime and it would also enable one to predict both the coating and the component lifetime.

The initial work of this thesis consisted of identifying possible phosphors with high temperature capabilities. Once high temperature phosphors were identified, their deposition by EB-PVD as a coating was assessed. The influence of the phosphor on other properties of the coating, such as its microstructure and its phase stability at high temperature, was also characterised.

The correct percentage of dopant, such that the luminescence intensity was a maximum, was determined along with the effect of aging and phase transformations on phosphorescence. This study led to the development of two techniques to quantitatively determine the extent of monoclinic phase formation during heat treatment using phosphorescence.

Once the correct systems had been developed, the next challenge was to develop a procedure to produce multilayer TBC systems using EB-PVD deposition techniques. The use of phosphors with different matrices was also investigated in order to extend the temperature sensitivity of sensing TBCs beyond 1500°C. Such compositions have never been deposited by EB-PVD and required the characterization of the deposition parameters and the manufacturing of the ingots to be evaporated. The last step was the deposition of a multilayer coating that would enable one to monitor the temperature at two different depths in the coating in the temperature range that would experience a TBC during service.

1. THERMAL BARRIER COATINGS

1.1. History

In all types of gas turbine engines, aircraft or industrial high pressure turbines, first stage turbine blades operate under the most arduous conditions of temperature and stress, experiencing a wide range of thermal and mechanical loadings during service such as creep, fatigue, thermomechanical fatigue, erosion and also oxidation and hot corrosion. For more than 50 years there has been a need to improve engine combustion efficiency, reduce specific fuel consumption and emissions of pollutants like CO_x, SO_x, NO_x and unburned particles. This has been achieved by increasing the operating temperatures and pressures within the turbine section of gas turbine engines to get close to the combustion stoichiometry of the fuel (**Figure 1**) and, therefore, it has necessitated the development of improved material systems with higher temperature capabilities.

This chapter will give a short history of the main steps that led to the current TBC systems. It will end with a brief description of the two main processes used to deposit TBCs and the resulting coating microstructures.
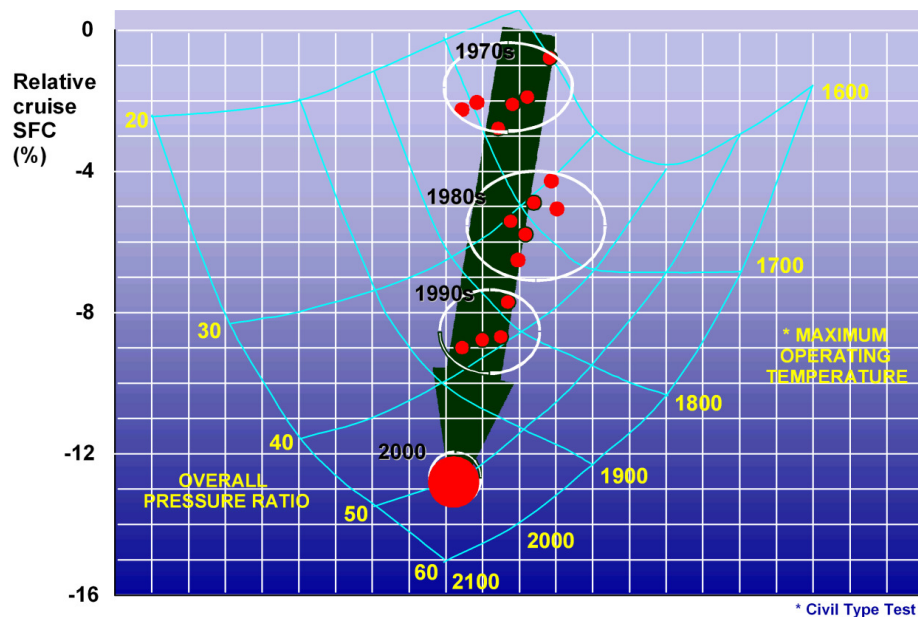
Figure 1: Improvement in efficiency with increasing operating temperature and pressure for a family of Rolls-Royce engines (SFC: Specific Fuel Consumption) [1].

1.1.1. *Evolution of gas turbine materials*

In the early years, improved performance was achieved by novel material design and nowadays only high temperature nickel-based superalloys are used. These alloys have matured over the years from wrought to cast, then to directionally solidified alloys with the latest generation of turbine blades being single crystal material (**Figure 2**) [1;2]. These technical advances have resulted in an improvement in creep resistance of 80°C to 120°C [3]. Reduction in metal surface temperature has also been achieved with the development of complex internal cooling systems as represented in **Figure 3**.
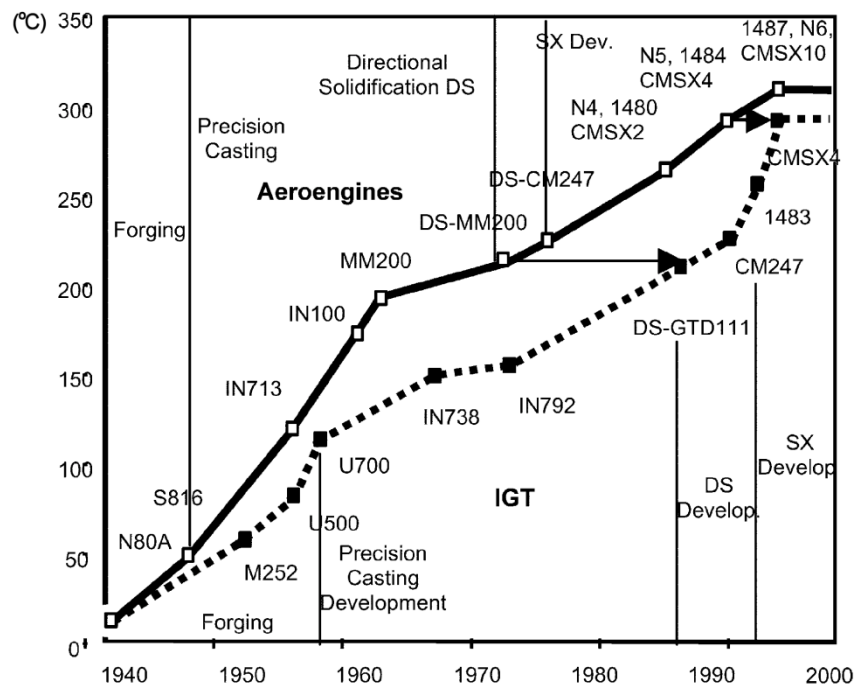
Figure 2: Increase of operating temperature of turbine materials enabled by alloy development and manufacturing technology (IGT: Industrial Gas Turbine, DS: Directionally Solidified, SX: Single crystal) [4].
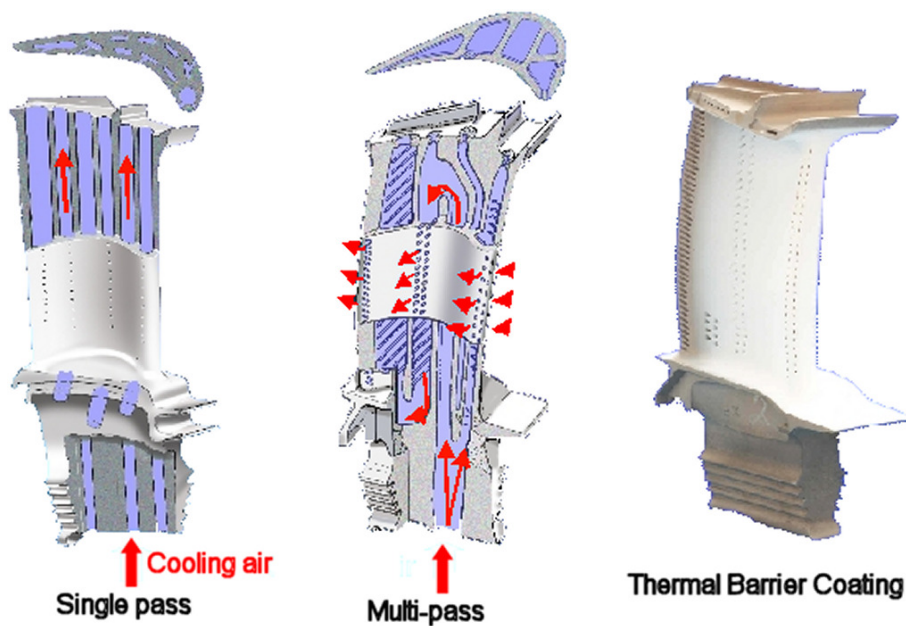
Figure 3: Turbine blade cooling [5].

Each step in the development of superalloys has led to materials with better mechanical properties such as creep or fatigue resistance. However, oxidation and corrosion

resistance are other factors that limit the increase in turbine entry temperature. Further gains in performance will require either a change in the family of turbine blade materials or coatings capable of supplying the necessary oxidation and corrosion protection.

1.1.2. Development of surface coatings

In the early 1960s, due to environmental degradation the blades failed prematurely and for the first time surface coating were considered. Diffusion aluminide coatings were the first environmental protection coatings introduced into service. They provided a cheap, cost effective solution and significantly extended component life. Such coatings could be applied using pack and slurry cementation or various kinds of chemical vapour deposition processes. The properties of aluminide coatings are strongly dependent on the substrate and the processing route, therefore, overlay coatings were introduced in the early 1970s [1;6].

The MCrAlY coatings, where M is Ni, Co or a mixture of Ni and Co, offer the capability of custom designing alloys, the composition of the MCrAl part of the system is selected to give a good balance between corrosion resistance and coating ductility while the active element additions (Y) in conjunction with aluminium and chromium are intended to enhance oxide-scale adhesion and decrease oxidation rates [1]. Many compositions have been developed adding singly or in combination tantalum, tungsten, titanium, hafnium, silicon, niobium, rhenium and zirconium, together with various precious metal additions, to adjust the properties of the coating for specific purposes [7].

The manufacture of these coatings is dominated by Electron Beam Physical Vapour Deposition (EB-PVD) and Low Pressure Plasma Spray (LPPS) [1;7]. Most recently, an alternative strategy which consists of designing a coating system that lowers the metal surface temperature has been introduced.

1.1.3. Introduction of Thermal Barrier Coatings

In today's engine, the hot gas temperature exceeds the melting point of the Ni-base alloys by more than 250°C [2]. Internal and external cooling is used, but further increases in cooling may not be a viable option since it reduces the overall thermal efficiency of the engine. Consequently, the melting point of the alloys clearly marks the limit for future developments based on metallic alloy designs [2;8]. Thermal Barrier Coatings (TBCs) have been developed to lower the metal surface temperature and with recent TBC systems a temperature gradient of 150°C can be achieved on internally cooled turbine parts [1].

Figure 4 illustrates the potential benefits that can be offered by TBCs for turbine blade applications. Due to the thermal insulating properties of TBCs, for a given cooling air flow turbine blades can operate at higher temperature, this results in higher engine thrust, or the metal surface temperature can be lowered hence improving the lifetime of the component. Moreover, to achieve the same metal temperature less cooling is required when using TBCs and therefore the performance of the engine can be improved [2;8].

The material used for the TBC, obviously, must have a low thermal conductivity but it must also withstand thermal shocks, hot corrosion, oxidation and erosion. It has to be stable at very high temperatures and have a density as low as possible to reduce the stresses due to the centrifugal loading. Ceramics are therefore the material of choice and in the 1970s TBCs based on partially stabilised zirconia were introduced [1;7].
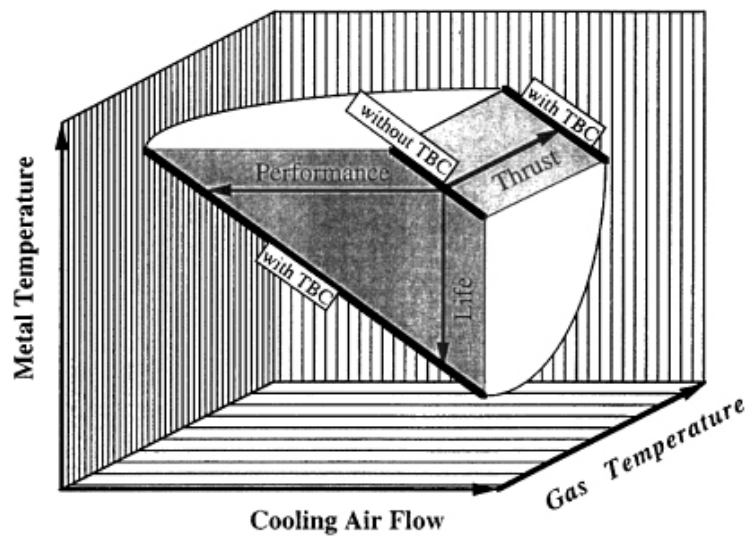
Figure 4 : Potential benefits of TBCs [8].

Early TBCs were zirconia stabilised with magnesia or calcia, but at temperatures above 1000°C there was significant diffusion of magnesium or calcium ions resulting in the formation of precipitates rich in MgO or CaO and this lead to an increase in thermal conductivity due to the formation of a monoclinic phase within the top coat [1;6;7]. Moreover, the phase transformation from monoclinic (the low temperature phase) to tetragonal (the high temperature phase) is associated with a volume increase between 4 and 6% which builds up stresses in the coating and on thermal cycling microcracks are generated which can lead to early failure of the TBC system.

This problem of phase instability was solved in the late 1970s by stabilising zirconia with yttria [1], providing a material which was stable at temperatures up to 1500°C for long periods. Y_2O_3 forms a solid solution with ZrO_2 thus enabling to lower the tetragonal to monoclinic transformation. The initial Yttria partially Stabilised Zirconia (YSZ) contained 12-20 wt.% of yttria to totally stabilise the cubic phase, but *Stecura et al.* [6] showed that better performance could be achieved by lowering the yttria content to 6-8 wt.% (**Figure 5a**) and nowadays 8 wt.% YSZ TBCs have become the industrial standard [6;9]. With 6-8 wt.% yttria, a *t'* phase is obtained which is a metastable phase. This *t'* phase has outstanding bend strength, high crack propagation energy, high thermal shock resistance and high fracture toughness, therefore, it is the most effective phase to provide durable TBCs. The *t'* phase is remarkably stable at temperatures up to 1200°C, therefore, the TBC remains single-phase over its useful life [10-12] (**Figure 5b**).

(a)   (b)
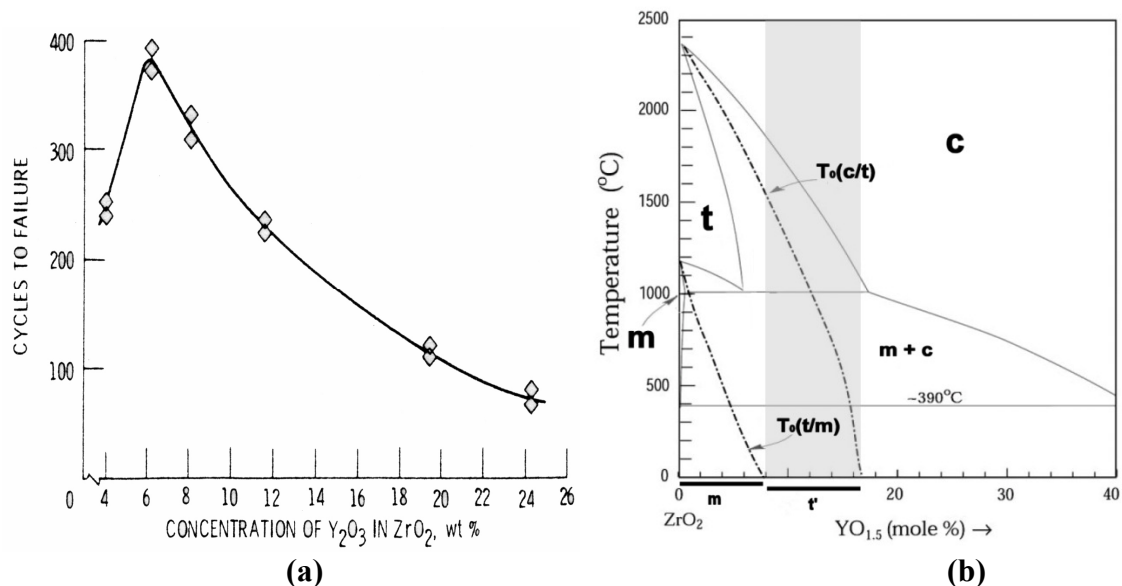
Figure 5: (a) Effect of Yttria content on the lifetime of TBCs [9], (b) phase diagram of the system ZrO_2-Y_2O_3 [13] (*c*: cubic, *t*: tetragonal, *t'*: metastable *t*, *m*: monoclinic phase).

1.1.4. A multilayer coating

Current TBCs consist of a two layer system, a 125-250 µm top coat which aims at reducing the heat transferred to the substrate and an oxidation-resistant metallic bond coat (**Figure 6**). The top coat is typically a layer of porous 6-8 wt.% YSZ applied by air-plasma spray (APS) or electron-beam physical vapour deposition (EB-PVD).
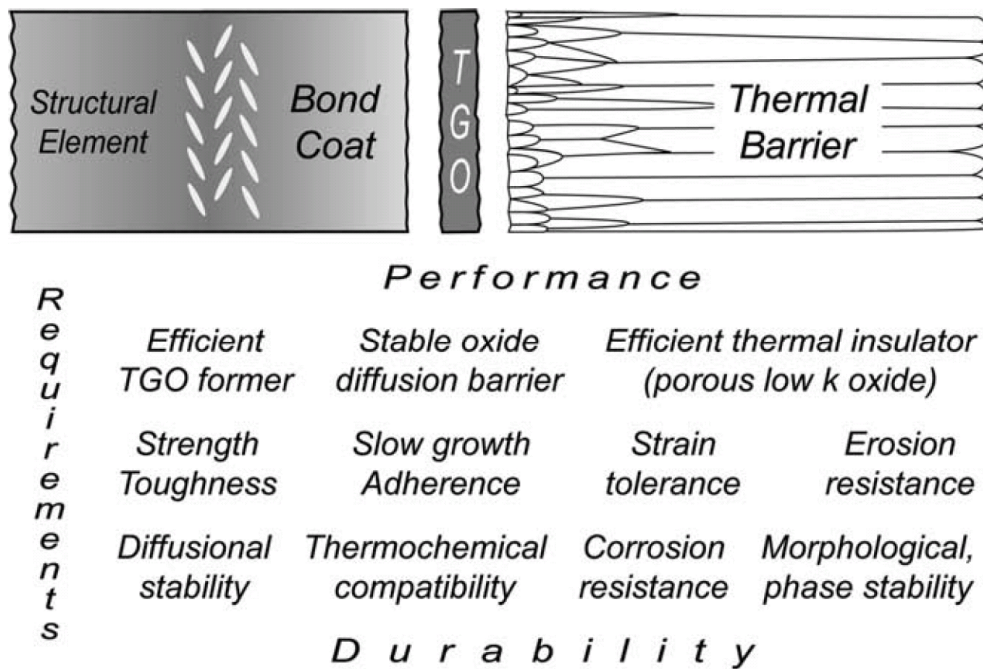
Figure 6: Schematic representation of a thermal barrier system [14].

The first layer, a bond coat, is applied to ensure the protection of the substrate against oxidation and high temperature corrosion but also to provide a good adhesion of the top coat to the substrate. For EB-PVD TBCs it is generally, a single phase β-(Ni,Pt)Al often referred to as a platinum aluminide bond coat system, an MCrAlY overlay coating or a platinum diffused surface treatment. Platinum aluminide coatings are applied by electrodeposition of Pt and subsequent aluminizing by some form of chemical vapour

deposition. Finally heat treatment ensures the formation of the β-phase by inter-diffusion. Depending on the process parameters their thickness ranges typically between 50-60 μm with Al and Pt contents between 17-21 wt.% and 25-28 wt.% respectively [15]. The two phase overlay (γ'+β/γ) MCrAlY coating is usually applied by Low Pressure Plasma Spray (LPPS) or by EB-PVD. A typical composition would be (Ni, Co)-15-28 wt.% Cr, 4-18 wt.% Al, 0.5-0.8 wt.% Y for a bond coat thickness between 75-125 μm [1;2;8].

During manufacture and subsequent service, a Thermally Grown Oxide (TGO) is formed, it is a layer of α-Al_2O_3 which grows by thermal oxidation of the underlying bond coat. This TGO plays an important role for the environmental protection and the adherence of the TBC [8]. So as shown in **Figure 6**, a typical modern TBC consists of a bond coat, a TGO and a thick ceramic layer. The effect of the bond coat composition on TGO and on the cyclic life of the coating will be discussed in a following chapter.

1.1.5. Deposition processes

Nowadays APS and EB-PVD are the two main competing processes to apply TBCs under industrial conditions. The EB-PVD process is mainly used for relatively small parts in aerospace turbines such as the blades and the vanes, however, for larger components like the combustion chamber or for blades and vanes for industrial gas turbine application, plasma spraying is the process of choice.

1.1.5.1. Plasma Spraying

In atmospheric plasma spraying (APS) a high velocity plasma flame is generated with an electric arc and an inert gas, generally argon. The ceramic is fed into the high temperature flame as a powder, the particles become semi-molten and are propelled onto the substrate, then they impact the surface, forming splats and building up a coating with a "*splat-type*" morphology (**Figure 7**). The different splats which form the coating principally mechanically interlock together and variations in this interlocking and consequently the amount of porosity are important material properties.
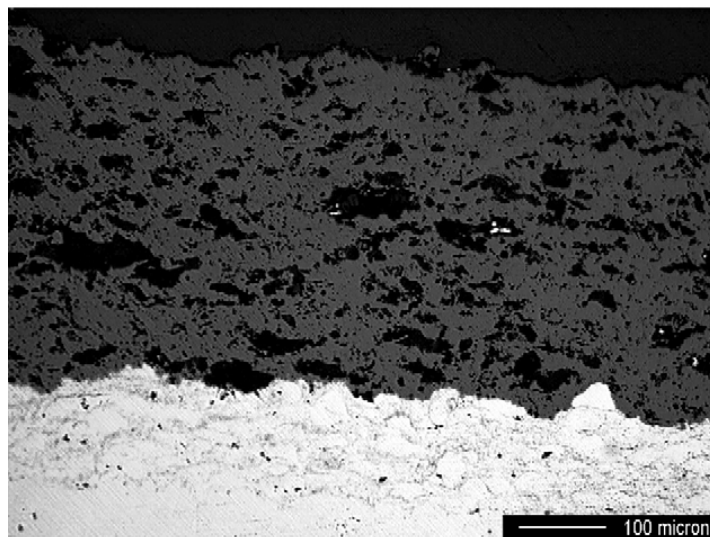
Figure 7: Micrograph of an APS TBC [17].

Plasma spray is a very versatile process and can be operated in various atmospheres and at different pressures. However, due to their poor surface finish, low corrosion resistance and poor mechanical compliance the use of plasma sprayed TBCs was not extended to high-pressure turbine blades for aero applications. This problem was overcome when the EB-PVD process emerged in the 1980s [1].

1.1.5.2. *Electron Beam Physical Vapour Deposition*

In this process a high energy electron beam is used to melt and transform the ceramic source ingot into a vapour phase. To ensure continuous TBC growth, ingots are bottom fed into the crucibles during evaporation. Substrates are preheated and then positioned in the vapour cloud. The vapour travels along the line of sight to the substrate surface where it condenses atom by atom at a deposition rate of 4-10 μm/min. This process is carried out under a low partial pressure of oxygen to preserve the stoichiometry of the zirconia.
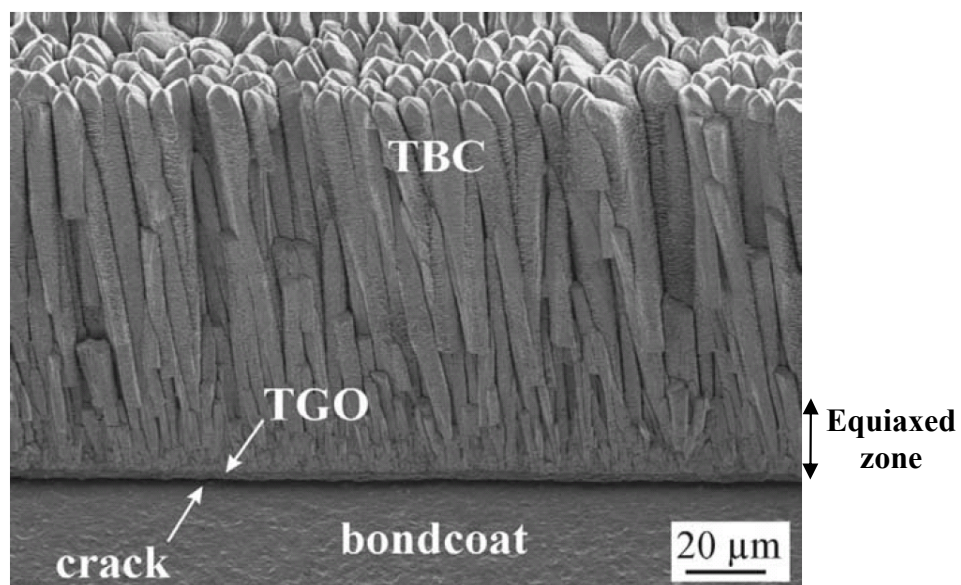
Figure 8: Micrograph of an EB-PVD TBC (Fractured sample, not polished) [2].

TBCs deposited by EB-PVD exhibit a unique columnar microstructure grown from the vapour phase (**Figure 8**). The microstructure of EB-PVD TBCs strongly depends on many parameters, including principally shadowing, surface diffusion, volume diffusion and desorption. The columnar microstructure will be also influenced by the surface roughness and the temperature of the substrate, the deposition rate, the gas pressure, the

degree of ionization of the vapour cloud, the chamber pressure, the vapour impact angle and the rotation of the substrate during deposition. The influence of each of these parameters will be discussed in a following section.

As has been shown in this chapter, the microstructures of the coatings produced by EB-PVD and APS are very different. The following chapter focuses on the unique properties of the EB-PVD coating, its particular microstructure, which leads to coatings with important variations in properties such as surface finish, erosion resistance and thermal conductivity, compared to APS TBCs.

1.2.   Properties of EB-PVD TBCs

1.2.1. Microstructure

TBCs deposited by EB-PVD possess two main microstructural features. The most obvious is their unique columnar microstructure, grown from the vapour phase. During the first rotation of the sample in the vapour cloud, a large number of nuclei start to grow forming a thin layer adjacent to the substrate of equiaxed grains of about 30 nm in diameter [18]. This layer is often referred as the equiaxed zone (**Figure 8**). The thickness of this zone varies from sample to sample and has no preferred orientation. Then grains that have a favoured growth direction will grow preferentially, the others being eliminated from the coating. This competitive growth results in the formation of columns with their diameter increasing and consequently their number decreasing as the top of the coating is approached. Contrary to the equiaxed zone, this part of the coating

has a preferred {100} crystallographic orientation [19]. The inter-columnar gaps separating the columnar grains are highlighted in **Figure 9** (denoted *type 1*).

The other characteristic feature of EB-PVD TBCs is their featherlike structure (*type 3* in **Figure 9**). This is the result of shadowing by growth steps on the column tips near the centre of the column [20]. These feather arms are often aligned at 45˚ toward the column axis and are typically between 5-20 nm across and 200-250 nm long [20;21].
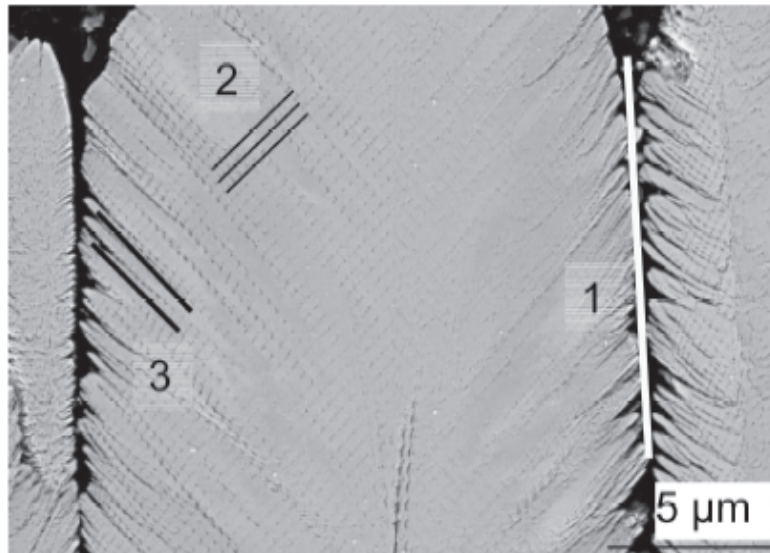
Figure 9: Morphology of a column of an EB-PVD TBC (Polished sample) [20].

Type 2 intra-columnar pores are mostly closed globular and elongated spheroids parallel to individual column tips. They are a consequence of rotation and generally range between 18 and 15 nm in diameter.

As it has been said, the processing parameters of EB-PVD TBCs affect their microstructure and therefore their properties. The microstructure of the coating can be roughly predicted using the *Thornton* or the *Movchan* and *Demchishin* structure

diagrams represented in **Figure 10**. In these diagrams the coating texture is divided into different zones according to the processing temperatures (*T*) normalized to the melting point of the coating material in Kelvin (*Tm*).
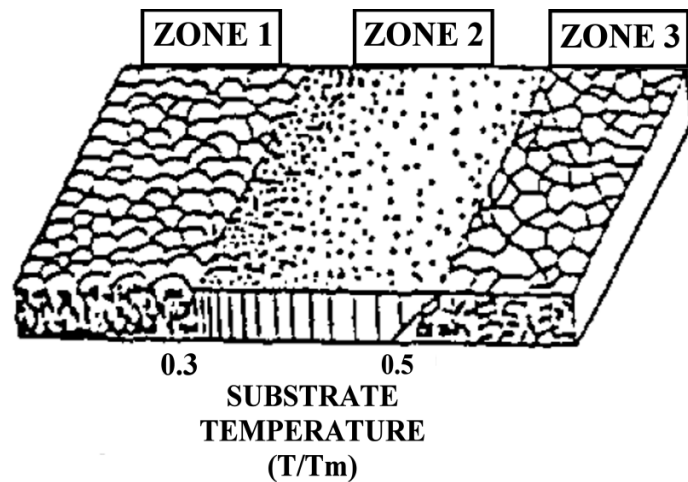
(a)
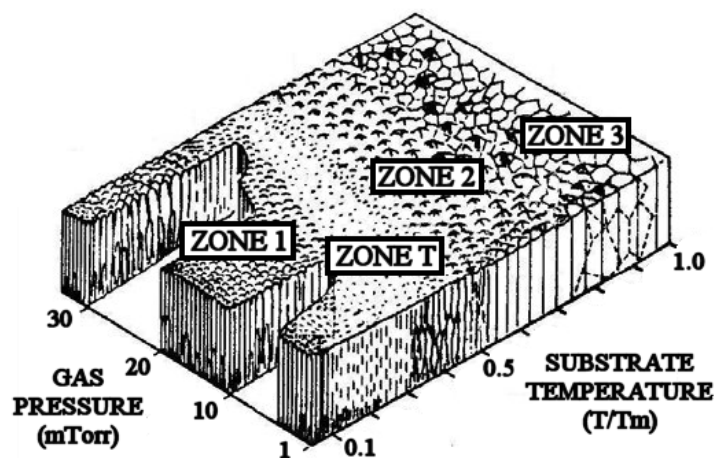
(b)

Figure 10: (a) *Movchan* and *Demchishin* **[22] and** *(b) Thornton* **[23] structure diagrams (*T*: Processing temperature, *T_m*: Melting point of the coating material).**

Various studies reported that the crystallographic growth direction depends on the vapour incident angle (VIA), defined as the angle between the vapour flux and the

substrate surface. Consequently, it varies with the sample geometry or its position in the coating chamber [24-27]. Moreover, as the VIA increases, the intercolumnar pores become larger and therefore the porosity of the coating is raised [27]. It was also found that the density of the TBC increases as the pressure in the chamber is increased and that sample rotation influences the columns' shape and diameter (**Figure 11**) and also the orientation of the coating and its density [24;26;28;29]. Finally, the crystal orientation, as well as the morphology of the columnar grains and the density of the TBC, change with chamber and substrate temperature [18;24;29]. This preheating temperature also influences the structure and orientation of the coating [30].
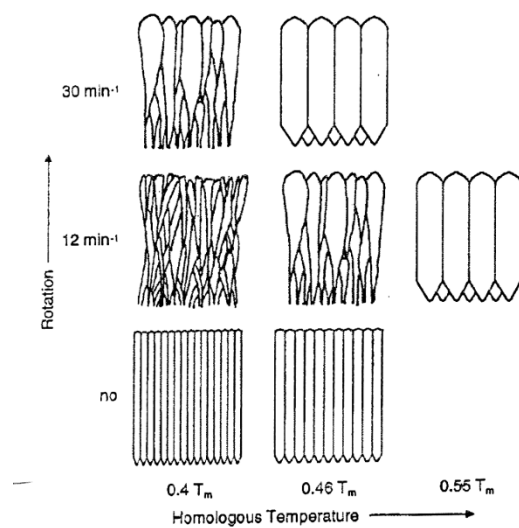
Figure 11: Influence of substrate temperature and rotation speed on the microstructure of EB-PVD TBCs (T_m: Melting point of the coating material) [26].

The performances of EB-PVD TBCs are linked to their microstructure therefore it is of primary importance to understand the effects of processing parameters on this structure, in order to control and improve TBC properties.

1.2.2. Surface finish

The EB-PVD technology produces coatings with a better surface finish compared to the APS TBCs, therefore, the need for final polishing is eliminated. Furthermore, the EB-PVD process does not block the cooling holes of the blade. Typically an EB-PVD TBC has a surface roughness of 1 μm compared to 10 μm for an APS TBC [31;32]. The smooth surface of EB-PVD TBCs is a clear advantage from the aerodynamics point of view, thus, it is a process of choice for turbine blades where the aerodynamics is of primarily importance. Moreover, if the surface does not have the required smoothness, the gas boundary layer becomes more turbulent causing increased mixing of turbine gases and this can result in an increase in the temperature of the TBC surface and therefore in the heat transferred to the substrate [8;33].

1.2.3. Thermal conductivity

The thermal conductivity of the YSZ strongly depends on the microstructure of the coating and hence on the method of deposition. APS TBCs have the lowest thermal conductivity, typically 0.8-1.1 W/mK, compared to 1.5-1.9 W/mK for EB-PVD TBCs and 2.2-2.9 W/mK for bulk YSZ [14;31;34].

The low thermal conductivity of the APS TBCs is due to a two dimensional microcrack network. During deposition the different splats do not interlock altogether perfectly, leading to a microcrack network parallel to the coating surface. When the splats cool down microcracks are formed generating a second network of cracks row perpendicular to the coating surface. Cracks parallel to the coating are very efficient in reducing the

thermal conductivity as they form interfaces which are directly perpendicular to the primary heat flux [31]. It should also be noted that after a few hours of operation the thermal conductivity of APS TBCs increases to 1.5 W/mK due to sintering of these lamellar crack networks [34].

Such cracks are not present in EB-PVD coatings. The *type 1* porosity, reported in a previous chapter, is aligned with the primary heat flux, thus, it is much less effective in lowering the thermal conductivity [31]. Consequently reduction in thermal conductivity relies principally on the *type 2* and *type 3* intra-columnar porosity. The porosity in EB-PVD TBCs is strongly affected by the processing parameters, therefore, it is possible to tailor their microstructure in order to improve thermal properties and this will be discussed in a later chapter. It is worth noting that the thermal conductivity is not homogenous across the entire thickness of the EB-PVD TBC. In the equiaxed zone, where there is a large number of interfaces, microporosity, grain boundaries and randomly oriented grains which scatter the thermal waves, the thermal conductivity is lowered to around 1 W/mK [31;34]. With increasing thickness, the grains are less numerous and have a higher aspect ratio resulting in a more crystallographically perfect structure, therefore, the thermal conductivity increases to approach that of bulk zirconia (2.2 W/mK) [31;34].

1.2.4. Erosion resistance

Another feature of EB-PVD TBCs that depends on the microstructure is erosion. The erosion mechanisms and properties will be fully reviewed in the following section. As

has been said previously, the unique columnar microstructure of EB-PVD TBCs offers improved mechanical properties, compared to their APS counterparts [35;36]. It is shown in **Figure 12** that the erosion resistance of EB-PVD TBCs is up to 10 times better than APS TBCs, but this depends on orientation.
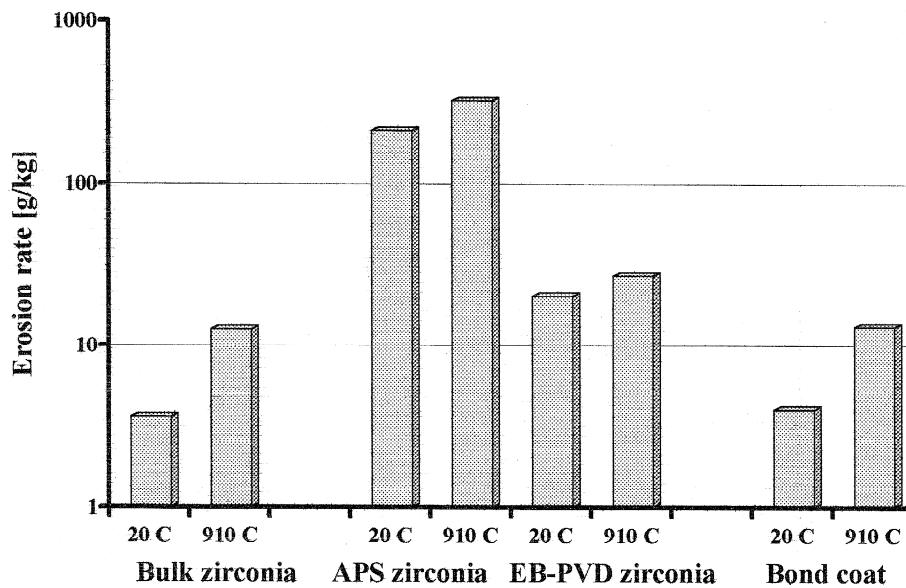
Figure 12: Erosion rates of zirconia–8 wt.% yttria TBCs by 100 μm alumina, 90° impact, at room temperature and 910°C [36].

APS TBCs have a horizontal splat-like structure which contains a critical network of favourably aligned cracks, and particle boundaries, parallel to the coating surface which make this coating more susceptible to particle impact damage [35-37].

On the contrary, the ceramic columns of EB-PVD TBCs provide excellent strain tolerance as they can move relative to each other under mechanical load or thermal cycling. Moreover, as EB-PVD TBCs do not have a crack network parallel to the surface, a much higher energy is required to generate a crack across individual columns [8;36;38]. Furthermore, the surface finish of EB-PVD TBCs is not widely affected by erosion as the damages are limited to the near surface region. However, with polished

APS TBCs, erosion rapidly reverses the surface finish to the as deposited state reducing the aerodynamic efficiency [33].

Nowadays, TBCs are commonly deposited onto hot gas path components of aero-engines and industrial gas turbines. The advantages provided by the EB-PVD technique enabled their use in more severe environments, like in the high pressure turbine section on high loaded turbine blades and vanes.

Even though TBCs are well engineered materials and significantly increase the turbine efficiency as well as the lifetime of its components, it is believed that they have not reached their full potential. The various failure modes of TBCs are well known and numerous research studies are aimed at improving the TBCs' properties. Bond coat optimization, progress in erosion resistance, resistance to chemical degradation, reduction in thermal conductivity are all areas where major improvements can be made to further increase the temperature capability and thus the lifetime of gas turbines. In the following section, the main TBC damage mechanisms will be briefly reviewed, mainly focussing on the possible loss of the ceramic top coat.

1.3. Failure modes

The type and cleanliness of the fuel, the cyclic loading, the maximum operating temperature and the times at temperature varies between industrial and aircraft gas turbines. Industrial gas turbines typically operate under continuous conditions at temperatures around 1100°C, with materials life requirement ranging between 25000

and 50000 hours. In aero-engine applications the temperature are generally higher, around 1500-1600°C, and the cycles significantly shorter. The different gas turbine applications lead to variations in the severity of the different degradation mechanisms.

1.3.1. Oxidation

Many failures in the TBC are linked with the oxidation of the bond coat, indeed, the growth of the TGO and the associated stresses and damage, often leads to the spallation of the ceramic top coat under thermal cycling [39;40]. The two main criterions for the failure of the TBC are the TGO critical thickness and the depletion of the aluminium reservoir used to grow the oxide layer [41]. A low concentration of aluminium at the bond coat surface results in the formation of spinels which are less effective in protecting the alloy compared to α-alumina [40].

Another mode of failure is associated with the buckling of the coating. The difference in thermal expansion between the coating and the underlying superalloy builds up compressive stresses in the bond coat upon cooling, leading to progressive interface separation at localized flaws and subsequent spallation [40;42-45]. These flaws come from the roughening of the bond coat during thermal cycling and it is only recently that two mechanisms have been proposed to explain the nucleation of such flaws.

The first one is attributed to "*racheting*" [40;46]. The growth of the TGO is associated with compressive stresses and, because of the constraints generated by the underlying bond coat, it can only release its strain energy by undulating via plastic deformation of the bond coat and the TGO itself.

The other mechanism is the result of the aluminium depletion of the bond coat. This depletion and the progressive enrichment of nickel that diffuses from the underlying superalloy, lead to the formation of γ'-Ni_3Al and martensitic β-NiAl within the bond coat. The formation of these phases is associated with volumetric changes which cause roughening of the bond coat to occur [47;48].

1.3.2. Erosion

During operating conditions, ingested erosive solid particles and also erodent resulting from the combustion process, can cause significant damage to the thermal barrier coating. This problem is of primary importance since even partial removal of the TBC results in an increase in surface temperature reducing the turbine component lifetime.

A good amount of work has been published on the erosion of EB-PVD TBCs in the as-received condition under various conditions of temperature, velocity, impact angles and with different types of erodent [35;36;38;49-52]. The erosion mechanisms of EB-PVD TBCs have also been well described by *Nicholls*, *Wellman* and *Evans et al.* [38;49;51]. The effect of heat treatments on the properties of TBCs is also well documented, *Wellman et al.* [53] have researched the erosion of aged samples at room temperature, as aged samples reflect the true erosion behaviour of EB-PVD TBCs in a gas turbine engine.

The erosion of EB-PVD depends on the temperature, the velocity and the size of the impacting particles and three modes of material removal have been observed depending

on the interaction of these factors. More relevant than the size of the particles, is the relative size between the column diameter and the contact footprint of the impacting particle, which will affect the various mechanisms that lead to ceramic loss [51].

The first mode, erosion, occurs at room and high temperature with small impacting particles. It involves crack initiation at the elastic/plastic interface caused by the impact on individual columns. *Mode II*, called compaction damage, is a transition mechanism between erosion and Foreign Object Damage (FOD). It is characterised by the densification of the individual columns and the absence of near surface cracking or gross plastic deformation. This mode has been observed for larger particles at room and high temperature at intermediate velocities. FOD, the third mechanism, is caused by large particles at low velocity or smaller particles at higher velocity. Under these conditions, impacts cause significant cracking and gross plastic deformation of the columns. Two types of FOD have been identified, the *type I*, associated with gross plastic deformation of the coating with bending and shear cracking of the columns often down to the bond coat interface and *type II*, where buckling of the columns and plastic deformation without any significant degree of cracking have been observed [49-51].

1.3.3. Chemical degradation

Miller et al. [54] reported that silica impurity in YSZ significantly reduces the thermal cyclic life of the TBC. They have shown that silica concentration as low as 1 wt.% can reduce, by more than a factor of five, the thermal cycle life of APS TBCs and that silica impurity can dramatically increase the sintering rate of the coating [54;55].

Early studies on the effect of silicates on yttria stabilised zirconia revealed that aluminosilicate compounds form an amorphous phase that can dissolve YSZ at the grain boundaries, resulting in rounded ceramic grains. It has also been reported that such compounds can "extract" yttria from the coating material making the TBC more susceptible to transform to the monoclinic phase [56].

The same types of compounds, commonly referred as calcium-magnesium alumino silicate (CMAS), are found in the sand and debris ingested with the intake air by turbine engines. Early studies, available in the open literature, started after the Gulf War in 1990-91 where the turbine engines of Black Hawk helicopters experienced significant damages due to erosion caused by ingested sand particles [57;58]. It was noticed that such particles can become molten during operation and an amorphous deposits were observed on the first stage turbine vanes. At that time, the main concern was the blockage of the cooling passage and the potential hot corrosion of aluminised airfoils.

Stott et al. [59] was the first to discuss the effect of CMAS deposits on YSZ TBCs. He reported severe grain-boundary attack and yttria absorption by the CMAS melt leading to the early destabilisation of the coating. With the introduction of EB-PVD TBCs, and because of its columnar microstructure, the infiltration of CMAS deposits became more critical. The thermochemical interaction and the infiltration of CMAS deposits in EB-PVD TBCs have been studied in detail by *Kraemer et al.* [60]. It was also reported that the infiltration of CMAS in EB-PVD TBCs can introduce large stresses in the coating during cooling which could cause the delamination of the TBC [61;62].

1.3.4.   High temperature exposure

The high temperature environment in which EB-PVD TBCs operate has a tremendous effect on their properties. Densification, sintering, cracking due to partial transformation of the metastable *t'* phase to the monoclinic phase, increase in hardness, erosion rates and thermal conductivity all contribute to shorten the durability of the TBCs.

1.3.4.1. Phase transformation

As it has been said before, zirconia partially stabilised (6-8 wt.%) yttria coating deposited by EB-PVD has a metastable *t'* phase after deposition. Subsequent high temperature annealing at temperatures above 1200˚C results in the rapid partitioning of the non equilibrium *t'* phase into a mixture of a low yttria tetragonal phase (*t*) and a high yttria cubic phase (*c*). Then upon cooling the disruptive *t*→*m* phase transformation can take place, via the yttria depleted *t* phase.

The ZrO_2-Y_2O_3 phase diagram presents numerous metastable phases due to diffusionless phase transformations (represented by the dotted T_0 lines in **Figure 5b**). T_0 is the temperature where the free energy of the parent and produced phase are equal. Therefore, during cooling, the high yttria phase transforms into a metastable phase often referred as *t''* or *c'* when it intersects the $T_0(c/t)$ line. Likewise the low yttria phase transforms into monoclinic phase when the $T_0(t/m)$ line is crossed. It is worth noting that this monoclinic phase is also a metastable phase and will transform back to the tetragonal phase during heating.

Table 1: Phase composition of YSZ samples after heat treatment.

Composition (mol% Y₂O₃)	Sample preparation	Heat Treatment	Cooling rate	Phase composition	Ref.
4.5	Plasma sprayed coating on C263 substrate removed by chemical etch Aged in a Pt crucible	100h at 1200°C	Rapid air cooling (>50°C/min)	100% t'	[10]
		100h at 1300°C		$t+t''+c$	
		100h at 1400°C		$t+c$	
		100h at 1500°C		45% t 55% t''	
		100h at 1600°C		27% t 73% t''	
5.7		100h at 1400°C		$t+c$	
		100h at 1600°C		t''	
6.9		100h at 1600°C		t''	
4.5	Free standing plasma sprayed coating	1000h at 1150°C	Heating/cooling: 10°C/min	$t+c$	[63]
		100h at 1450°C		$c+m$	
3.9	Plasma sprayed coating on superalloy with an MCrAlY bond coat	500h at 1020°C	Cycled: heated 10-12h then cooled for 12-14h down to 300°C	26% m	[64]
3.9	Powder in alumina crucible	140h at 1400°C	<10°C/min	32% m	[65]
3.9	Plasma sprayed coating on steel substrate removed with an acid solution	50h at 1200°C	NA	$t + c$	[66]
		50h at 1400°C		$c + m$	
4.5	Acid stripped plasma sprayed coating	100h at 1400°C + 24h at 1480°C	<10°C/min	8.7% m	[67]
4.0	Powder synthesized by pyrolysis of solution precursor, aged in alumina crucible	24h aging cycles every 50°C from 1200 to 1400°C	Quenched in air	37% m	[13]
6.0		… from 1200 to 1500°C		15% m	
4.2	EB-PVD coatings on polycrystal alumina substrate	989h at 1200°C	Air cooled 300°C/min	18% t' 38% $c+t''$	[68]
		195h at 1450°C		44% t	
3.9-4.5	Milled free standing EB-PVD coating	200h at 1200°C	Slow enough to allow the $t \rightarrow m$ transformation	1% m, 26% c, 30% t'', 43% t	[69]
		100h at 1300°C		11% m, 41% c, 48% t''	
		100h at 1400°C		21% m, 54% c, 25% t''	
4	Plasma sprayed coatings on SUS304 substrate, acid stripped	200h at 1400°C	NA	No m phase	[70]
4.4	EB-PVD YSZ on polycrystal alumina	300h at 1500°C	Quenched in air	No m phase	[71]
4.5	EB-PVD coating on alumina 96% substrate	24h at 1500°C	NA	Large amount of m phase	[53]
3.9	EB-PVD coating on alumina sapphire	350h at 1400°C	NA	No m phase	[11]

The $t \to m$ phase transformation is associated with a volume increase of between 4-5% introducing a significant amount of stress in the coating which can lead to the formation of cracks and the spallation of the TBC. It is also reported that the cubic phase has a shorter cyclic lifetime and poor erosion resistance, compared to coatings with t' phase [9;29].

Depending on the heating and cooling conditions, the method of sample treatment, the type of substrate used, the presence of contaminants, or if the experiments are carried out on powders, ground or free standing TBCs, the time and temperature of destabilisation can vary significantly as illustrated in **Table 1**.

1.3.4.2. Sintering

High temperature causes the columns of EB-PVD TBCs to sinter together (**Figure 13**). During sintering the featherlike structure of the columns is smoothed out due to surface diffusion and undulations grow on the surface of the columns. Where the undulation of a column touches one of another column, a neck is formed and the columns sinter together [11]. These contact points between columns has the effect of increasing the young's modulus of the coating [72]. Further, the loss of nano-porosity reduces the thermal conductivity.

Sintering also leads to shrinkage of the coating and due to the constraint applied by the bond coat and the substrate, the gap between groups of sintered columns extends and "*mud-cracks*" are formed. This lateral shrinkage also has the effect of introducing

compressive stresses in the substrate which does not remain flat and tends to curve [11;53;71].
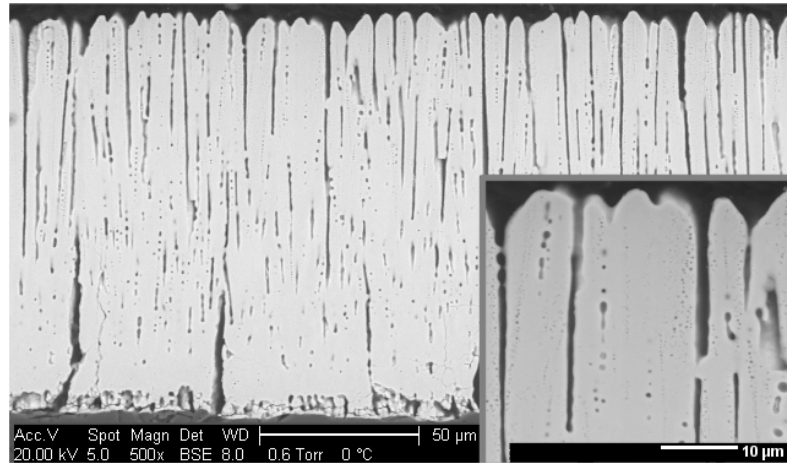
Figure 13: Sintered EB-PVD TBC.

Aging at high temperature causes changes in the pore size and distribution. At temperatures as low as 900˚C, the EB-PVD TBC microstructure becomes more coarse. The fine featherlike structure of EB-PVD columns transforms into large globular pores. The intra-columnar surface porosity is also reduced due to the conversion of small pores into larger ones. Since porosity is considered to reduce the thermal conductivity of the coating, sintering reduces the effectiveness of thermal barriers [69;71].

Wellman et al. [53] have shown that aged EB-PVD TBCs have a lower erosion resistance when compared to as received TBCs. Sintering causes columns to join together enabling cracks to propagate to the neighbouring columns resulting in a higher material loss per impact. The changes in porosity and mechanical properties, such as hardness or fracture toughness, also contribute to lower the erosion resistance. Reduction of column microporosity, column sintering and phase transformation increase

the coating hardness making it less defect tolerant (more brittle) and therefore less resistant to impacting particles [21;73;74].

1.4. Lowering the thermal conductivity

The theory of thermal conductivity in TBCs is well described in the literature [75;76]. In ceramic TBCs, heat can be transferred by lattice vibrations and radiation, their energies consist of quanta called phonons and photons respectively. A reduction of the thermal conductivity involves lowering the mean free paths and/or the velocity of these heat carriers or to lower the density of the material. This is achieved by introducing imperfections in the lattice such as vacancies, dislocations, grain boundaries, local strain fields in order to scatter phonons. The techniques to engineer low thermal conductivity TBCs can be divided into two groups: those which change the chemical composition of the coating and those which change the coating microstructure.

1.4.1. Coating microstructure

Tailored microstructures are generally obtained by varying the deposition parameters. For instance by lowering the substrate temperature an imperfect coating with low density is deposited and a reduction in thermal conductivity up to 15% can potentially be achieved with this technique [20].

Another way is to produce a coating with inclined columns. The deviation of the substrate from the normal vapour incidence by tilting the rotational axis, for example can produce a "*zig-zag*" microstructure (**Figure 14**). The increase in porosity at the

boundaries between the layers enables a reduction in thermal conductivity up to 40%. However the inclined columns suffer from poor erosion resistance compared to standard EB-PVD TBCs [20].
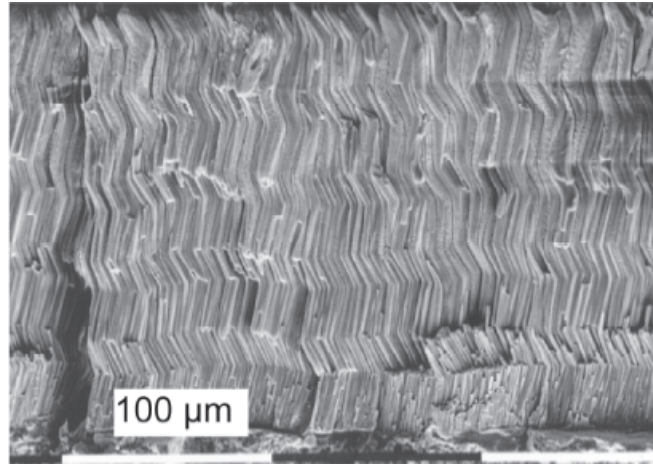
Figure 14: EB-PVD TBC with a "zig-zag" structure [20].

Nicholls et al. [76] highlight the fact that the equiaxed zone of the EB-PVD coating possesses a much lower thermal conductivity due to a large number of grain boundaries. Another effective way would be to maintain this microstructure in the entire coating. This can be achieved by sequentially inserting and removing the sample from the deposition chamber or by inserting a contaminant atmosphere in the deposition chamber to interrupt the growth and cause the re-nucleation of the coating [77]. This could lead to a maximum reduction of 30% in the thermal conductivity.

1.4.2. Chemical composition

The other approach is to use alternative coating compositions. This means the substitution of yttria by another stabiliser (mainly ions with different ionic radius and/or mass to increase the disorder in the crystalline lattice) or ternary additions of dopants.

For compositions where yttria is totally substituted by another dopant, Ceria-Stabilised Zirconia (CeSZ) offers promising improvements. Compositions of zirconia stabilised with yttria-ceria can provide thermal conductivity reduction up to 50% [20]. Improvement in the corrosion resistance, the phase stability and the thermocyclic resistance were reported however, the deposition of these compositions using standard EB-PVD process turned out to be difficult due to an important difference in vapour pressure between zirconia and ceria. They also have poor erosion resistance and an increase in the coating density [20;29;34;78;79].

Other rare earth oxides, like dysprosia, to substitute yttria seem to be a more successful alternative. Substitutions with 4 mol% of dopant result in a 14% reduction of thermal conductivity and with stabilisations with higher percentage of dysprosia, a 40% reduction can be achieved [3].

Ternary additions can be rare earth oxides like erbia, ytterbia, neodymia and gadolinia as studied by *Nicholls* and co-workers [31;76]. They provide effective phonon scattering centres. A thermal conductivity reduction of 42% was reported with gadolinia addition, lowering the thermal conductivity to 0.88 W/mK, that is to say close to the APS TBC which has a thermal conductivity of 0.8 W/mK [31]. Such additions have a great potential in improving the coating durability. Doped coatings have significantly better cyclic life and offers better sintering resistance resulting in a lower increase in thermal conductivity due to aging compared to standard YSZ [80;81]. Dopants produce highly distorted lattice structures and introduce defect clusters which are essentially immobile hence reducing the movements of atoms in the coating and therefore increasing the

sintering resistance. Rare earth additions were also found to improve the stability of the *t'* phase of the coating providing better temperature phase stability at high temperature [13]. However the author has highlighted a reduction in erosion resistance of doped coatings at room temperature. This behaviour is balanced by an advantageous improvement of the erosion properties at high temperature compared to standard TBC [82] but this is thought to be dependent on the column diameter.

Other material compositions where yttria is completely replaced by rare earth oxide stabilisers have been investigated. A review of such coatings can be found in [20]. Rare-earth zirconates could also be seen as potential candidates for thermal barrier coatings. It has been found that such compositions can be deposited by EB-PVD and have a lower thermal conductivity compared to the standard YSZ coatings [83-85].

The importance of the interaction between the TBC and the high temperature environment, in which it operates, has been highlighted in the previous sections. It is clear that an accurate measurement of the temperatures that a TBC experiences would help to further the understanding of the failure mechanisms and would provide useful data for future development and to exploit the full potential of TBCs.

1.5. Techniques to determine the temperature of TBCs in service

The main techniques to monitor the temperature in a gas turbine and their limitations are reviewed in this section.

1.5.1. Thermocouples

Embedded wire thermocouples are a common contact technique for temperature measurements. Generally, they are bonded into grooves machined in the blade surface. The disadvantage of this technique is the need of interconnection between the sensor element and the surface of measurement making it difficult to use for rotating components. Moreover, temperature readings are limited to pre-installed points (one or two points per blade) and cannot be changed during operation. Finally, it is intrusive and perturbs the gas flow pattern inside the engine and thus distorts the heat path, making accurate, reliable temperature measurement difficult. Thermocouples with a proper design can be accurate to approximately ±1°C however the installation cost makes it an expensive technique.

Thin film thermocouples constitute an improvement in temperature measurement techniques. They offer a faster response time and, as they are only a few microns thick, they generate fewer perturbations and provide more accurate surface temperature measurements [86].

1.5.2. Pyrometry

Optical pyrometry was first used in the late 1960's for gas turbine research and development. The probe collects radiations from a target size typically ranging from 1 to 10 mm in diameter. For turbine blade temperature measurement, the optic probe can be placed on the turbine casing. The radiations are then transmitted to pyrometer's

detector via optical fibres. The intensity of emitted radiation is mathematically converted to temperature based on Planck's law of black body radiation [87;88]:

$$E(\lambda,T) = \varepsilon(\lambda,T)\frac{C_1}{\lambda^5[\exp(\frac{C_2}{\lambda T})-1]}$$

Equation 1

, where E is the spectral emissivity power, λ is the wavelength, T is the absolute temperature of the surface, ε is the spectral emissivity and C_1 and C_2 are radiation constants. Optical pyrometry is widely used for engine control and blade health monitoring in industrial gas turbines.

Compared to thermocouples, pyrometry offers several advantages. It does not have inherent thermal inertia enabling fast response, it is non-intrusive and immune to electromagnetic interference in the surrounding environment. Limitations to this technique include, all the atmospheric effects that can mask the signal like reflected radiations from other surfaces, absorption by the medium between the pyrometer and the radiation source and emission from the hot combustion gas, making it very dependent on the environment in which it operates. Moreover, the changes of emissivity (ε in **Equation 1**) of the observed surface due to oxidation, contamination, erosion, which affects the roughness of the surface, and the deterioration of the cleanliness of the pyrometric system during operation of the engine reduce the accuracy of the measurements. For instance, when the reflected radiations represent more than 50% of the temperature signal the accuracy is dramatically reduced [89]. Finally, EB-PVD coatings are semi-transparent in the spectral range used for surface temperature

measurements therefore the pyrometer gives the temperature somewhere between the coating surface and the metal surface, hence, the temperature measurements are a function of coating thickness. A detailed overview of the errors measurement associated with pyrometer systems has been published by *Kerr et al.* [88].

1.5.3. Thermal Paints

Thermal paints, or temperature sensitive paints, are the main technique used to obtain the temperature distribution of gas turbine components [90]. Thermal paints permanently change colour when exposed at a particular temperature. The paint colouration is then compared with calibration charts to obtain the surface temperature distribution of the component. The main advantages of this method are that it can be easily applied on complex shapes and it produces a temperature profile over the whole surface rather than just discrete points as with thermocouples or pyrometry.

The principle limitation is that the colour change is also time dependent. This implies that the same colouration can be obtained with a longer exposure at a lower temperature. Therefore thermal paints must be carefully calibrated for a particular testing condition and the component must be brought to the operating condition as quickly as possible and kept constant for a fixed period of time [91].

Furthermore, it is a "*one shot*" test and the parts have to be dismantled and re-painted to make another measurement. The paint also acts as a thermal insulator and can influence the temperature measurements.

Thermal paints can be used to measure temperatures up to 1300°C [92]. However, the paint cannot survive long periods under such conditions. For example, a test on turbine blades or nozzles should not last more than five minutes to avoid paint removal [91].

1.5.4. Thermographic phosphors

Thermographic phosphors for gas turbine applications have been studied for more than twenty years. They are usually applied as paints on the surface of interest but they can also be coated using more sophisticated methods. The theory behind temperature measurement using phosphorescence will be explained in detail in the next chapter.

Many workers over the past several decades have investigated various phosphor-based thermometry systems. In 1937 *Neubert et al.* [93] patented a device using phosphors to measure temperature distribution of hot bodies. Laser-induced fluorescence was first employed as a mean to measure temperature in combustion research by *Dyer* and *Crosley et al.* [94] in 1982. A history of phosphor based thermometry has been assembled by *Dowell* [95], *Baumann* [96] and most recently by *Allison* [97]. The following paragraphs will concentrate on the development in the field of gas turbines.

The first step of the research consisted in characterizing the luminescence of various phosphors in terms of intensity and temperature dependence to determine their possible use as thermographic phosphors. A list of rare earth based phosphors along with some of their characteristics is given in **Table 2**. The most comprehensive work was carried out by *Noel* [98-101], *Goss* [102], *Alaruri* [103-105], *Allison* [97;106-108], *Feist* [109-

120], *Gentleman* [121-124] and *Eldridge et al.* [125-127] who, between them, have tested numerous phosphors for high temperature applications.

The first approach in commercial instrumentation was to mix phosphor powders with a binder and paint it on the surface of interest. Another technique consists of a fibre optic probe in which the phosphor material is attached at the end of an optical fibre [103;128]. Other coating methods like electron beam deposition [89;110] and RF magnetron sputtering [129] have been investigated to overcome the poor durability of phosphor paints. Characterization of luminescent materials is generally done in a furnace using powders, with more realistic research carried out using rotating samples. In 1987, *Mannik et al.* [130] measured temperatures between 60-150°C on a sample rotating at 1725 rpm. Later *Tobin et al.* [89] monitored the temperature of turbine blades rotating in a jet fuel flame up to 1000°C. In 1991 *Noel et al.* [98] realized tests on first-stage stator vanes in an operating turbine engine. Remote thermometry was also developed to enable two dimensional temperature measurements [104;109;131-135] and *Alaruri et al.* [104] made surface temperature mapping of a sample at temperature between 500-750°C.

Most recently *Choy*, *Feist* and *Heyes* [114] introduced the notion of "*sensing thermal barrier coatings*" (sensing TBCs). Instead of applying a phosphor layer to the surface where the temperature needs to be measured, they proposed to locally modify the composition of the TBC so that it acts as a thermographic phosphor. This technique enables surface temperature measurement but also could provide a means to measure temperature within the TBC and at the metal/coating interface. They studied a powder

of standard YSZ doped with 1 mol% Eu_2O_3 (YSZ:Eu1%) over a temperature range from 20 to 800˚C showing that YSZ:Eu can be successfully used in a TBC system to determine temperature. In further work, *Feist et al.* [110] produced a YSZ coating doped with 10% of dysprosium (YSZ:Dy), deposited by EB-PVD, and showed that temperatures between 260°C and 675°C can be measured with this technique using the intensity ratio method, to an accuracy of ±5°C. In a paper published in 2003, *Eldridge et al.* [126] addressed the problem of depth temperature measurement. They used a paint of Y_2O_3:Eu applied on plasma-sprayed 8 wt.% yttria-stabilised zirconia coating. They demonstrated that a temperature reading up to 830°C with a phosphor layer beneath a 100 μm thick TBC is possible. Finally, *Gentleman et al.* [124] started working in the field of luminescence sensing using rare earth doped YSZ (YSZ:RE) and also $Gd_2Zr_2O_7$ as phosphorescent materials. Recent advances in the field of sensing TBCs will be described more in details in the chapter entitled "*Sensing TBCs*".

Table 2: Phosphors in thermometry applications.

Phosphor	Excitation wavelength	Fluorescence line	Temperature Range	Measurement Mode	Application	Accuracy	Ref/Year
Y_2O_3:Eu	Pulsed N_2 laser 337.1 nm	612 nm	600-900°C	Decay Time	Furnace test of phosphor samples	NA	*Noel*[99]-1986
Y_2O_2S:Tb	Pulsed N_2 laser 337.1 nm	545 nm	200-550°C	Decay Time	Furnace test of phosphor samples	NA	*Noel*[99]-1986
La_2O_2S:Eu	Pulsed N_2 laser 337.1 nm	537 nm	100-200°C	Decay Time	Furnace test of phosphor samples	NA	*Noel*[99]-1986
La_2O_2S:Eu	Pulsed N_2 laser 337.1 nm	514 nm	0-100°C	Decay Time	Furnace test of phosphor samples	NA	*Noel*[99]-1986
YAG:Dy	Pulsed Nd:YAG 355 nm	467/496 nm	27-1427°C	Intensity Ratio	Furnace tests of a ceramic coated with a phosphor layer	3%	*Goss*[102]-1989
YVO_4:Eu	Pulsed N_2 laser 337nm	618 nm	500-725°C	Decay Time	Mixed with a binder at 30% phosphor. 30-40 μm layer applied by airbrush. Turbine blade specimen in rotation immersed in flame environment	5.1°C at 725°C	*Tobin*[89]-1990
Y_2O_3:Eu	Pulsed N_2 laser 337nm	611 nm	500-1200°C	Decay Time	8 μm EB-PVD coating on the blade surface. Turbine blade specimen in rotation immersed in flame environment	14.3°C at 934°C	*Tobin*[89]-1990
YVO_4:Eu	YAG:Nd 355nm	618 nm	300-700°C	Decay Time	Strips attached with a binder on the vanes of a commercial engine (7.5k-10k rpm)	NA	*Noel*[98]-1991
YAG:Tb	Pulsed YAG:Nd 266 nm	544 nm	550-1000°C	Decay Time	Furnace test of phosphor samples	5%	*Alaruri*[105]-1993
Y_2O_3:Eu	Pulsed YAG:Nd 266 nm	611 nm	550-1000°C	Decay Time	Furnace test of phosphor samples	5%	*Alaruri*[105]-1993
La_2O_2S:Eu	Pulsed YAG:Nd 355nm	510/620 nm	20-60°C	Intensity Ratio	2D temperature measurements of a copper block coated with 100 μm phosphor layer applied using a settling technique	0.15°C	*Chyu*[135]-1994
$LuPO_4$:Dy,Eu	353 and 390 nm	484 / 575 / 584 nm	Up to 350°C	Intensity measurement	Furnace tests of single crystal samples	NA	*Allison*[108]-1995
YAG:Tb	Pulsed YAG:Nd	543.1 nm	Up to 1000°C	Decay Time	Furnace tests of powder samples	NA	*Feist*[114] – 1998

Phosphor	Excitation wavelength	Fluorescence line	Temperature Range	Measurement Mode	Application	Accuracy	Ref/Year
YAG:Dy	Pulsed YAG:Nd 355 nm	493/455 nm	850-1200°C / 600-1200°C	Decay Time / Intensity Ratio	Furnace tests of powder samples	0.5°C at 1100°C	Feist[119]-1999
Y_2O_3:Eu	XeCl 308 nm	611 nm	500-750°C	Amplitude of the 611 nm line	Mapping of SiNC ceramic matrix composite and YSZ TBC coated with phosphor using a 2D laser	5%	Alaluri[104]-1999
YAG:Dy	Pulsed YAG:Nd 355 nm	458/500 nm	90-1030°C	Intensity Ratio	YAG:Dy3% powder brazed in nickel coupons	0.7-13%	Edge[132]-2000
YSZ:Eu	Pulsed YAG:Nd 266/355 nm	591/607 nm	20-800°C	Decay Time	Furnace tests of powder samples	11.5/0.05°C	Feist[111]-2000
YSZ:Eu	Pulsed YAG:Nd 266 nm	591/606 nm	Up to 830°C	Decay Time	Ni based superalloy coated by ESAVD deposition	NA	Choy[112]-2000
Y_2O_2S:Sm	Pulsed YAG:Nd 266 nm	607/646 nm	Up to 830°C	Intensity Ratio	Furnace tests of powder samples	1%	Feist[113]-2000
Y_2O_2S:Sm	Pulsed YAG:Nd 266 nm	607 nm	Up to 1550°C	Decay Time	Furnace tests of powder samples	0.10%	Feist[113]-2000
YSZ:Dy	Pulsed YAG:Nd 355nm	455/482 nm	261-677°C	Intensity Ratio	180μm deposited by EB-PVD on an aluminized C263 substrate	2.60%	Feist[110]-2001
YAG:Dy	Pulsed YAG:Nd 266/355 nm	455/494 nm	300-600°C	Intensity Ratio	Temperature distribution within an experimental combustion chamber at a scaled take-off condition and at atmospheric pressure	0.5-3.7%	Feist[109]-2002
Y_2O_3:Eu	Pulsed YAG:Nd 532 nm	611 nm	600-1100°C	Decay Time	25 μm painted phosphor layer beneath 100 μm of plasma sprayed 8YSZ TBC	NA	Eldridge[126]-2003
YAG:Dy	NA	480 nm	1600°C	Decay Time	NA	NA	ORNL*, USA
YAG:Tm	NA	NA	1400°C	Decay Time	NA	NA	ORNL, USA
YAG:Tb	NA	NA	1400°C	Decay Time	NA	NA	ORNL, USA
YAG:Eu	NA	NA	1300°C	Decay Time	NA	NA	ORNL, USA
$LuPO_4$:Dy	NA	NA	1200°C	Decay Time	NA	NA	ORNL, USA
Y_2O_3:Dy	NA	NA	550°C	Decay Time	NA	NA	ORNL, USA
YVO_4:Dy	NA	NA	450°C	Decay Time	NA	NA	ORNL, USA
Mg_4FGeO_6:Mn	NA	NA	700°C	Decay Time	NA	NA	ORNL, USA
Y_2O_3:Eu	Pulsed N_2 laser 337nm	611 nm	Near 830°C	Decay Time	Furnace test of silica coated with phosphor	10 mK	Cates[136]-2003

Phosphor	Excitation wavelength	Fluorescence line	Temperature Range	Measurement Mode	Application	Accuracy	Ref/Year
YAG:Dy	Pulsed YAG:Nd 355nm	584 nm	Up to 950°C	Decay Time	YSZ:Dy APS coating, furnace test	NA	Chen[118]-2005
Mg$_3$F$_2$GeO$_4$:Mn	355 nm	NA	Up to 750°C	Decay Time	Coating stainless steel plate in tube furnace	NA	Brübach[133]-2006
YSZ:Eu	Pulsed YAG:Nd 532nm	610 nm	Up to 1100°C	Decay Time	Powder pressed into pellets	NA	Gentleman[123]-2006
Eu$_2$Zr$_2$O$_7$	Pulsed YAG:Nd 532nm	610 nm	Up to 1200°C	Decay Time	Powder pressed into pellets	NA	Gentleman[123]-2006
(Sm,Eu)Zr$_2$O$_7$	Pulsed YAG:Nd 532nm	610 nm	Up to 950°C	Decay Time	Powder pressed into pellets	NA	Gentleman[123]-2006
(Gd,Eu)Zr$_2$O$_7$	Pulsed YAG:Nd 532nm	610 nm	Up to 1100°C	Decay Time	Powder pressed into pellets	NA	Gentleman[123]-2006
YAG:Tb	Pulsed YAG:Nd	NA	Up to 1200°C	Decay Time	Plasma sprayed coating	NA	Feist[115] - 2007
YAG:Eu	Pulsed YAG:Nd	597.5 nm	Up to 1400°C	Decay Time	Plasma sprayed coating	NA	Feist[115] - 2007
YAG:Tm	Pulsed YAG:Nd 355 nm	NA	Up to 1300°C	Decay Time	Plasma sprayed coating	NA	Feist[115] - 2007
YAG:Dy	Pulsed YAG:Nd 355 nm	NA	Up to 1500°C	Decay Time	Plasma sprayed coating	NA	Feist[115] - 2007
YAP:Eu	Pulsed YAG:Nd	NA	Up to 1150°C	Decay Time	Plasma sprayed coating	NA	Feist[115] - 2007
YAP:Sm	Pulsed YAG:Nd	NA	Up to 1350°C	Decay Time	Plasma sprayed coating	NA	Feist[115] - 2007
GdAlO$_3$:Dy	Pulsed YAG:Nd	NA	Up to 1300°C	Decay Time	Plasma sprayed coating	NA	Feist[115] - 2007
GdAlO$_3$:Sm	Pulsed YAG:Nd	NA	Up to 1250°C	Decay Time	Plasma sprayed coating	NA	Feist[115] - 2007
GdAlO$_3$:Tb	Pulsed YAG:Nd 266 nm	544 nm	Up to 1250°C	Decay Time	Powder pressed into pellets and sintered	NA	Chambers[137]-2007

*Oak Ridge National Laboratory. Data available from [97;100;138].

2. INTRODUCTION TO PHOSPHORESCENCE

In 1889 *Wiedemann* [139] was the first to introduce the term of luminescence to define many phenomena involving the emission of light under the influence of incident radiations. These radiations may be ultraviolet, X-rays, cathode rays, neutrons, gamma rays and in some applications visible light. Luminescence may also results from friction (triboluminescence) or chemical reaction (chemiluminescence), phenomena easy to differentiate with their prefixes, however the distinction between fluorescence and phosphorescence is much more arbitrary. It is generally admitted that in fluorescence the emission stops almost simultaneously once the exciting light ceased whereas phosphorescence is characterized by an afterglow which lasts at least 10^{-8} s [140].

Phosphors can be divided into two classes depending on their compositions: organic and inorganic and usually inorganic crystalline solids have a better phosphorescence in terms of duration [97;140]. In this study only inorganic phosphors were investigated. They can be defined as an inorganic host material which contains "*impurities*" or activators which act as phosphorescent centres. **Figure 15** is a schematic representation of the luminescence process. It is assumed that the host material (H) does not absorb radiations. When excited, the atoms of the activator (A) move from a ground state to a higher electronic state, they will then return to a lower energetic state by releasing the energy absorbed to reach the excited state via a radiative way, that is to say the emission of light or via thermal dissipation.

EXCITATION

H H H H H

H H H H H

EMISSION

H H A H H

HEAT

H H H H H

H H H H H
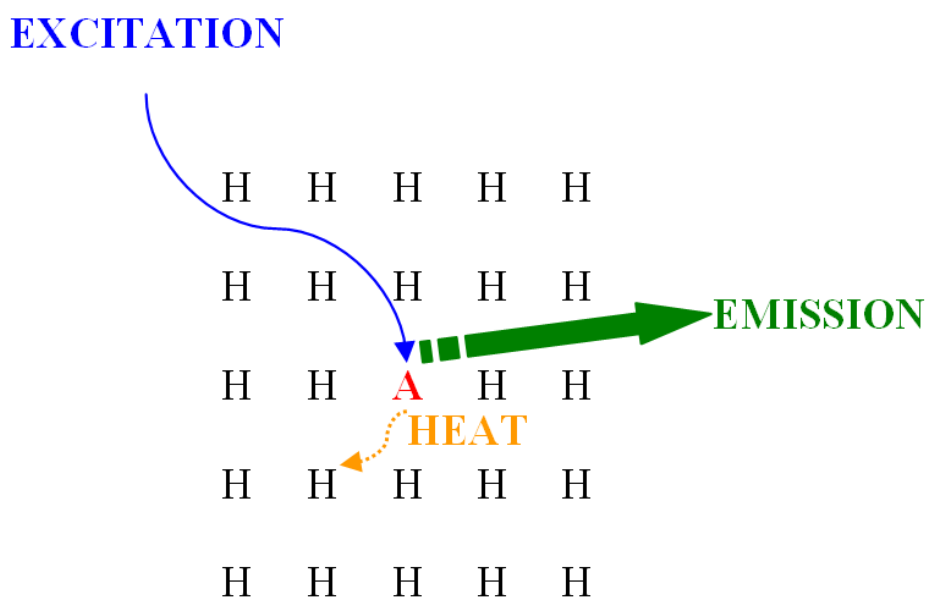
Figure 15: Schematic representation of the luminescence process.

In this work the role of activator is played by one of the ions of the rare earth metals also known as lanthanides. In order to be able to understand the emission properties of rare earth phosphors it is necessary to have a clear understanding of their particular electronic configuration along with their energy levels.

2.1.   The energy levels of rare earth ions

Rare earths in solids can be either divalent or trivalent, the most common being the trivalent one. The latter have a $4f^N\ 5s^2\ 5p^6$ electronic configuration with N $\in$ {0,14}. In 1908, *Becquerel* [141] was the first to observe the optical spectrum of rare earth compounds and to highlight the sharpness of the lines generally characteristic of the spectra of free atoms. It was not until 1930 that *Bethe* [142], *Kramers* [143] and *Becquerel* [144] started to understand the characteristics of these lines and their link with optical transition within the *4f* shell. The sharpness of the lines is related to the fact that the electrons of the *4f* shell are shielded by the filled *5s* and *5p* orbitals which have a larger radial extension [145;146]. Consequently the *4f* electrons are weakly affected by the crystal lattice and play no part in the interaction with neighbouring ions. Hence they can be treated as free ions and the energy levels of free rare earth ions are very close to that of rare earth ions embedded in various hosts. The various transitions between the *4f* energy levels and therefore their splitting and interactions are of primary importance in the phosphorescence process.

If an isolated atom is considered, its electrons give rise to discrete energy levels separated by regions of forbidden energies. The allowed energy states are defined by *Schrodinger*'s equation. In a crystalline structure, these discrete states are disturbed due to the interactions between atoms and therefore form bands of allowed energy separated by forbidden energy bands. Immediately above the highest filled band which is occupied by the valence electrons of the crystal atom, lies an empty band which is known as the conduction band. The addition of activating impurities provides

additional discrete energy levels, these levels may be situated between the valence and the conduction band and are called luminescent centres.

Assuming that the *4f* electrons are not perturbed by the charge distribution in the crystal or the other electronic shells, the energy levels of rare earth ions can be determined by only taking into account the interactions between the *4f* electrons themselves. The *Hamiltonian* equation which describes these interactions can therefore be written as follows [145;147]:

$$H = -\frac{h^2}{2m}\sum_{i=1}^{N}\nabla_i - \sum_{i=1}^{N}\frac{Z \times e^2}{r_i} + \sum_{i<j}^{N}\frac{e^2}{r_{ij}} + \sum_{i=1}^{N}\zeta(r_i)\vec{s}_i \cdot \vec{l}_i$$

Equation 2

, where *N* is the number of *4f* electrons ($N \in [1,14]$), *h* is *Planck*'s constant, *m* the mass of the electron, *e* the charge of the electron, r_i the distance relative to electron *i*, *Z.e* the screened charge of the nucleus, *ζ(r$_i$)* the spin-orbit coupling function, *s* the spin vector and *l* the orbital vector of the electron *i*.

The first two terms, which represents the kinetic energy of the *4f* electrons and their *Coulomb* interaction with the nucleus respectively, can be neglected as they are spherically symmetric and do not remove any of the degeneracies in the *4f* electron configuration.

The last two terms, which are the *Coulomb* interaction and the spin-orbit interaction of the *4f* electrons respectively, mostly affect their energy structure and split up the energy levels. The energy splitting of the *4f* shell due to *Coulomb*, spin-orbit and crystal

interactions is represented in **Figure 16**, it clearly shows their relative influences with

Coulomb interaction>spin-orbit interaction>crystal field interaction.
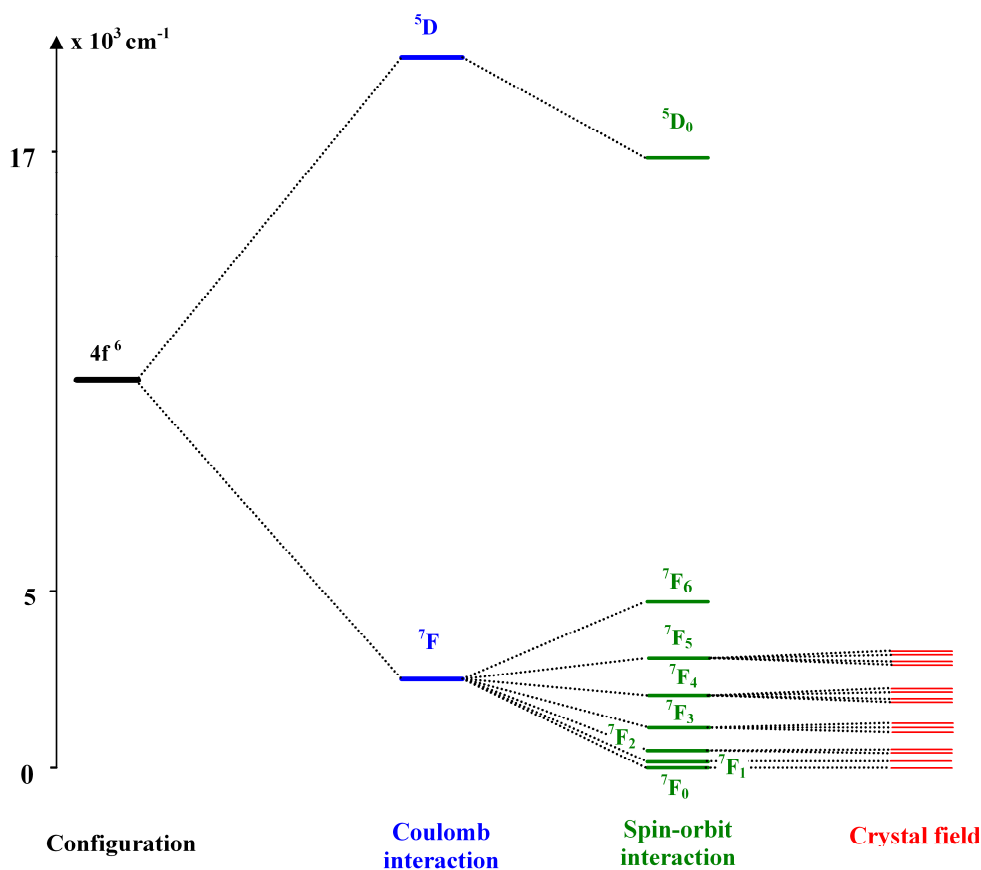
Figure 16: Energy splitting of the *4f* shell of Eu^{3+} (Redrawn from [148]).

Generally an atomic state is represented using "*term*" symbols also called *Russell-Saunders* symbols due to their first use by *Russell* and *Saunders* [149] in 1925. They describe the energy and the position of the optical electrons. The different states or energy levels constitute the energy diagram, an example of which is represented in **Figure 17**. As *Dieke* [150] was the first to give an overview of the energy levels of the *4f* shell for all trivalent lanthanides in the 1960s, this diagram is also called the *Dieke diagram*.
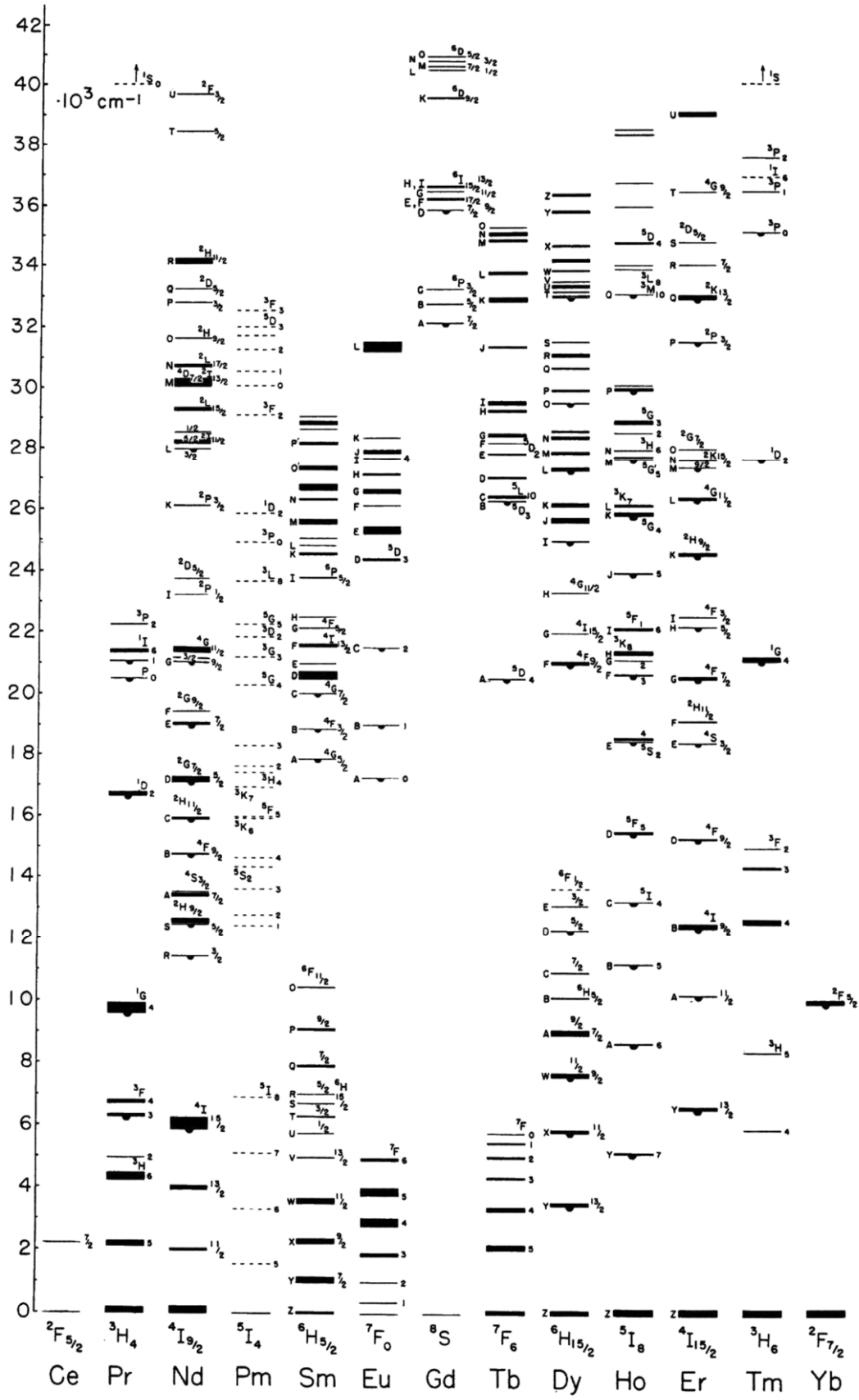
Figure 17: *Dieke diagram*. **Energy levels of the** *4f* **configurations of rare earth trivalent ions [146].**

A term symbol is represented as follows:

$$^{2S+1}L_J$$

Where L is the total orbital momentum and defines the energy state of the system of electrons. S is the total spin angular momentum and therefore is the result of the coupling of spin quantum numbers for the separate electrons. *2S+1* is the term multiplicity, it indicates the maximum number of values J can have and J is the resultant of the vectorial combination of L and S.

The basic structure of the energy-level diagram of rare earth ions is now well defined and the various transitions between these levels should now be considered. In lanthanides it can be observed intraconfigurational *4f^n→4f^n* transitions and also interconfigurational transitions between the *4f* shell and the *5d* shell (*4f^n → 4f^{n-1}5d* transition) or between the *4f* shell and the valence band of the surrounding ions (Charge transfer transition) giving rise to additional levels. These interconfigurational transitions can be explained by the fact that a state is in a very stable configuration when the electron shell is completely or half-filled. Consequently in the case of Eu^{3+} which has a *4f^6* configuration (half-filled less one) one electron of the valence band can be favourably promoted to the *4f* shell thus the charge-transfer state has a low energy. While in the case of Tb^{3+} which has a *4f^8* configuration (half-filled plus one) one of the *4f* electrons can be raised to the *5d* shell to gain stability therefore the *4f^n → 4f^{n-1}5d* transition takes place at low energy. It is worth noting that these energy levels depend to a great extent on the lattice

Having discussed the energy levels associated with trivalent rare earth ions, the next section reviews the optical transitions between the *4f* levels.

2.2. Optical transitions

2.2.1. Between 4f levels

According to *Laporte*'s selection rule for an electric-dipole transition to be allowed there must be $\Delta l = \pm 1$ therefore transitions between *4f* levels are strictly forbidden. Moreover if an electric-dipole transition implies a change in the spin quantum number S the transition is also forbidden. Therefore if Eu^{3+} is considered, the ground state being $^7F_0$ ($S=3$, $L=3$, $J=0$) and the excited state $^5D_0$ ($S=2$, $L=2$, $J=0$), transitions between these levels is strictly forbidden. Radiation is the combination of electric-dipole and magnetic-dipole transitions. The latter being ruled by $\Delta J = 0 \pm 1$ ($J=0 \rightarrow J=0$ is forbidden), magnetic-dipole radiations are possible but they obviously account for very few of the observed transitions and their intensity is about 10^3 less compared to electric-dipole transitions. Hence in the case of Eu^{3+} the only possible transition accompanied by the emission of radiation is $^5D_0 \rightarrow {}^7F_1$. As expected it can be seen on the emission spectrum of Eu^{3+} (**Figure 18**) that there are emission lines corresponding to the $^5D_0 \rightarrow {}^7F_1$ transition however there are also lines for the $^5D_0 \rightarrow {}^7F_0$, $^5D_0 \rightarrow {}^7F_2$ and $^5D_0 \rightarrow {}^7F_3$ transitions.

In fact the spin and parity prohibition are not that strict and the transitions can be partially allowed. Due to the *j-j* coupling observed for heavy ions like rare earths, ^5D

and ^7F are not pure states, for instance, there is a mixture between $^5D_0$ and $^5D_2$ and between $^7F_0$ and $^7F_2$ lifting the spin prohibition. Concerning the parity, in 1937 *van Vleck* [151] suggested that it can be cancelled by the influence of the crystal lattice. If the rare earth ion occupies a crystallographic site where the parity is different, the odd crystal field term can mix with the $4f^6$ configuration hence lifting the parity prohibition. The influence of the crystal field is illustrated in **Figure 18** by the multiple emission peaks corresponding to the $^5D_0 \rightarrow {}^7F_1$ transition.
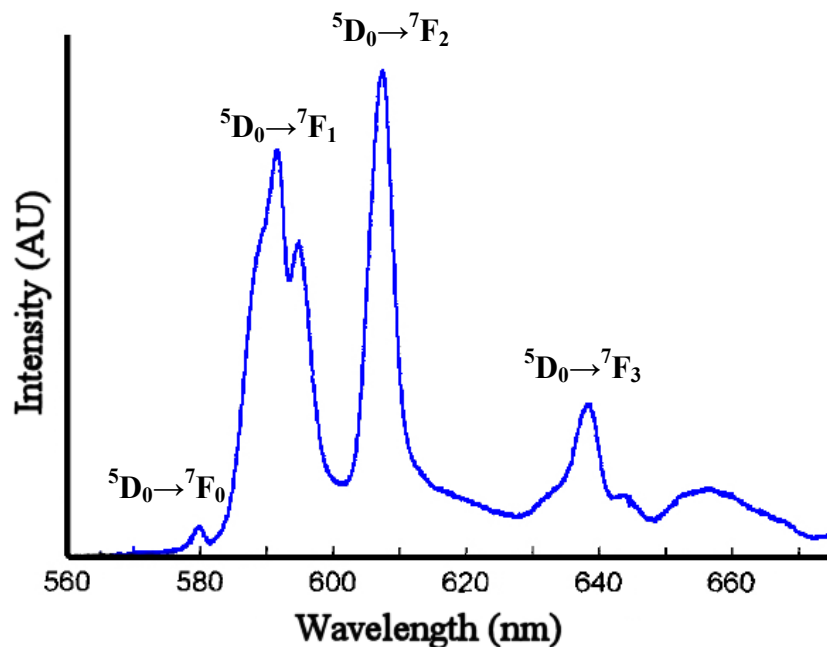
Figure 18: Emission spectrum of YSZ:Eu Phosphor [105].

2.2.2. Configurational-coordinate diagram

In the previous chapter it has been seen that luminescence comes from electron transitions between the various energy levels of the *4f* shell. In order to determine

whether a transition gives luminescence or not, a model based on the configurational-coordinate diagram has been proposed by *Seitz* [152] in 1939. It represents the potential energy of the normal and excited states of the luminescent centre as a function of the configurational coordinate (**Figure 19**). At the minimum of these parabolic curves the luminescent centre occupies the lowest vibrational level however if the temperature is increased for instance it can occupy higher levels which are represented by horizontal lines on the graph.

By direct absorption of radiation the centre is raised to an excited state (*AA'*). After this transition the centre is not necessarily in its minimum energy configuration, it will therefore return to an equilibrium state by dissipating heat to the surrounding material (*A'B*). Finally the system does not remain excited, it returns to the ground state by emitting radiation (*BB'*) followed by heat dissipation to reach a stable state (*B'A*). It should be noted that, since the absorption and emission occur very rapidly compared to vibrational movements, the transition *AA'* and *BB'* are represented by straight lines (*Franck-Condon* principle [153]). It is also clear from the graph that the emitted light is of lower energy compared to the absorbed radiation and therefore has a longer wavelength (*Stokes* law).

In the case of absence of emission (**Figure 19b**), after excitation the centre goes to the equilibrium configuration of the excited state (*A'B*) however it reaches first the intersection point of the ground state (*C*). Consequently it relaxes non-radiatively to the ground state by thermal dissipation.

(a)   **(b)**
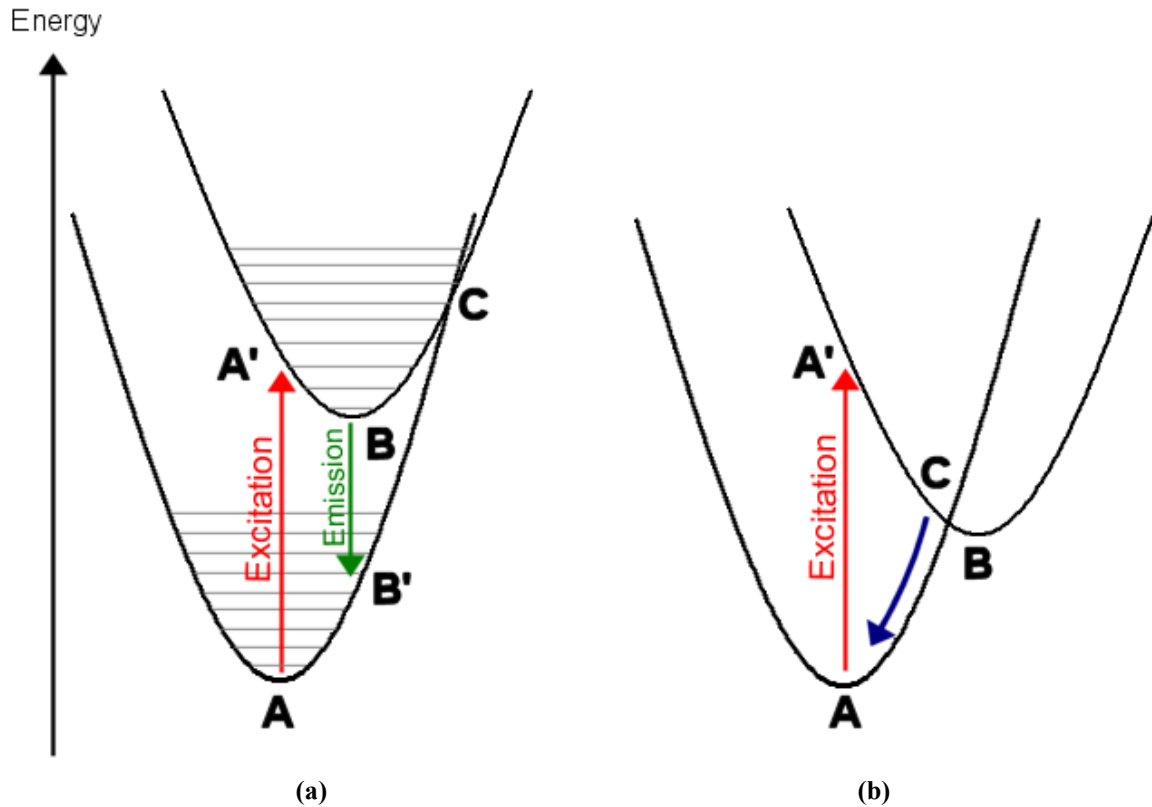
Figure 19: Configurational-coordinate diagram (Redrawn from [140]).

2.2.3. Phosphorescence decay

As has been said previously phosphorescence is characterized by an afterglow and in his work *Becquerel* found that after excitation the emission intensity decays exponentially with time. This delay in emission is due to the forbidden nature of the transition therefore if p is the optical transition probability, the time dependence of the intensity (I) can be expressed as follows [140]:

$$I(t) = -\frac{dn}{dt} = pn$$

Equation 3

, where n is the number of excited centres. The integration of this equation gives:

$$I(t) = I_0 \exp(-pt)$$

Equation 4

, where I_0 is the intensity at the beginning of the decay. **Equation 4** can also be written as:

$$I(t) = I_0 \exp\left(-\frac{t}{\tau}\right)$$

Equation 5

, where τ is the phosphorescence lifetime.

According to the latter equation, the luminescence decay rate is independent of the temperature, which is not true. Changes in temperature have a marked effect on the phosphorescence process. The previous model was used to describe a situation where the electrons occupy the lowest vibrational level of the ground state, however at higher temperature, higher vibrational levels can be occupied following a *Boltzmann* law, enabling different paths for relaxation. On top of that, the return to the ground state can not only be achieved by emission of photons (radiative process) but also by emission of phonons (non-radiative process) and the temperature dependence becomes very important when there is competition between radiative and non-radiative de-excitation.

2.3. Temperature dependence of phosphorescence

2.3.1. Temperature dependence of the emission intensity

In general, the emission intensity of phosphors becomes weaker as the temperature of the material increases. The example of La_2O_2S:Eu is given in **Figure 20**.
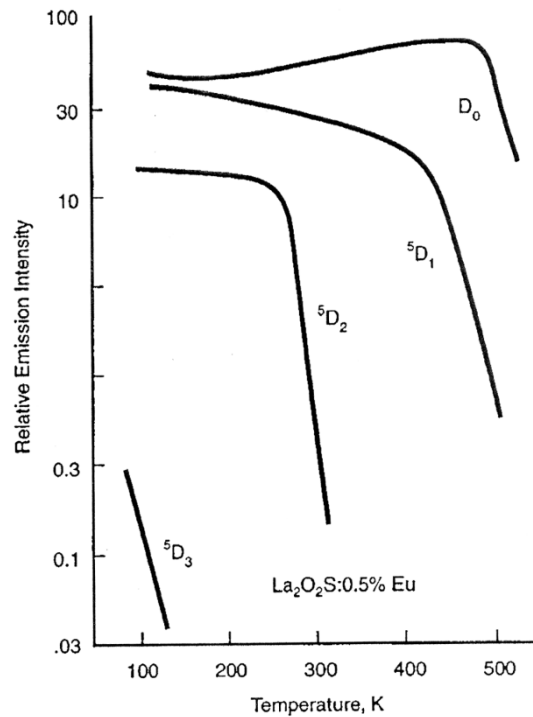
Figure 20: Emission intensity as a function of temperature for La$_2$O$_2$S:Eu [97].

It can be seen that there is a clear break in the curves, the intensity drops dramatically when a certain temperature is reached. This temperature is called the *quenching temperature* and can be explained using configurational diagrams. Due to thermal activation, electrons can occupy a higher vibrational levels situated closer or above the intersection point *C* (**Figure 19**). Electrons can therefore return non-radiatively to the ground state by dissipating heat. The population of the various energy levels is governed by the *Boltzmann* law:

$$n_1 = n_0 \cdot \exp\left(-\frac{\Delta E}{kT}\right)$$

Equation 6

, where n_0 and n_1 are the electron populations of the ground and an excited state respectively, ΔE the energy gap between these two states, k the *Boltzmann* constant and T the temperature in Kelvin.

If the intensity of the phosphorescence is considered proportional to the electron population it can be written:

$$I_1 = I_0 \exp\left(-\frac{\Delta E}{kT}\right)$$

Equation 7

, where I_1 and I_0 are the emission intensity from the excited and ground state respectively.

It is clear that the ratio depends on the temperature but also on the energy difference between the two levels. Temperature measurement using the *intensity ratio technique* is based on this temperature sensitivity [102;109;110;113;119;135]. When two emitting levels are closely spaced (around 1000 cm^{-1}), variations in temperature will change the relative electron population of these levels according to the *Boltzmann* law, resulting in a change of their phosphorescence intensity. Consequently by monitoring the variations of phosphorescence intensity of one level relative to the other, temperature can be determined. Dysprosium and samarium are the only lanthanides which are known to produce an intensity response at high temperature.

A different process has been proposed by *Struck* and *Fonger* [154;155] to explain the temperature quenching of Eu^{3+} in oxysulfides. As it has been shown previously, Eu^{3+} has a low energy charge transfer state (CTS) because its *4f* shell can favourably accept an electron from the valence band. In terms of configurational diagram, the charge transfer state can be represented as a parabola that intersects the excited and ground state curves (**Figure 21**). In the example of Eu^{3+}, electrons can be thermally promoted

from the excited ^5D levels to the CTS which can directly feed lower ^5D or the ground states. This explains why ^5D emissions quench sequentially in the order $^5D_3$, $^5D_2$, $^5D_1$, $^5D_0$ with increasing temperature as observed in **Figure 20**. CTS offers an additional path for non radiative relaxation, its position strongly depends on the host material and obviously the quenching temperature of the phosphorescence decreases for lower CTS energy.
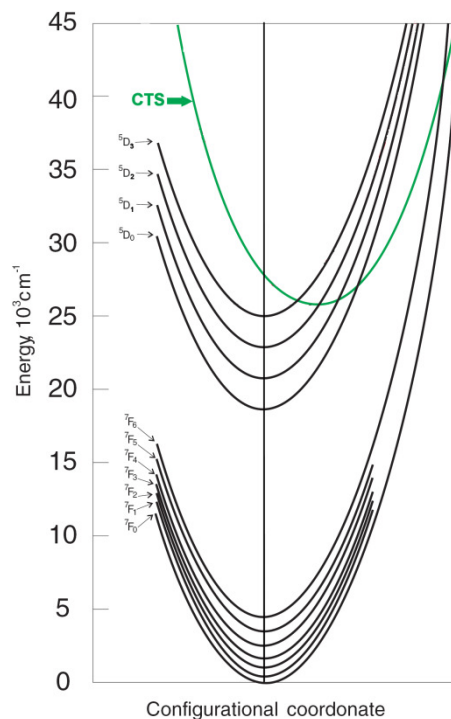
Figure 21: Configurational coordinate diagram of the *4f *^{7} and CTS of Eu^{3+} in La$_2$O$_2$S (CTS: Charge Transfer State) [155].

2.3.2. *Temperature dependence of the luminescence lifetime*

Previously, the crystal of the host material has been considered static and its effect was called crystal field interaction. In fact, the ions of the crystal move around their equilibrium positions and this constitutes the lattice vibrations of the host material the quantum of which is called a phonon. As mentioned, relaxation from an excited state

can not only take place by direct transition to a lower state via the emission of photons but also by releasing energy in the form of phonons to the surrounding crystal. Consequently the total luminescence lifetime can be expressed as a function of the probability of the occurrence of these two processes:

$$\tau = \frac{1}{P_R + P_{NR}}$$

Equation 8

, where τ is the lifetime and P_R and P_{NR} the radiative and non-radiative components respectively.

A simple relationship can be determined for P_{nr} using the theory of multiquantum emission [145;156-158]:

$$P_{NR}(n,T) = P_{NR}(n,T=0)\left[1 - \exp\left(-\frac{E_{phonon}}{kT}\right)\right]^{-n}$$

Equation 9

, where $P_{NR}(n,T=0)$ is the probability of the spontaneous emission of n phonons at T=0K, E_{phonon} the energy of the phonon under consideration. $E_{Phonon} = \hbar\omega$ where $\hbar$ is the *Dirac* constant and ω the angular frequency.

The radiative rate P_R does not depend on temperature and is usually small compared to P_{NR}. The non-radiative component P_{NR} increases with temperature, consequently, the lifetime decay τ becomes smaller as temperature is increased. This temperature dependence leads to the *lifetime decay method* for temperature measurement. The number of phonons n involved in the process can be determined from $n = \Delta E / \hbar\omega$

where ΔE is the energy gap that has to be bridged [159]. The energy gap between two levels is typically 1000 cm^{-1}. The maximum phonon energy is about 500 cm^{-1}, therefore, non-radiative decay takes place by a multiphonon process.

It is worth noting that the constant $P_{NR}(n,T=0)$ is highly dependent on the order n of the process. *Weber* [156;159] and *Risenberg* and *Moos* [145;159;160] calculated the values of $P_{NR}(n,T=0)$ for various levels of different trivalent rare earth ions in different host materials and they found that there is an exponential dependence on the energy gap to the next lowest level (ΔE):

$$P_{NR}(n,T=0) = A \exp(-\alpha \Delta E))$$

Equation 10

Consequently, the bigger the energy gap that has to be bridged, the lower $P_{NR}(n,T=0)$. Therefore important light emissions are observed for transitions between energy levels that are separated by a large energy gap and one might expect that these transitions might have longer high temperature lifetimes.

2.3.3. Temperature measurement using the lifetime decay method

As mentioned, the lifetime of the phosphorescence decreases with increasing temperature. This temperature dependence of the phosphorescence process is preferred over the *intensity ratio method* and is the most commonly used to perform temperature measurements. The *lifetime decay method* involves the calibration of the phosphor

materials in order to determine its temperature sensitivity. The calibration process is generally performed under isothermal conditions in a furnace. The phosphorescence lifetime is recorded from room temperature until the complete temperature quenching of the phosphorescence signal is observed. From this experiment, a calibration curve, that is to say the lifetime of the phosphorescence as a function of temperature, can be plotted (**Figure 22**). A phosphor is characterized by a temperature range over which it is sensitive, which corresponds to the steep slope of the curves in **Figure 22**, and a maximum operating temperature. Obviously the maximum temperature capability of a phosphor depends on the minimum decay time that can be recorded by the measurement device.
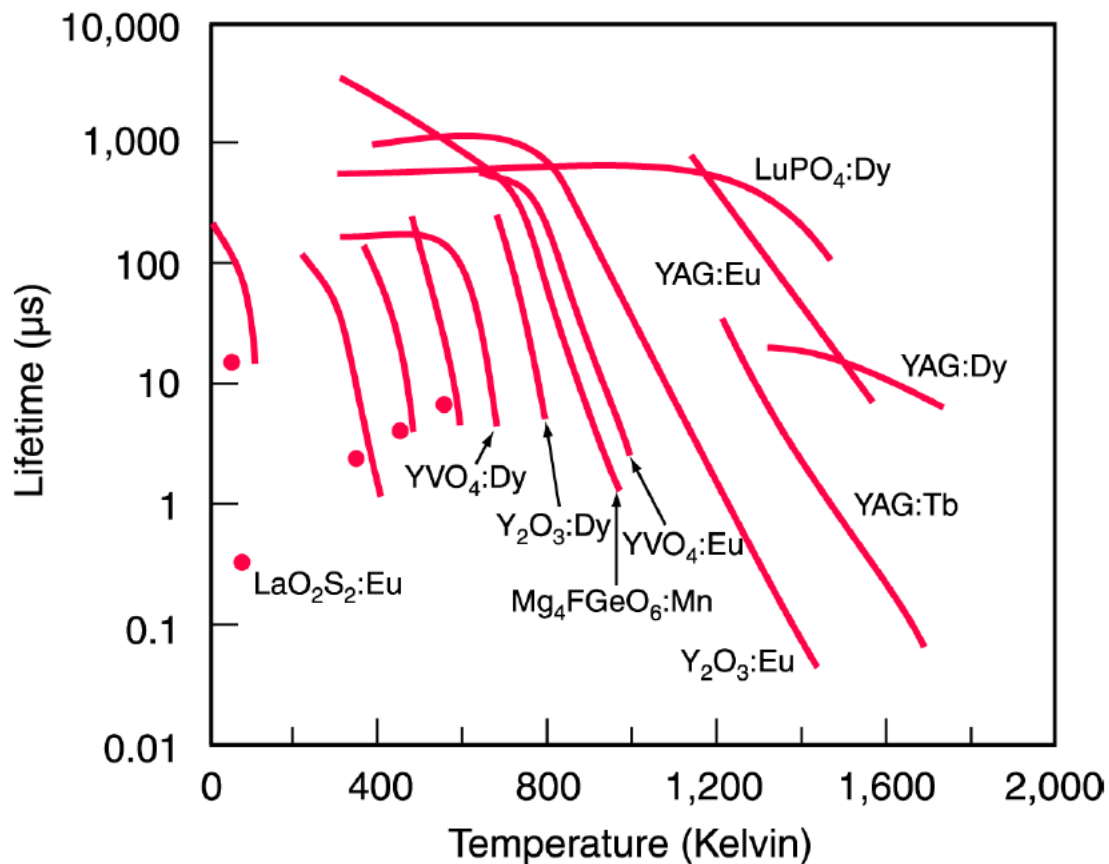
Figure 22: Calibration curves for various phosphors [100;138].

In order to determine the temperature, the lifetime decay of the phosphorescence is recorded and the temperature is read from the calibration curve. It is worth noting that the steeper the slope of the calibration curve the more accurate will be the temperature measurements.

2.4.   Factors influencing the phosphorescence process

2.4.1.   Dopant concentration

It is highly desirable to maximise the brightness of the phosphor and it would seem obvious that by increasing the concentration of the activating impurity higher emission intensity could be obtained. However this is not always the case, **Figure 23** illustrates that there is a critical concentration above which luminescence intensity drops dramatically. As the concentration of phosphor dopant is increased, there is a greater interaction between activator ions increasing the probability of non-radiative energy transfer between dopant ions. This non-radiative de-excitation is also known as *concentration quenching*. Phosphorescence intensity, decay time, rise time and temperature response are all affected to some extend therefore dopant concentration is seen as an important factor in the design of sensing TBCs.

2.4.2.   Saturation effects

High laser excitation energy could give rise to luminescence saturation effects. Generally increasing the energy beam results in a high luminescence intensity however

above a certain threshold the intensity starts to decrease [97]. It has been reported that a high laser flux could also decrease the phosphorescence decay time [161].
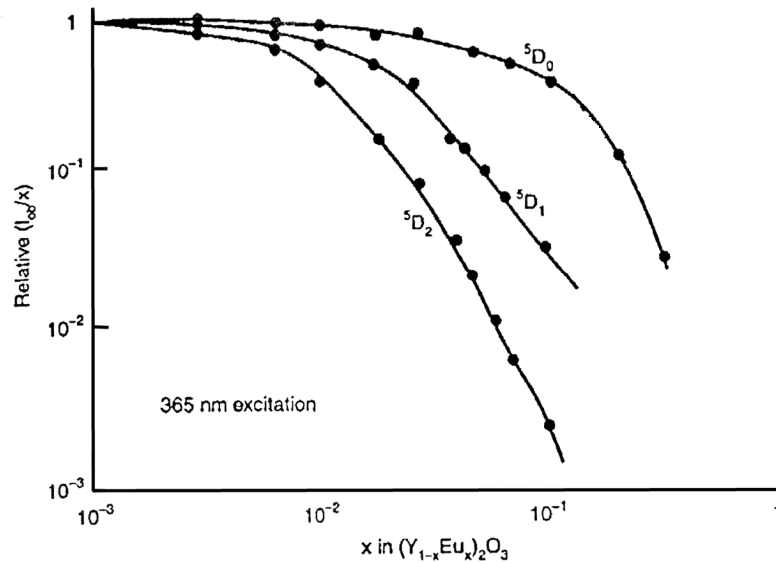
Figure 23: Fluorescence intensity in function of dopant concentration for Y_2O_3:Eu [97].

2.4.3. Impurities

The presence of impurities can affect the phosphorescence by absorbing at wavelengths similar to those of the activators, hence decreasing the energy available to excite phosphorescent centres. Impurities can also absorb the emitted wavelength, reducing the intensity of the phosphorescence or shorten the lifetime decay due to energy transfer from the activator to the impurities [97].

2.4.4. Sensitizers

It is also possible to indirectly excite the activator via a sensitizer. The processes involved are more complex since the excited sensitizer can return to the ground state by

luminescing, transferring its energy to another sensitizer or to the activator or dissipating heat to the lattice [146]. Sensitizer materials can be used to increase the luminescence intensity or, for example, in particular cases where for instance the wavelength required to excite the activator is not available. A suitable sensitizer must not absorb the emission wavelength that is to be monitored or provide a path to de-excite luminescent centres non-radiatively. *Weber* [162] has found that erbium is a sensitizer for dysprosium and gadolinium for terbium.

2.4.5.   *Rare earth energy level location*

The location of the energy levels of rare earth oxides in various host materials has mainly been studied by *Dorenbos et al.* [163]. The performance of a phosphor depends on the locations of these levels with respect to the valence and the conduction band. If an excited state is situated just below the conduction band the electrons excited to this state can be thermally ionized to the conduction band and hence can be considered as lost for the phosphorescence process. Consequently, electronic transitions from this state will be quenched at high temperatures.

As it has been shown in a previous section, the position of the charge transfer state (CTS) will have an effect on the phosphorescence process. Its position depends on the host material and low energy CTS provides additional paths for non radiative relaxation leading to a decrease in the intensity of the phosphorescence with increasing temperature.

3. SENSING TBCS

Recently, the so-called sensing TBCs have been of particular interest for monitoring TBC performance in-situ. Most of the work in this research area has been published in the open literature over the past six years. The concept of a sensing TBCs was patented by *Choy et al.* [114] in 1998. Results on YSZ:Eu powders were published in 2000 [111], while the first results on sensing EB-PVD TBCs were published in 2001 [110]. The coating tested was a monolayer coating of standard YSZ co-doped with dysprosia. In 2001, *General Electric* patented a means of measuring the extent of monoclinic phase formation in a TBC using the phosphorescence of YSZ:Eu material [164]. Later, *Feist* and co-workers showed that the degradation of the TBC due to hot corrosion could be monitored by phosphorescence [165]. In 2005, *Gentleman et al.* [123] reported the temperature sensitivity of YSZ:Eu phosphors as well as europia doped pyrochlore zirconates. The latter may be seen as a potential replacement for YSZ materials due to

its lower thermal conductivity. *Gentleman et al.* [122] also showed that the temperature at the TGO/TBC interface could be measured with thermographic phosphors, using a bi-layer EB-PVD coating (a 150 μm YSZ layer on top of a 10 μm YSZ:Eu layer). Work on air plasma sprayed coatings was first published in 2005 [118]. *Eldridge et al.* [125;127] concentrated on the detection of damage in the TBC in the form of delamination and erosion using phosphorescence. In 2006, they reported an innovative way of detecting the delamination of TBCs based through the observation of the luminescence of a YSZ:Eu phosphor layer deposited at the TGO interface. They found the luminescence is greatly enhanced in the presence of underlying delamination cracks [127].

3.1. Sensing concept

The concept of sensing TBCs has been recently reviewed by *Gentleman et al.* [124]. The use of phosphors as sensors can be broadly divided into two main types: temperature measurement sensors and health measurement sensors.

3.1.1. Temperature measurement sensor

As mentioned before, it is very desirable to monitor the temperature at the bond coat/top coat interface but also at the surface of the TBC. By applying an inner layer adjacent to the bond coat and another layer at the surface of the TBC, using two different types of phosphors (that is to say phosphors with distinct luminescent lines) monitoring both temperatures should be possible. By simultaneously measuring the temperature at at least two different depths in the coating the temperature gradient in the TBC can be

determined. Therefore, a multilayer sensing coating could also be used as a heat flux gauge in order to monitor the thermal gradient and to determine the heat flux through the thickness of the TBC. More precise measurements can be achieved by incorporating another layer in the middle of the coating to provide a third temperature measurement using a third type of phosphor. Knowing that the thermal conductivity of YSZ TBC varies through its cross section [76;166], it is very difficult to predict the temperature within the coating without the use of a third phosphor, therefore, it would provide useful data for future development to include three or more phosphor layers.

3.1.2. Health measurement sensor

Degradation of the TBC will result in an increase in the metal surface temperature. This variation in temperature can be measured by a layer deposited adjacent to the bond coat and therefore the area where the coating is damaged can be monitored.

In 1987, *Amano et al.* [167] patented a non-destructive way of determining the remaining thickness of a TBC by using a multilayer coating containing luminous activators. Indeed, in order to monitor the health of the TBC at various stages, several doped layers should be deposited. Each layer should have a different dopant that luminesces at a specific frequency so that under excitation, when the TBC is intact, the characteristic luminescence of each layer can be detected. As the coating starts to be eroded the first doped layer will be removed therefore the luminescence of this layer will no longer be collected and hence the remaining thickness can be determined. Such a coating was successfully tested by *Eldridge et al.* [125]. The multilayer coating

consisted of layers of YSZ:Eu, YSZ:Tb and undoped YSZ successively applied during a single deposition run using a six electron beam gun evaporator with three different ingots. Under UV illumination, only the phosphorescent layers exposed by erosion luminesced providing an immediate visual indication of where the coating is eroded and also an estimation of the remaining coating thickness.

Another approach would consist in superposing several layers, the layer on the top, being opaque to the luminescence wavelength of the underneath layers, acts as a barrier. When the TBC is intact no signal is collected, but when the "barrier layer" is removed the luminescence of the underneath layer can be picked up and therefore the remaining thickness can be assessed.

A similar system, based on the opacity of YSZ-based TBCs to ultraviolet excitation wavelength, could be used. By using a UV laser to excite the phosphor, the phosphorescent layer can only be excited when exposed due to erosion or spallation for example, hence providing a mean to determine the remaining thickness of the TBC and whether the coated component has to be replaced.

Last but not least, alterations of the local atomic surrounding of the activator ion were found to affect the phosphorescence process. Therefore, phase transformations in the TBC due to high temperature aging [164] or chemical degradation caused by hot corrosion [165] for instance, could be monitored by phosphorescence.

3.2.   Requirements

3.2.1.   Depth of penetration

An important obstacle, related to in-depth temperature measurement, is the possible attenuation of the exciting wave or the absorption of the fluorescence emission by the TBC. EB-PVD TBCs are generally around a 125-200 μm thick, therefore, to measure the temperature at the bond coat/top coat interface the laser must be able to excite the phosphor layer at this depth and the emission must be able to be monitored. Consequently, it is of primary importance to select a phosphor that exhibits significant excitation and emission peaks that can be transmitted through the TBC. Moreover, due to cracks and defects present in TBCs, the light transmission will be further decreased and so will be the penetration depth. However, EB-PVD TBCs exhibit a columnar microstructure and therefore the major defects are vertically oriented resulting in less absorption.

In 2003, *Eldridge et al.* [126] showed that it is possible to take temperature measurements through a 100 μm thick APS layer. Most recently, *Gentleman et al.* [122] managed to make lifetime decay measurements in an EB-PVD TBC, through a 140-170 μm YSZ layer.

3.2.2.   Moving surfaces

If the surface where the temperature that is to be measured is rotating at high speed, it should move by a non-negligible distance during the amount of time required to make a

temperature measurement. The fluorescing area that has been excited by the laser may move significantly with regard to the detector during the measurement period and consequently the amount of light reaching the detector will vary with time and therefore as a function of the rotation speed. To minimise this problem careful calibration must be made and phosphors with short decay time should be chosen preferentially so as to minimise the displacement during the measurement period.

For the case of the turbine blades, the measurements have to be made before the blade rotates out of view therefore, the speed of laser excitation and data acquisition but also the phosphorescence decay time, are critical parameters. The maximum time allowed to do a single temperature measurement can be easily estimated. In the *Rolls-Royce Trent 900* engine, which has a single stage high pressure turbine with 70 blades, the rotor maximum speed is about 12500 rpm [168]. Hence, the time window for measurement would be about 70 µs. In reality, the measurement has to be made even faster since the excited area on the blade surface will move away from the detector during this period of time. This effect on displacement is illustrated in **Table 3** for various decay times.

Table 3: Displacement at the blade surface for various decay times.

τ *(µs)*	*Displacement (mm)*
100	49-57
50	25-28
10	5-6
1	0.5-06
0.1	0.05-0.06

This shows that temperature measurements on rotating parts are very challenging, however, this is an extreme case, for an industrial gas turbine the rotation speeds are much lower.

3.2.3. Selection of the phosphor dopant

As it has been shown, the choice of phosphor is already limited by the "*depth of penetration*" and "*moving surfaces*" requirements. Other important parameters that will further shorten the list of possible candidate materials have also to be taken into account. If phosphors are used to monitor the health of the TBC, this may be done at room temperature as an inspection mode, therefore, the choice of rare earth is not very restricted. However, for temperature measurement the phosphor must have, over the temperature range of interest, a temperature sensitivity which can be monitored accurately. For industrial turbine blades the surface temperature will reach typically 900˚C, whereas for aero blades it can be as high as 1200˚C and the challenge resides in selecting a phosphor which is sensitive at this temperature.

Moreover, for in-situ measurements, the luminescence must be detectable from all the background radiations such as the blackbody radiations from the surrounding components, the hot gas or even the coating itself. **Figure 24** represents the blackbody radiation curves calculated from *Planck*'s law. It indicates that for the luminescence to be detected above the blackbody background radiation the wavelength must be below 600 nm.

Further, if several layers constituted with different dopants are to be used to measure temperature at different depths, the phosphors must be chosen so that there is a minimum overlap between the luminescence lines of the different dopants. All of these factors make the choice of dopant much more restrictive for temperature measurement, than for room temperature TBC health monitoring.
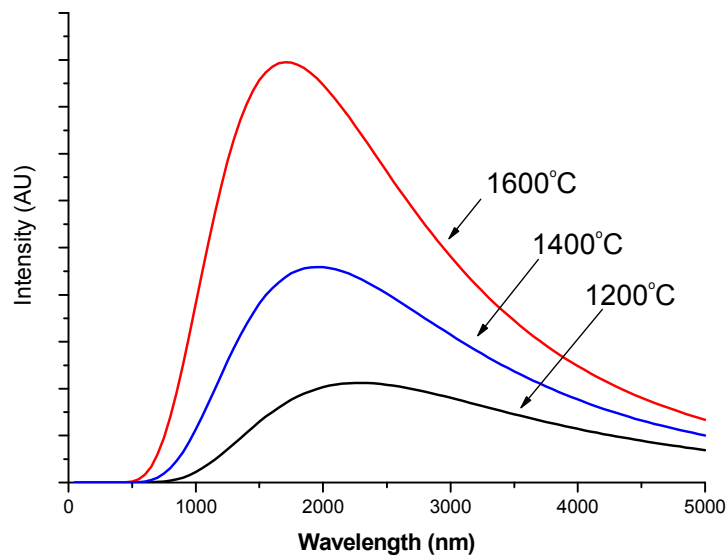
Figure 24: Blackbody radiation curves at 1200°C, 1400°C and 1600°C.

3.2.4. *Dopant concentration*

The intensity, the relative spectral distribution, the decay time and the response to temperature will all be affected to some degree by the phosphor dopant concentration. For a certain concentration, depending on the phosphor but also on the host material, the luminescence will reach a maximum, therefore, it is important to establish its useful range of concentration. It is essential to determine, for a particular application, the right concentration that will give maximum luminescence intensity and the proper lifetime decay over the temperature range of interest.

The phase stability of the TBC must also be taken into consideration. A TBC has the highest thermomechanical resistance when stabilised with between 6-9 wt.% of yttria (3.5-5 mole%). Rare earth oxides are also stabilisers, so the total concentration of stabiliser should be kept within this range to ensure good properties for the TBC.

Furthermore, as stated previously, rare earth oxides additions enable to further decrease the thermal conductivity of EB-PVD TBCs. Ternary addition of rare earth oxides up to 8 mol% results in a significant drop in thermal conductivity with the most important drop observed for additions between 4 and 8 mol% for gadolinia, neodymia or ytterbia [31;166]. If those rare earths additions could be used in this kind of concentration range it could be also beneficial from the thermal conductivity point of view, although it could have a negative effect with respect to lifetime.

4. *TEMPERATURE SENSITIVITY OF YSZ PHOSPHORS*

In the selection of high temperature phosphors the most straightforward approach is to co-dope standard YSZ material with rare earth oxides (YSZ:RE). Firstly, because YSZ:RE materials have been shown to luminesce at high temperatures (**Table 2**). At the beginning of this research, in October 2004, the only data available in the open literature regarding YSZ-based phosphors was the work conducted by *Feist et al.* [110-112]. They reported lifetime decay measurements up to 800°C using a YSZ:Eu powder and a YSZ:Eu coating deposited by electrostatic spray assisted vapour deposition. Additionally, the only results on EB-PVD TBCs were on YSZ:Dy and these indicated a temperature measurement capability up to 630°C using the *intensity ratio technique* [110]. However no work was published on lifetime decay measurements for this EB-PVD TBC.

Secondly, small additions of dopants should not dramatically change the properties of the TBC. It was shown by *Nicholls et al.* [31] that a 4 mol% addition of rare earth dopant could significantly reduce the thermal conductivity of TBCs and that such compositions were easily deposited by EB-PVD. Further, *Rebollo et al.* [13] reported that, even though gadolinia is a less effective stabiliser than yttria, small ternary additions of gadolinia could improve the high temperature phase stability of the coating.

4.1. Sample production

4.1.1. Selection of rare earth dopant and concentration

As mentioned in **Section 2.3.2** trivalent rare earth oxides with a high energy gap should be quenched at a higher temperature, therefore, according to the *Dieke diagram* in **Figure 25**, Sm_2O_3, Eu_2O_3, Gd_2O_3, Tb_2O_3 and Dy_2O_3 are potentially the best candidates to dope YSZ from the luminescence point of view. Unpublished work carried out at *Southside Thermal Science*, London (*STS*) showed that the temperature sensitivity of YSZ:Tb and YSZ:Sm do not exceed that of YSZ:Eu, consequently this study will concentrate on YSZ:Eu, YSZ:Gd and YSZ:Dy phosphors. Recently *Chambers et al.* [137] showed that Tb_2O_3 was not a viable dopant for YSZ because Tb^{3+} could easily be oxidised into Tb^{4+}.

First of all, the dopant concentration was chosen so that the total amount of stabiliser (rare earth oxide plus yttria) remained in a range that guaranteed the formation of the metastable *t'* phase after deposition (see phase diagram in **Figure 5b - page 11**). The coating compositions used for this study are listed in **Table 4**. Three different

concentrations of dysprosia, 0.3, 1 and 2 mol%, were chosen in order to determine the influence of dopant concentration on the phosphorescence. Compositions with 2 mol% of Eu_2O_3 and Gd_2O_3 were also investigated to compare the temperature capabilities of these three phosphors at the same dopant concentration level. Finally concentrations of 4 mol% were studied since such a level of dopant would give a significant reduction in the thermal conductivity of the TBC [31].
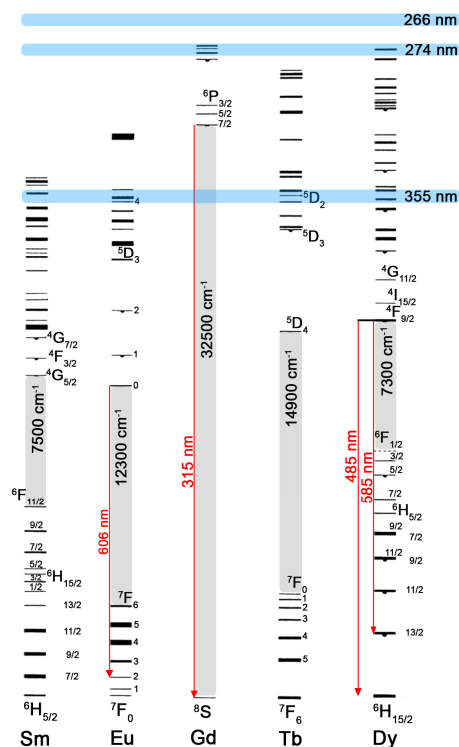
Figure 25: *Dieke diagram* **for rare earth trivalent ions with high energy gaps.**

Table 4: Ingot compositions used for coating deposition.

Designation	Composition	Total Stabiliser concentration (R_2O_3)
7YSZ	ZrO_2 + 7 wt.% Y_2O_3	3.9 mol%
YSZ:Dy0.3%	ZrO_2 + 7 wt.% Y_2O_3 + 0.3 mol% Dy_2O_3	4.3 mol%
YSZ:Dy1%	ZrO_2 + 7 wt.% Y_2O_3 + 1 mol% Dy_2O_3	5 mol%
YSZ:Dy2%	ZrO_2 + 7 wt.% Y_2O_3 + 2 mol% Dy_2O_3	6.1 mol%
YSZ:Eu2%	ZrO_2 + 7 wt.% Y_2O_3 + 2 mol% Eu_2O_3	6.1 mol%
YSZ:Eu4%	ZrO_2 + 7 wt.% Y_2O_3 + 4 mol% Eu_2O_3	8.3 mol%
YSZ:Gd2%	ZrO_2 + 7 wt.% Y_2O_3 + 2 mol% Gd_2O_3	6.1 mol%
YSZ:Gd4%	ZrO_2 + 7 wt.% Y_2O_3 + 4 mol% Gd_2O_3	8.3 mol%

4.1.2. Coating deposition

All the coatings were deposited at *Cranfield University* on alumina substrates using the single source EB-PVD evaporator represented in **Figure 26**. High purity single crystal alumina substrates♦ were used rather than a nickel based superalloy, in order not to be limited by the melting point of the superalloy during the phosphorescence furnace calibration.

Prior to deposition the substrates were polished with a 1200 grit SiC paper and cleaned with acetone. Then, they were placed on *NIMONIC 75* holders which were fixed on the substrate rotators of the deposition chamber. The substrate holders rotated at 10 rpm during the deposition and they were heated to about 900°C, prior to the start of deposition. The pressure inside the chamber was kept between 1 and $5x10^{-2}$ mbar and a 10% oxygen / 90% argon gas mixture was introduced to preserve the stoichiometry of the zirconia deposit. The electron beam gun which is located in the lower chamber at around 3.10^{-4} mbar, is bent through 270° magnetically and focussed onto a 33 mm diameter ingot• (The ingots had the compositions listed in **Table 4**). The ingot is evaporated, with the deposition lasting typically 60 minutes to achieve a coating thickness of about 100-120 μm. During deposition the temperature increases to circa 1000°C. After deposition the samples were left to cool down in the coater. Each coating was characterised by X-ray diffraction (XRD) and scanning electron microscopy (SEM) in order to determine the microstructure and the crystallography of the doped coatings and compare these with the standard 7YSZ.

♦ Single crystal alumina, random orientation, 99.99% purity supplied by PI-KEM, UK.
• Ingots supplied by Phoenix Coating Resources, USA.
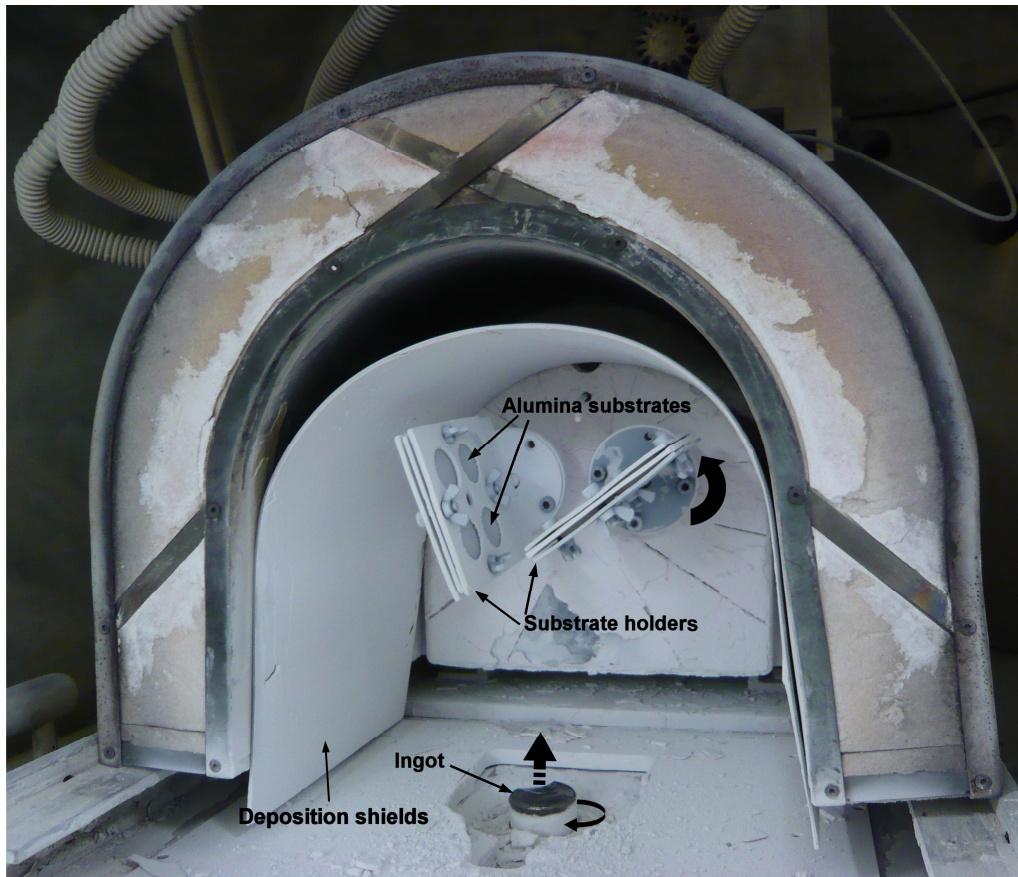
Figure 26: Single source EB-PVD coater.

4.2. Coating characterisation

4.2.1. Coating crystallography

XRD analysis was carried out on the as deposited TBCs and on powdered coatings removed from the holders in order to determine the phase composition and the crystallographic orientation of the EB-PVD TBCs. The diffractometer used was a *Siemens D5000* with a CuKα radiation. The powders were analysed using a glass slide and clear double-sided tape. Broad spectra were recorded between 20° and 90° with a

step size of 0.04° and a time per step of one second. Finer scans with a step size of

0.002° and a time per step of two seconds were used to calculate the lattice parameters.

As it can be seen from the diffraction patterns in **Figure 27**, the powdered coatings have

all the characteristic peaks of the metastable *t'* phase (only the graphs for the coatings

with 2 mol% of dopant are represented for clarity). From this study, it can be stated that

for all the compositions, only the *t'* phase was present in the coating after deposition.

The graphs in **Figure 28** compare the XRD patterns of two standard 7YSZ coatings and

a powdered one. It highlights the characteristic textured microstructure of EB-PVD

TBCs. All the EB-PVD coatings studied had a preferential *(200)* or *(311)* orientation.

Whether the coating was mostly *(200)* or *(311)* orientated depended on the position of

the substrate on the holder and was caused by the shadowing by the wing nuts used to

assemble the holder. The same characteristic was found for all the coatings.
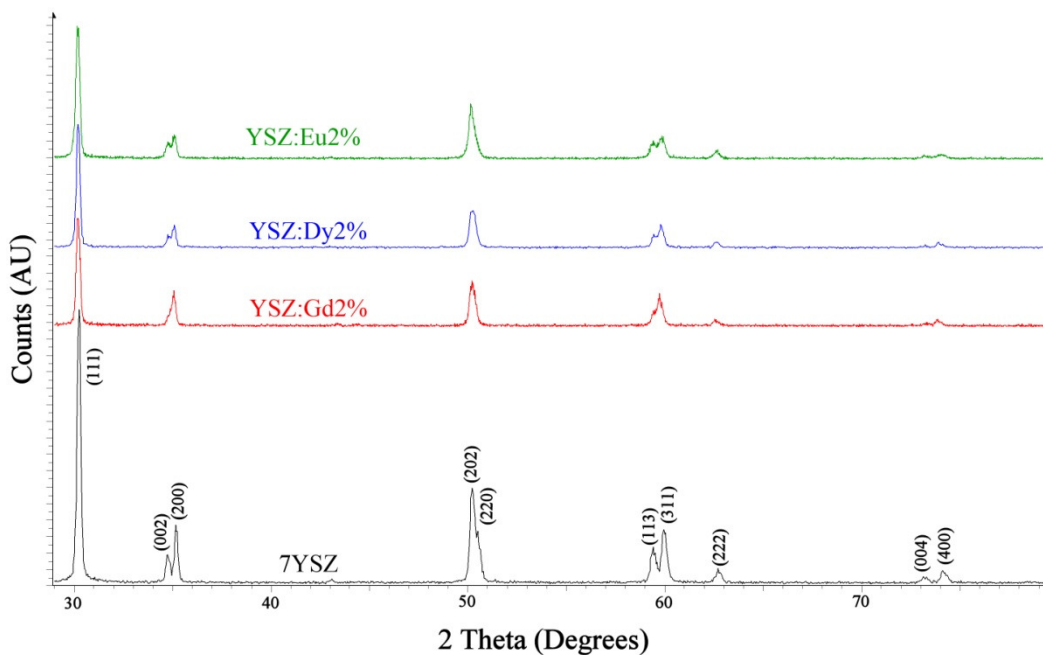
Figure 27: XRD graphs of 7YSZ and YSZ:RE2% powders.
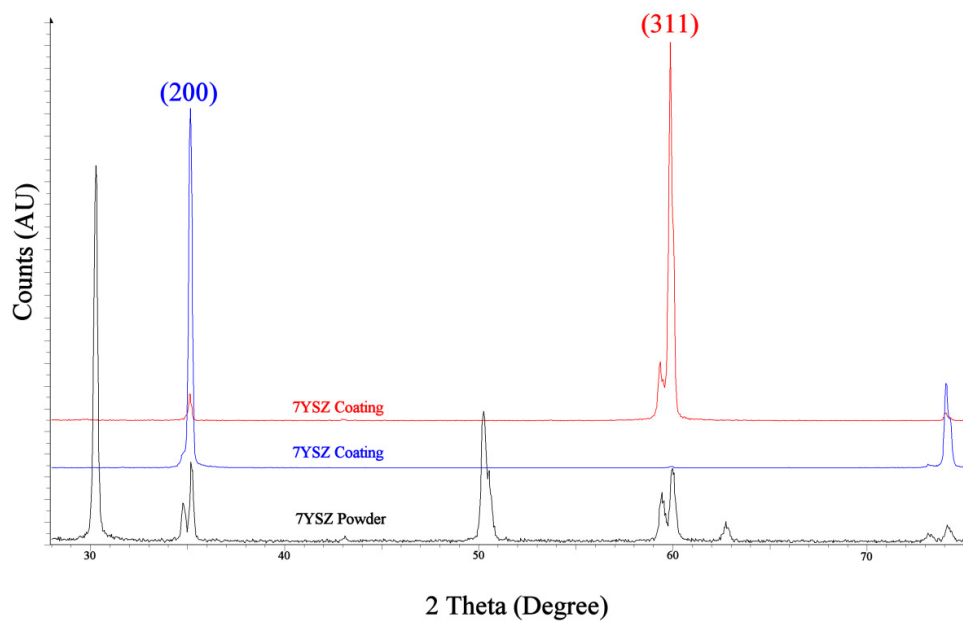
Figure 28: Comparison of the XRD pattern of 7YSZ powder and 7YSZ coatings.

The *(002)* and *(200)* diffraction peaks of the XRD patterns of the powders shows that ternary additions of rare earth oxides affects the crystallography of the coating. Indeed, it can be seen from **Figure 29** that the *(200)* and *(002)* peaks move towards lower and higher 2θ values respectively with increasing concentrations of dopant. The same behaviour is observed for the *(311)* and *(113)* peaks.
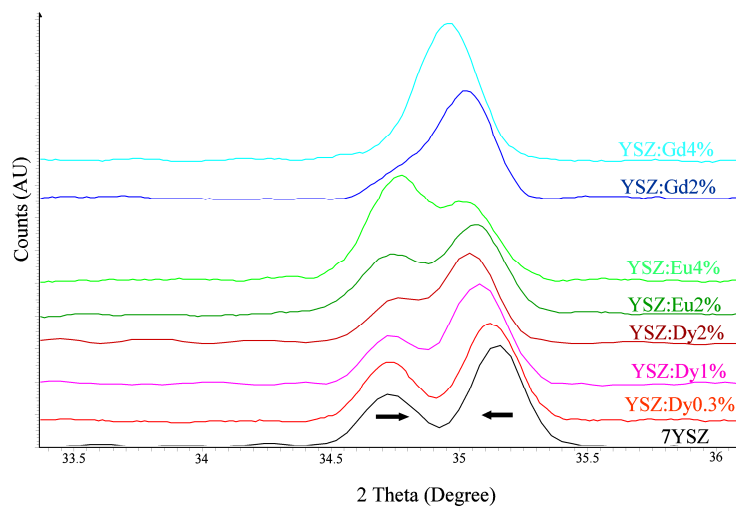
Figure 29: XRD pattern of the *(002)* and *(200)* reflections.

This clearly reflects some changes in the lattice parameters due to rare earth oxide additions. In a tetragonal structure the *(200)* and *(002)* plains are distinguishable, hence the two peaks on the XRD pattern. However, in a more symmetrical lattice like the cubic one, these two plains are identical and only the peak corresponding to the *(200)* reflections appear on the XRD graph. Consequently, it can be said that the coating becomes more cubic as the concentration of dopant is increased, highlighting the "*stabiliser*" effect of gadolinia, dysprosia and europia on zirconia. This result was confirmed by the calculation of the lattice parameters. The lattice parameters for each composition were calculated using the equation of the *d* spacing for a tetragonal cell:

$$\frac{1}{d^2} = \frac{h^2 + k^2}{a^2} + \frac{l^2}{c^2}$$

Equation 11

, where *d* is the distance between the atomic planes in a crystal, *(hkl)* the *Miller* indices, *c* and *a* the lattice parameters. The *c* and *a* values in **Table 5** were calculated from the *(111)* and *(200)* reflections.

Table 5: Lattice parameters of 7YSZ and YSZ:RE samples.

Composition	*a (nm)*	*c (nm)*	*c/a*
7YSZ	5.100	5.163	1.012
YSZ:Dy0.3%	5.105	5.16	1.011
YSZ:Dy1%	5.112	5.165	1.01
YSZ:Dy2%	5.117	5.151	1.007
YSZ:Eu2%	5.114	5.166	1.01
YSZ:Eu4%	5.119	5.169	1.01
YSZ:Gd2%	5.119	5.145	1.005
YSZ:Gd4%	5.130	5.131	1

The tetragonality of the coating is characterised by the *c/a* ratio and this ratio is equal to one for a cubic cell. The results in **Table 5** show that the tetragonality decreases due to

dopant additions which confirms that a more "*cubic-like*" microstructure is obtained. The influence of stabilisers on the tetragonal zirconia cell is illustrated in **Figure 30**.
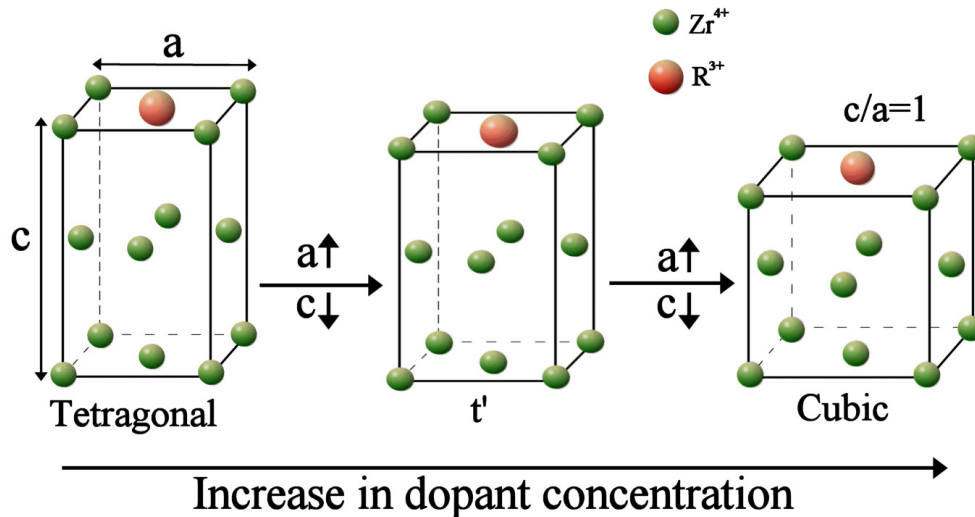
Figure 30: Zirconia cell distortions caused by dopant additions.

It is worth noting that the various dopants do not produce the same degree of "stabilisation". If the compositions with 2 mol% dopant are compared the following trend for stability is observed: $Eu_2O_3 < Dy_2O_3 < Gd_2O_3$. A concentration of 4 mol% of gadolinia seems to completely stabilise the cubic phase. On the other hand an increase from 2 to 4 mol% of europia does not appear to affect the *c/a* ratio.

4.2.2. Coating microstructure

4.2.2.1. Sample preparation for SEM analysis

The samples were cut in half for cross section analysis using a diamond wheel[*] rotating at 1200 rpm with a feeding rate of 1 mm/min. One half was ground manually with a 220 grit SiC paper prior to mounting, in order to flatten the irregularities caused by the

---

[*] High concentration diamond wheel supplied by Metprep, UK.

cutting. The samples were mounted in black phenolic resin[¥] in a *Buehler Simplemet 2000* mounting press. For some specimens, the 200 bar pressure applied during mounting, caused cracking of the alumina substrate. Nevertheless, this type of mounting was preferred to the epoxy cold mounting because the phenolic resin is harder and facilitates the polishing of hard materials like alumina. Moreover, contrary to the epoxy, the phenolic resin is conductive and reduces the charging during the SEM examination of non conductive samples like zirconia. The samples were polished down to a surface finish of 3 μm with a final stage using colloidal silica (0.5 μm). Microscopic analysis was carried out with a *Philips XL30* Environmental-SEM (E-SEM) or with a *Philips XL30 SFEG*, coupled with an Energy Dispersive X-ray (EDX) for compositional analysis. Alumina and zirconia are non-conductive therefore the samples were coated with carbon or gold/palladium when using the SFEG.

4.2.2.2. SEM analysis

It can be seen from the SEM micrographs of the top surface and the cross-section presented in **Figure 31** and **Figure 32** that all the TBCs have the characteristic columnar microstructure of EB-PVD coatings. However, even though all the coatings were deposited on the same alumina substrates, under the same conditions and for the same length of time, there were important variations in the column diameters and the coating thicknesses between the various compositions, two extremes being YSZ:Dy0.3% and YSZ:Gd4%.

[¥] Conducto-Mount, phenolic resin supplied by Metprep, UK.
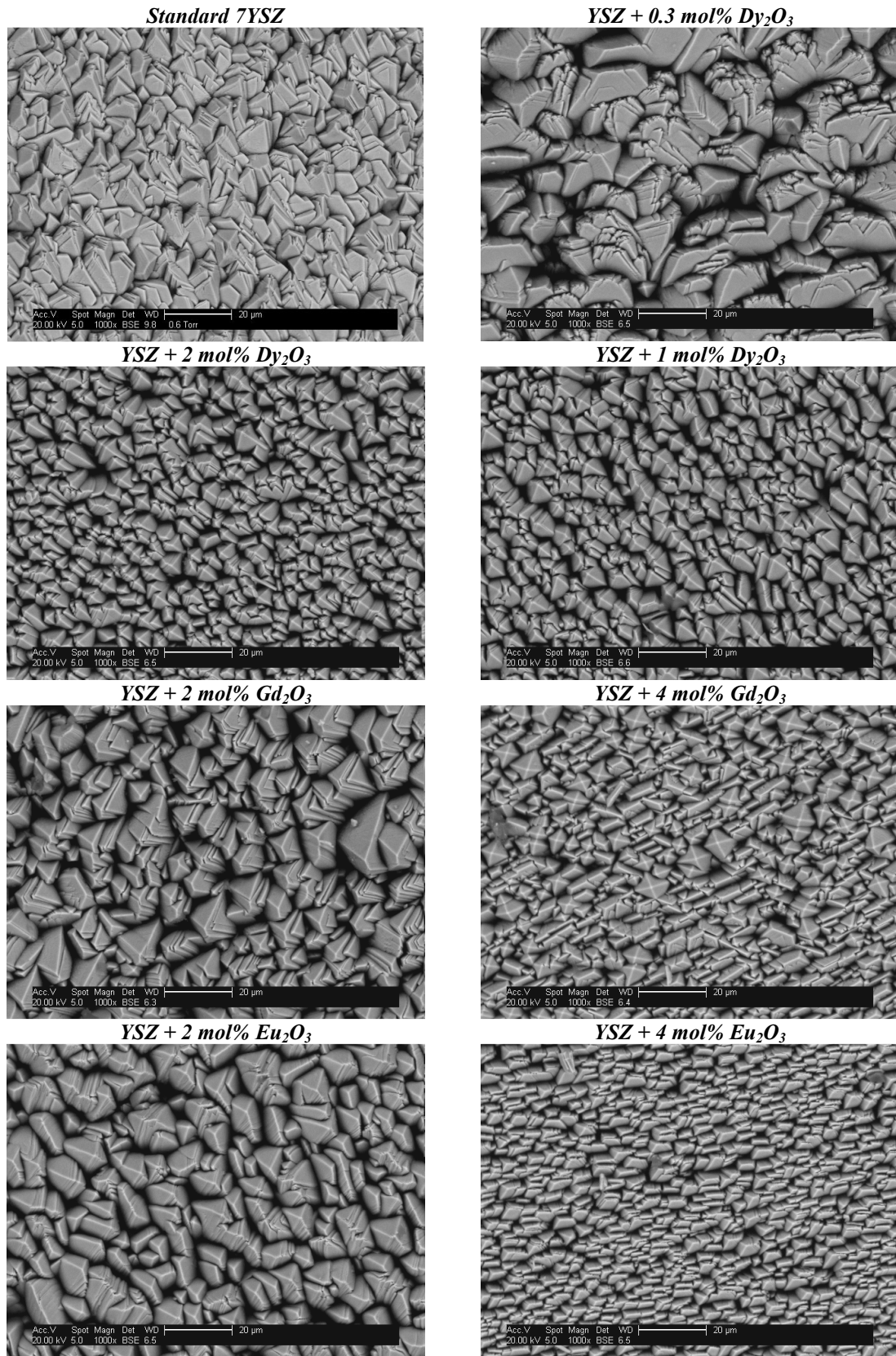
Figure 31: Top view micrograph of the TBCs.

Standard 7YSZ

YSZ + 0.3 mol% Dy₂O₃

YSZ + 2 mol% Dy₂O₃

YSZ + 1 mol% Dy₂O₃

YSZ + 2 mol% Gd₂O₃

YSZ + 4 mol% Gd₂O₃

YSZ + 2 mol% Eu₂O₃

YSZ + 4 mol% Eu₂O₃
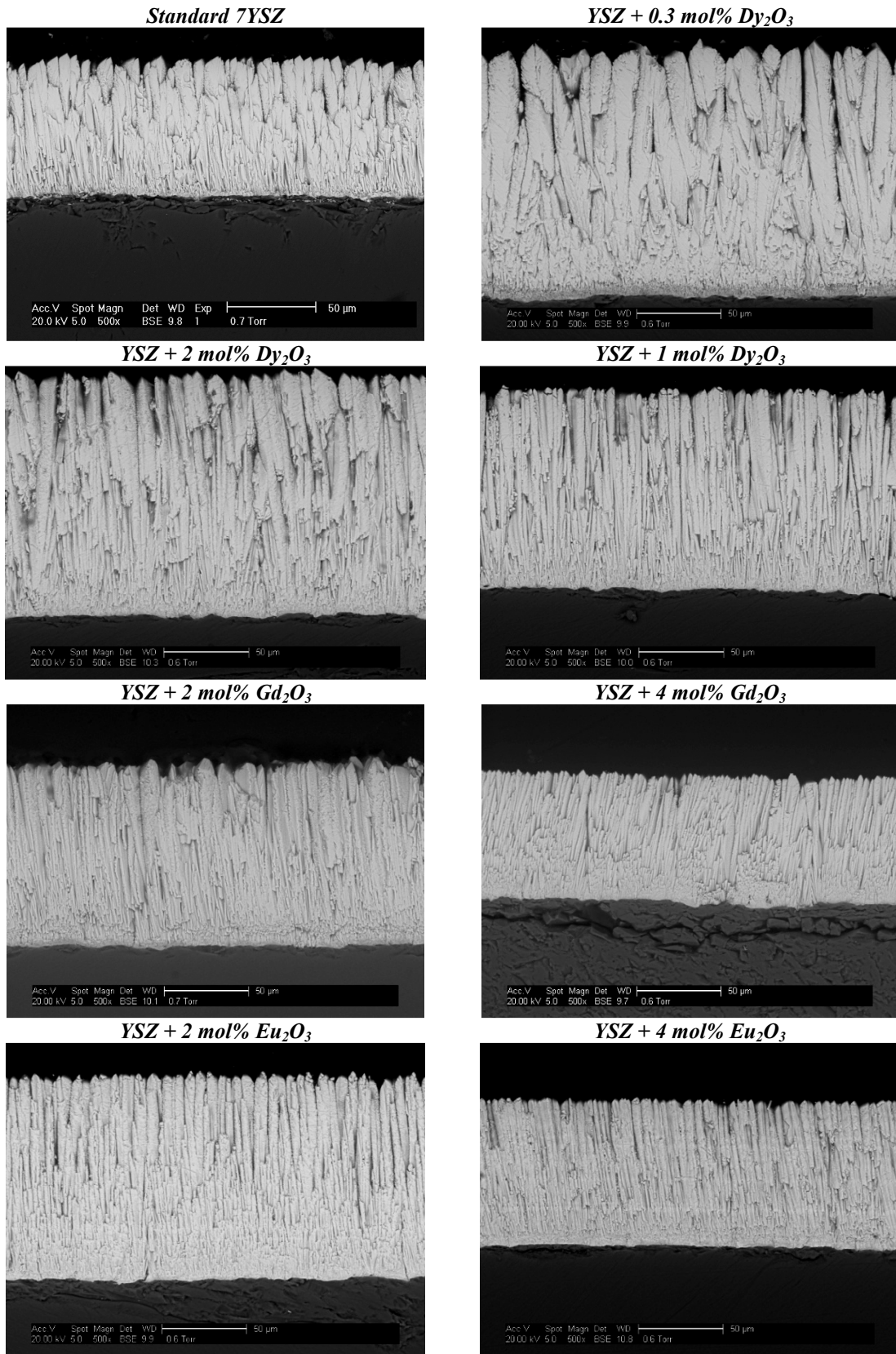
Figure 32: Cross-section micrographs of the TBCs.

YSZ:Dy0.3% is a thick coating with very coarse columns, whereas, YSZ:Gd4% is about half as thick with very fine columns closely entangled. In the 7YSZ and the YSZ:Dy0.3% coating there is frequent branching and the columns grow in a cone-like manner with a large aspect ratio from foot to top. As the percentage of dopant is increased there is less branching, the columns are finer and more regular. They are closely spaced and grow very parallel to each other.

The column tips of the 7YSZ and YSZ:Dy0.3% TBCs do not have any particular shape, they look very sharp and angular and for YSZ:Dy0.3% it is very difficult to distinguish individual columns. As the concentration of dysprosia is increased from 0.3 to 1 and 2 mol%, the morphology of the coatings becomes more regular and the tips have a more geometrical shape. The coatings with 2 mol% of dopants seem to have a more open microstructure with a clear intercolumnar porosity. The column tips also look more facetted, especially for the YSZ:Gd2% TBC. The YSZ:Gd4% coating clearly has two different types of columns with almost perfect pyramidal tips or with a "*roof-top*" shape, whereas, the composition with 4 mol% of europia has a very regular morphology with mostly "*roof-top*" column tips.

The typical grain size, or the column diameter, at the top surface of the coating was determined using the lineal intercept technique [169]. Two perpendicular lines were drawn in an area where the grain size was to be evaluated and the number of grain boundaries crossed by one line (or intercept) was counted. The grain size for each direction is given by:

$$D = 1.56 \frac{C}{MN}$$

<div align="right">**Equation 12**</div>

, where C is the total length of the test line, N the number of intercepts and M the magnification of the micrograph. The measurements were repeated four times on two different samples.

For an EB-PVD TBC, the diameter of the columns increases towards the top the coating due to the competitive growth of the grains, therefore, the ratio between the column diameter and the coating thickness (D/t) is a more appropriate measure to compare the various compositions. The column diameter, the coating thickness and the D/t ratio for each coating are reported in **Table 6.**

Table 6: Thickness (t), column diameter (D) and *D/t* ratio of the TBCs.

Composition	Coating thickness (µm)	Column diameter (µm)	D/t
7YSZ	80-100	12.8-13.0	0.128-0.163
YSZ:Dy0.3%	140-150	18.4-18.4	0.123-0.131
YSZ:Dy1%	100-120	10-11.1	0.083-0.111
YSZ:Dy2%	110-140	10.8-11.7	0.077-0.106
YSZ:Eu2%	115-125	10.5-12.7	0.085-0.11
YSZ:Eu4%	85-88	5.7-6.4	0.065-0.094
YSZ:Gd2%	110-140	8.5-8.6	0.061-0.078
YSZ:Gd4%	80-95	4.3-7.5	0.045-0.094

It can be seen from **Table 6** that, due to rare earth oxide additions, the coating thickness increases by up to 90% and the columns can be three times thinner compared to the standard 7YSZ. Moreover, the graph in **Figure 33**, presenting the D/t ratio as a function of the total concentration of stabiliser (yttria plus rare earth oxide), shows that ternary

additions of dopants tend to produce coatings with finer columns and that the column

diameter seems to decrease with increasing dopant concentration.
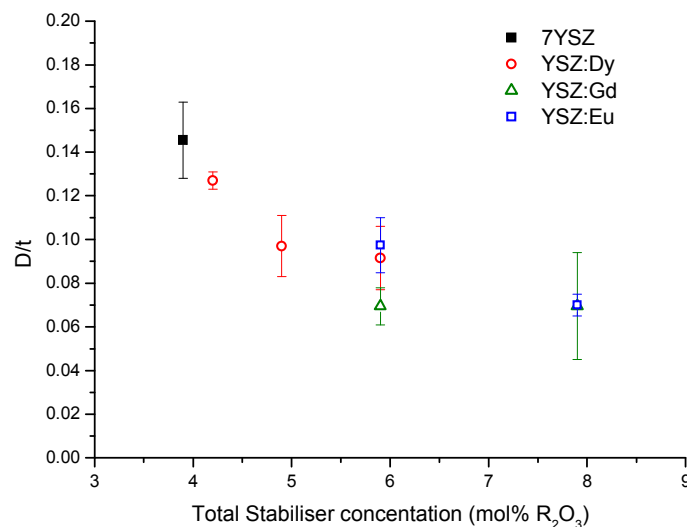
Figure 33: Ratio between the column diameter and the coating thickness (*D/t*) as a function of the total stabiliser concentration.

4.3.   Discussion

The values of the *c/a* ratio calculated from the XRD patterns are compared with

predictions from equations proposed by *Miller* [10], *Brandon* [10] and *Kim* [170] for the

ZrO_2/Y_2O_3 system in **Figure 34**. For the YSZ:RE compositions the *c/a* ratio is plotted

as a function of the total concentration in stabilisers, that is to say Y_2O_3 plus RE_2O_3. For

the 7YSZ and the YSZ:Dy compositions there is a very good agreement between the

values obtained and those predicted using these equations. However, the YSZ:Gd and

YSZ:Eu compositions show large discrepancies from those predicted. Those differences

are probably due to the fact that these equations were established for yttria additions and

therefore do not take into account the variations in the ionic radius between yttria and

the rare earth oxides. Indeed, the ionic radii are 0.1019 nm for Y^{3+}, 0.1027 nm for Dy^{3+},

0.1053 nm for Gd^{3+} and 0.1066 nm for Eu^{3+} [171] leading to differences between Y^{3+} and rare earth ions of 0.8%, 3.3% and 4.6% respectively. However, *Yoshimura* [172] and *Sheu* [173] have shown that, even though the lattice parameters are dependent on the ionic radii of the dopants, the tetragonality of the unit cell is almost independent of the R_2O_3 dopant (for R=Nd, Sm, Y, Er, Yb). As can be seen in **Figure 34**, the *c/a* ratio of zirconia stabilised with gadolinia is very similar to that of YSZ. These data were obtained for a TBC completely stabilised with Gd_2O_3, i.e. with a complete substitution of yttria by gadolinia, thereby a different behaviour might be expected than when gadolinia is used as a ternary dopant.
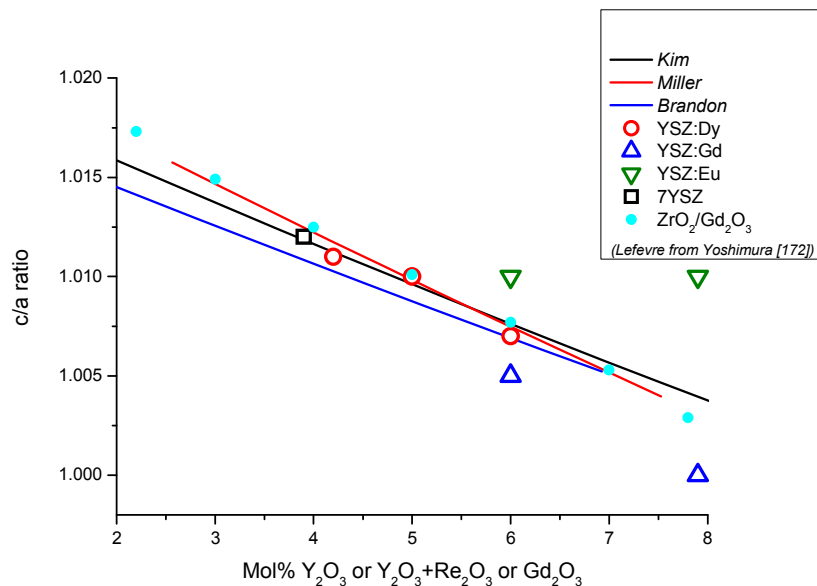
Figure 34: Variation of the *c/a* ratio with Y_2O_3 or Y_2O_3 + RE_2O_3 or Gd_2O_3 content.

This study shows that ternary additions of gadolinia further decrease the tetragonality of the *t'* phase compared to the YSZ composition with the same concentration of dopant. This suggests that the zirconium ions are not randomly and isotropically substituted by gadolinium in the tetragonal lattice. Such behaviour is not observed when YSZ is co-doped with dysprosia. Since the size of Dy^{3+} is very close to that of Y^{3+} it can be

assumed that the decrease in the c/a ratio is related to the oversize of Gd^{3+} ions. The misfit between Zr^{4+}, Y^{3+} and Gd^{3+} could lead to the substitution of Zr^{4+} by Gd^{3+} at preferential sites in the zirconia cell.

The author is not aware of any work published on the effect of ternary additions of rare earth oxides on the lattice parameters of YSZ, however, these results can be related the work done by *Rebollo et al*. [13] on the phase stability of Y+Gd co-doped zirconia. Indeed, the improved phase stability of the *t'* phase due to small additions of gadolinia can be explained by the fact that such additions further decrease the tetragonality of *t'* leading to a more "*cubic-like*" microstructure which would be less susceptible to partition and form the monoclinic phase. They also reported that they observed the formation of the monoclinic phase after they had heat treated the zirconia powder, doped with 4 mol% of yttria and 4 mol% of gadolinia, for 24 hours at 1350°C (the system had been previously heat treated for three 24 hour cycles at 1200, 1250 and 1300°C). In the present study, coatings with a similar composition were fully stabilised and no monoclinic phase formation was detected after aging 200 hours at 1500°C, followed by 200°C for 200 hours (A low temperature aging was performed in order to allow any tetragonal phase to fully transform into the monoclinic phase [56;174]).

Because the atomic radius of Eu^{3+} is bigger than that of Gd^{3+}, it was expected that the tetragonality of the YSZ:Eu powder would be further reduced. However this is not the case and the c/a ratio of the YSZ:Eu samples are even higher than the predicted one for zirconia with an equivalent concentration in yttria (**Figure 34**). More surprisingly, no decrease in the tetragonality is observed when the europia content is increased from 2 to

4 mol%. As expected, the lattice parameter *a* increases due to europia additions, however, *c* is also found to be higher, compared to the 7YSZ sample, leading to only a small or no reduction in the *c/a* ratio (**Table 5**).

The XRD graphs of the YSZ:Eu4% powders in **Figure 29** show that the *(002)* and *(200)* diffraction peaks are shifted towards higher and lower *2θ* values respectively. According to **Equation 11** this should reflect a decrease in the lattice parameter *c* and an increase in *a*. Moreover, it can be observed that, contrary to the other compositions, the *(002)* peak has a higher intensity than the *(200)* peak for the YSZ:Eu4% powder. The reason why these changes appeared only when YSZ is doped with europia remains unknown. There is clearly a concentration effect, since the intensity of the *(002)* peak of the YSZ:Eu2% sample is unusually high, but it is still lower than the *(200)* one. It is believed that due to its large ionic radius (4.8% larger than Y^{3+}), Eu^{3+} is abnormally incorporated into the zirconia lattice. A possible explanation is the partial reduction of Eu^{3+} to Eu^{2+} during deposition. Several cases of valence change from RE^{3+} to RE^{2+} in various compounds have been reported when the samples were prepared at high temperature. The explanation given is that, due to the substitution by RE^{3+}, defects are created in order to preserve the charge balance hence favouring the transfer of electrons from the defect to the RE^{3+} ions. In this particular case Zr^{4+} is substituted by Eu^{3+} creating oxygen vacancies [175;176].

The XRD and SEM results show that ternary additions of rare earth oxides not only decrease the tetragonality of the coating but also produce TBCs with a finer microstructure. According to the *Movchan* diagram **Figure 10** (Page 18), finer columns

could be obtained by decreasing the ratio between the deposition temperature and the melting point of the coating material (*T/Tm*). Since the deposition temperature was the same for all the depositions the refining of the columns could be caused by an increase in the melting point of the ingot material due to dopant additions.

Rouanet [177] reported an increase in the melting temperature of zirconia with increase in the concentration of yttria or dysprosia (**Figure 35**). Consequently it is reasonable to assume that ternary additions of dysprosia will also result in an increase in the melting point of YSZ and could account for the observed reduction in the column diameter. As it can be seen in **Figure 35**, gadolinia additions tend to reduce the melting temperature of zirconia, however, the column diameter is further decreased in the YSZ:Gd2% coating compared to the YSZ:Dy2% TBC. An even finer microstructure is observed when the gadolinia concentration is increased from 2 to 4 mol%.
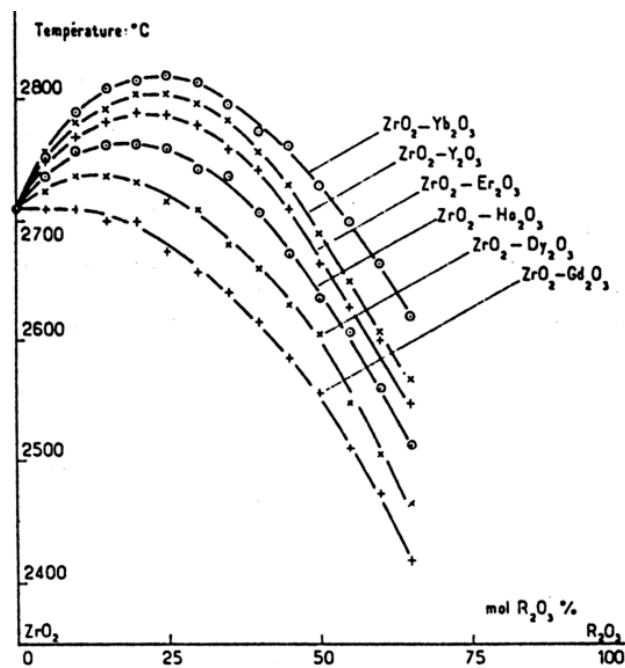
Figure 35: Melting temperature of zirconia as a function of secondary additions of yttria and rare earth oxides [177].

Rouanet noticed that the increase in the melting point of zirconia was less pronounced for trivalent rare earth ions with a large ionic radius. Since the ionic radius of Eu^{3+} is larger than the one of Gd^{3+}, it was expected that europia additions would not result in an increase in the melting point. Nevertheless the YSZ:Eu samples also have a finer microstructure compared to the YSZ coating therefore it is rather unlikely that the reduction in the column diameter observed for YSZ:Dy samples is caused by an increase in the melting temperature of the ingot material due to ternary additions of rare earth oxides.

Another explanation refers to the variations in tetragonality between the various compositions. Depending on the ionic arrangements the surface energy of the condensed coating will vary and therefore the crystal growth conditions will be different for the cubic and the *t'* phase [178]. **Figure 36** presents the ratio between the grain size and the coating thickness as a function of the tetragonality. This shows a refinement of the microstructure of the TBC with decrease in *c/a* ratio.

It is believed that because the tetragonal cell is distorted compared to the cubic one, the columns can have slightly different growth directions. Only the one with a favourable orientation will grow preferentially and reach the top of the coating hence the coarse microstructure observed for 7YSZ and YSZ:Dy0.3%. On the contrary, the more symmetrical cubic cell will produce a very "ordered" TBC with finer and more parallel columns. Indeed, since the grains are more likely to have the same orientation, there will be less competitive growth, thus, more grains will be "allowed" to grow at the same speed and parallel to each other.
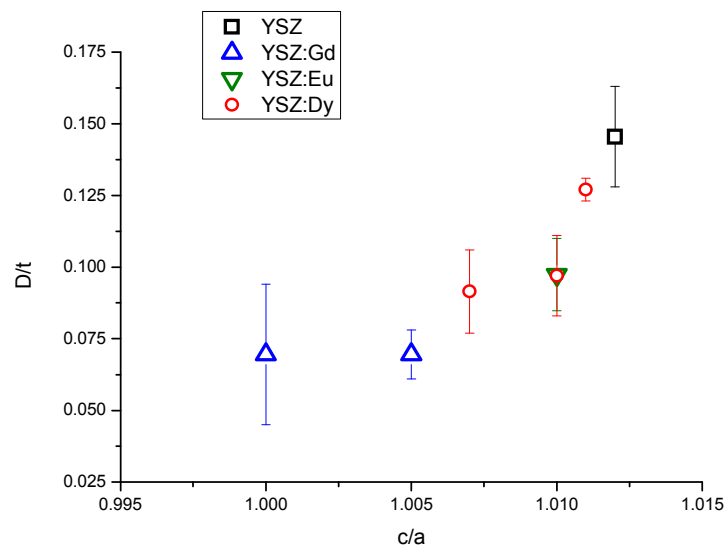
Figure 36: Ratio between the grain size and the coating thickness as a function of the tetragonality for the various compositions.

Figure 37 is an SEM micrograph of a ZrO_2-4.8mol% Y_2O_3 TBC. According to the phase diagram in **Figure 5b** such a composition has a more cubic microstructure compared to the standard 7YSZ. It can be seen that this TBC also has a finer and more "ordered" columnar microstructure. Consequently the refinement of the TBC microstructure seems to be predominantly governed by the tetragonality and therefore should be independent of the type of stabiliser.
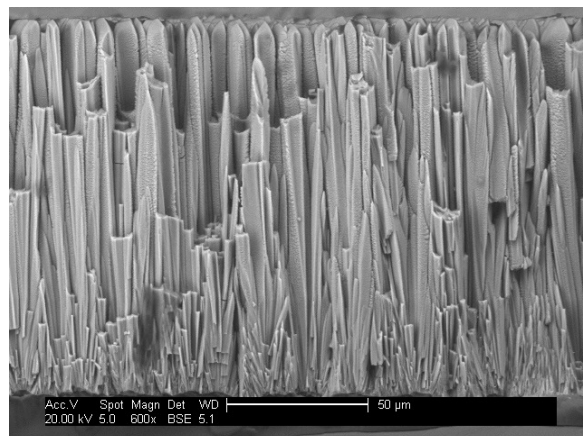
Figure 37: SEM micrograph of a ZrO_2-4.8mol% Y_2O_3 TBC (Fractured sample).

As mentioned at the beginning of this chapter, ternary additions of rare earth oxides not only decrease the thermal conductivity [31], but could also improve the phase stability of the TBC [13]. However, it has been reported that the impact and erosion resistance of a TBC is also related to the zirconia lattice parameters. It has been predicted that the erosion and impact resistance should decrease with decreasing *c/a* ratio [179]. Therefore, since rare earth additions reduce the tetragonality of the TBC, a decrease in the erosion and impact resistance could be expected for doped coatings. This is consistent with the results published by the author on the erosion of YSZ:Gd2% EB-PVD TBCs [82]. It was found that such coatings have a lower erosion resistance at room temperature compared to the standard 7YSZ, however, these results are balanced by an observed reduction of the erosion rate at high temperature (825°C). It is believed that these changes in mechanical properties with decreasing *c/a* ratio are also related to changes in the coating microstructure, rather than the *c/a* ratio and can be associated with the tetragonality through the influence the *c/a* ratio has on the growth microstructure.

4.4. *Phosphorescence*

4.4.1. *Experimental set-up for phosphorescence measurements*

All the phosphorescence measurements were done at *Southside Thermal Sciences Limited* (*STS*) at *Imperial College*, London. The calibration curves of the EB-PVD coatings, that is to say the decay time of the phosphorescence as a function of temperature, were determined using the experimental set-up shown in **Figure 38**.
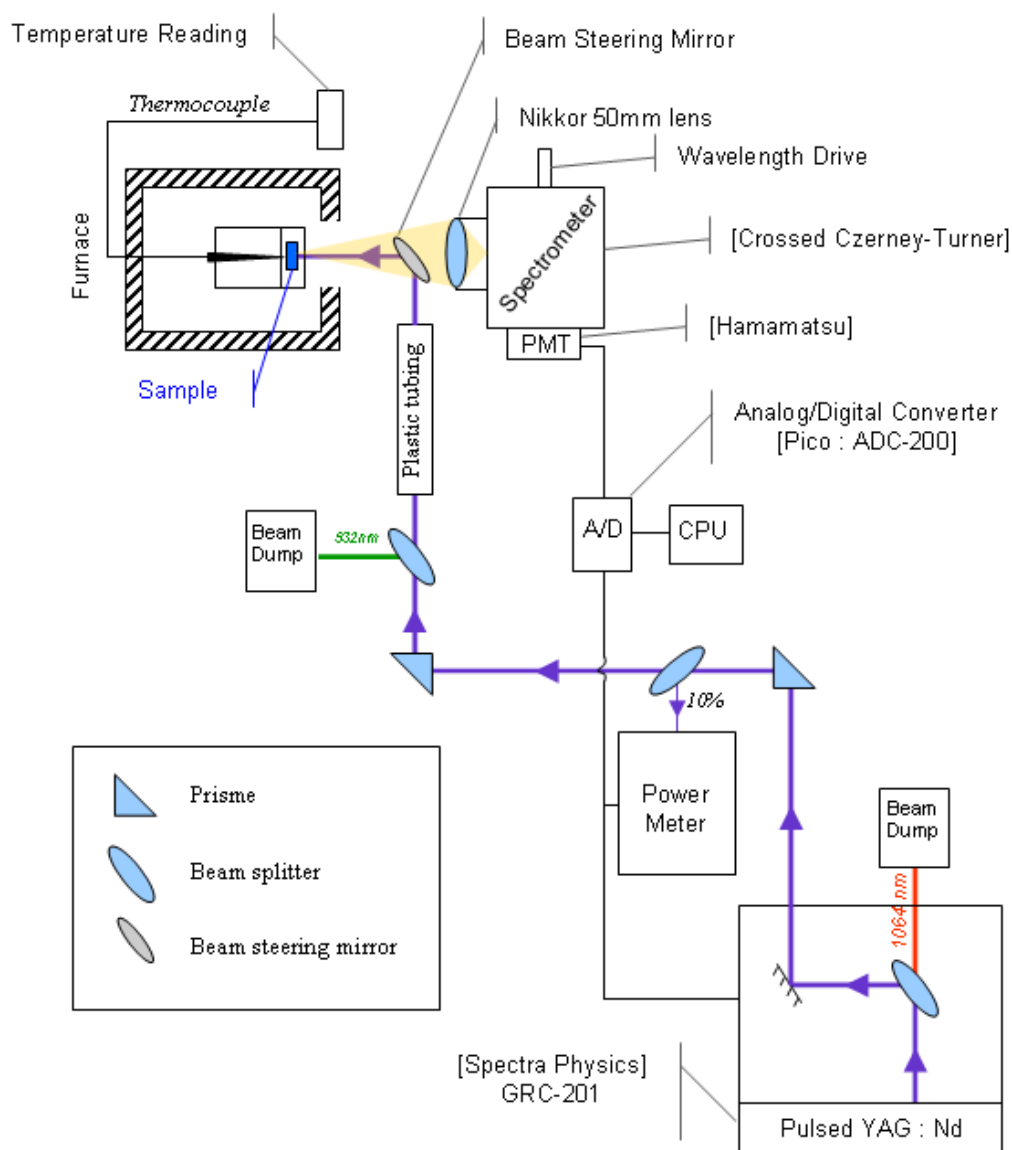
Figure 38: Experimental set-up for lifetime decay measurements. The phosphorescence spectrum is observed by replacing the photomultiplier by a linear CCD array.

A pulsed YAG:Nd laser with an output energy of about 20 mJ per pulse was used to excite the phosphorescent coating. The laser was operated at 266 nm or 355 nm depending on the phosphor sample at a pulse rate of 16 Hz. A light leakage with a wavelength of 532 nm coming from the harmonic crystal assembly of the laser was prevented from hitting the sample using an external beam dump. The beam was steered through the furnace window and the resulting luminescence was focussed on the

entrance slit of the spectrometer by a 50 mm lens. The lifetime decay of the phosphorescent signal was measured using a photomultiplier placed at the exit slit of the spectrometer. The recording of the phosphorescence was triggered by the laser Q-switch. The exponential decay was fitted to the average of 15 recorded pulses using commercial software and was recorded as a function of temperature. The recorded phosphorescence decay was evaluated using a single exponential *Levenburg/Marquart* optimisation (curve fitting algorithm). The temperature was determined with a thermocouple placed at the back of the sample. For each temperature five lifetime decay measurements were taken and averaged. In order to record the phosphorescence spectrum, the photomultiplier is replaced by a CCD linear array (*Alton LS2000*).

4.4.2. Lifetime decay measurements of YSZ phosphors

Only the results for the coatings doped with 2 mol% of rare earth oxide are presented in this chapter in order to compare the temperature capabilities of various dopants.

4.4.2.1. Dysprosia doped YSZ phosphor

The author is not aware of any results published in the open literature concerning lifetime decay measurements of YSZ:Dy phosphors. The phosphorescence spectrum was recorded between 470 and 610 nm when excited at 355 nm (**Figure 39**). All the emission peaks correspond to *f-f* transitions and the multiple structure of the spectrum is attributed to the splitting of the dysprosium *4f* shell due to the *t'* YSZ crystal field. The emission at around 585 nm which corresponds to $^4F_{9/2} \rightarrow {}^6H_{15/2}$ transitions, is the most intense and was used for the lifetime decay measurements.
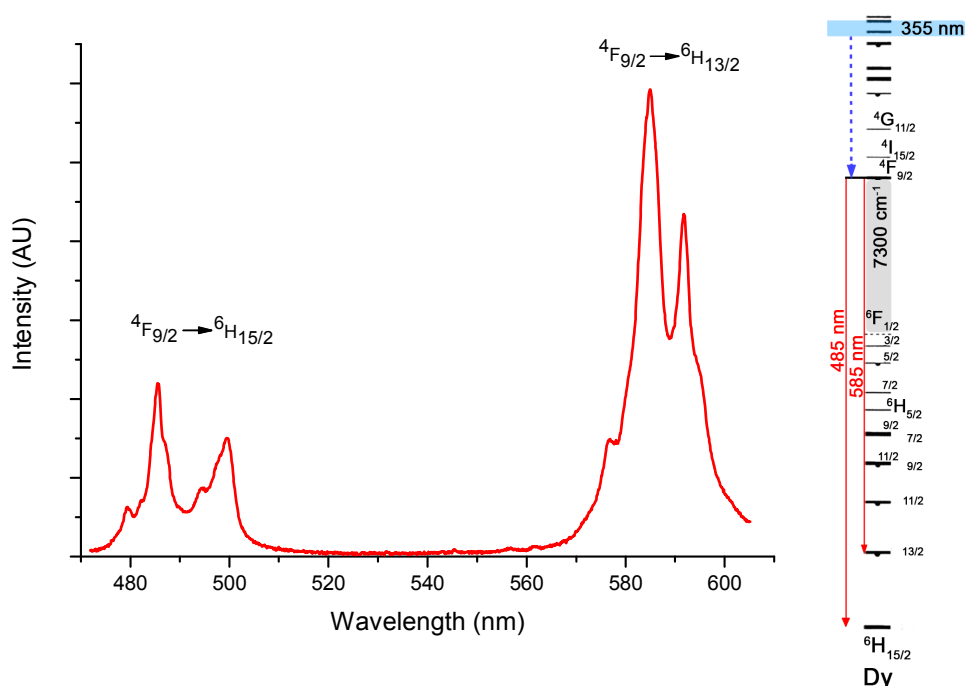
Figure 39: Luminescence spectrum of YSZ:Dy2% phosphor excited at 355 nm and energy levels of Dy^{3+}.

After excitation at 355 nm, the electrons decay from the close spaced high energy levels down to the $^4F_{9/2}$ level via non-radiative processes. Since the average phonon energy for a YSZ crystal is about 520 cm^{-1}, 15 phonons are required to bridge the 7300 cm^{-1} energy gap between the $^4F_{9/2}$ and $^6F_{1/2}$ levels and therefore the probability of multiphonon relaxation is very low, especially at room temperature (**Equation 9**). Consequently the electrons return to the ground state by emitting radiation at 585 or 485 nm.

As shown in **Figure 40**, as the temperature increases the lifetime of the phosphorescence (τ) decreases. τ was determined by fitting these curves with a single exponential decay for the different temperatures (**Equation 5**) in order to obtain the calibration curve represented in **Figure 41**.
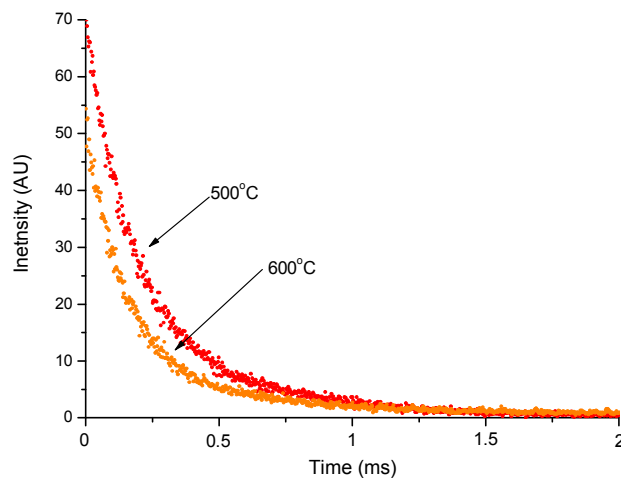
Figure 40: Phosphorescence decay curves at 500°C and 600°C of the YSZ:Dy2% EB-PVD TBC.

The temperature sensitivity range of YSZ:Dy2% phosphor was between around 500 and 950°C. The calibration curve was fitted by combining **Equation 8** and **Equation 9** for an energy gap of 7300 cm^{-1} and phonon energy of 385 cm^{-1} which means that 18 phonons are involved in the process.
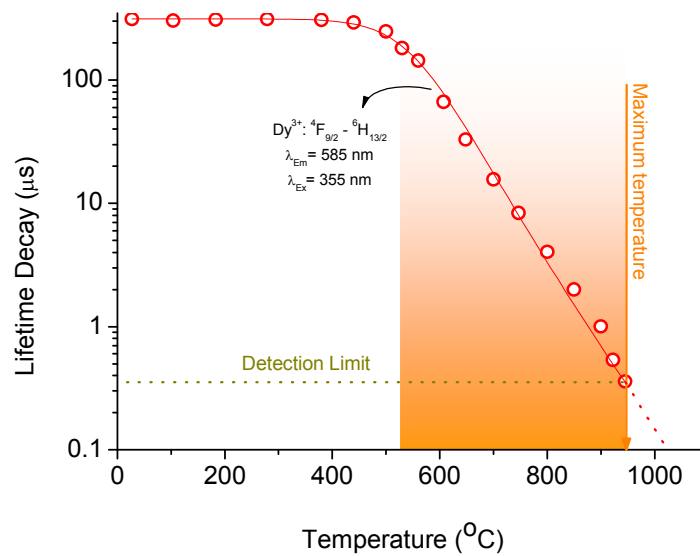
Figure 41: Calibration curve of the YSZ:Dy2% EB-PVD TBC.

The maximum temperature capability was found to be 950°C, for a lifetime of around 0.3 μs. The detection limit of the system is governed by the response time of the photomultiplier which was estimated to be between 0.3 and 0.4 μs [116], therefore, by using a photomultiplier with a faster response time temperatures in excess of 1000°C should be measurable with a YSZ:Dy phosphor, which is typically the temperatures observed at the interface between the thermally grown oxide (TGO) and the ceramic top coat, consequently YSZ:Dy could be used as an inner layer to determine the temperature at this interface in an operating gas turbine.

4.4.2.2. Europia doped YSZ phosphor

Feist et al. [111;114;120] studied the YSZ:Eu phosphor powder and reported temperature capabilities up to 800˚C, however, most recently *Gentleman et al.* [121;122] reported temperature measurements up to 1100˚C using the same phosphor, but in the latter study as part of a TBC system.

In the current work, the YSZ:Eu phosphor was exited using a 266 nm radiation and the luminescent transitions which could be observed between 570 and 670 nm are represented in the energy level diagram in **Figure 42**. The strongest lines observed are generally $^5D_0\rightarrow^7F_{1,2}$ since the $^5D_{1,2,3}$ levels can be depopulated by non-radiative multiphonon processes because of the small energy gap within the $^5D_0$ level. The $^5D_0\rightarrow^7F_1$ emission line is a magnetic dipole allowed transition and is almost independent of the host material. The strongest peak at around 606 nm corresponds to the $^5D_0\rightarrow^7F_2$ electric dipole transition. It is said to be "*hypersensitive*" and is more affected by the environment than normal $f\rightarrow f$ transitions. It is this particular sensitivity

to the phosphor host material that is used for the monoclinic phase detection in YSZ:Eu coatings [164].
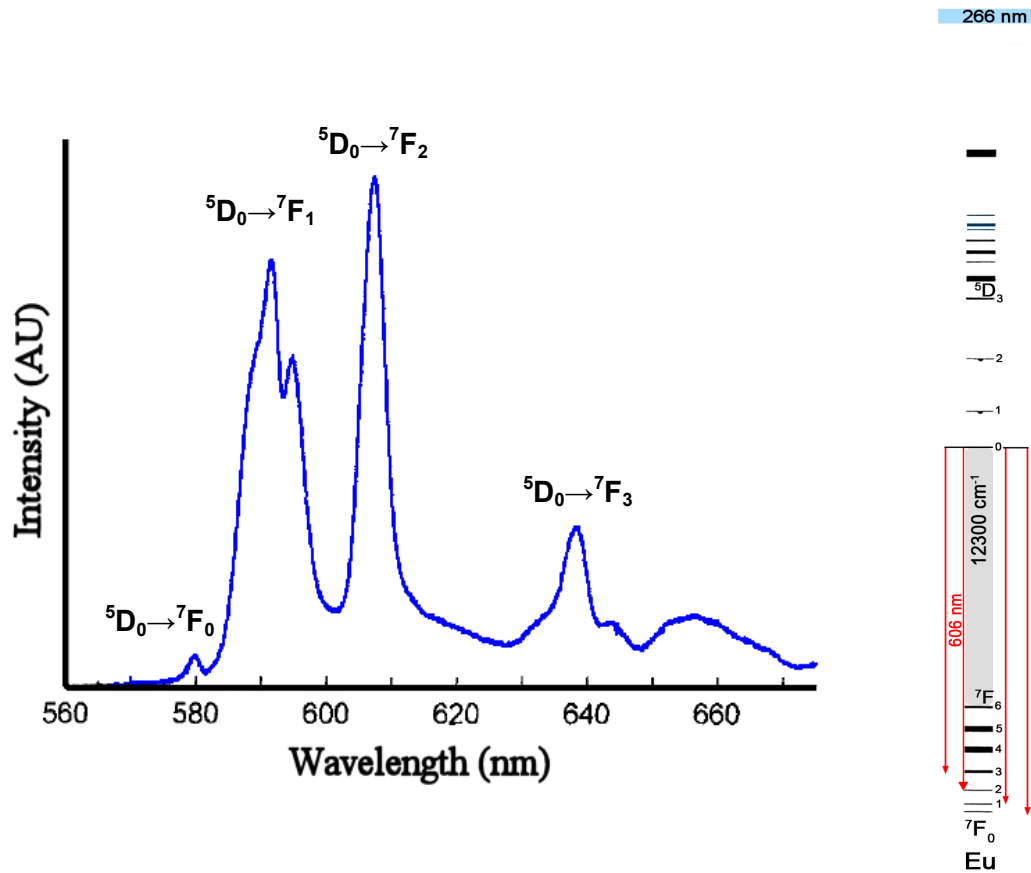
Figure 42: Luminescence spectrum of YSZ:Eu excited at 266 nm and energy levels of Eu^{3+} [116].

The lifetime decay (LTD) was calculated from the emission line with the highest intensity at around 606 nm, which corresponds to energy transitions from $^5D_0 \rightarrow ^7F_2$. As can be seen in **Figure 43**, the YSZ:Eu phosphor can be used to measure temperatures from 500°C up to around 800˚C. The detection limit of 0.3 μs of the system at *STS Ltd* was not reached because the YSZ:Eu phosphorescence was quenched at 800°C and consequently the luminescence could not be recorded and the decay time calculated above this temperature.
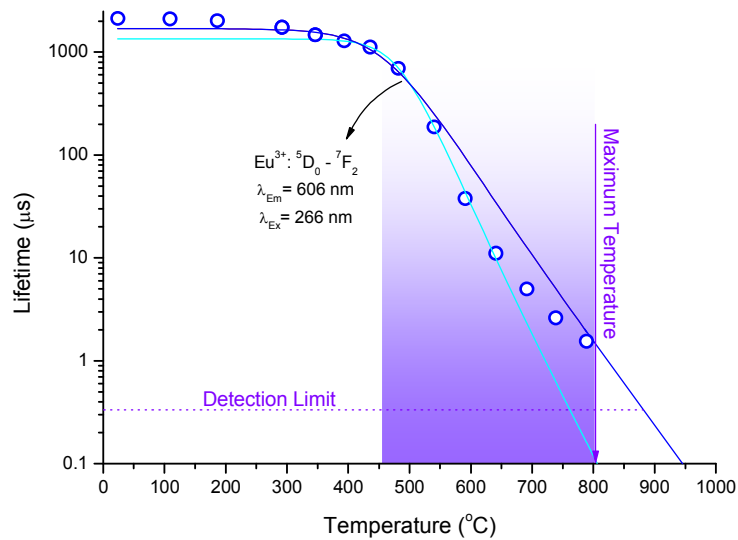
Figure 43: Calibration curve of the YSZ:Eu2% EB-PVD TBC.

Contrary to YSZ:Dy phosphor, the lifetime of the YSZ:Eu luminescence does not decrease exponentially with the temperature, there is a curvature in the slope at around 600°C. This was found to be due to a notable decrease in the intensity of the luminescence which made the phosphorescence signal very "noisy" and difficult to fit. Consequently the decay time fitting for an energy gap of 12300 cm^{-1} gives a phonon energy ranging from 437 to 505 cm^{-1} and therefore 24-28 phonons are involved in the non-radiative process. If the fitted curves are extrapolated for a detection limit of 0.1 μs, then YSZ:Eu would show maximum temperature capability between 800°C and 950°C.

The temperatures that have to be measured for aero-gas turbine service range from 900˚C to 1500˚C, therefore, YSZ:Eu cannot be used for this application, but it is still a potential candidate for use in industrial gas turbine applications when operating at lower temperatures.

4.4.2.3. Gadolinia doped YSZ phosphor

Gadolinia was studied as a potential phosphor because it was shown from previous studies carried out at *Cranfield University* that ternary additions of gadolinia can also significantly reduce the thermal conductivity of the TBC and because it has the biggest energy gap of all the trivalent rare earth ions (**Figure 17**). The YSZ:Gd2% EB-PVD coatings were excited at 274 nm using a dye laser and the luminescence line at 315 nm was observed to determine the lifetime decay as a function of temperature. This emission line comes from the transition between the $^6P_{7/2}$ excited state to the ^8S ground state. The energy levels of Gd^{3+} are located at exceptionally high energies owing to the extreme stability of its half-filled *f*-shell (f^7). The results are presented in **Figure 44**.
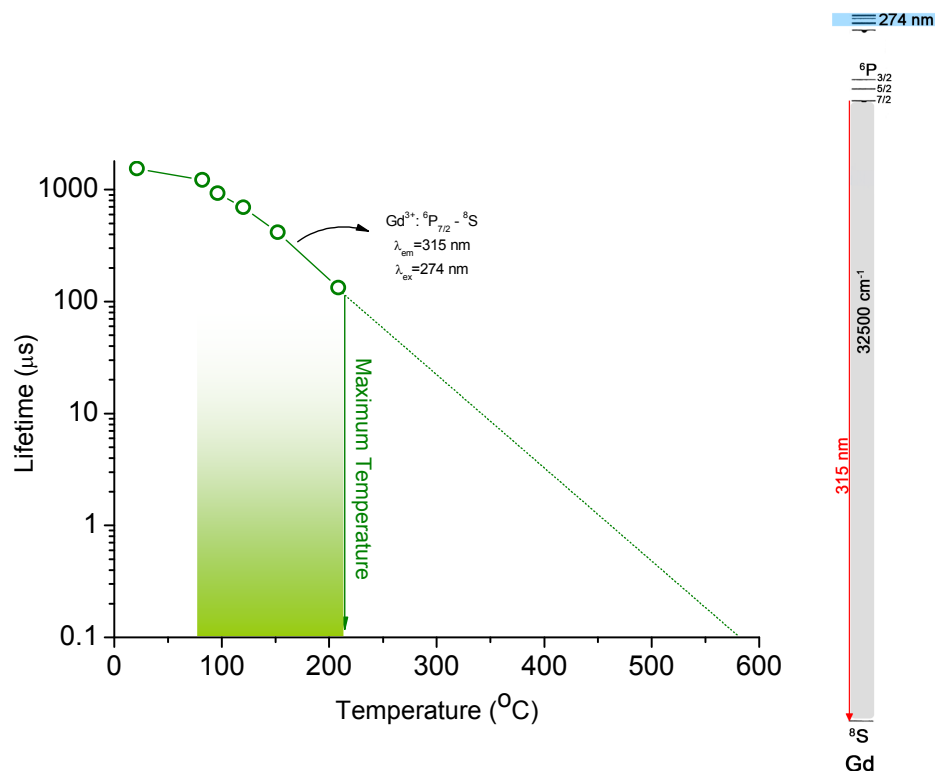
Figure 44: Calibration curve of the YSZ:Gd2% EB-PVD TBC and energy levels of Gd^{3+}.

Contrary to YSZ:Eu and YSZ:Dy coatings, where the lifetime decay remains relatively constant up to around 400˚C, rapid quenching is observed as soon as the temperature starts to increase. The YSZ:Gd calibration could not be fitted with **Equation 9** suggesting that different quenching mechanisms are involved in the rapid decrease of the YSZ:Gd phosphorescence lifetime. Lifetime decays at temperatures up to just in excess of 200˚C were measured, meaning that the temperature capabilities of YSZ:Gd phosphor are rather poor, although it could be used as a low temperature thermographic phosphor.

4.5. *Discussion*

Gentleman et al. [123] from the *University of California*, Santa Barbara (*UCSB*) reported temperature measurements up to 1100˚C with a YSZ:Eu phosphor, whereas in this study the maximum temperature capability of such a phosphor was found to be around 800°C. Both calibration curves are presented in **Figure 45**.

With their laboratory set-up, they can measure lifetimes as short as 20 ns compared to 300-400 ns for the set-up used for these experiments. However, as can be seen in **Figure 45**, at the highest temperature (800°C) the phosphorescence lifetime is still around 1.5 μs, well above the measurement limitations of either system. One of the main differences between the two systems is the fact that *Gentleman et al.* use a sapphire fibre to collect the phosphorescent signal very close to the sample [121]. While in the set-up used at *STS*, the spectrometer was situated at around 30 cm from the sample and at above 800˚C the intensity of the phosphorescent signal was so low that

the decay time could not be evaluated. These thermographic phosphors are being developed as coatings for high pressure turbine blades, for in-situ temperature measurements, therefore, the use of a fibre array that almost touches the rotating turbine blade is not a viable option. Although, experimentally, the YSZ:Eu phosphor could have a sensitivity up to 1100°C, the low intensity of the returned signal prevents remote temperature measurement much above 800°C.
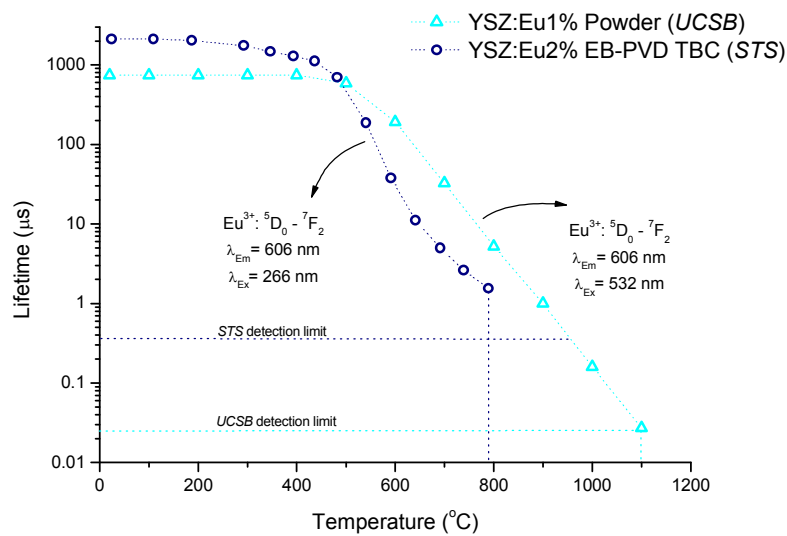
Figure 45: Comparison of the YSZ:Eu calibration curves measured at *STS* and *UCSB* (*UCSB* data redrawn from [180]).

It is believed that the extinction of the YSZ:Eu phosphorescence is caused by the depopulation of the $^5D_0$ emission level via charge transfer state at high temperature. The mechanisms involved in the emptying of the ^5D energy levels by charge transfer state has been described in **Chapter 2.3.1**. Because Eu^{3+} has a $4f^6$ configuration (electron shell half-filled less one) an electron from the YSZ valence band can be favourably promoted to the $4f$ shell. Consequently the charge transfer state of YSZ:Eu should have a low energy (lower than Dy^{3+} which has a $4f^9$ configuration) providing a non-radiative path for electron relaxation at high temperatures.

However, if the quenching of the phosphorescence is not taken into account, allowing the curves in **Figure 45** to be extrapolated to a detection limit of 0.02 μs, it would appear that the calibration curve of *Gentleman et al.* would be able to measure higher temperatures (1100°C compared to 875-1000°C for the sample measured at *STS*). A YSZ:Dy2% EB-PVD sample deposited at *Cranfield University* was tested on the experimental set-up at *UCSB* in order to investigate the differences obtained between the *UCSB* system and the *STS* system. The calibrations curves of YSZ:Eu and YSZ:Dy phosphors are represented in **Figure 46**.
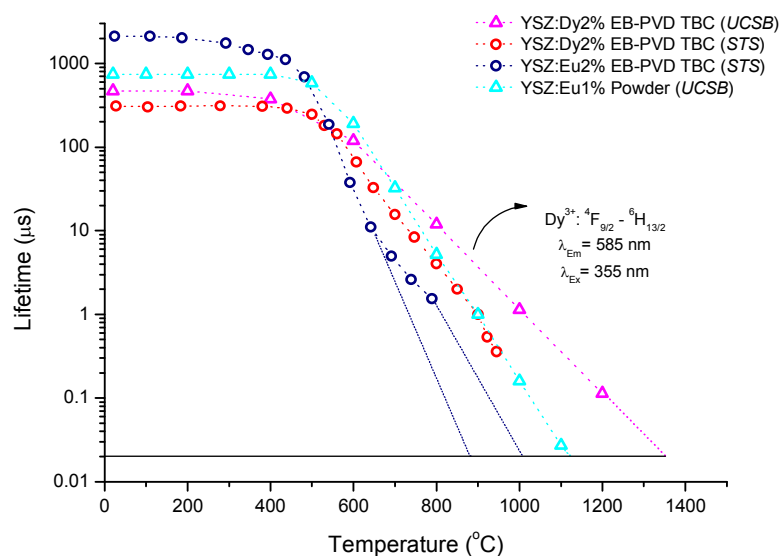
Figure 46: Comparison of the YSZ:Eu and YSZ:Dy calibration curves measured at *STS* and *UCSB*.

Firstly, these results show that higher temperature capabilities were also obtained for YSZ:Dy using the *UCSB* set-up. Secondly, it confirms that YSZ:Dy has higher temperature sensitivity, when compared to YSZ:Eu. It is believed that the way the phosphorescence signal is collected is not the only source of the discrepancies. The

differences could also come from the luminescence decay fitting routine used to determine the lifetime at the various temperatures.

In the *STS* set-up the luminescence decay was automatically fitted with a single exponential decay function for every phosphor tested, whereas, *Gentleman et al.* used a second order exponential decay function to model the lifetime of the YSZ:Eu luminescence [122]:

$$I(t) = I_1 e^{\frac{-t}{\tau_1}} + I_2 e^{\frac{-t}{\tau_2}}$$

Equation 13

and from the longer lifetime (τ_2) the calibration curves were plotted.

The decay curves presented in **Figure 47** indicates that the phosphorescence decay of YSZ:Eu is not modelled very accurately by a simple exponential decay. The second order exponential decay (**Equation 13**) better fits the data.
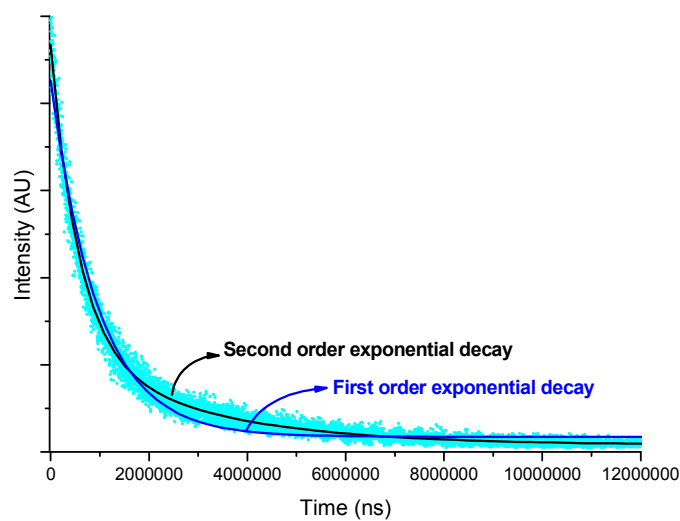
Figure 47: YSZ:Eu phosphorescence decay fitted with a first and second order exponential decay function.

STS has tested a YSZ:Eu10% powder, such a high dopant concentration gave a very intense phosphorescence signal and the extinction of the luminescence was not observed at 800°C. The decay curves were fitted with **Equation 13** using a commercial software[♦] and τ_1 and τ_2 are plotted in **Figure 48.**
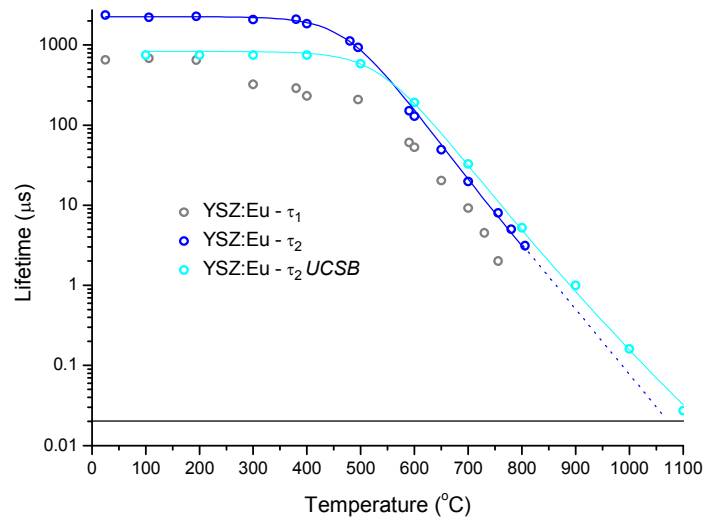
Figure 48: Calibration curves of YSZ:Eu phosphor when fitted with a second order exponential decay function (τ_1 and τ_2).

The temperature sensitivity of YSZ:Eu is increased up to 1075°C using the longer decay (τ_2), showing the importance of choosing the correct fitting routine in the determination of the lifetime. However, the *UCSB* calibration curve still permits prediction to higher temperatures. The fact that they use a fibre optic almost in contact with the sample makes their measurements less susceptible to background radiations, the signal-to-noise ratio is improved, the phosphorescence decay will be "clearer" and consequently the fitting more accurate. Their calibration curves represent the "ideal" conditions, however, such a set-up cannot be used for in-situ measurements in service on rotating components. In an open flame environment the measurements will be influenced by

---

[♦] Origin 7.0, OriginLab[TM].

background radiations. Consequently it is believed that the calibration curves obtained with the *STS* set-up are more conservative and more representative of the phosphor temperature dependence under service conditions.

The measurements carried out on equipment at *STS* and *UCSB* showed that YSZ:Dy has higher temperature measurement capabilities, compared to YSZ:Eu. Further, the origin of the differences between YSZ:Gd, YSZ:Eu and YSZ:Dy are not fully understood, indeed $P_{NR}(n,T=0)$ in **Equation 9** is highly dependent on the order of the process (n) therefore, the larger the energy gap the more important the radiative decay compared to the non-radiative one. Consequently, it was to be expected that doping with rare earth oxides with large energy gaps would give phosphors with high temperature capabilities, however, lifetime decay measurements have shown the exact opposite trend:

YSZ:Gd<YSZ:Eu<YSZ:Dy.

The lifetime of the phosphorescence of YSZ:Gd2% started to decrease at around 80°C and above 200°C the intensity of the luminescence was so low that the lifetime could not be measured. Such behaviour was not to be expected, since the energy gap between the $^6P_{7/2}$ and the ^8S level is about 32500 cm^{-1} and would require 65 phonons each of 500 cm^{-1} to be bridged. The phosphorescence of YSZ:Dy and YSZ:Eu is not quenched significantly below 400°C and the energy gaps of these phosphors are much smaller than the one of YSZ:Gd, therefore, it is not believed that the $^6P_{7/2}$ is depopulated by multiphonon relaxation. *Robbins et al.* [181] reported similar performances on a YAG:Gd phosphor. They noticed that the intensity of the cathodoluminescence

(luminescence occurring after electron bombardment) decreases rapidly above -150°C. The quenching was attributed to a decrease in the excitation efficiency of the $^6P_{7/2}$ state.

If it is assumed that, for YSZ, the maximum optical frequency of phonons is about 500 cm^{-1}, then, 65, 25 and 15 phonons are required to depopulate the emitting energy levels of YSZ:Gd, YSZ:Eu and YSZ:Dy respectively by non-radiative decay. At room temperature this process is too slow to contribute to the lifetime, and for this reason τ remains relatively constant between room temperature and about 400°C for YSZ:Eu and YSZ:Dy. As the temperature increases, more phonons are available and the non-radiative contribution increases. **Figure 49** is a plot of $P_{NR}(n.T)$ without taking into account the constant $P_{NR}(n,T=0)$ for a phonon energy of 500 cm^{-1} using three different decay modes. The temperature dependences are quite distinct for the various modes.
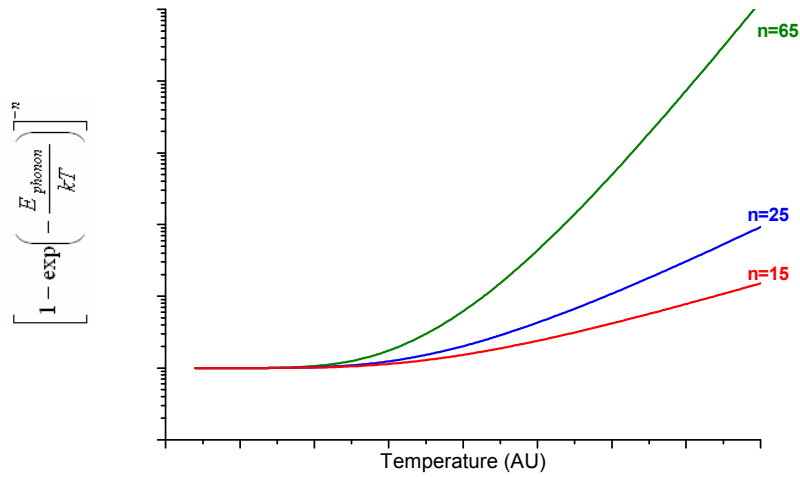
Figure 49: Plot of $\left[1-\exp\left(-\dfrac{E_{phonon}}{kT}\right)\right]^{-n}$ **for three different decay modes.**

Obviously at the same temperature a 65 phonon mode is a lot less probable than a 15 phonon mode and this will be reflected in the $P_{NR}(n,T=0)$ value, however, it seems that low phonon modes are less dependent on temperature.

The quenching parts of the calibration curves of Yttrium Aluminium Garnet (YAG) phosphors are represented in **Figure 50a** and they are normalised in **Figure 50b** in order to compare the temperature dependence of the quenching process for different rare earths in a YAG host material. The phosphors are arranged from the slowest to the fastest temperature quenching:

YAG:Tb<YAG:Eu<YAG:Dy<YAG:Tm

The results for YAG based phosphors show that faster quenching is observed for larger energy gaps and therefore for higher multiphonon relaxation modes, which confirms the theoretical behaviour seen in **Figure 49**. Because for YSZ:Eu a higher phonon mode is involved, it was expected that YSZ:Eu would start to quench at higher temperatures compared to YSZ:Dy however this was not the case and for both phosphors the quenching process started at around 400°C. Since YSZ:Eu quenches faster, it has a lower temperature capability compared to YSZ:Dy. It is worth noting that the steeper slope of the YSZ:Eu calibration curve would give temperature measurements with a better accuracy, but shorter dynamic range.

(a)   (b)
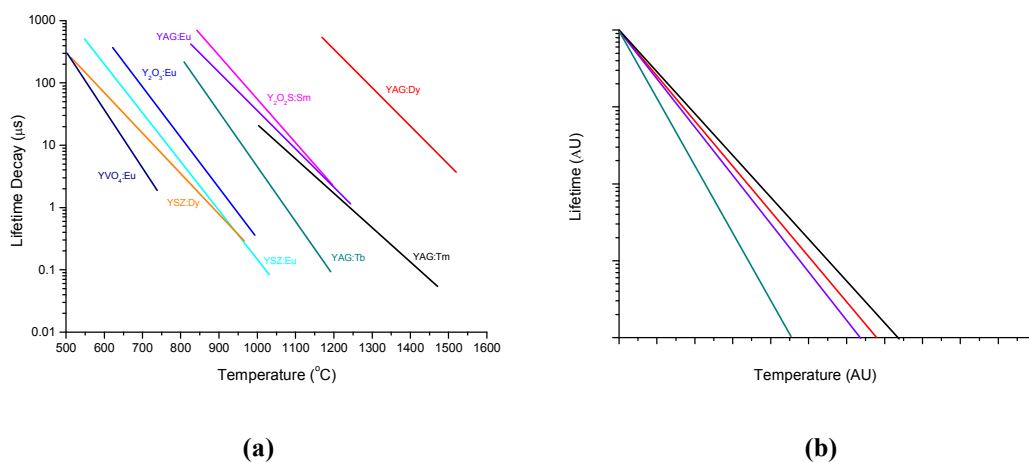
Figure 50: (a) Quenching parts of the calibration curves of various YAG phosphors, (b) normalised [115;138].

Even if they are traditionally called "rare earths" and dysprosium comes from the Greek word *dysprositos* which means "hard to obtain" lanthanides are relatively abundant in the earth's crust. Nevertheless, their prices remain very high compared to that of zirconia and yttria and varies a lot from one rare earth to another. Europia is eight times more expensive than dysprosia and therefore YSZ:Dy sensor coatings would be cheaper to produce, whilst offering an increased dynamic temperature measurement range, albeit at a slightly reduced precision.

Table 7: YSZ and rare earth prices in 2005 [182;183].

Material	Price ($/kg)	Material	Price ($/kg)
Ceria	19.2	Praseodymia	36.8
Dysprosia	120	Samaria	360
Erbia	155	Scandia	6,000.00
Europia	990	Terbia	535
Gadolinia	130	Thulia	2,300.00
Holmia	440	Ytterbia	340
Lanthana	23	Yttria	88
Lutetia	3,500.00	YSZ (3 mol%)	22.1
Neodymia	28.5	YSZ (8 mol%)	24.1

It has been shown that YSZ:Dy phosphor offers the best potential in terms of price, temperature sensitivity and luminescence intensity at high temperatures. Such a system could be used to measure temperatures between 500 and at least 1000°C which makes it a good candidate to be used as an inner sensing layer in the TBC to monitor the temperature at the TGO/ceramic interface. In the following section the YSZ:Dy phosphor is further investigated. The influence of dopant concentration, aging and multilayering will be discussed.

5. STUDY OF DYSPROSIA DOPED YSZ PHOSPHOR TBCS

5.1. Influence of dopant concentration

As highlighted previously, it is very desirable to maximise the brightness of the phosphorescence. The surface of the TBC will get dirty during service and this will further reduce the intensity of the phosphorescence that could be detected. The emission spectra of as deposited coatings co-doped with 0.3, 1 and 2 mol% of dysprosia for a laser excitation of 20 mV♦ are reproduced in **Figure 51**. As shown in **Figure 52** the intensity of the emission peak at 585 nm used for the lifetime decay measurements and the one at 592 nm (same electronic transition) decreases linearly with increasing dysprosia concentration. This is not the case for the emissions coming from the $^4F_{9/2} \rightarrow {}^6H_{15/2}$ transitions (485, 500 nm). As the concentration of dysprosia is increased

---

♦ The laser power was observed with a power meter and the output was given in mV instead of mJ.

from 0.3 to 2 mol% the luminescence intensity of the 585 nm emission line is almost 6 times lower.
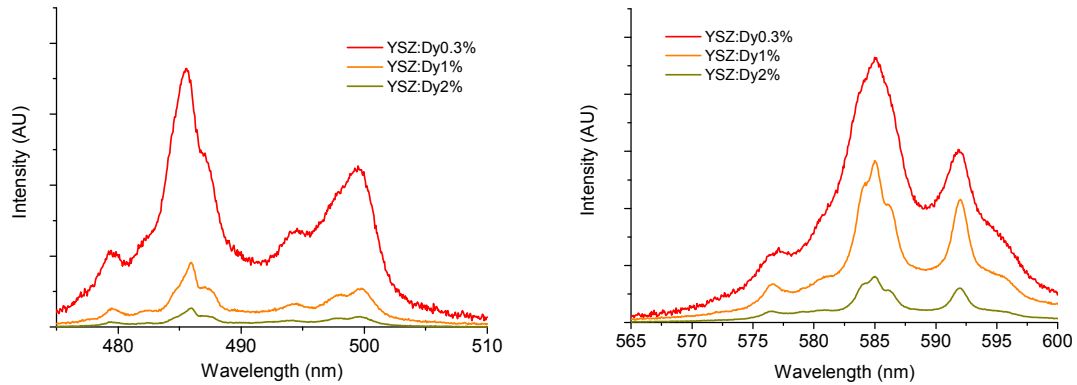
Figure 51: Effect of dysprosia concentration on the luminescence intensity of YSZ:Dy TBCs at room temperature.
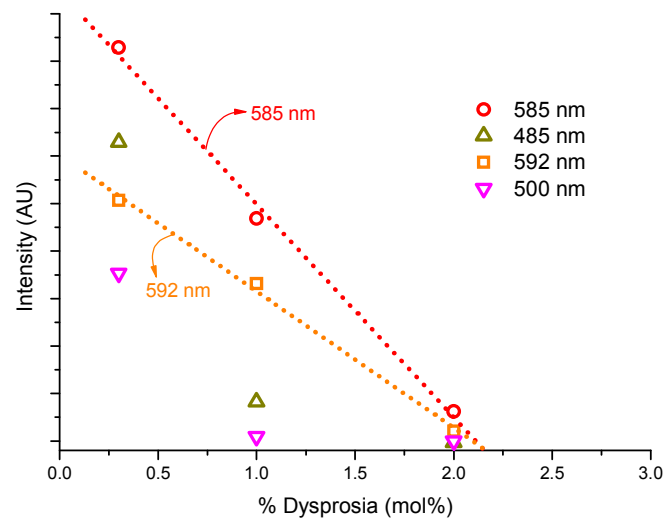
Figure 52: Intensity of the emission lines at 485, 500, 585 and 592 nm as a function of dysprosia concentration.

The influence of dysprosia concentration on the lifetime is presented in **Figure 53**. At temperatures below 500°C lower dopant concentrations give longer decay times however at higher temperatures, the temperature measurement capabilities are very similar for the different concentrations. Lowering the concentration of dysprosia also

shifts the onset of thermal quenching to lower temperatures extending slightly the range of the temperature sensitivity of the phosphor.
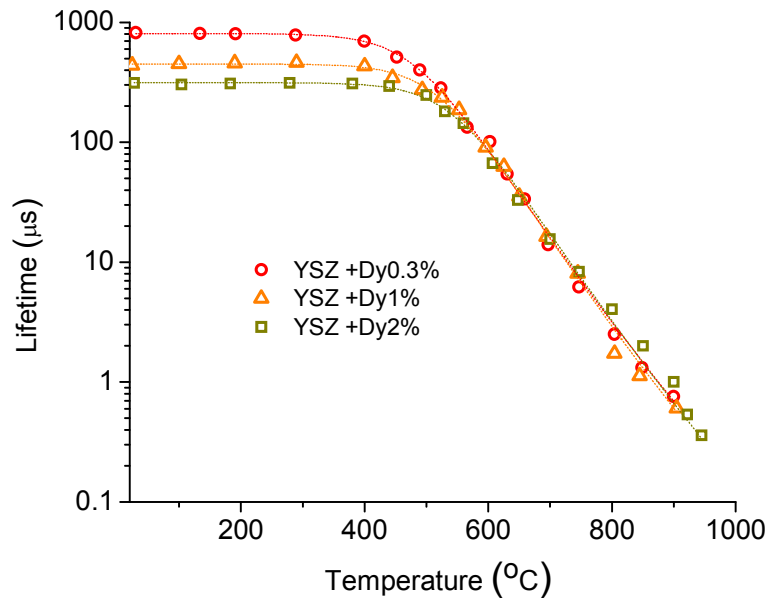
Figure 53: Effect of dysprosia concentration on the luminescence lifetime of YSZ:Dy TBCs.

5.2.   Influence of aging

During aging the coating undergoes phase transformations from the as deposited metastable *t'* phase to a mixture of tetragonal and cubic phases and upon cooling the tetragonal phase can transform to monoclinic. A YSZ:Dy2% coating was tested in the as deposited condition and after a heat treatment of 300 hours at 1500˚C, followed by a slow cooling in the furnace to ensure the formation of the monoclinic phase, in order to determine whether the transformations in the crystal structure would affect the lifetime of the luminescence. The detection and the collection of the luminescence was not affected by the heat treatment and the calibration curves for the aged and as deposited TBCs are closely similar as shown in **Figure 54**.
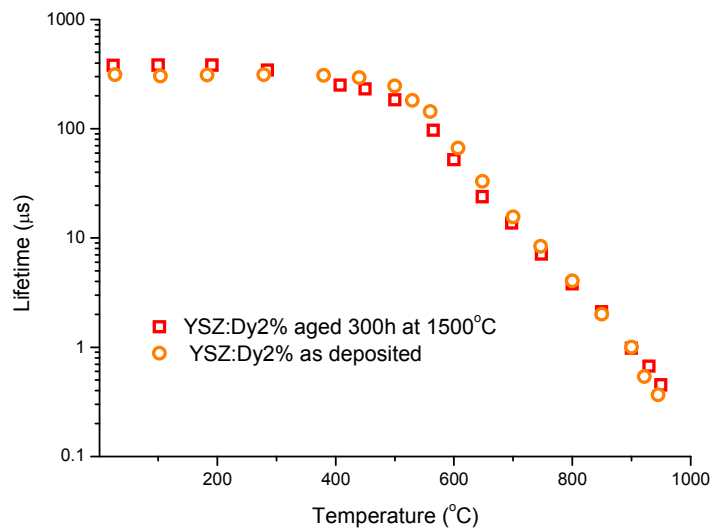
Figure 54: Effect of aging on the phosphorescence lifetime of YSZ:Dy2% TBCs.

At low temperatures the lifetime of the phosphorescence from the aged sample is somewhat longer than for the as deposited sample and the onset of thermal quenching is shifted towards lower temperatures. However it can be seen that, in the temperature range of interest, there are very small differences in lifetime decay due to the heat treatment.

5.3.   *Using different emission lines*

As presented in **Figure 55** YSZ:Dy has several emission lines corresponding to different transitions which could be used to build a calibration curve. Lifetime measurements were carried out using the emissions at 458 nm, 485 nm and 585 nm. The corresponding electronic transitions are represented on the energy level diagram in **Figure 55**.
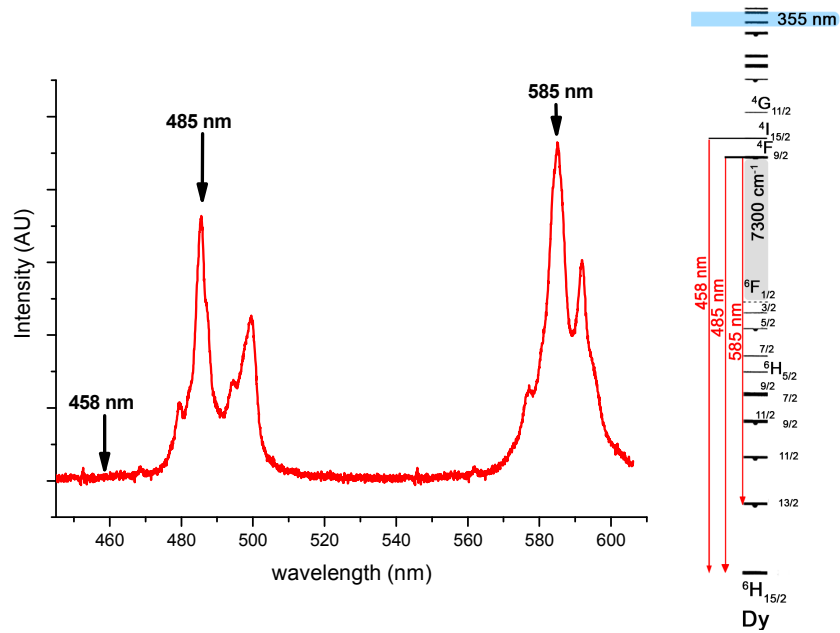
Figure 55: Emission spectrum of YSZ:Dy phosphor at room temperature and energy levels of Dy^{3+}.

The emission peak at 458 nm corresponding to $^4I_{15/2} \rightarrow {}^6H_{15/2}$ transitions is not visible in the room temperature luminescence spectrum. Indeed, after excitation at low temperatures the electrons relax non-radiatively down to the $^7F_{9/2}$ energy level, therefore, only emissions coming from this state are visible. Because the $^7F_{9/2}$ and $^4I_{15/2}$ states are closely spaced (around 930 cm^{-1}) the $^4I_{15/2}$ energy level is thermally populated at elevated temperatures and consequently the relative intensity of the 458 nm emission line increases with increasing temperature. Hence at temperatures below 400˚C it was not possible to detect the decay of the luminescence at 458 nm and therefore phosphorescence lifetime measurements could not be made using this emission line. The intensity ratio between the peaks at 485 and 585 nm can be used for temperature measurements (*intensity ratio technique* [110]).

Figure 56 shows the excellent agreement of the values obtained with the three different wavelengths. Emissions at 485 nm and 585 nm both come from transitions from the

$^4F_{9/2}$ state however this is not the case for the emission at 458 nm, yet the same temperature sensitivity was still obtained.
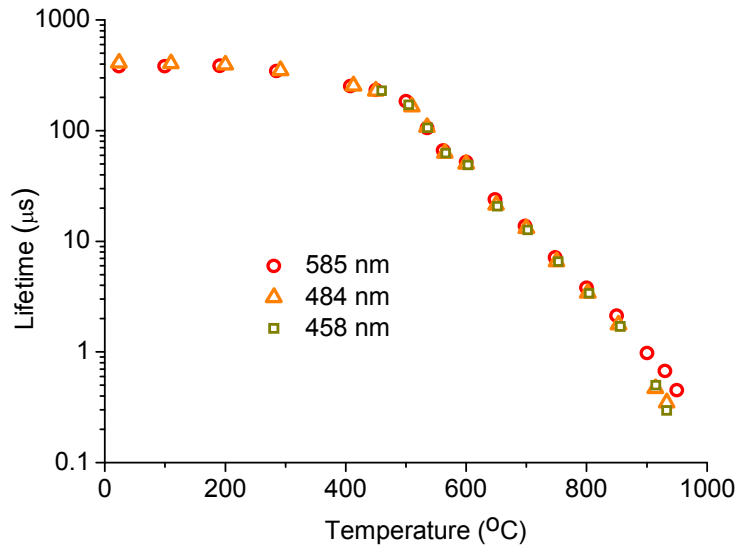
Figure 56: Lifetime decay measurements using three different wavelengths.

At around 900°C, the phosphorescence intensities at 458 and 485 nm were very weak and obviously the fitting was strongly influenced by the background radiations which explains the small variations in lifetime at the high temperature end of the calibration curves.

5.4. *Multilayer coating*

The temperature sensitivity of YSZ:Dy phosphor was shown to be suitable for such a phosphor to be used as an inner layer in a TBC. The next step in the development of a sensing TBC was to deposit and test a multilayer EB-PVD TBC.

A dysprosia concentration of 2 mol% was chosen for the doped layer as it represents the worst case scenario in terms of luminescence intensity compared to the other concentrations available (0.3 and 1 mol%). This multilayer coating could only be deposited using a single source evaporator. Thus for this purpose, a multistage ingot was manufactured to allow the various changes in source material composition during the deposition. The multistage rod is shown in **Figure 57** and was machined according to the drawing in **Appendix 1**. The thicknesses of the different stages of the rod were estimated from the evaporation rates of the previous depositions, in order to have a total coating thickness of 145 μm with 15, 30, 100 μm layers of 7YSZ, YSZ:Dy2% and 7YSZ respectively.

Figure 57: Multistage rod used for the multilayer coating deposition.

There was no problem during the deposition and the ingot melt was stable during the whole process. An SEM micrograph of a fractured sample (not polished) is shown in **Figure 58(a)**. First of all, the coating microstructure is not affected by the incorporation

of the phosphor layer. The growth of the columns is continuous, there is no interruption at the interface between the layers and so it is not possible to actually see the doped layer as a change in the microstructure. Further, the dysprosia concentration in the doped layer was not sufficient to be seen in the backscatter micrograph and the only way to determine its position in the coating was by using EDX analysis (**Figure 58 (b)**). A fractured sample was preferred for the EDX analysis to avoid any "spreading" of materials that could occur during the polishing in order to determine the precise location of the doped layer. The layer thicknesses obtained are very close to the predicted ones (30-36 μm for the YSZ:Dy layer) and the position of the doped layer is highly localised, there is no gradient in the concentration of dysprosia at the interfaces with the 7YSZ layers.

(a) (b)
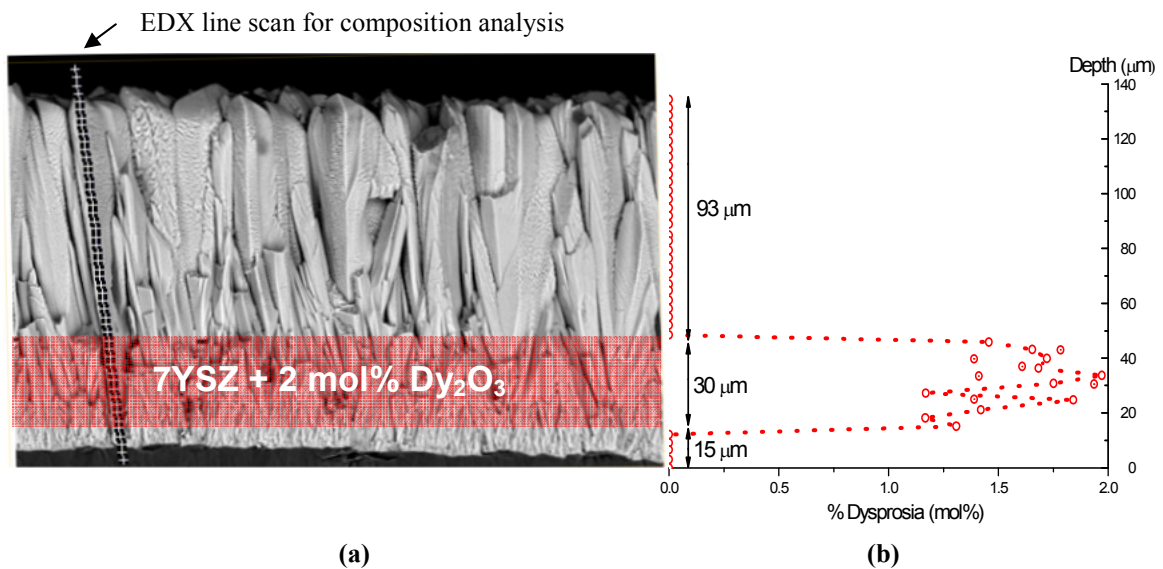
Figure 58: SEM micrograph of the multilayer coating (fractured sample) and EDX analysis.

Concerning the lifetime decay measurements, there was no problem either with the phosphor excitation or with the detection of luminescence through the 100 μm undoped layer. At low temperatures, the multilayer coating has longer phosphorescence lifetimes.

However, at 500°C, the onset of temperature quenching, the lifetimes are very similar

for the single and the multilayer coatings (**Figure 59**).
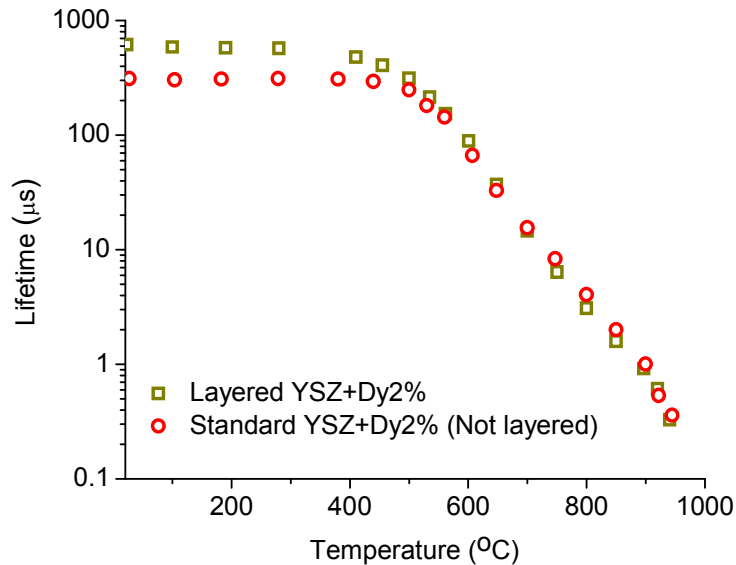
Figure 59: Effect of layering on lifetime decay.

5.5. Discussion

These results show that the precision of the temperature measurement using

phosphorescence will not be affected for dysprosia concentration ranges from 0.3 to 2

mol%. However, low dysprosia contents are to be preferred as they give higher

luminescence intensities. A brighter signal is easier to detect (especially when the

measurement surface gets dirty during service) and, therefore, the lifetime decay fitting

is more accurate and the temperature reading more precise. It is believed that the

decrease in phosphorescence intensity, and lifetime, at low temperatures with increase

in dysprosia concentration is caused by concentration quenching. Indeed, at high dopant

concentrations there is a greater interaction between activator atoms and this increases

the probability of non-radiative energy transfers between dopant atoms. As the temperature increases, temperature quenching becomes the dominant mechanism, thus above 500°C, the calibration curves for the different compositions are very similar.

Additionally, as shown in the previous chapter, small dysprosia additions do not change the morphology of the coating and YSZ:Dy0.3% TBC has almost the same tetragonality as the standard 7YSZ coating. Consequently, the mechanical properties such as the erosion and the impact resistance should not be significantly affected by very small dysprosia additions.

Temperature measurements using the dysprosia phosphor are also insensitive to high temperature aging and any associated phase transformations, even though the formation of the monoclinic phase will change the crystal field surrounding the activator atoms. A similar alteration is expected for large dysprosia additions since, as shown in the previous chapter, this would affect the crystallography of the coating by reducing its tetragonality; however, these variations in the crystal field do not seem to have a noticeable effect on the lifetime of the $^4F_{9/2} \rightarrow {}^6H_{13/2}$ electronic transitions. This highlights the benefit that aging during service will not change the temperature measurement capabilities of the coating. *Chambers et al.* [180] reported a similar behaviour following high temperature aging for YSZ:Eu phosphor.

The lifetime of emission lines at 458, 485 and 585 nm have been all successfully monitored for calibration purposes. This gives the possibility of using three different wavelengths, offering more flexibility if there is any overlapping with emissions from

the burning fuel or from another phosphor layer in the TBC. In this case, another wavelength could be used to measure the temperature. These results imply that the three transitions have the same quenching mechanisms. The fact that the lifetimes of the emissions coming from $^4I_{15/2} \rightarrow {}^6H_{15/2}$ and $^4F_{9/2} \rightarrow {}^6H_{13/2-15/2}$ transitions have the same temperature dependence suggests that the thermal population of higher energy levels at high temperature do not account for the decrease in lifetime. Decay as a result of energy transfers to other activator ions is also negligible at high temperature, since, for the dysprosia concentrations investigated the temperature quenching was identical.

A multilayer EB-PVD TBC comprising a YSZ:Dy2% inner phosphor layer was successfully deposited and tested. At high temperatures, its calibration curve was identical to a non-layered coating. The differences at low temperature are believed to be caused by "*saturation effects*". As shown in **Figure 60**, the lifetime of the phosphorescence decreases with increase in laser intensity. Since, in the case of the multilayer TBC, the laser has to penetrate through the 100 μm 7YSZ layer before the YSZ:Dy phosphor is excited, it loses intensity and hence longer lifetimes are observed.
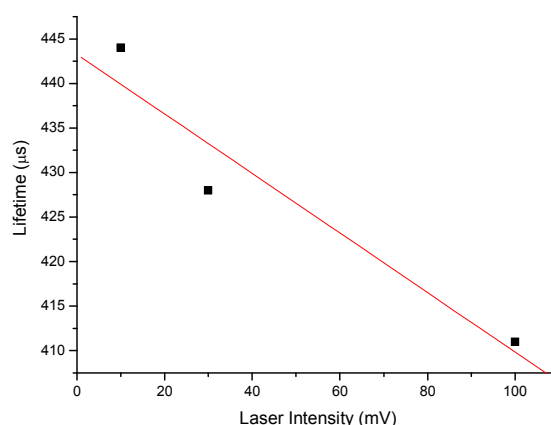
Figure 60: Lifetime against laser intensity at room temperature for YSZ:Dy1% TBC.

Studies conducted at *STS* have shown that, with the same type of multilayer coating, but deposited by air plasma spraying (APS), the intensity of the phosphorescence was very weak. Consequently, even with only a 50 μm YSZ top layer, the lifetime of the phosphorescence could not be measured above 800°C, whereas, with the EB-PVD multilayer coating with a top layer twice as thick, lifetime decay measurements were performed up to the detection limit of the measurement system, 950°C (**Figure 61**). There was good agreement between the response curves of the layered, doped, APS and EB-PVD coatings.
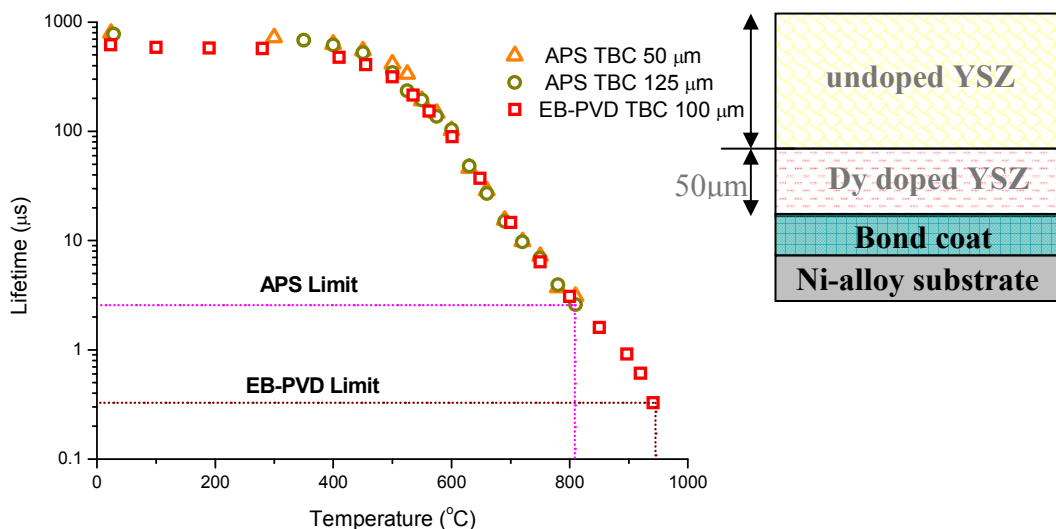
Figure 61: Comparison of the calibration curves of APS and EB-PVD TBCs (redrawn from [184]).

This loss in intensity for the APS coating reflects the microstructure. In EB-PVD TBCs, the porosity is mainly perpendicular to the surface (intercolumnar porosity) and therefore does not scatter the luminescence as much as for the APS TBCs, which have a highly scattering microcrack network parallel to the coating surface. **Figure 62** shows that the EB-PVD TBC has a significantly greater transmittance, for the excitation and

emission wavelengths at room temperature, compared to the APS coating. It is worth noting that even after aging, when the columns of the EB-PVD coating start to sinter together, the same temperature measurements were achieved.
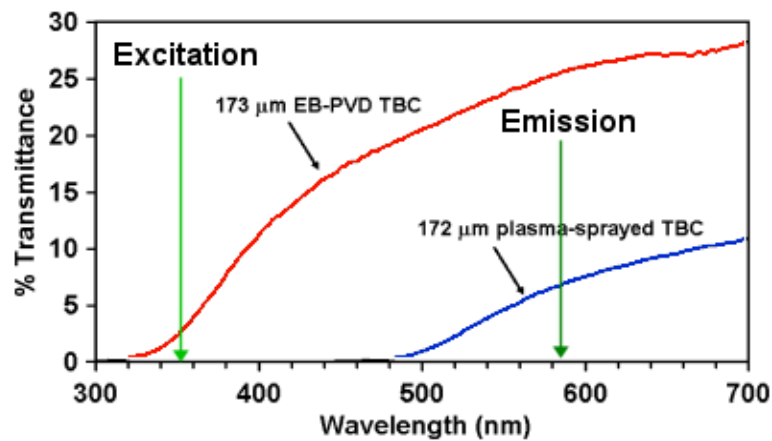
Figure 62: Comparison of the transmittance of freestanding EB-PVD and APS TBCs at room temperature [127].

The results obtained from these multilayer coating studies suggest that YSZ:Dy is a suitable phosphor to be used as an inner layer in a TBC in order to measure the temperature at the interface between the bond coat and the top coat. It is of primary importance that ternary additions of dysprosia do not degrade other properties of the TBC, such as the thermal conductivity, thermal stability and erosion resistance. As this phosphor is to be used as an inner layer, its erosion properties are less crucial. Concerning the thermal conductivity, *Nicholls et al.* [31] have shown that, as a member of the lanthanide family, dysprosia should be beneficial by further reducing the thermal conductivity of the TBC. However the influence of co-doping YSZ with dysprosia on the phase stability of the TBC needs further investigation.

5.6. Influence of Dy₂O₃ additions on the phase stability of a YSZ TBC

During heat treatment, the as deposited metastable *t'* phase may transform into a mixture of tetragonal phase (*t*) with a low concentration of stabiliser and a cubic phase (*c*) with a high concentration of stabiliser. If the aging is long enough the stabiliser content of the *t* phase will decrease so as to be low enough to transform into monoclinic upon cooling. Likewise, the content of yttria in the cubic phase may not be high enough to stabilise it at room temperature such that it will transform into the so called *t''* phase, with a high concentration of yttria which has a tetragonality close to unity. In the following discussion the distinction between the *c* and *t''* phase will not be explicitly made and both will be referred as cubic. The *t→m* phase transformation is associated with a volume increase of between 4-6% and can lead to severe cracking in the TBC and therefore must be avoided.

Wellman et al. [53] reported extensive monoclinic phase formation in EB-PVD coatings deposited on low purity polycrystal alumina substrate aged for only 24 hours at 1500°C, whereas, *Lughi et al.* [11] showed that EB-PVD TBCs on high purity alumina sapphire remain principally *t'* after 350 hours at 1400°C. Similarly, in their study *Azzopardi et al.* [71] did not report any monoclinic phase formation for an EB-PVD TBCs heat treated 300 hours at 1500°C. It is believed that the differences in phase stability observed are mainly due to the purity of the substrates used for annealing experiments at high temperature due to the fact that contaminants contained in alumina substrates can migrate into the coating and thus cause the early formation of the monoclinic phase.

Prior to studying the influence of ternary additions of dysprosia on the high temperature phase stability of the coating, the effect of the purity of the substrate was investigated, in order to rule out any side effects coming from the substrate.

5.6.1. Influence of substrate purity on the phase stability

5.6.1.1. Test procedure

Standard 7YSZ coatings were deposited on three different alumina substrates with different purities. These substrates were polycrystal alumina 96% and 99.5% purity (PX96 and PX99 respectively) and single crystal alumina 99.99% purity (SX99). Such substrates are commonly used for high temperature isothermal aging when the melting point of nickel based superalloys is exceeded.

The samples were isothermally heat treated in a box furnace at 1500°C for 0.5, 1, 2, 5 and 8 hours to study the $t' \rightarrow t + c$ phase separation. A different sample was used for each heat treatment. Longer agings were performed until the monoclinic phase was formed using a single sample of each substrate. Such a high temperature was chosen to minimise the time of thermal exposure before the appearance of the monoclinic phase. The samples were rapidly cooled and immediately examined by XRD to determine the phase composition of the aged coating. The experiments were done on the coating rather than powder or powdered coatings to provide more realistic results on the influence of minor coating contamination. In this way not only the internal constraints of the coating

but also those generated by the substrate, sintering and the tetragonal to monoclinic phase transformation could be taken into account.

The *t' → t +c* phase separation is commonly studied using the *(400)* type reflections (2θ=72.5°-75.5° region) [10;12]. The *(200)* reflections (2θ=34°-35.5° region) can also be used, however, due to peak overlap, quantitative analysis using *(200)* reflections becomes less accurate as the monoclinic phase starts to form [185]. Quantitative analysis of the monoclinic phase in zirconia powder samples has been attempted by a number of methods using the *(111)* tetragonal/cubic and *(111)* and (11$\bar{1}$) monoclinic reflections (2θ=27°-32° region) [10;12;174;186-188], however, as seen in the previous chapter, the EB-PVD coatings produced are highly textured and have mainly a *(200)*, *(311)* and *(400)* orientation. The main monoclinic peaks appear at *2θ* values of around 34° and 55° and overlap with tetragonal and cubic reflections in this position, making the deconvolution even more difficult. Furthermore, XRD is not very sensitive to the monoclinic phase and the peaks are rather broad when they first appear so, even if the XRD pattern does not show clear monoclinic peaks, there might already be some monoclinic phase formed in the coating. The phase composition of the various coatings was calculated using the integrated intensity of the *(400)* reflection peak, which was determined by fitting the diffraction peaks with a Pseudo-Voigt function using a commercial software♦. During annealing *t'* will separate into a mixture of tetragonal and cubic phase and according to the ZrO_2/Y_2O_3 phase diagram (**Figure 5**) and the XRD analysis. It was found that, when the partitioning is complete, there is about 55% of *t* and 45% of *c* phase. Eventually, the percentage of the *t* phase starts to decrease; this

---

♦ Origin 7.0, OriginLab™.

decrease can be associated with the $t \rightarrow m$ phase transformation and was used to calculate the percentage of monoclinic phase in the EB-PVD coatings. The reader should refer to **Figure 75** in order to understand the evolution of the XRD pattern of the EB-PVD TBC with aging time. Using the integrated intensity may not give a precise measurement of the phase composition of the coating, as has been explained in [185], but it still provides a consistent criterion to compare the phase stability of the various coatings. The presence of the monoclinic phase was also checked using Raman spectroscopy.

Finally, each sample was examined under SEM and analysed with EDX to see the evolution of sintering with aging time and to determine the chemical composition of the coating.

5.6.1.2. Results and discussion

The phase compositions of the coatings on the three different substrates for each heat treatment are summarized in **Figure 63**. It clearly shows that the $t' \rightarrow t + c$ phase separation is much faster for the coatings deposited on the low purity alumina substrates PX96. It is almost complete after a 5 hour aging at 1500˚C, whereas the coatings on high purity alumina (PX99 and SX99) still contain a high percentage of t' phase even after 8 hours at 1500˚C (14% and 24% respectively). On top of that, a significant amount of monoclinic phase is already formed after 8 hours at 1500˚C for the coating on PX96 (confirmed by Raman spectroscopy in **Figure 64**). With longer aging the t' phase is completely partitioned after 10 and 16 hours at 1500°C for coatings on PX99 and SX99 respectively. Monoclinic phase is formed after 64 hours for coatings on PX99

and 500 hours on SX99. The difference of phase stability between these two substrates was confirmed by Raman spectroscopy (**Figure 64**). The Raman spectrum of the coating on PX99 heat treated for 128 hours at 1500˚C shows the characteristic monoclinic doublet at 182 and 191 cm^{-1} [189-191] and the content of monoclinic phase determined by XRD is about 20%. To the contrary, all the peaks for the Raman spectrum of the coating deposited on SX99 correspond to the tetragonal phase, even after annealing for 300 hours at 1500°C. It is worth noting that the peaks become sharper and more symmetric after aging, this has been reported to be associated with the formation of the cubic phase [191].
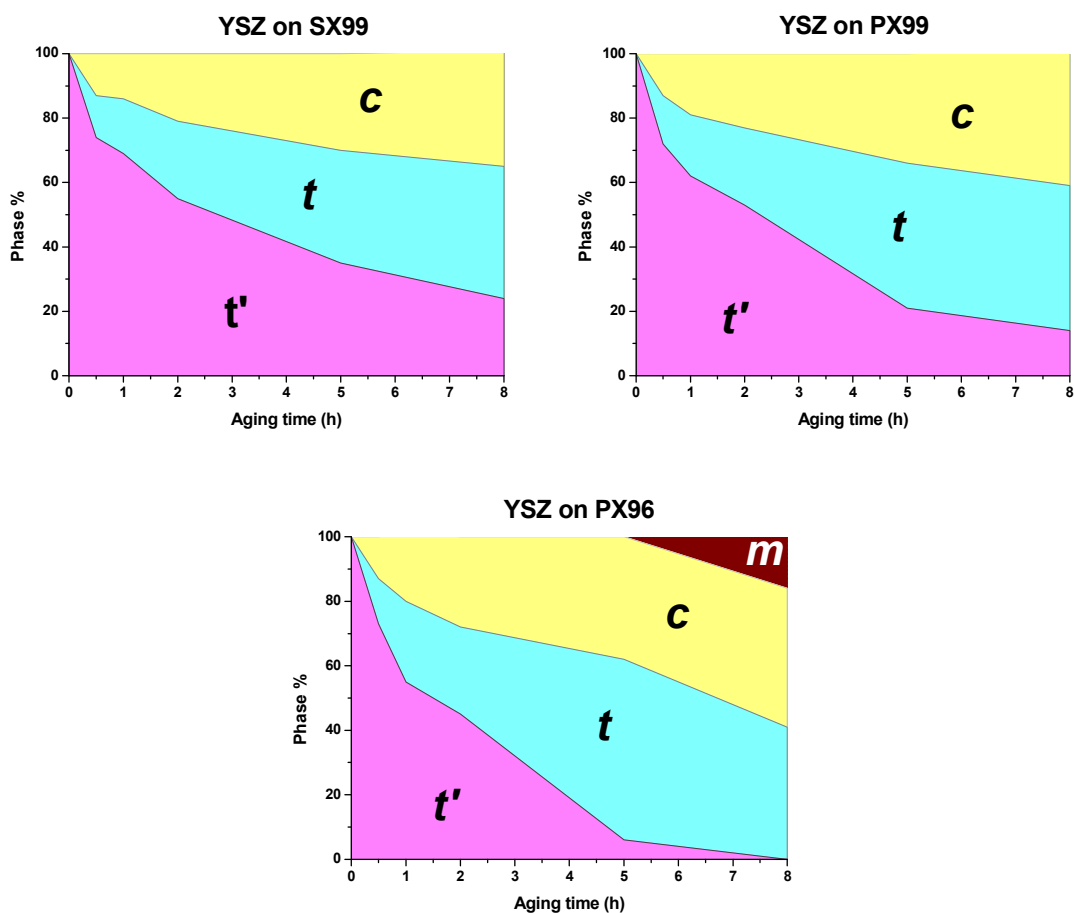
Figure 63: Maps of phase evolution at 1500°C of 7YSZ EB-PVD TBCs on alumina substrates with 3 different purities.
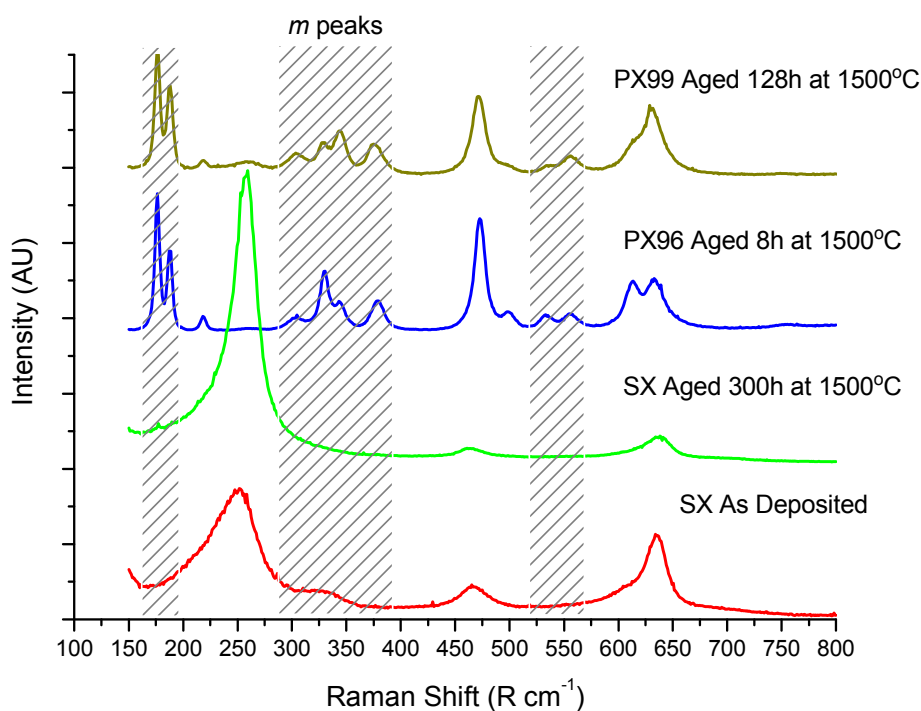
Figure 64: Raman spectra of 7YSZ EB-PVD TBCs, on SX99 in the as deposited condition and after 300h at 1500°C, on PX96 after 8h at 1500°C and on PX99 after 128h at 1500°C.

The phase composition calculated from the XRD results on coatings on SX99 gave 57% and 43% of tetragonal and cubic phase respectively after 300 hours at 1500˚C and only 7% of monoclinic phase was formed after 500 hours. Even if the partitioning of the *t'* phase is complete after 16 hours, it requires longer aging for the monoclinic phase to form. The percentage of tetragonal and cubic phase remains unchanged until 500 hours at 1500˚C, however, both XRD peaks are slowly moving towards higher and lower 2θ angles respectively indicating that *t* is becoming gradually poorer in yttria and *c* richer in yttria until the *t* phase reaches a critical yttria content and cannot remain non-transformable upon cooling (**Figure 65**).

The only difference between the various coatings was the substrate purity and structure. It is believed that the early destabilisation highlighted above is caused by the impurities present in the substrate material. Even a small difference in substrate purity can have a tremendous effect on the monoclinic phase formation. The substrate compositions were determined by X-Ray Fluorescence♦ (XRF), the results are presented in **Table 8**.
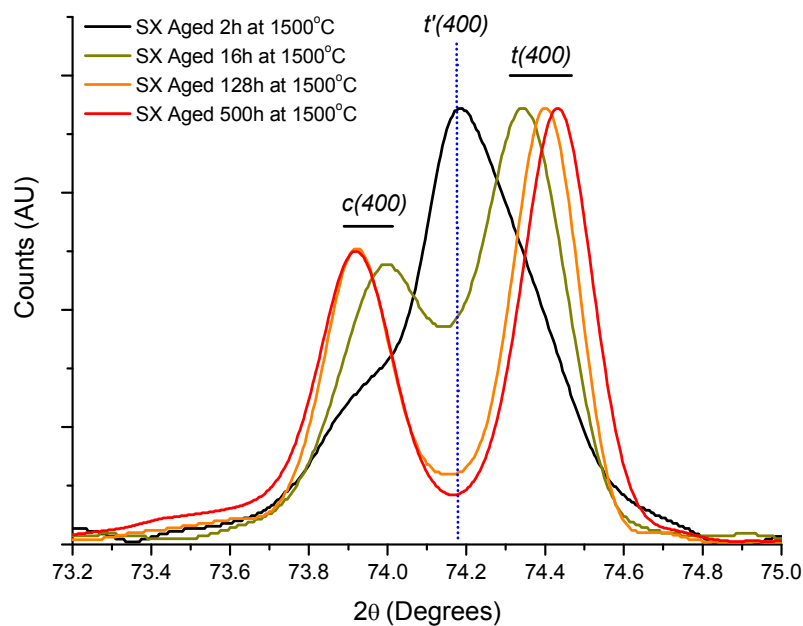
Figure 65: XRD patterns of 7YSZ EB-PVD TBC on SX99 aged at 1500°C between 2 and 500 hours.

Table 8: Chemical composition of alumina substrates in mol%.

	$AlO_{1.5}$	SiO_2	MgO	CaO
PX96	97.6	1.4	0.6	0.4
PX99	99.0	1.0	0	0
SX99	99.8	0.2	0	0

♦ XRF, *Bruker AXS.*

The main impurities are SiO_2, MgO and CaO. The chemical composition of the TBC was determined by EDX before and after heat treatment. The oxide contents were calculated from the values of the elements, assuming a stoichiometric formula. The composition of the as deposited TBC was 7.5 mol% of $YO_{1.5}$ and 1 mol% HfO_2 however the graphs in **Figure 66** show that substrate impurities as well as alumina are also present in the coatings deposited on PX96 after annealing. The percentage of CaO is not plotted on this graph since its content varies only from 0.2 to 0.5 mol%.

Even after a 30 minute heat treatment the impurities rapidly migrate from the substrate into the coating and after 8 hours there are already at 5.8, 3.8 and 3 mol% of $AlO_{1.5}$, SiO_2 and MgO respectively at the top of the coating. Such impurities were not present or were under the detection limit of the EDX for coatings deposited on SX99 and for this substrate even alumina does not seem to diffuse from the substrate to the coating. For the coatings on PX99, a small amount of SiO_2 and MgO was detected in the substrate but after 8 hours at 1500°C they do not seem to diffuse, even the amount of Al_2O_3 in the coating remains under one mol%. The fact that alumina is found after heat treatment in the coatings on PX96 and not on those deposited on PX99 could mean that the impurities migrate as a Al-Si-Mg-Ca compound with a low melting point rather than single elements.

It is well known that Calcium Magnesium Alumino Silicate (CMAS) deposits have a detrimental effect on the lifetime of the TBC. They generate cracking, promote sintering and destabilisation of EB-PVD coatings [60-62;192].
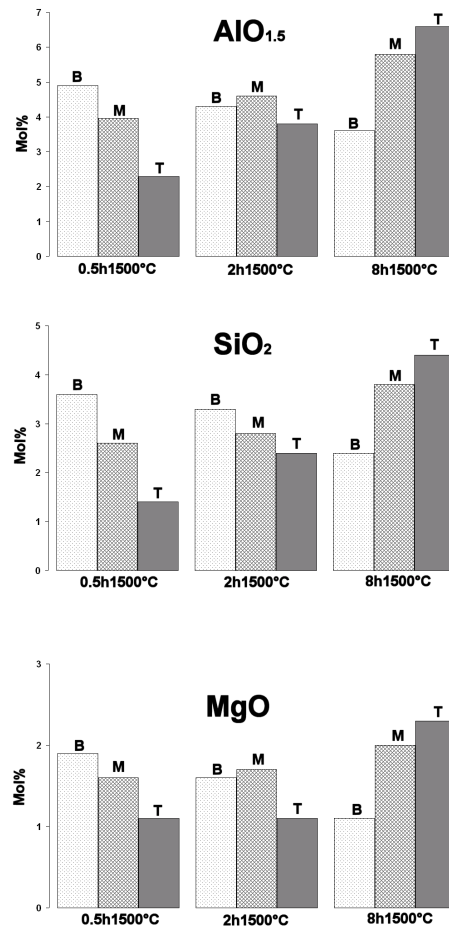
Figure 66: Concentration of AlO$_{1.5}$, SiO$_2$ and MgO impurities at 3 different depths in 7YSZ EB-PVD TBC (B: bottom, M: middle, T: top) aged 0.5, 2 and 8h at 1500°C.

Figure 67 represents the XRD graph of a 7YSZ coating deposited on SX99 with CMAS powder on the top surface aged 5 hours at 1500°C. The CMAS powder had a composition of 35% CaO, 10% MgO, 7% Al$_2$O$_3$ and 48% SiO$_2$ in mole percent. It shows that after a short heat treatment a large amount of monoclinic phase is already formed highlighting the destabilisation effect of CMAS deposits.

It is believed that just like in a CMAS or aluminosilicate attack, the substrate impurities form a glassy phase which "extracts" yttria from zirconia making the coating more susceptible to transform to the monoclinic phase [56;192].
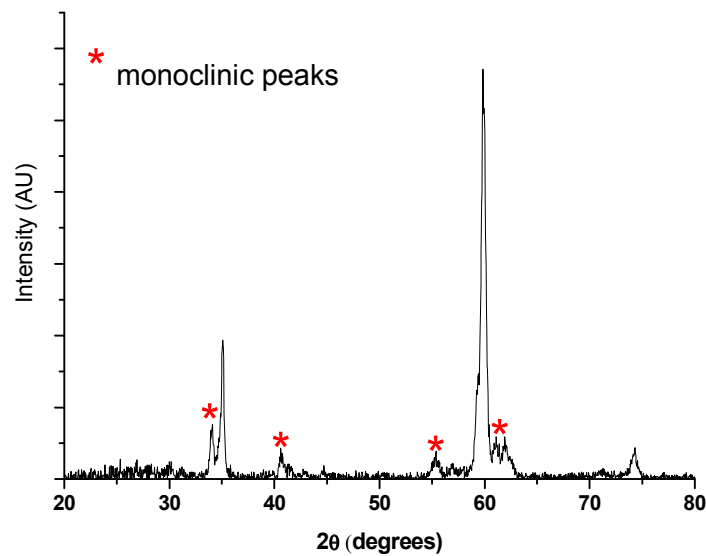
Figure 67: XRD pattern of 7YSZ EB-PVD TBC on SX99 aged 5h at 1500°C with CMAS powder.

This is confirmed by the EDX map of the sample on PX96 aged 8 hours at 1500°C (**Figure 68**). The darker areas were initially thought to be intercolumnar porosity however elemental mapping shows that these regions are in fact $AlO_{1.5}$ and SiO_2 rich. This phase also contains ZrO_2 and $YO_{1.5}$ and has the following composition: 38.7 mol% SiO_2, 35 mol% $AlO_{1.5}$, 11 mol% MgO, 6.8 mol% ZrO_2, 6 mol% $YO_{1.5}$ and 2.5 mol% CaO. The coating appears to be depleted in yttria and contains only 5 mol% of $YO_{1.5}$ compared to about 7.5 mol% in the as deposited condition. Even though Zr is also incorporated in the CMAS phase, the Y/Zr ratio is about 0.9 compared to 0.08 for the as deposited *t'* coating and hence the depletion of yttria in the heat treated coating (Y/Zr ≈ 0.05). As a result, when the concentration of yttria in the TBC is sufficiently low, the coating cannot remain non-transformable and the monoclinic phase can be formed. It is worth noting that the coating itself is free from SiO_2, $AlO_{1.5}$, MgO and CaO. An attempt to explain the thermochemical interactions between CMAS and the TBC has been given by *Kraemer et al.* [60].
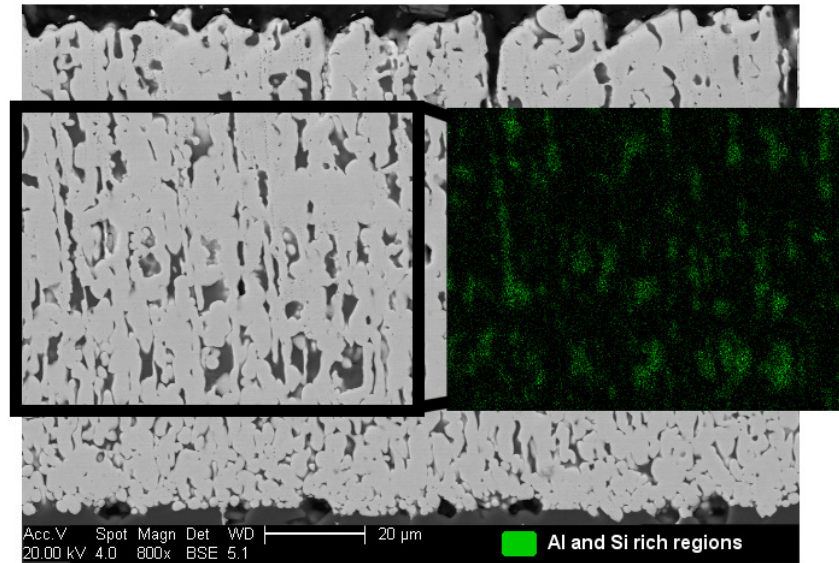
Figure 68: Elemental map of 7YSZ EB-PVD TBC on PX96 aged 8h at 1500°C.

A coating deposited on SX99 was aged at 1500˚C for 64 hours with the top of the TBC in contact with a PX96 substrate (**Figure 69**). XRD showed that the coating contains 10% of the monoclinic phase after aging. This shows that, if during annealing the samples are in contact with such contaminants or if powders are aged in low purity alumina crucibles, these impurities could still diffuse and promote the early formation of the monoclinic phase.
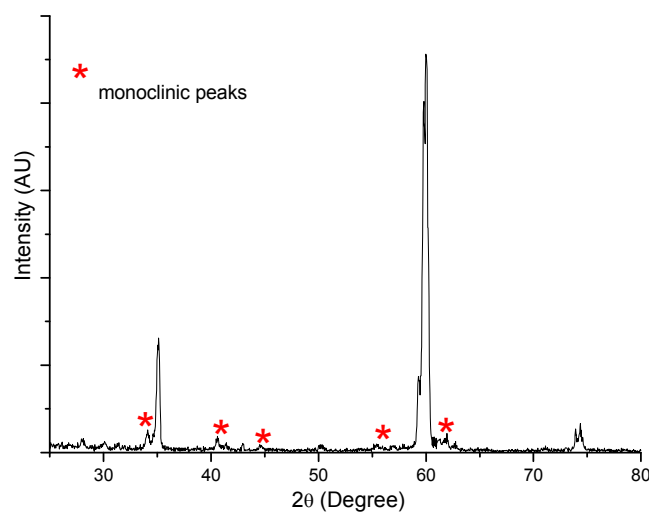
Figure 69: XRD graph of 7YSZ EB-PVD TBC on SX99 aged 64 hours at 1500°C in contact with a PX96 substrate.
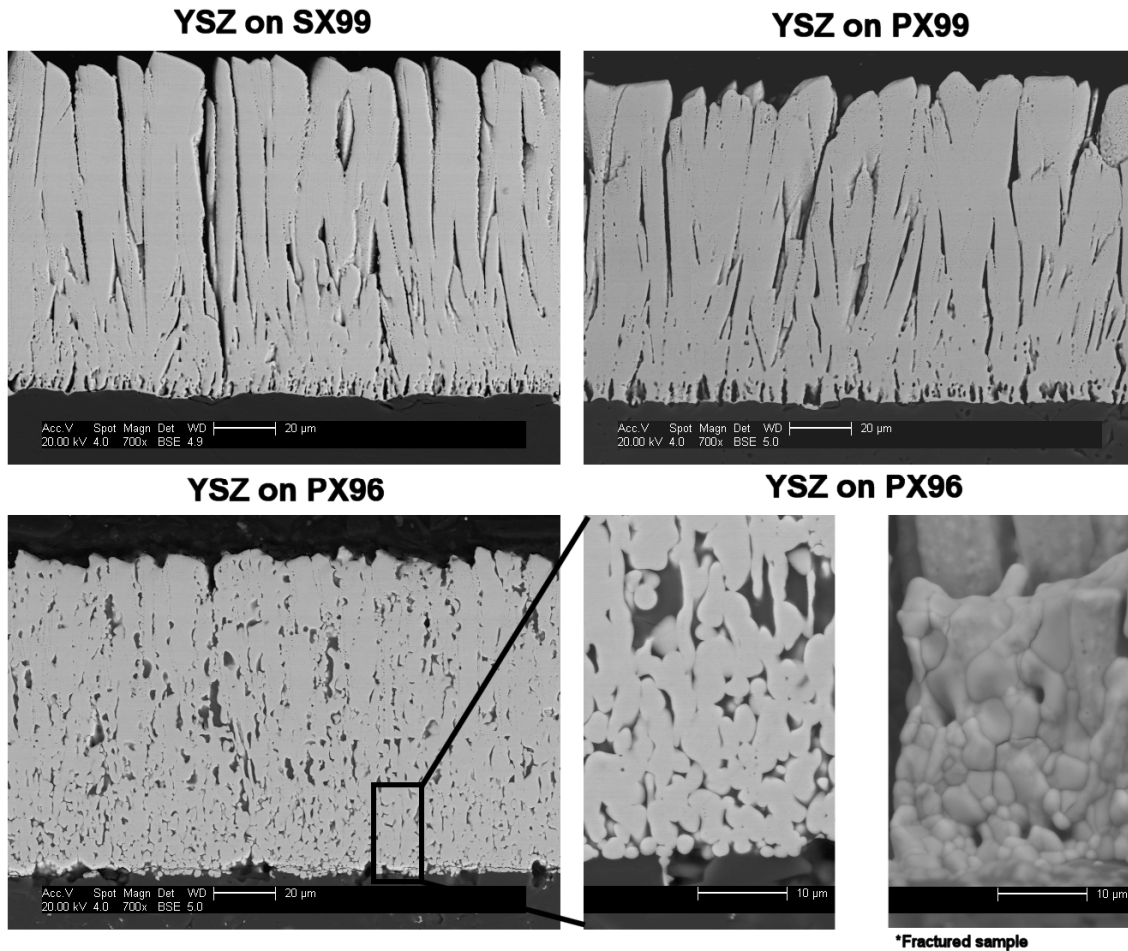
Figure 70: SEM micrographs of 7YSZ EB-PVD TBCs on SX99, PX99 and PX96 substrates aged 5h at 1500°C.

Not only do substrate impurities strongly reduce the phase stability of the coating but it also affects the sintering of the TBC. **Figure 70** shows cross-section micrographs of coatings deposited on SX99, PX99 and PX96 substrates after a heat treatment of 5 hours at 1500°C. TBCs on SX99 and PX99 show "normal" sintering behaviour, the characteristic featherlike structure of the columns is smoothed out, the columns sinter together but it is still possible to distinguish individual columns. This is not the case for the TBC on PX96 substrate, the columns completely lose their identity and the equiaxed zone of the TBC at the interface with the substrate is replaced by small spherical particles. Such sintering is very similar to the liquid phase sintering observed by *Lin et al*. [56], where aluminosilicate glass segregates to the grain boundary resulting in

rounded zirconia grains. The intercolumnar porosity is filled with CMAS melt coming from impurities from the substrate resulting in destabilisation and the formation of a monolithic structure. The result is the loss of the strain compliance of the EB-PVD TBC that could also influence erosion and FOD behaviour as shown by the author in [82].

As shown in **Figure 66** the migration of substrate impurities in the TBC was already observed after only 30 minutes at 1500°C. The "attack" of the columns was clearly evident, even after such a short heat treatment, and the coating was highly sintered, almost half way through its thickness (**Figure 71**).
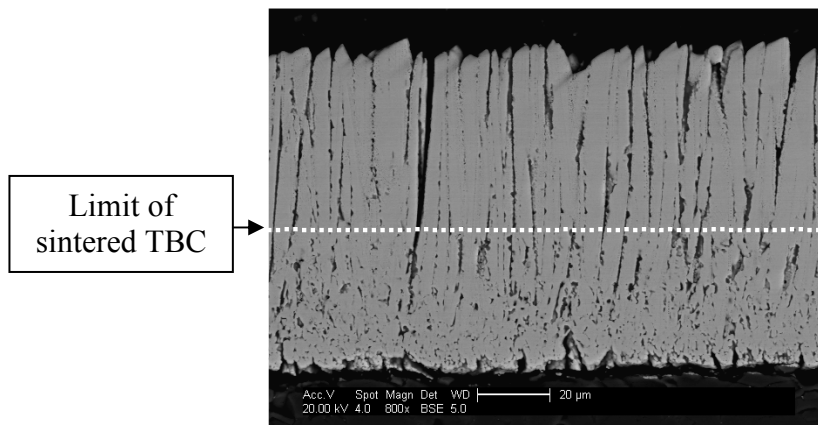
Figure 71: SEM micrograph of a YSZ TBC on PX96 substrate aged 30 minutes at 1500°C.

This study has shown that substrate impurities such as SiO_2, $AlO_{1.5}$, MgO and CaO can have a significant influence on TBC properties as a result of enhanced sintering and associated destabilisation. It is believed that the additions form a liquid phase that migrates into the TBC during annealing at 1500°C and extracts yttria from the coating leading to the early formation of the monoclinic phase. Consequently, it was decided that high purity alumina substrates should be used to study the effect of dysprosia on the TBC properties at very high temperatures.

5.6.2. Influence of dysprosia on the phase stability

7YSZ, YSZ:Dy0.3%, YSZ:Dy1% and YSZ:Dy2% samples were deposited by EB-PVD on high purity single crystal alumina. In order to determine whether dysprosia is a better stabiliser than yttria, a YSZ coating with the same content of stabiliser has also been tested. So for instance YSZ:Dy1% (3.9 mol% Y_2O_3 + 1 mol% Dy_2O_3) must be compared with a composition of zirconia partially stabilise with 4.9 mol% (3.9+1) of yttria. To deposit such a coating a composite rod was used, made from zirconia + 7wt.% (3.9 mol%) yttria and zirconia + 20wt.% (12 mol%) yttria ingots (**Figure 72**). The drawings used to machine the rod and the calculations to estimate the dimensions of the two parts of the rod in order to achieve an yttria concentration of 4.9 mol% can be found in **Appendix 2**.
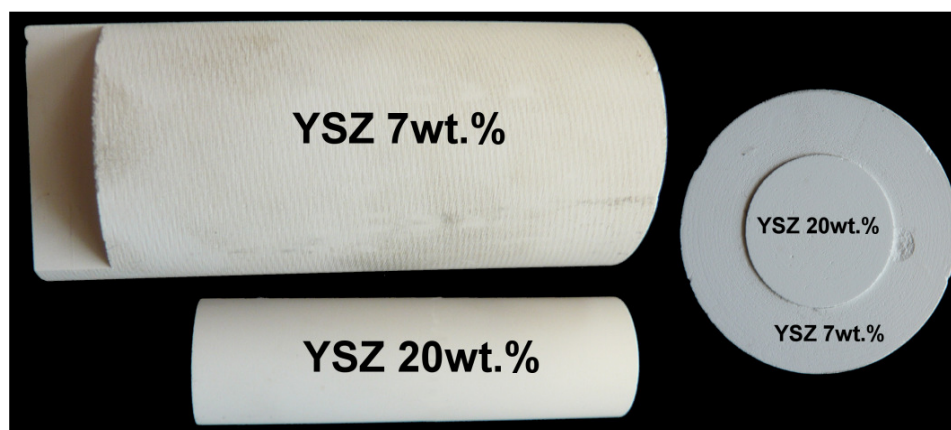
Figure 72: Composite rod used to deposit the YSZ 4.9 mol% TBC.

The compositions of the coatings were determined by EDX, four different areas of the coating were analysed and the average values are listed in **Table 9**. Hafnia is typically found in YSZ TBCs since it is a naturally-occurring impurity in zirconium oxide.

Table 9: Chemical composition of the TBCs.

(mol%)	*ZrO₂*	*HfO₂*	*Y₂O₃*	*Dy₂O₃*
3.9YSZ (7YSZ)	95	1.1	3.9	0
YSZ:Dy0.3%	94.7	1.1	3.9	0.3
4.9YSZ	94.4	1	**4.6**	0
YSZ:Dy1%	93.9	1	3.9	1.1
YSZ:Dy2%	93.1	0.9	3.7	2.2

The samples were aged in air at 1500˚C for up to 1100 hours. For each composition a sample was heat treated 1, 2, 4, 8, 16, 32, 64, 128, 256 hours (9 cycles) and a second one 350, 500, 800, 900, 1100 hours (5 cycles) at 1500°C. During heat treatment the samples were only in contact with high purity alumina to avoid any contamination. The samples were placed on high purity alumina tubes (99.5%) to avoid contact with the firebrick* (75% Al_2O_3 / 25% SiO_2) (**Figure 73**).
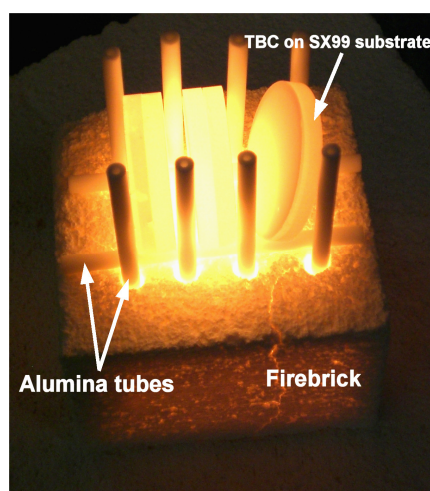
Figure 73: Samples on the furnace holder after heat treatment.

The same experimental procedure as for the study of the influence of substrate purity on the phase stability was used to determine the phase composition of the various coatings after heat treatment. The maps that were obtained of phase evolution during heat treatments are presented in **Figure 74**.

---

* JM30 Firebrick, Thermal Ceramics UK Limited.
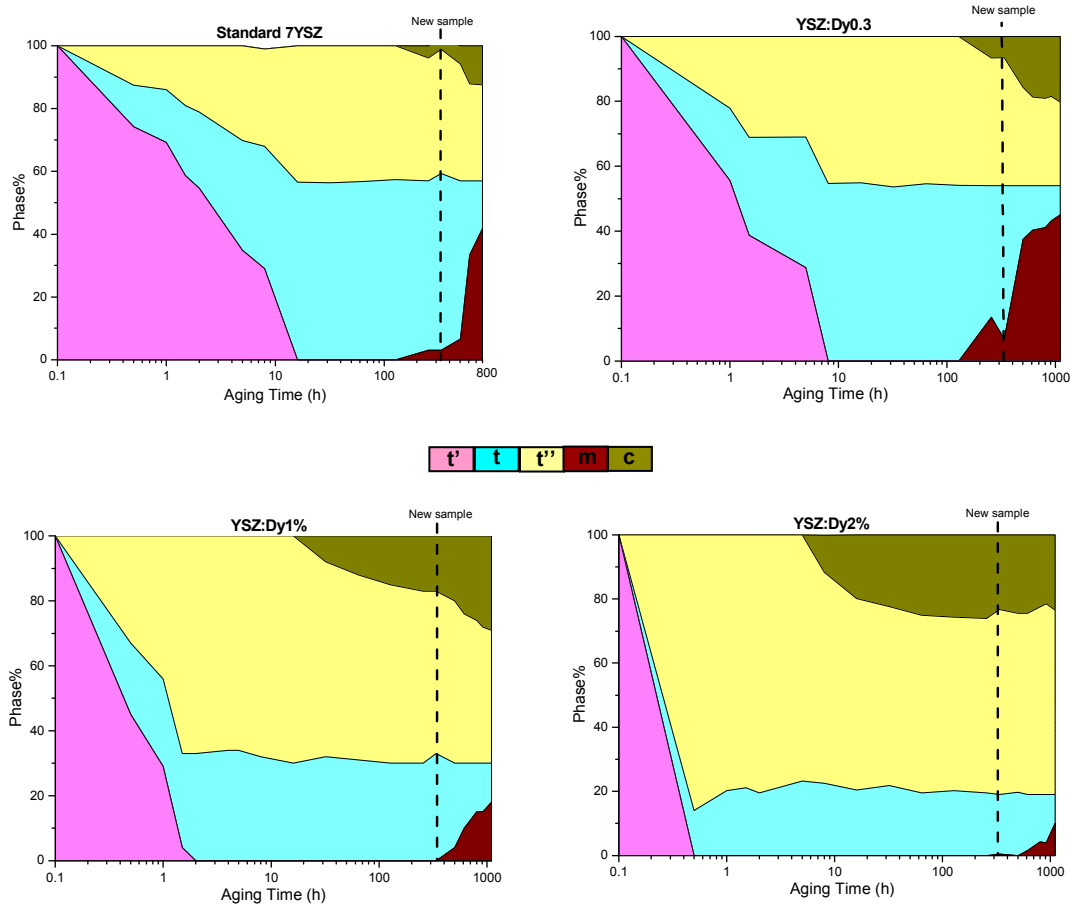
Figure 74: Maps of phase evolution of 7YSZ, YSZ:Dy0.3%, YSZ:Dy1% and YSZ:Dy2% TBCs at 1500°C.

The partitioning of *t'* into the low and high stabiliser phases was very rapid for the YSZ:Dy2% sample and it was complete after around 30 minutes at 1500°C, compared with around 10 hours for the standard 7YSZ coating. After this, the phase composition remained relatively constant. This means that the *t'* phase does not shift its composition abruptly to the equilibrium formation of low and high stabiliser phases, but that the depletion in stabiliser in *t* and the enrichment in *t''* is a progressive process. When the *t* phase cannot retain sufficient supersaturation to remain non-transformable the *m* phase is formed and thereafter the percentage of the *t* phase drops. The evolution of the XRD pattern with aging time for the YSZ:Dy1% sample is represented in **Figure 75**.
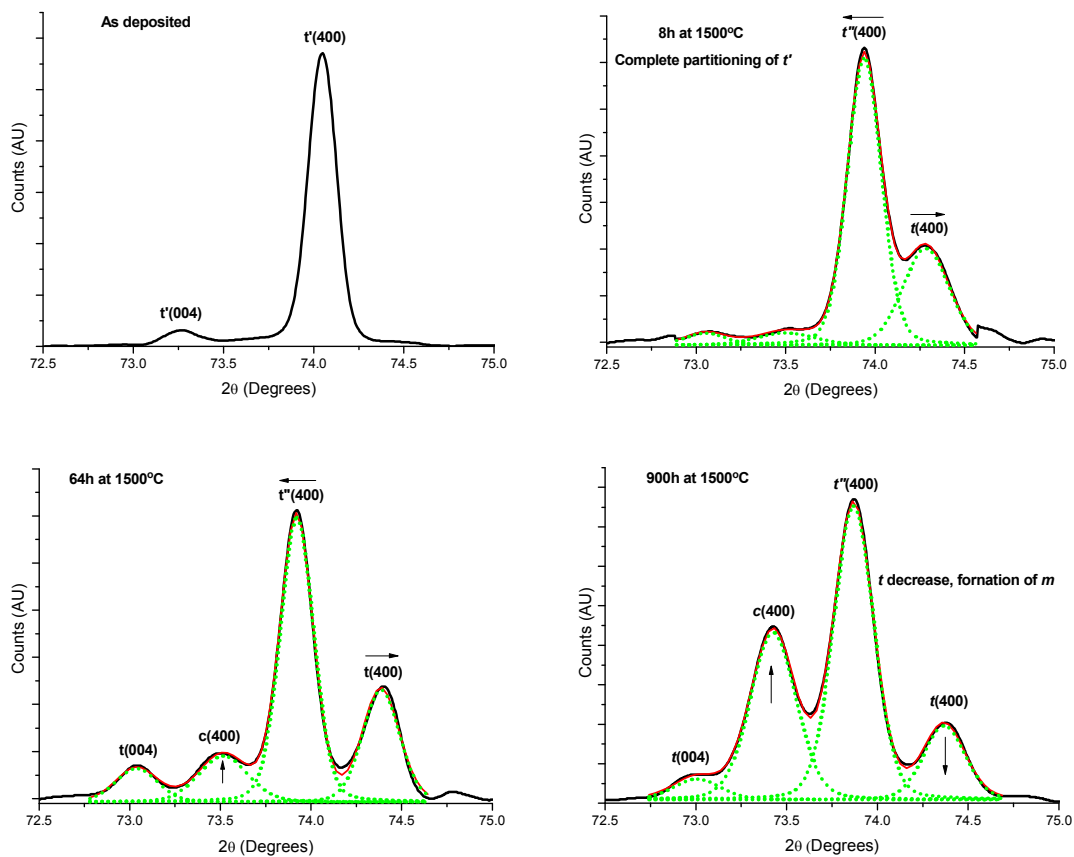
Figure 75: XRD graphs of YSZ:Dy1% TBC in the as deposited condition and after 8, 64 and 900 hours at 1500°C.

On the cycled samples the monoclinic phase started to form after 250 hours at 1500°C however only very low percentages of monoclinic phase were found for the 7YSZ and YSZ:Dy0.3% samples that were heat treated directly for 350 hours at 1500°C. This suggests that, for 7YSZ and YSZ:Dy0.3%, the onset of monoclinic phase formation takes place at around 350 hours for an aging temperature of 1500°C. The monoclinic phase was only found in YSZ:Dy1% and YSZ:Dy2% after 500 hours at 1500°C. Early formation of the monoclinic phase was certainly caused by the heating and cooling cycles. Due to a furnace break down, only the results after 350 hour aging are available for the coating with 4.6 mol% of yttria (**Figure 76**). The monoclinic content for the various coatings after 800 hours of aging is compared in **Table 10**.
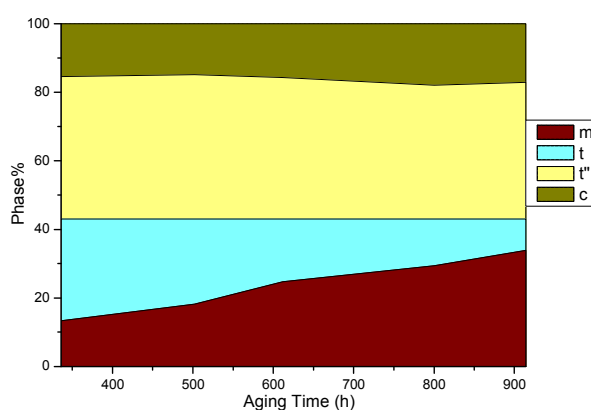
Figure 76: Map of phase evolution of zirconia + 4.6% yttria coating at 1500˚C.

It can be seen that the percentage of monoclinic phase decreases as the concentration in dysprosia increases highlighting the stabilisation effect of dysprosia. Unfortunately the coating deposited with the composite rod has only 4.6 mol% of yttria (instead of 4.9 mol% that was intended) and consequently none of the YSZ coatings have exactly the same stabiliser content as the YSZ:Dy TBCs therefore it is not possible to ascertain whether dysprosia is a better stabiliser than yttria. Nevertheless this study shows that dysprosia additions are not detrimental to the phase stability of the coating and further reduce the extent of the monoclinic phase formation.

Table 10: Percentage of monoclinic phase in the TBCs after 800h at 1500˚C.

Coating composition	*% monoclinic phase*
7YSZ	41.8
YSZ:Dy0.3%	39.8
ZrO_2 + 4.6% Y_2O_3	20.7
YSZ:Dy1%	15.8
YSZ:Dy2%	5.3

It is worth further mentioning that the standard YSZ sample and the one with 4.6 mol% of yttria spalled after 800 hours and 900 hours respectively, however no spallation was observed for the dysprosia doped coatings not even after 1100 hours.
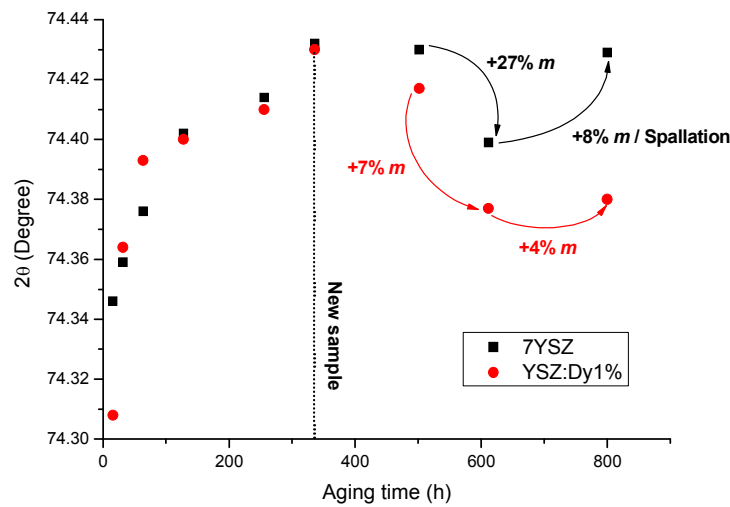
Figure 77: Tetragonal *(400)* XRD peak displacement against aging time at 1500°C for 7YSZ and YSZ:Dy1% TBCs.

Figure 77 presents the displacement of the XRD peak of the tetragonal phase with aging time at 1500°C for the 7YSZ and the YSZ:Dy1% TBC. Up to 330 hours the *t* peak is shifted to higher *2θ* values as the tetragonal phase becomes poorer in yttria (the *c/a* ratio increases). Between 500 and 600 hours the XRD peak position drops suddenly and these changes cannot be attributed to a yttria enrichment of the *t* phase. The decrease in the *c/a* ratio is more likely to be caused by the volume expansion associated with the tetragonal to monoclinic phase transformation. This peak displacement clearly highlights the stresses in the TBC generated by the formation of the monoclinic phase. Further transformation seems to be well accommodated by the YSZ:Dy1% coating, however, spallation of the 7YSZ coating is observed after 800 hours at 1500°C. As a consequence the stresses in the TBC are released and the *t* phase peak returns to the position it had before the large formation of monoclinic phase. The YSZ:Dy0.3% coating contained 43% of *m* phase after a 1100 hours at 1500°C and yet the TBC was still intact.

It has been shown that YSZ:Dy offers temperature measurement capabilities above 900˚C and also that ternary additions of dysprosia further improve the phase stability of the coating, therefore it is seen as a promising phosphor to be used in a TBC.

5.7. Influence of aging on the phosphorescence and lifetime decay behaviour of the phosphor

5.7.1. Influence on the phosphorescence

It was shown that high temperature aging, and therefore phase transformations within the TBC, has affected the temperature measurement capabilities of the sensing coating. However, the comparison of the phosphorescence spectra revealed that the pattern of the aged sample has some characteristic features; such as new emission peaks and a shift in the wavelength of certain peaks. In order to investigate if these characteristic properties are sensitive to the duration of the heat treatment and thus the extent of phase transformations, a series of YSZ:Dy0.3%, YSZ:Dy1% and YSZ:Dy2% samples were aged 100, 300, 500 and 700 hours at 1500°C. The luminescence spectra of the samples aged 1100 hours, used to study the influence of dysprosia additions on the phase stability, were also recorded. The graphs in **Figure 78** are normalised to the peaks with the highest intensity (485 and 585 nm) in order to compare the relative intensities of the various emissions after heat treatment.

YSZ:Dy0.3%

Normalised to 485 nm **Normalised to 585 nm**

YSZ:Dy1%

YSZ:Dy2%

■ As deposited	■ 500h at 1500°C	
■ 100h at 1500°C	■ 700h at 1500°C	
■ 300h at 1500°C	■ 1100h at 1500°C	
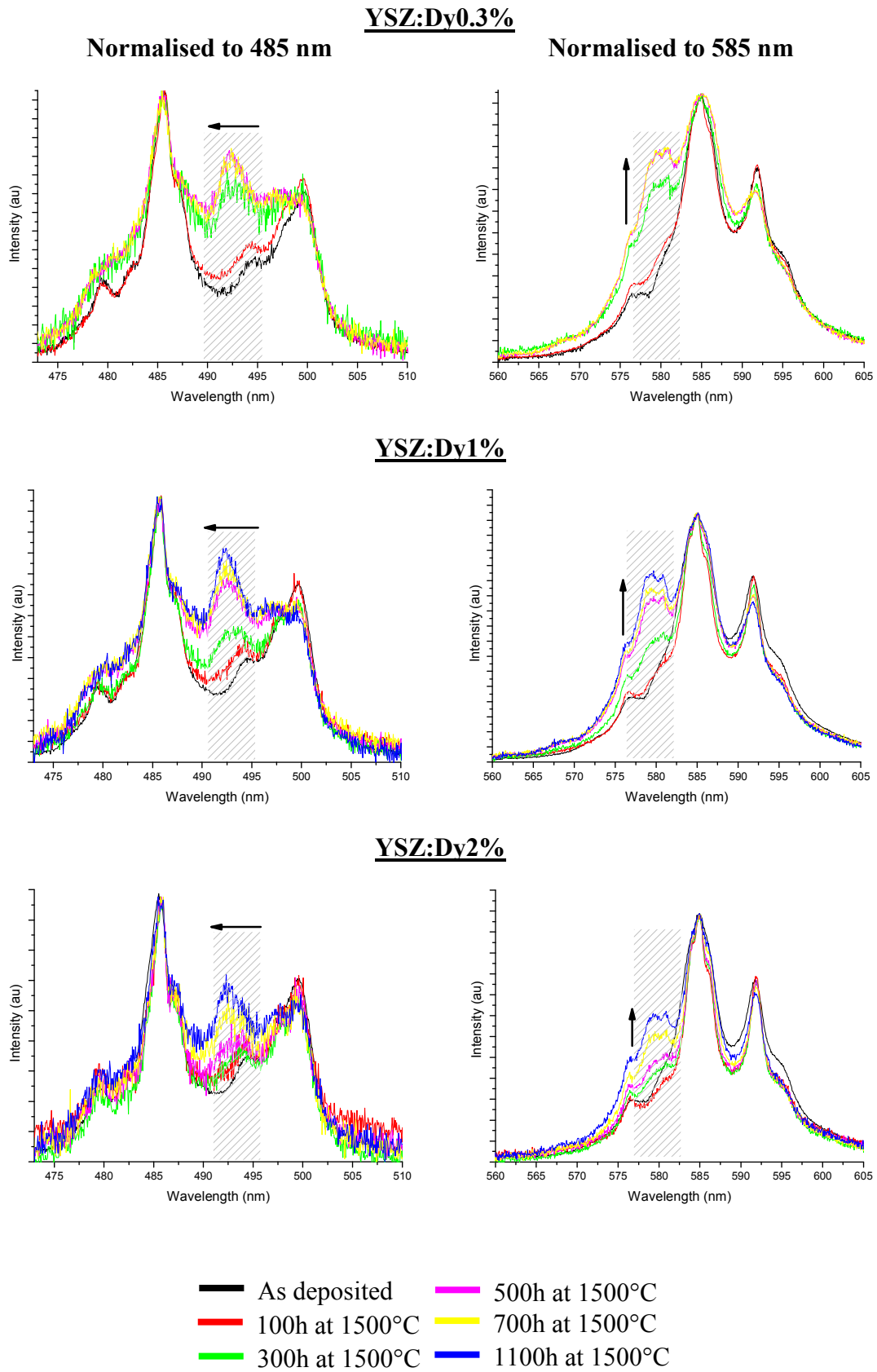
Figure 78: Effect of aging on the phosphorescence spectrum of YSZ:Dy (normalised graphs).

The aged coatings have a new emission peak (or set of peaks) at around 580 nm which grows with increasing aging time. The peak at 494.5 nm has a similar behaviour but it is also shifted towards lower wavelengths (up to 492.3 nm after long heat treatments). The growth of these characteristic peaks is less pronounced for high dysprosia concentrations. The intensity and the position of all other peaks remain relatively constant even after 1100 hours at 1500°C.

The phase composition of the TBCs was determined by XRD using the same method as in the study on the influence of substrate purity on phase stability. In the graphs in **Figure 79,** the ratio between the height of the peak at 585 and 580 nm and at 485 and 493 nm are plotted against the percentage of monoclinic phase in the coating. The TBCs aged for only 100 hours at 1500°C contained some monoclinic phase because they were tested more than two months after being heat treated and, even at room temperature, the yttria poor tetragonal phase slowly transforms to the monoclinic phase [56]. The XRD analysis was carried out two days after the phosphorescence spectra were recorded.

The 585/580nm and 485/493nm ratios both decrease with the percentage of *m* phase for the three compositions tested. The 485/493nm ratio was calculated taking into account the shifting of the 493 nm emission peak. These results suggest that the formation of the monoclinic phase is responsible for the appearance of the new emission peaks and that their intensity could be used to determine quantitatively the extent of the coating destabilisation.

YSZ:Dy0.3%

YSX:Dy1%

YSZ:Dy2%
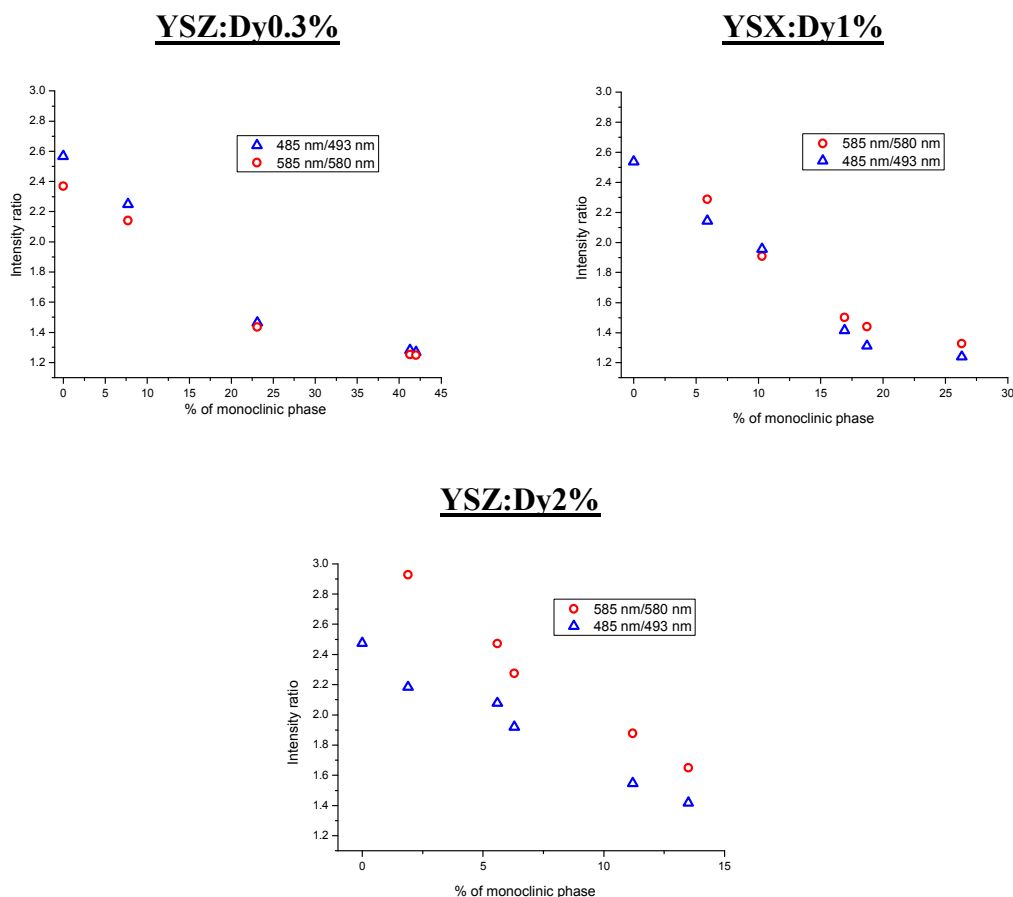
Figure 79: Height ratio between the 580nm and 585nm peaks and between the 485nm and 493nm peaks as a function of monoclinic percentage in the coating.

5.7.2. Influence on lifetime decay at room temperature

As seen in **Figure 54** there are some differences in the calibration curves of the as deposited and aged samples at low temperatures. In order to determine precisely how the phase transformations observed influence the luminescence spectrum as reported in the previous chapter, the lifetime of the series of aged YSZ:Dy1% samples were measured at room temperature. For each sample the measurements were repeated five times under the exact same conditions and the results are plotted in **Figure 80** against the percentage of monoclinic phase.
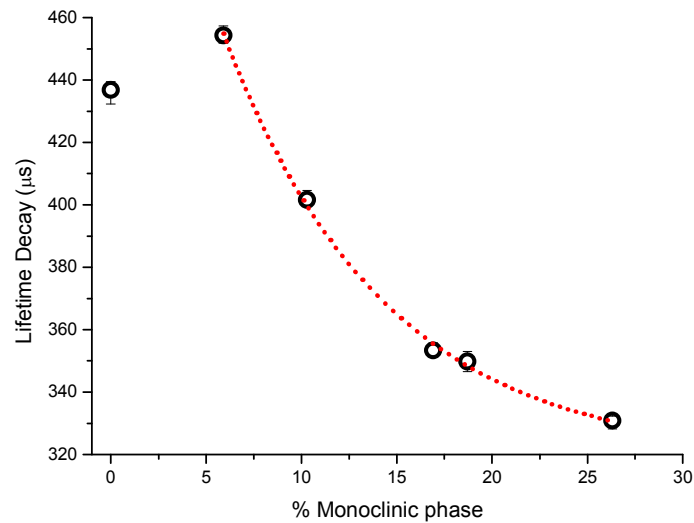
Figure 80: Effect of aging on the luminescence lifetime of YSZ:Dy1% TBC.

First, when the coating transforms from 100% *t'* to cubic and tetragonal phases, plus a small percentage of monoclinic phase, the luminescence lifetime increases and then it decreases non-linearly as the monoclinic phase content increases.

5.8. Discussion

The energy levels of the *4f* configuration of Dy_2O_3 represented in **Figure 55** shows only the energy splitting caused by the coulomb and spin-orbit interaction however the crystal field of the host material also gives energy state splitting (or *Stark* components). Even if the effect of the crystal field is small with respect to the spin-orbit, because the *4f* electrons are well screened from the environment, it could give rise to new emission lines (**Figure 16**). As shown in **Figure 81** an electronic transition between Dy^{3+} energy levels in YSZ does not give a single emission line. At room temperature at least eight

and twelve peaks for the $^4F_{9/2} \rightarrow {}^6H_{13/2}$ and $^4F_{9/2} \rightarrow {}^6H_{15/2}$ transitions respectively can be observed.
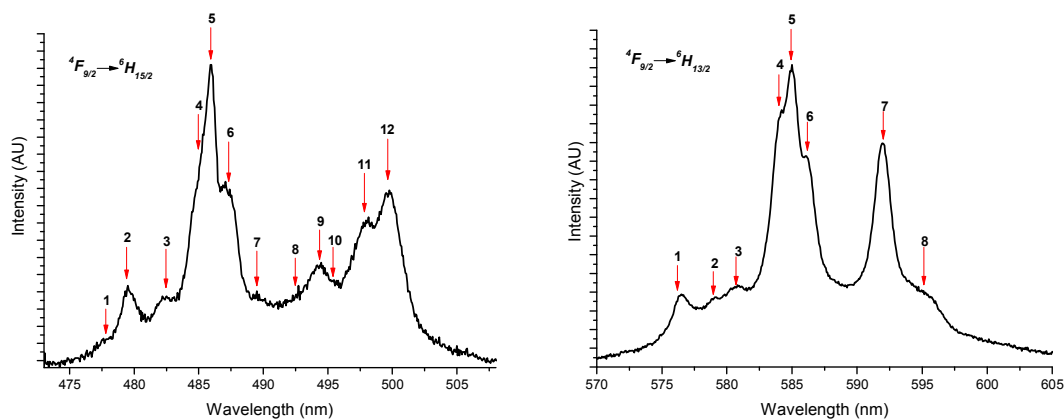
Figure 81: Phosphorescence spectrum of YSZ:Dy1% TBC.

If Dy^{3+} ions occupy a site with a tetragonal symmetry the $^6H_{13/2}$ and $^6H_{15/2}$ energy levels are split in to seven and eight *Stark* components respectively therefore at least seven and eight emissions lines arising from transitions to these levels should be observed. More peaks are observed on the YSZ:Dy spectrum because the high energy $^4F_{9/2}$ level also splits into five components. At room temperature all the *Stark* components will be occupied therefore, in theory, there should be 35 and 40 lines for $^4F_{9/2} \rightarrow {}^6H_{13/2}$ and $^4F_{9/2} \rightarrow {}^6H_{15/2}$ transitions respectively. The extra peaks on the luminescence spectrum of the as deposited sample could also mean that Dy^{3+} occupies non-equivalent sites in the YSZ matrix. A detailed analysis of the YSZ:Dy spectrum at such a temperature is difficult due to the large overlap of the various emission lines. The number of sub-levels created by the crystal field for Dy^{3+} occupying sites with different symmetries is listed in **Table 11**. It can be seen that, for lower symmetry than tetragonal, such as monoclinic, the spectrum can become very complicated.

Table 11: Number of *Stark* levels of Dy^{3+} in sites of cubic, tetragonal and monoclinic symmetry [193-196].

Symmetry	$^4F_{9/2}$	$^6H_{13/2}$	$^6H_{15/2}$
Cubic	3	5	5
Tetragonal	5	7	8
Monoclinic	10	14	16

Since aging causes phase transformations and therefore modifies the crystal field around the phosphor dopants it is believed that the appearance of new luminescence peaks is directly linked to phase transformations in the coating. It is expected that the separation of the as deposited *t'* phase into tetragonal and *t''* phase will not have a great influence since these phases have the same symmetry. However, when the tetragonal phase transforms into the low symmetry monoclinic phase, Dy^{3+} is more likely to sit in a site with lower symmetry hence the new emission peaks observed in the spectrum from the aged samples.

The 585/580nm ratio should be preferred to monitor the phase changes in the TBC using phosphorescence because the intensity of the emission line at 585 nm is 2.7 times higher than the one at 485 nm. Furthermore the peak at 494 nm which is sensitive to the phase transformations, is shifted towards lower wavelengths with increasing percentage of monoclinic phase hence making the determination of its intensity more difficult. An alteration of the crystal field felt by Dy^{3+} ions could be responsible for the shift in the 494 nm emission peak. As shown in **Figure 77** the volume expansion associated with the formation of the monoclinic phase, both introduces stresses in the coating and changes its crystallography and therefore must affect the crystal field.

In **Figure 82**, the 585/580nm intensity ratio for the different dysprosia concentrations are plotted on the same graph as a function of the percentage of monoclinic phase. The errors bars on the percentage of monoclinic phase come from the uncertainty in the fitting of the XRD graphs.
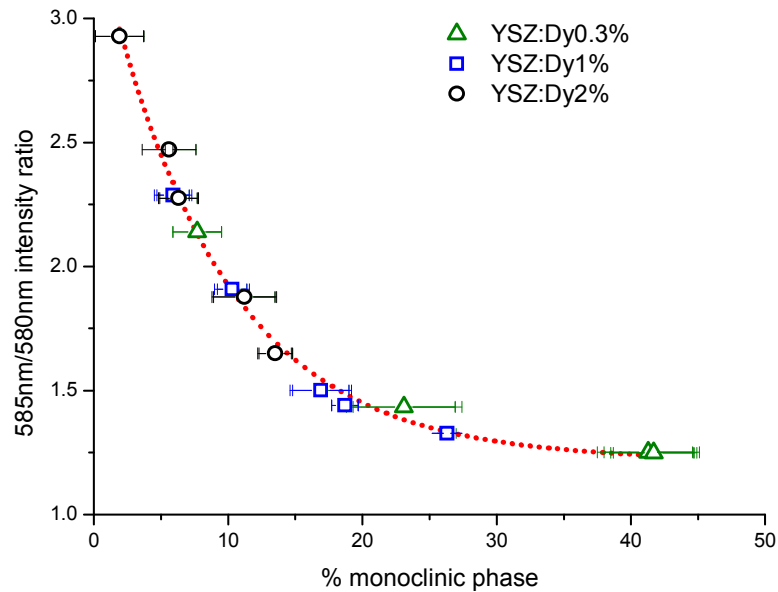
Figure 82: 585/580nm intensity ratio against the percentage of monoclinic phase in YSZ:Dy TBCs.

The experimental points were fitted with the following first order exponential decay function:

$$IR = 2.15 \times e^{(-\frac{\%m}{8.98})} + 1.22$$

Equation 14

, where *IR* is the intensity ratio between the strongest emission line and the peak characteristic of the monoclinic phase and *%m* is the percentage of monoclinic phase.

It would appear that the 580 nm emission is only related to the content of monoclinic phase in the coating and is independent of the concentration of dysprosia. These results show that phosphorescence could be used to determine quantitatively the extent of monoclinic phase formation in the coating by monitoring the intensity ratio of two specific emission lines and utilising a calibration curve such as the one produced for YSZ:Dy phosphor (**Equation 14**).

Srivastava [164] *and Chambers* [180] *et al.* also reported the appearance of a new emission peak at 615 nm in the luminescence spectrum of YSZ:Eu phosphor containing monoclinic phase. *Srisvastava et al.* showed that the intensity ratio of the 615 nm peak to the 605 nm peak increases linearly with the percentage of monoclinic phase (based on four measurements). However based on the spectra presented in [180] there would appear to be only a small decrease in the same intensity ratio even when the monoclinic phase content increase from 0% to 50% (IR≈0.5→0.4).

The analysis of the lifetime of the luminescence of the aged dysprosia doped TBC samples, at room temperature, revealed an innovative way of monitoring the phase transformations in a TBC. As the as deposited *t'* phase partitions into *t* and *c* phase the lifetime at room temperature increases, then as the percentage of *m* phase in the coating increases it decreases exponentially. Consequently the increase in the phosphorescence lifetime could be attributed to the *t'*→ *t + c* phase transformation and the decrease to the *t* → *m* phase transformation. The data were found to fit a first order exponential decay function:

$$LTD_{RT} = 274.5 \times e^{-\frac{\%m}{8.4t}} + 318.5$$

Equation 15

, where LTD_{RT} is the lifetime of the phosphorescence measured at room temperature and *%m* the percentage of monoclinic phase in the TBC.

This model can be linked to the results reported earlier on the influence of dopant concentration on LTD (**Section 5.1**, **page 114**). It was found that as the percentage of dysprosia increases the LTD at room temperature decreases (**Figure 51**). This was attributed to concentration quenching, however, the crystal structure of the host material could also play a part, indeed dysprosia additions change the lattice structure and tend to form a coating with a more "cubic-like" microstructure. The changes of LTD at room temperature, induced by phase transformation, are of the order of a 100 μs compared to several hundreds of microseconds for dopant concentration quenching, therefore even though this could have an effect, concentration quenching is still the main factor.

The reasons for the observed variations in the phosphorescence lifetime at room temperature are not fully understood. As explained in the literature review, the atoms of the crystal host move around their equilibrium positions and this constitutes the lattice vibrations of the host material, the quantum of which is called a phonon. Relaxation from an excited state can take place, not only by direct transition to a lower state via the emission of photons, but also by releasing energy in the form of phonons to the surrounding crystal. Clearly, the type and crystal structure of the host material will influence the lifetime decay of the phosphorescence. During aging, there is not only the appearance of new phases, but also stresses coming from the volume expansion cause

by the $t \rightarrow m$ phase transformation. Further, the XRD analysis highlighted the various changes in crystal structure caused by the high temperature aging. Consequently, the crystal field felt by Dy^{3+} ions will vary with increase in heat treatment time and, as a result, so will the phosphorescence lifetime.

Thermal barrier coatings need to be inspected on a regular basis for any sign of deterioration. A common inspection methodology may require taking the engine component out of service and visually assessing the extent of spallation of the coating. Such a method, does not give any information concerning the degree of deterioration of an intact coating, its past service conditions and its remaining life. For high pressure turbine blades, it is usual to perform destructive tests at each inspection interval to decide whether repair or replacement is necessary. Such an inspection is time-consuming, requires specialized equipment, cannot be conducted on site and extrapolates the results obtained for one part to other similarly used parts and therefore may not provide an accurate condition of those parts. Inspection for phases changes in the TBC, that occurs with exposure at high temperature, using a non-destructive examination method, could be a way to determine the health of the coating as well as its past service condition. In this study, it has been shown that such phase transformations could be monitored using phosphorescence, by measuring the luminescence lifetime at room temperature or by determining the intensity ratio between two characteristic luminescence lines. Both techniques provide a simple, fast, non destructive way of determining the past service condition of the TBC and its degree of deterioration.

In summary, YSZ:Dy is a promising phosphor to be used as an inner layer in a TBC, it permits the ceramic/bondcoat interface temperature to be accurately measured, ±5°C. Dysprosia further stabilises the *t'* phase, YSZ:Dy phosphor presents no problem of deposition by EB-PVD, it can be used to measure temperatures up to at least 950˚C and also to monitor the health of the TBC. However phosphors based on YSZ matrix and a rare earth activator have not been found to have a temperature sensitivity above 1200˚C. Therefore, they cannot be used as a top layer to measure the surface temperature of the TBC under aero-engine applications. Consequently, a different phosphor based on a different matrix, with temperature capabilities up to at least 1200˚C, must be used as a top layer.
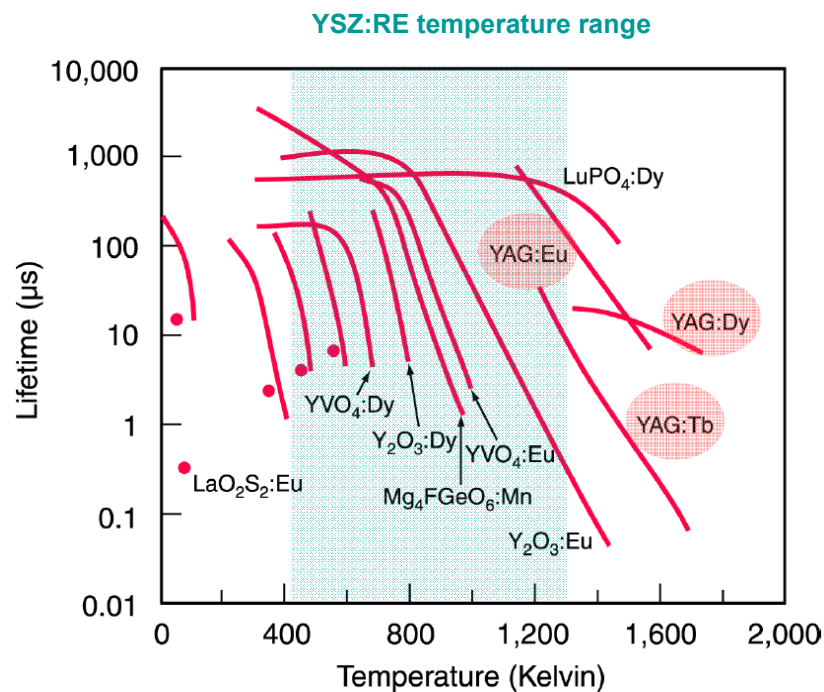
Figure 83: Calibration curves for various phosphors [100;138].

As shown in **Figure 83**, Yttrium Aluminium Garnet (YAG) compositions would be potential candidates from the phosphorescence point of view, and phosphors like

YAG:Dy have been reported to luminesce up to at least 1500°C [115;138]. However, they have never been used as TBC material and they have never been deposited by EB-PVD before.

6. *YAG* PHOSPHORESCENT COATING

6.1. YAG properties

Yttrium Aluminium Garnet (YAG) has been chosen, firstly, because of its temperature sensitivity as a host for suitable phosphors, and secondly, because of such properties as maximum temperature capability, hardness, elastic modulus, density, thermal expansion and thermal conductivity, all of which are beneficial in TBCs. Thus, based on these properties, YAG offers great potential as a material for TBC applications [75;197]. The essential properties for a good TBC material are compared in **Table 12** for zirconia, yttria, alumina and YAG. The thermal conductivity of YAG is somewhat higher than that of zirconia however it will only be used as a thin layer on top of the TBC therefore it is believed that it will not have a significant influence on the overall thermal conductivity of the coating. Moreover the low thermal conductivity of an EB-PVD TBC

is mainly attributed to the inner equiaxed zone which is very effective in scattering phonons due to the large number of defects and grain boundaries [76]. One should consider that, just like ternary additions of rare earth oxides are used to reduce the thermal conductivity of YSZ TBCs, a similar alloying addition could have the same effect on YAG material. Oxygen diffusivity is also an important property for TBC application since a low diffusivity will retard the oxidation of the bond coat or the superalloy and the oxygen diffusivity of YAG is 10^{10} times lower than that of zirconia at 1000°C. The low density of YAG is also considered beneficial as it will reduce the stresses due to the centrifugal load.

Table 12: Comparison of the properties of zirconia, yttria, alumina and YAG [197].

	Thermal conductivity at 1127°C (W/mK)	*O_2 diffusivity at 1000°C (m^2/s)*	*Thermal expansion coefficient at 1000°C ($x10^{-6}$/K)*	*Maximum temperature capability (°C)*	*Hardness (GPa)*	*Density (g/cm^3)*
Zirconia	2.7	10^{-10}	10	1425	14	6.4
Yttria	2.7	10^{-12}	7.9	2400	NA	5
Alumina	5.5	10^{-19}	9.5	2050	20	4
YAG	3.2	10^{-20}	9.1	1970	17	4.5

However, for the present application, the most critical properties are the maximum temperature capability, the hardness and the thermal expansion coefficient. The maximum use temperature of YAG is almost 40% higher than that of zirconia and YAG is 20% harder than zirconia which is very desirable for good erosion resistance properties since it will be used at a top layer in the TBC. The last parameter of interest is the coefficient of thermal expansion. Because the YAG top layer will be in contact with the YSZ ceramic TBC, matching of the coefficient of thermal expansion between YAG and zirconia is of primary importance in order to reduce the stresses generated

between the two layers. The thermal expansion for the two materials should be close enough to prevent the spallation of the YAG phosphor layer during thermal cycling.

YAG/YSZ multiplayer TBCs have been successfully deposited by air plasma spraying [198]. However, the author is not aware of any work published in the open literature on YAG deposited by EB-PVD. The following chapters develop a method to deposit a YAG phosphorescent layer by EB-PVD, using a single source evaporator, and the measurement of the performance of the YAG based phosphor deposited by EB-PVD.

6.2. Deposition of a YAG coating

6.2.1. From an yttria/alumina rod

The first deposition was made by evaporating an ingot[*] of yttria and alumina in the right stoichiometry (62.5 mol% alumina and 37.5 mol% yttria). The ingot was made by physically blending the powders followed by an isostatic pressing and then a firing step. The composition of the rod was checked by XRD (**Figure 84**). The ingot was in fact a complex mixture of yttria, alumina and yttria/alumina compounds. The XRD analysis revealed that, during the manufacturing of the rod, Yttrium Aluminium Perovskite (YAP - $YAlO_3$) and Yttrium Aluminium Monoclinic (YAM - $Y_4Al_2O_9$) were formed however, the rod did not contain any YAG (Yttrium Aluminium Garnet) phase.

---

[*] Ingot supplied by Phoenix Coating Resources, USA.
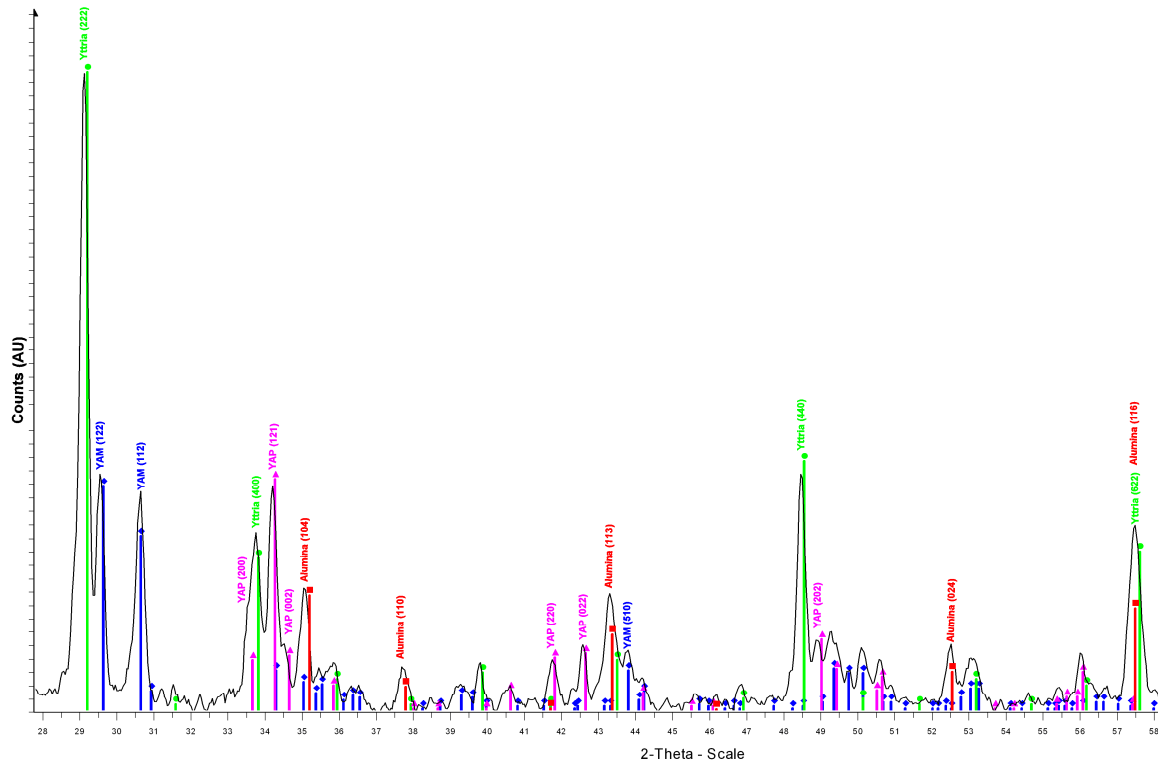
Figure 84: XRD graph of the yttria/alumina ingot.

As for YSZ, where the rod is made of zirconia and yttria that react during evaporation and condense as an yttria partially stabilised zirconia coating, it was expected that yttria would react with alumina to form a YAG coating. To start, the same deposition parameters as for a YSZ deposition were used. During the deposition, the top of the rod exploded, as soon as the electron beam hit the ingot, (**Figure 85**) and the melt was very unstable before it started to evaporate, so the beam intensity had to be lowered to 0.3-0.4 A. At a higher intensity (0.5 A) the melt could no longer be contained within the rod and it poured out of the melt pool, like wax from a candle, and jammed the rotation of the ingot so the deposition had to be stopped. For the next depositions, only a small piece of rod (3-5 cm) was placed in a water cooled hearth in order to prevent problems caused by the uncontrolled and excessive melting of the ingot.
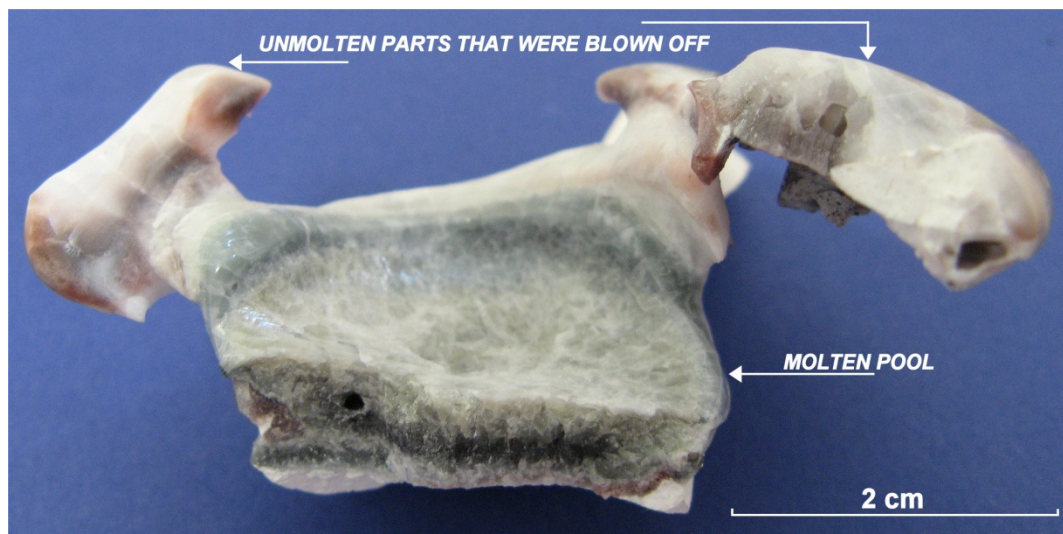
Figure 85: Picture of the rod that blew apart during deposition.

It is believed that the cracking of the ingot cap was due to a thermal shock problem due to the high density of the partially fused ingot. However, it was noted that when the top of the ingot was completely molten prior to deposition, the thermal shock was reduced and the evaporation became quite stable. The EB gun could be run at normal intensity (0.5 A). Following this attempted deposition run, the molten part of the ingot was powdered and analysed by XRD. The XRD pattern shows that, once the rod had melted, yttria and alumina have completely reacted and YAG is the main phase present in the spectrum (**Figure 86**). A deposition was carried out by evaporating a pre-molten ingot (5 minutes at low power) during 60 minutes under the same conditions of pressure and substrate temperature as for a standard YSZ deposition. The coatings, from this evaporation trial, were deposited directly on high purity single crystal alumina substrates and on a standard YSZ coating produced in a previous deposition. The as deposited coatings were observed to be pearlescent (**Figure 87**) and the substrate could be seen through the coating. It is believed that the as deposited samples were amorphous or partially amorphous.
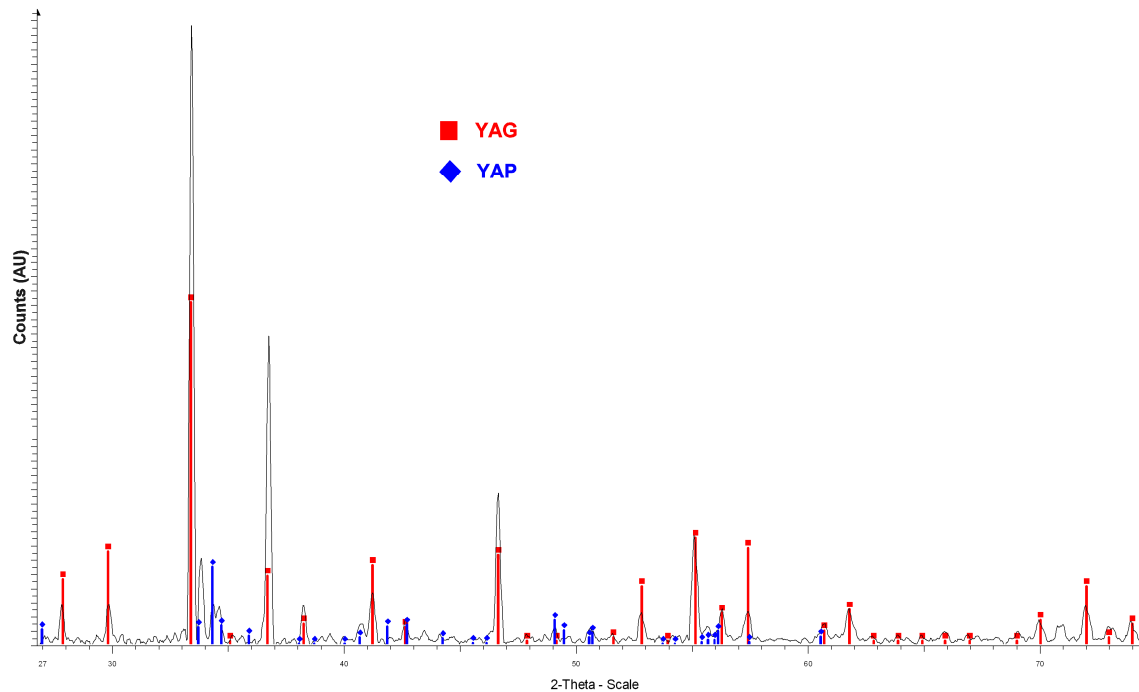
Figure 86: XRD graph of a pre-molten ingot.

The samples were aged two hours at 1100˚C so they could recrystallise and XRD was carried out on the as deposited and aged samples (**Figure 88**). All the peaks in the XRD pattern of the as deposited coating could not be identified, however, after the short heat treatment the spectrum had the characteristic diffraction peaks of the $Y_4Al_2O_9$ (YAM) and $YAlO_3$ (YAP) phases. The YAG phase was still not detected in the coating, before or after the heat treatment, using XRD.
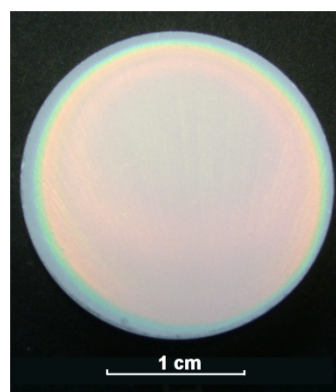
Figure 87: Pearlescent sample after deposition from an yttria/alumina ingot.
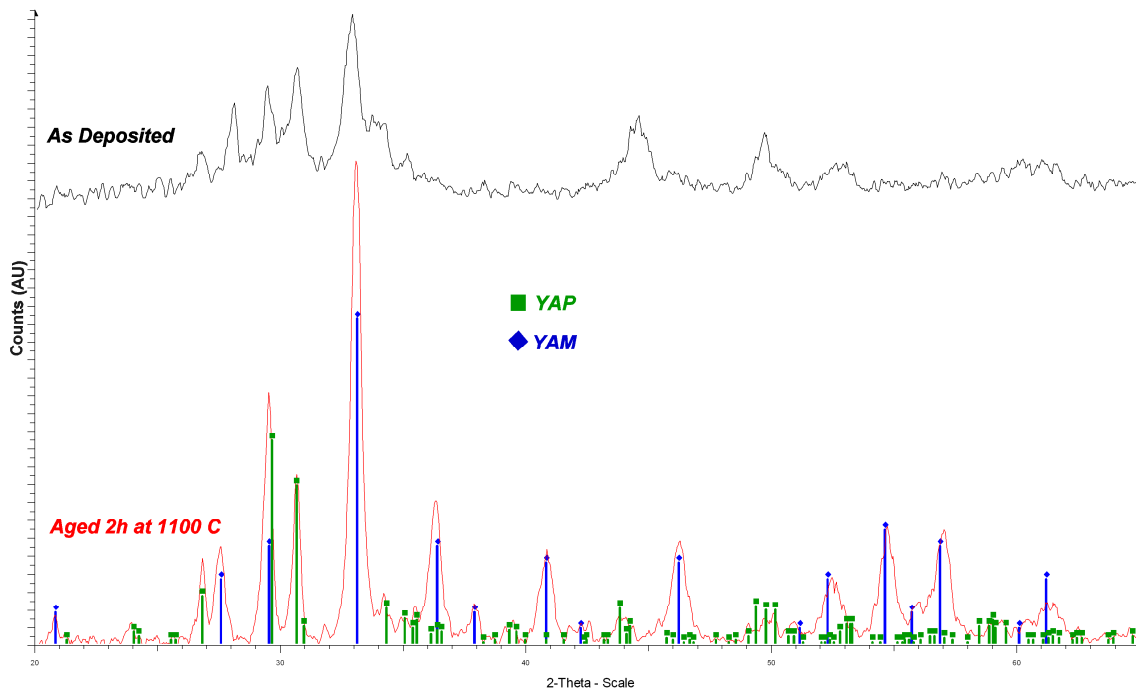
Figure 88: XRD graphs of the as deposited and aged samples deposited from an yttria/alumina ingot.

A sample was then cut, mounted and polished for SEM analysis as described in **Section 4.2.2.1**. A cross section micrograph, as well as an EDX analysis, are presented in **Figure 89**. The coating is clearly not homogenous over its thickness and it is very difficult to distinguish the substrate from the beginning of the coating. In the backscatter image the yttria rich regions appear lighter and the alumina rich darker. The coating consists of layers with different concentrations of yttria and alumina and it seems to be divided in two parts, first a thick layer with a relatively homogenous composition (the first 15 µm) and then successive graded layers which become richer in yttria towards the outer coating surface.

(a)   (b)
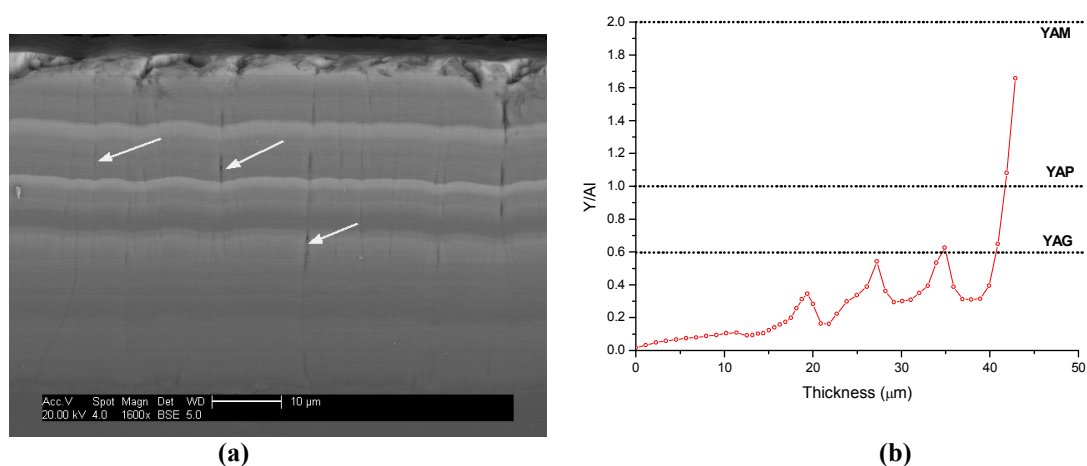
Figure 89: (a) SEM cross section and (b) EDX analysis of an aged coating.

The coating is mostly monolithic, however, large columns or "blocks" which seem to originate at the interface with the first yttria rich layer can be seen (pointed to by the arrows in the SEM picture in **Figure 89**). Furthermore, the columnar microstructure is maintained for the coating deposited on top of a standard 7YSZ TBC. The newly deposited material grew from the YSZ column tips and the intercolumnar porosity was not sealed by the top layer. However, the morphology of the top of the columns was somewhat different to that expected from the evaporation of YSZ; they look very fibrous and had a rounded top (**Figure 90**).
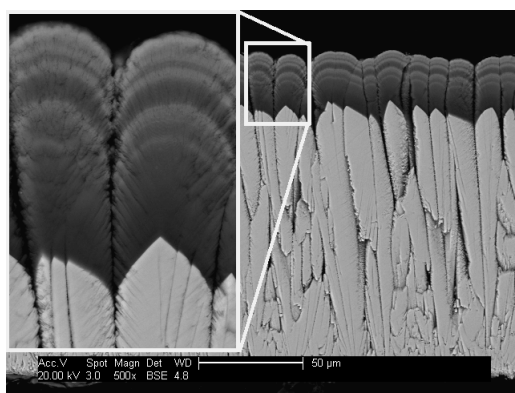
Figure 90: SEM micrograph of a "YAG" coating deposited on top of an 7YSZ EB-PVD TBC.

It is worth noting that, due to the limited penetration of the X-rays, the XRD pattern represented in **Figure 88** characterizes only the first five microns of the coating. The EDX analysis (**Figure 89**) and the phase diagram in **Figure 91** suggest that the top five microns of the coating should be a mixture of YAP and YAM which is in good agreement with the XRD results (**Figure 88**). Consequently, as the *Y/Al* plot in **Figure 89** crosses twice the YAG composition line, the YAG phase might still be present in some of the layers in equilibrium with alumina or YAP (see phase diagram in **Figure 91**).
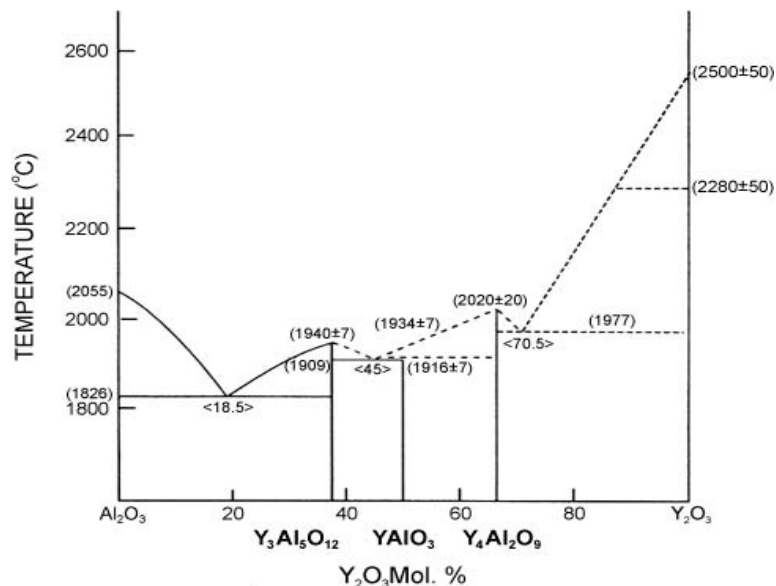
Figure 91: Equilibrium phase diagram of the alumina/yttria system [199].

Another deposition was made under the exact same conditions as the previous one but it was stopped at half time (after 30 minutes) in order to be in the composition range where YAG is in equilibrium with alumina (as predicted from **Figure 89**). The coating was only a 25 μm thick layer (**Figure 92**) with a relatively homogenous composition comparable to the one observed following the previous deposition.
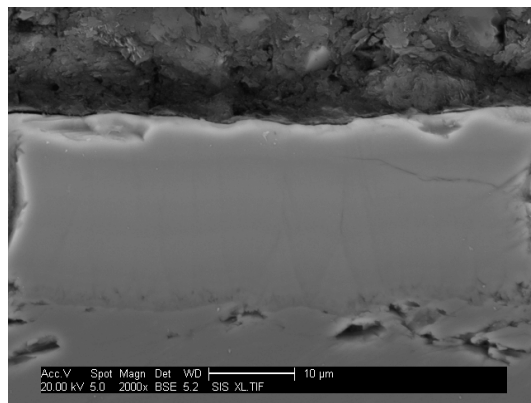
Figure 92: SEM cross section of the aged coating from the "short" deposition.

These samples were also pearlescent and the XRD analysis showed that the as deposited coating was completely amorphous (**Figure 93**). A similar observation was reported when the YAG phase was prepared by solid-state reaction [200;201], precipitation [202], spray-pyrolysis [201] and magnetron sputtering [203]. Subsequent annealing was performed at temperatures between 900 and 1000°C in order to obtain crystalline YAG. Published studies using a DSC analysis showed that the crystallisation of YAG occurs between 930 and 1075°C [204;205]. The XRD pattern of a heat treated sample has the characteristic spectrum for YAG, plus an alumina phase, which confirms that some of the layers in the first coatings contained the YAG phase.

6.2.2. Deposition from a YAG rod

A deposition from a pure YAG ingot$^{\diamond}$ was carried out (the composition of the rod was verified with an XRD analysis of powder taken from the ingot). Depositing directly from a YAG material, rather than a mixture of yttria and alumina, could change the evaporation process. There was little chance the rod would evaporate as YAG, it was

---

$^{\diamond}$ Ingot supplied by Phoenix Coating Resources, USA.

expected that the evaporant would rather break down into individual atom components. It could also affect the relative evaporation rates of yttrium and aluminium atoms. Due to the very small size of the rod it was placed in a water cooled hearth and the deposition lasted only 20 minutes.
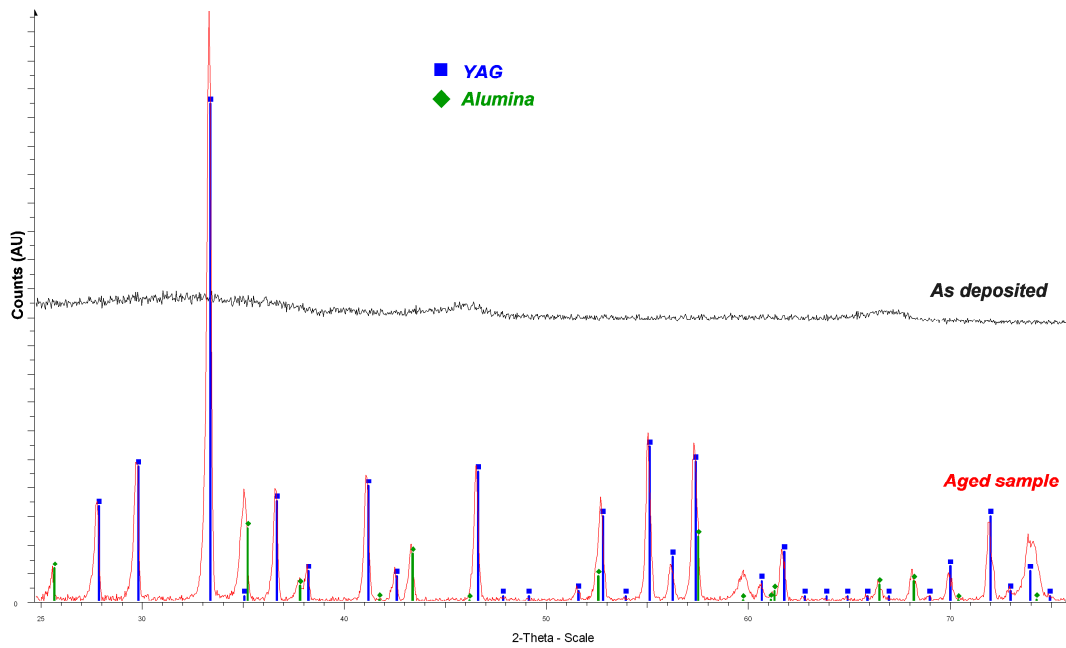
Figure 93: XRD graph of an as deposited and aged coating from the "short" deposition.
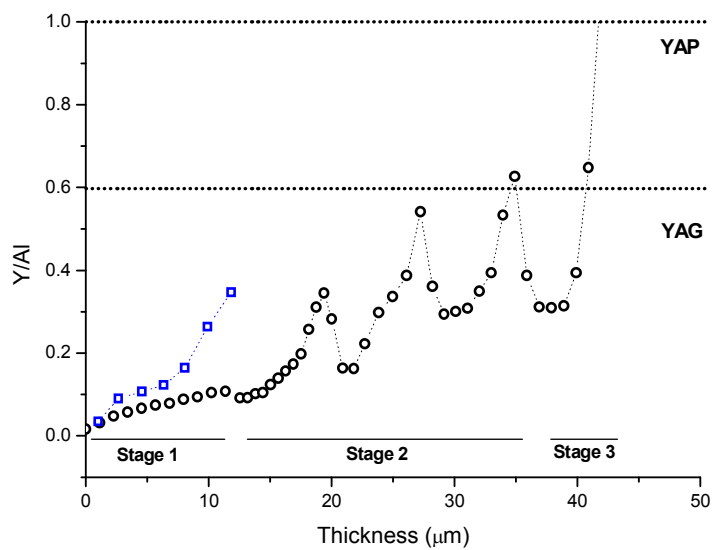
Figure 94: Y/Al molar ratio as a function of coating thickness obtained from EDX analysis of a coating deposited from a YAG (□) and yttria/alumina ingot (○).

As expected, a graded structure was obtained. The composition of the first five microns of the coating was very similar to that of the coating deposited from an yttria/alumina ingot. The yttria concentration in the coating increased rapidly afterwards since, due to the limited size of the rod, the molten pool was rapidly saturated in yttria. Evaporating from a YAG ingot, or a mixture of alumina and yttria with the stoichiometry of YAG, produces a multilayer coating which is thought to reflect the difference in the vapour pressures between alumina and yttria.

6.2.3. Deposition analysis

The evaporation rate of the rod material can be calculated using the *Hertz-Knudsen* equation:

$$\frac{dn}{Sdt} = \alpha_v \frac{1}{\sqrt{2\pi m k_B T}} \left(P_v - P^* \right)$$

Equation 16

, where P_v is the vapour pressure of the evaporant at a temperature T (in K), P^* is the ambient hydrostatic pressure acting upon the evaporant in the condensed phase, α_v the sticking coefficient for vapour molecules onto the surface, m the mass of a molecule, k_B the Boltzmann constant, S the evaporation surface area and dn/dt the atomic rate of evaporation per unit of time and unit of surface area.

The maximum evaporation rate is attained when $\alpha_v=1$ and for a pressure in the deposition chamber lower than 0.1 mbar the evaporation rate is independent of the

residual gas pressure due to the negligible resistance offered. As the deposition takes place between 1 and $5x10^{-2}$ mbar $P^*=0$. Therefore the maximum mass evaporation rate is given by:

$$\Gamma = m\frac{dn}{Sdt} = P_v\sqrt{\frac{m}{2\pi k_B T}}$$

Equation 17

The evaporation rates of yttria and alumina were calculated for three different evaporation temperatures using the vapour pressures for the evaporant found in the literature [206]:

Table 13: Vapour pressure and evaporation rates of alumina and yttria at 2100, 2200 and 2300°C.

Temperature (°C)	Vapour Pressure (mbar)		Evaporation Rates			
			$(g.cm^{-2}.s^{-1})$		$(mol.cm^{-2}.s^{-1})$	
	Alumina	Yttria	Alumina	Yttria	Alumina	Yttria
2100	1	0.1	$9.07x10^{-3}$	$1.34x10^{-3}$	$8.90x10^{-5}$	$5.93x10^{-6}$
2200	3.5	0.35	$2.84x10^{-2}$	$4.63x10^{-3}$	$2.79x10^{-4}$	$2.05x10^{-5}$
2300	10	1	$8.71x10^{-2}$	$1.30x10^{-2}$	$8.54x10^{-4}$	$5.76x10^{-5}$

These calculations show that, because alumina has a much higher vapour pressure than yttria, it evaporates about 15 times faster than yttria $(mol.cm^{-1}.s^{-1})$.

The bits of rod left after deposition were analysed by EDX. For the deposition stopped after 30 minutes the rod was not completely molten and it had a uniform composition. It was composed of two phases, both yttria rich, as represented in **Figure 95**. The global composition was around 87% yttria and 13% alumina compared to 37.5% yttria and

62.5% alumina for the original composition highlighting the faster evaporation of alumina compared to yttria. During the first minutes of the deposition the composition of the molten pool becomes gradually richer in yttria, however, it is constantly fed by the newly molten material and the alumina seems to be channelled from the bottom to the top of the pool. Consequently the composition of the vapour cloud remains relatively constant therefore the first 15 microns of the coating does not contain large variations in composition (*Stage 1* in **Figure 94**).

	% Yttria	*% Alumina*	*Y/Al*
Phase 1	80	20	4
Phase 2	88.5	11.5	7.7
Global composition	87	13	6.7
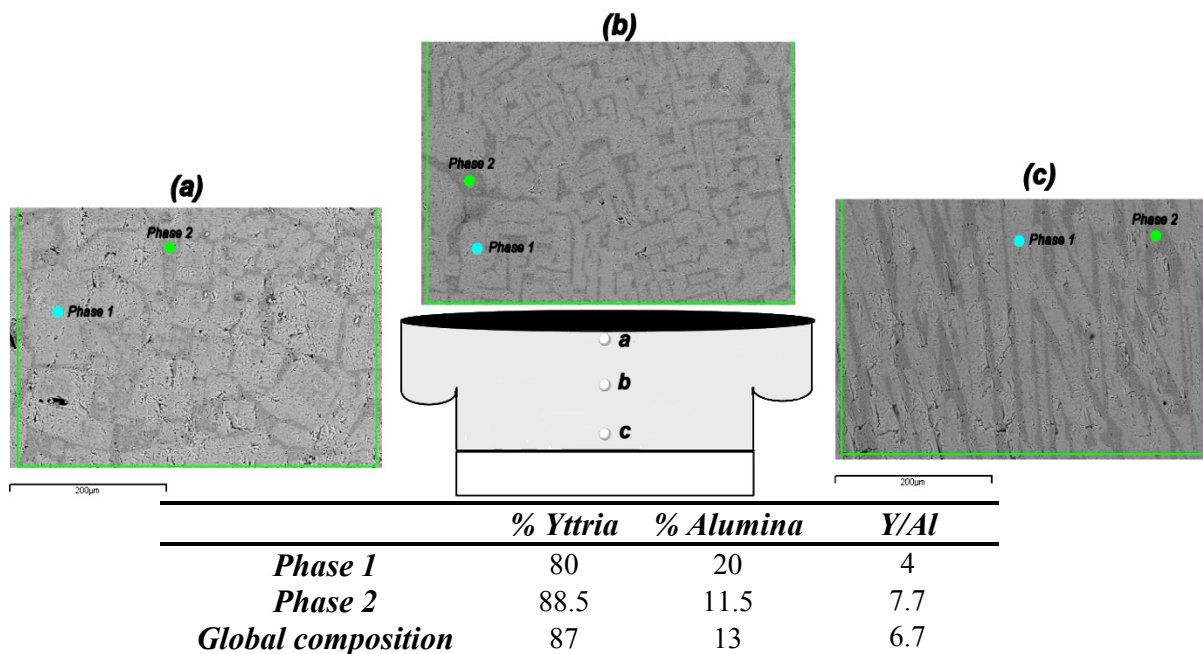
Figure 95: SEM micrograph and composition of the molten ingot after the "short" deposition.

The rod from the first analysis (60 minute deposition) was completely molten. It shows that the molten pool was gradually enriched in yttria from the bottom to the evaporation surface at the top (table in **Figure 96**). In the second stage, the molten pool is so saturated with yttria that it prevents the evaporation of alumina, therefore the vapour cloud has a very high concentration in yttria, hence clear layers rich in yttria are observed in **Figure 89**. Finally, since the rod has a finite length, when the bottom of the

rod is reached the reservoir of alumina becomes depleted so the top of the molten pool becomes richer and richer in yttria and the concentration in yttria in the coating increases rapidly (Stage 3 in **Figure 94**).

(a)   **(b)**   **(c)**

(e)   **(d)**

	%Yttria	%Alumina	Y/Al
a	94	6	15.7
b	87	13	6.7
c	80	20	4
d	60	40	1.5
e	55	45	0.8
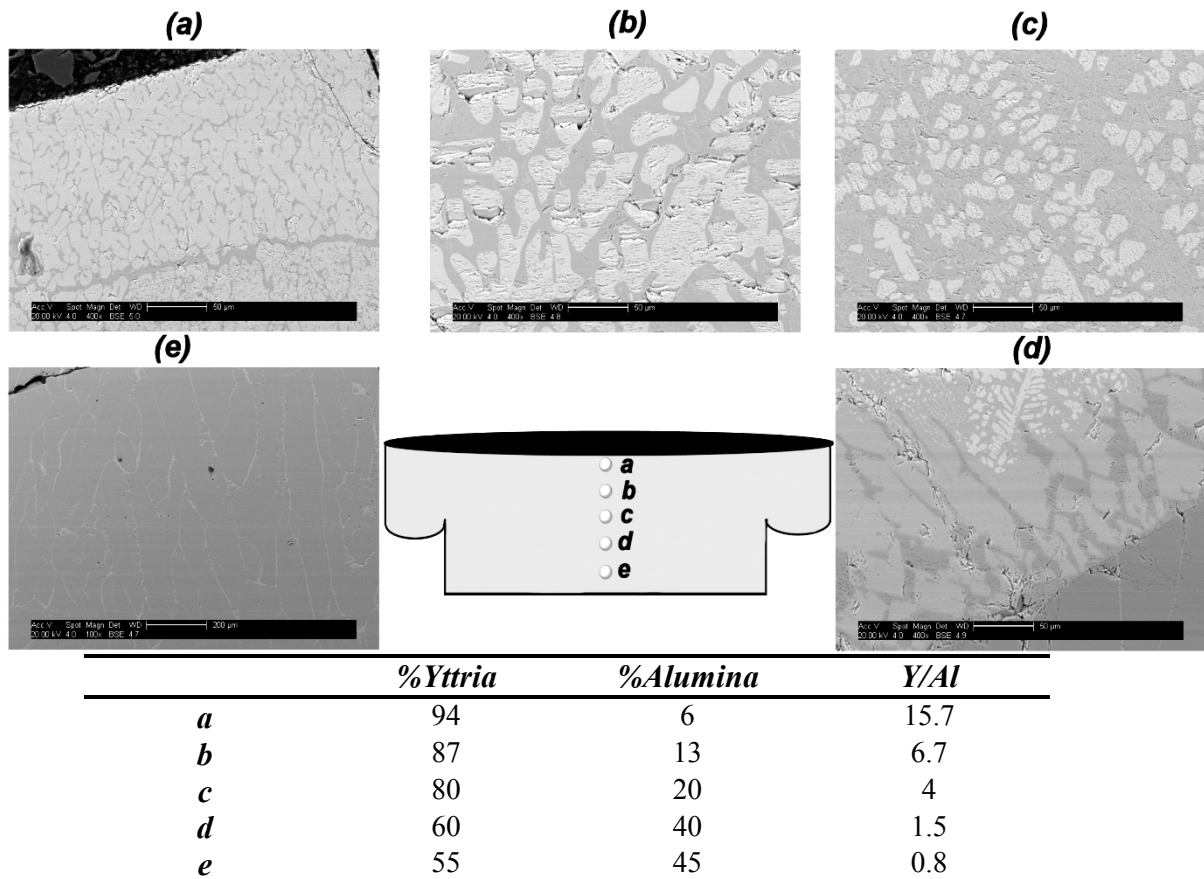
Figure 96: SEM micrograph and composition of the molten ingot after the "long" deposition.

As shown previously, the alumina and yttria concentrations in the molten pool highly influence the evaporation rates of these materials however it is not reflected in **Equation 16** or **Equation 17.** A correction factor β is introduced to take the concentration of each constituent in the molten pool into account. Since yttria and alumina evaporate at different rates β changes with time. β is taken as the molar percentage of each constituent in the molten pool. The number of moles of yttrium and aluminium in the vapour cloud at an instant *t* can be estimated by:

$$n_{y_v}(t) = 2\Gamma_{Y_2O_3}\beta_Y(t - \Delta t)S$$

$$n_{Al_v}(t) = 2\Gamma_{Al_2O_3}\beta_{Al}(t - \Delta t)S$$

Equation 18

The coating compositions calculated from **Equation 18** are compared with the EDX results found for the short and long depositions using an yttria/alumina ingot. The values of β were determined by EDX analysis of the molten rods after deposition (**Table 14**).

Table 14: Comparison between the experimental and theoretical coating compositions.

	β_Y	β_{Al}	*Yttrium/Aluminium (atomic ratio)*	
			EDX coating	*Calculated*
t=0 min Short deposition	0.375	0.625	0.06	0.04
t=0 min Long deposition			0.03	
t=30 min Short deposition	0.87	0.13	0.47-0.51	0.45
t=60 min Long deposition	0.94	0.06	1.08	1.05

The coating compositions were calculated using the maximum evaporation rates for each constituent at 2300°C (α_v=1), under the assumption that aluminium and yttrium atoms travel from the ingot to the substrate and condense onto the deposition surface in a similar manner. The theoretical results, presented in **Table 14,** are in good agreement with what has been observed experimentally.

These experiments showed that, due to the large difference in vapour pressure between alumina and yttria, it is not possible to deposit a pure YAG coating using a single source evaporator. According to the phase diagram in **Figure 91**, if the yttria concentration in the coating remains under 37.5%, the YAG phase will be in equilibrium with alumina. Obviously it is highly desirable to get as close as possible to the YAG composition in order to limit the alumina content in the coating. It is also very important not to exceed

37.5% of yttria otherwise the YAP phase will be present in the coating. *Feist et al.* [184] showed that YAP is also a good phosphor host and, therefore, the YAG:RE and YAP:RE luminescence might overlap making the temperature measurements more difficult to interpret.

Equation 18 suggests that the yttrium and aluminium concentration in the vapour cloud could be adjusted by changing the yttria/alumina stoichiometry in the ingot so the condensed material would have a composition close to that of YAG (*Y/Al*=0.6). In other words, the evaporation rate of yttria could be increased relatively to the one of alumina by increasing its concentration in the rod. The composition of the first 10 μm of the coating was calculated from **Equation 18** assuming an evaporation temperature of 2100°C, for three different rod compositions: *Y/Al*=0.6, 2 and 4. The coating thicknesses were determined from the depositions made from the yttria/alumina ingot (≈1 μm/min). The calculations also take into account the variations in the pool composition due to newly molten ingot material, estimated from the length of rod consumed, during a deposition.

The results found for a rod with a YAG stoichiometry (*Y/Al*=0.6) are in good agreement with the experiments for the first 15 μm, before the molten pool is completely saturated with yttria. The calculations were made assuming a homogenous composition of the molten pool, however, as shown in **Figure 96**, yttria concentrates at the surface of the pool as alumina evaporates preferentially. Once yttria reaches a critical concentration it evaporates quickly hence the peak observed at 20 μm (**Figure 97**). Since the *Y/Al*=2 and 4 ingots have a higher yttria content it is expected that the molten pool will be saturated

much more rapidly limiting the coating thickness that could be deposited (the *Y/Al*=0.6 limit must not be exceeded to prevent the formation of the YAP phase). From this theory, an ingot composition of 33.3 mol% alumina and 66.6 mol% yttria (*Y/Al*=2), a "YAG" layer with a maximum thickness of about 10 μm could be deposited with a limited concentration of alumina compared to a coating deposited from a rod with a YAG stoichiometry. A deposition using a customised rod was carried out in order to confirm these theoretical results and the following paragraph deals with the manufacturing of this special rod.
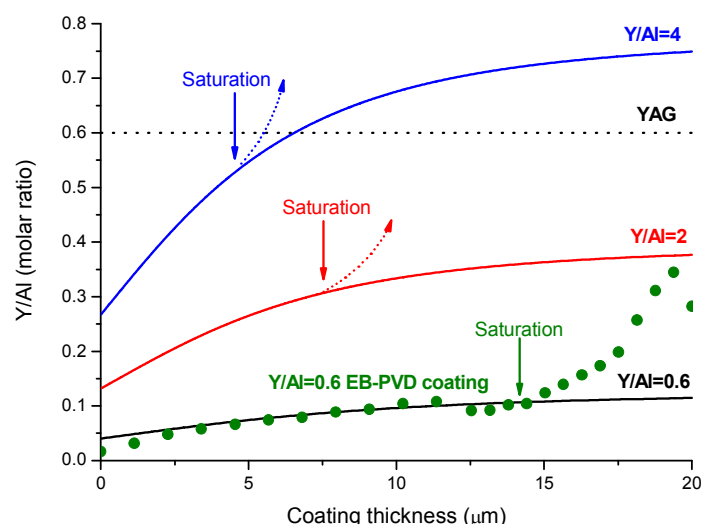
Figure 97: Composition of the first 20 μm of the coating (individual points ●) and calculated data for three different rod compositions (Y/Al=0.6, 2 and 4).

6.2.4. Rod manufacturing

To increase the yttria concentration in the ingot a hole with the right diameter was drilled into an yttria/alumina rod and filled with yttria powder in order to achieve a 33.3 mol% alumina and 66.6 mol% yttria composition. However a trial run showed that,

during the deposition, yttria was blown away, as soon as the electron beam hit the powder. This suggests the material to be evaporated has to be in the compact form in order to be deposited by EB-PVD. A rod was manufactured from powder pressed at room temperature using a cold isostatic press (CIP). Alumina* and yttria• powders in the right proportion in order to achieve a *Y/Al* molar ratio of 2 were mixed in an automatic shaker for 30 minutes. The powder was then poured into a rubber tube with two rubber bungs at each end and sealed with metallic wires (**Figure 98**). The tube was pressed at 50000 psi (≈3450 bar). The CIPped rod was dense enough to be handled and cut in half and no cavities were seen in the cross sections (**Figure 98**).
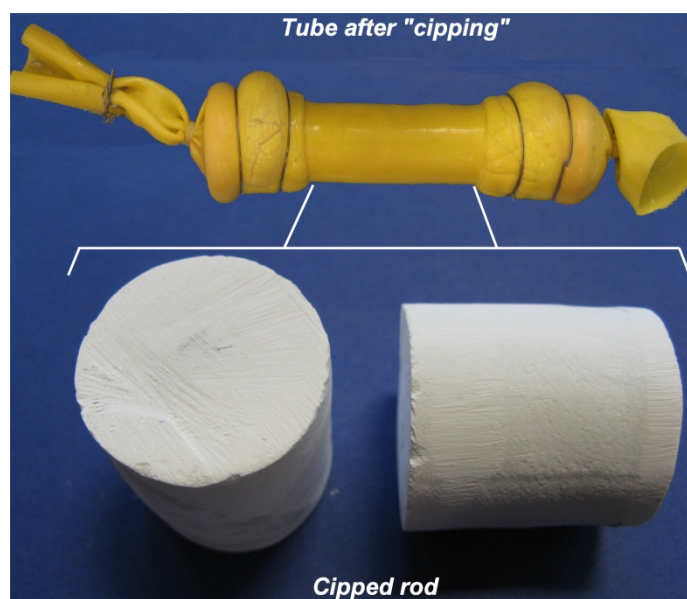
Figure 98: Yttria/alumina rod after cold isostatic pressing.

One half of the ingot was placed in a water cooled hearth in the EB-PVD chamber and evaporated. The melt was very unstable and the rod evaporated poorly, constantly spitting and erupting. After ten minutes the deposition had to be aborted. A picture of

---

* Alumina powder, 99.9% purity supplied by PI-Kem LTD, UK.
• Yttria powder, 99.9% purity supplied by Alfa Aesar, USA.

the molten ingot in **Figure 99** clearly shows a solidified bubble of material that formed at the surface of the rod. As these gas bubbles burst during the deposition, large droplets of fused material are ejected onto the alumina substrate as can be seen on the samples in **Figure 99**. *Bruce et al.* [207] suggested that "spitting" comes from gas and water vapour entrapped in the porosity of the rod and impurities that can react to form gaseous compounds at high temperature. As 99.9% powders were used it is not believed that impurities were the main source of "spitting".
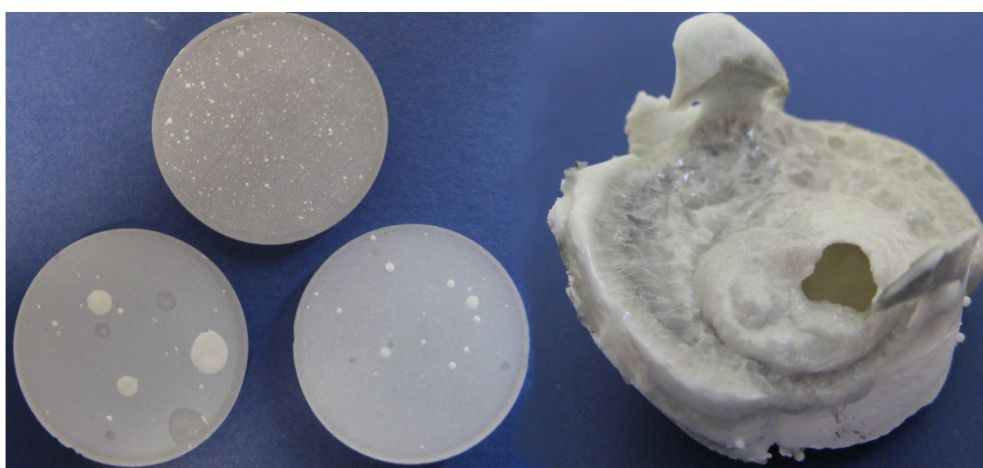
Figure 99: Samples and CIPped ingot after deposition.

The other half of the ingot was therefore heat treated two hours at 1500°C in a box furnace in order to remove any traces of water and to increase its density through sintering. The rod was heated and cooled slowly (15°C/min) in order to avoid thermal shocks and it was bagged after treatment to prevent the re-absorption of water vapour. During the deposition, as soon as the electron beam hit the heat treated rod, it did not melt but cracked and exploded. Even though the aging was only for two hours it seems that such a high temperature excessively sintered the ingot and therefore it could not withstand the thermal shock caused by the E-beam's rapid heating.

More rods with the same composition were manufactured following the process described above. The heat treated rod was calculated to be about 75% dense compared to 60% dense after CIPping, therefore, the aging temperature was decreased to 1200°C in order to reduce the amount of sintering. After this treatment, the ingot was still about 70% dense and it also exploded at the beginning of the deposition. With a heat treatment of two hours at 1050°C the rod was about 63-65% dense. During the deposition, the ingot melted at low power like the rods supplied by *Phoenix LTD*. The melt was stable and there was almost no evidence of spitting, only 1-2 small spits were found on the surface of the samples after deposition. The samples were analysed by EDX and XRD in order to determine the influence of the increase in yttria concentration in the rod on the coating composition.
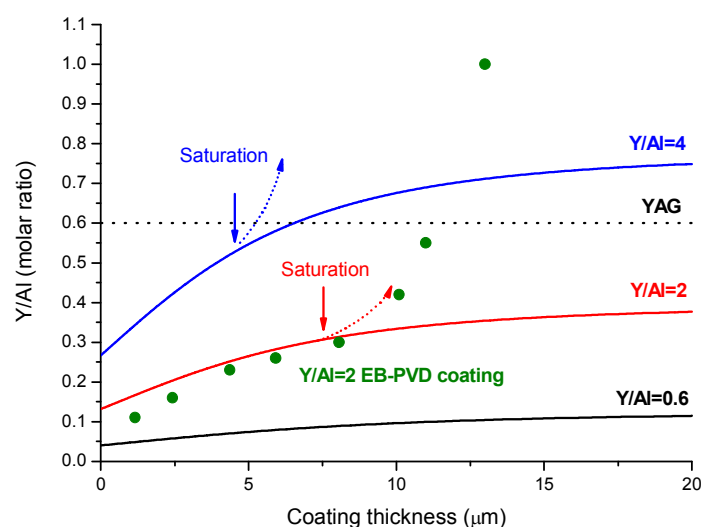
Figure 100: EDX analysis of the coating deposited from a Y/Al=2 ingot.

The EDX results are in good agreement with the calculated concentrations for the first eight microns (**Figure 100**). As it was expected, yttria saturation occurred much faster since the rod had a higher yttria concentration as manufactured (after 8 μm compared to

15 µm for a coating deposited with a rod with a *Y/Al* ratio of 0.6). The concentration of yttria and alumina in the first 11 µm of the coating remained under the stoichiometric YAG composition (*Y/Al*=0.6). Therefore it should be possible to deposit a 10 µm coating which does not contain the YAP phase and with a surface composition very close to the YAG phase.
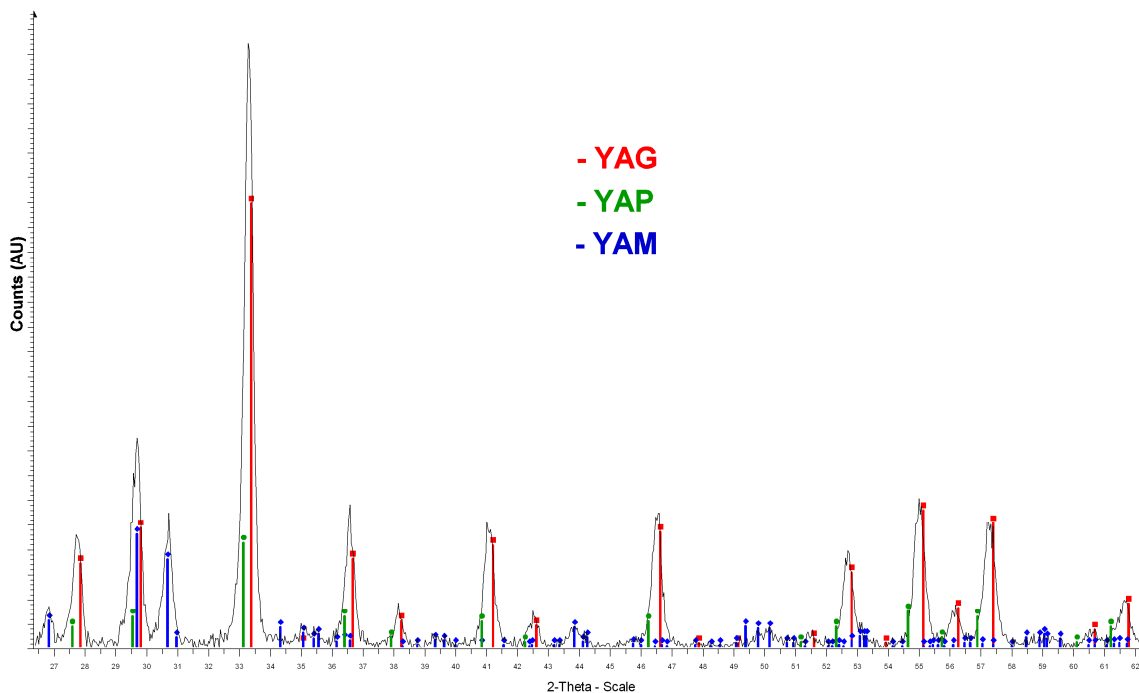
Figure 101: XRD analysis of the coating deposited from a Y/Al=2 ingot.

The EDX results were confirmed by XRD analysis (**Figure 101**). The YAG composition was exceeded in the last 2-3 µm of the coating consequently the XRD pattern shows the characteristic YAP and YAM peaks however YAG remains the dominant phase. The next step was to add rare earth oxides into the rod composition in order to deposit a YAG:RE phosphorescent coating.

6.3.   YAG:Dy phosphorescent coating

6.3.1.   Coating deposition

YAG powder, containing one mol% of dysprosia[♦], was mixed with yttria powder in order to achieve a *Y/Al* molar ratio of two. The powders were pressed in a rubber tube with a larger diameter in order to obtain a rod with the same dimensions as those supplied by *Phoenix*. The ingot was cut in half, faced off and machined to the correct diameter (33.3 mm). In order to further improve the stability of the melt during the deposition the rod was heat treated in a vacuum furnace with the following sequence:

20°C–*(10°C/min)*→**40°C**–*(4°C/min)*→**400°C**–*(10 min)*→**400°C**–*(4°C/min)*→**1000°C**–*(2h)*→**1000°C**–*(-4°C/min)*→ **20°C**

The resulting ingot had a very good surface finish and it was difficult to distinguish from a rod supplied by *Phoenix*. The ingot was placed on top of a long 7YSZ rod so it could be evaporated without using the water cooled hearth (**Figure 102**). During the deposition the melt was very stable, without spitting and it was contained on top of the 7YSZ ingot. One half of the rod was evaporated for 15 minutes and the other half during 25 minutes and in both cases the deposition was stopped before the 7YSZ ingot started to melt. The longer deposition was carried out to determine how the presence of the YAP or YAM phases in the coating would influence the phosphorescence.

[♦] YAG:Dy powder supplied by *STS*, UK.
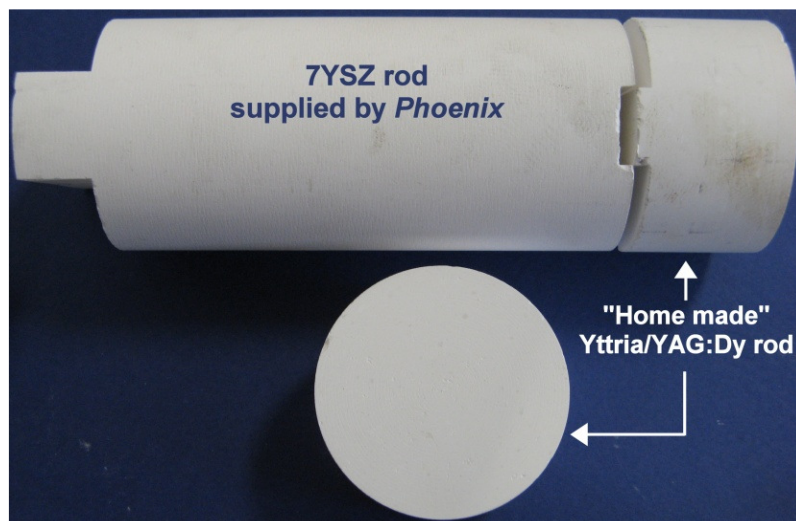
Figure 102: "Home made" yttria/YAG:Dy rod after machining.

Both coatings were heat treated for two hours at 1100°C before XRD analysis. For the longer deposition the top layers were found to be a mixture of YAP, YAM and yttria, whereas, for the shorter deposition the coating was only composed of YAG and alumina (**Figure 103**).
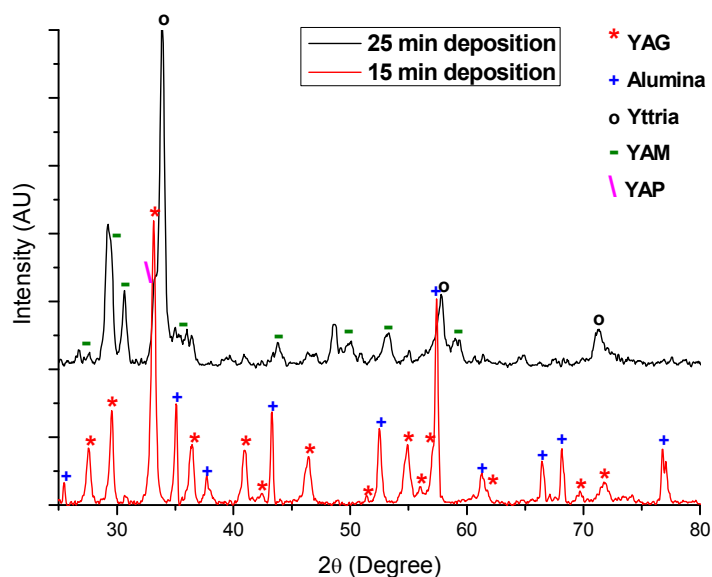
Figure 103: XRD spectra of the coatings deposited from a "home made" YAG:Dy/yttria ingot after heat treatment.

6.3.2. YAG:Dy phosphorescence

The phosphorescence spectra of both coatings were recorded between 470 and 610 nm when excited at 355 nm as described in Section 4.4.1. The normalised graphs in **Figure 104** show that all the peaks of the YAG/alumina coating spectrum correspond to YAG:Dy emission lines. However, as expected, the spectrum of the coating containing the YAP and YAM phases had characteristic emission peaks between 560 and 580 nm including a very intense line at around 572 nm. The phosphorescence spectrum was compared to the YAP:Dy spectrum found in the literature [184] and the extra emission peaks do not seem to correspond to the YAP:Dy luminescence. Therefore, it is very likely that these peaks are characteristic emissions of the YAM:Dy phosphor.
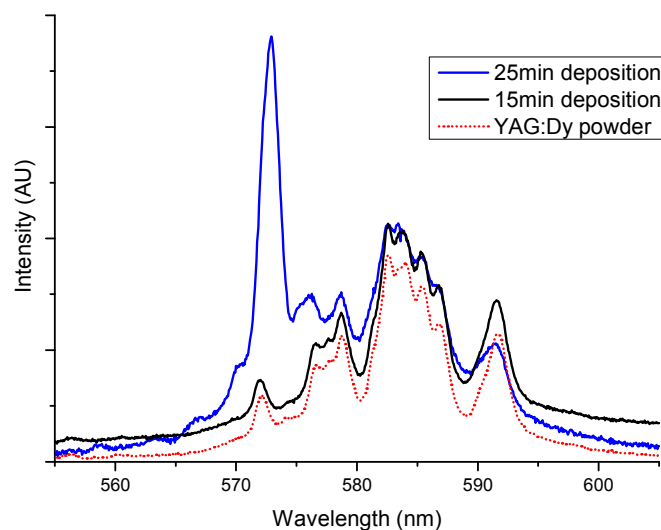
Figure 104: Luminescence spectra of the coatings deposited from an yttria/YAG:Dy ingot and YAG:Dy powder.

The calibration curve of the alumina/YAG:Dy coating was determined for an excitation at 355 nm, recording the lifetime of the 585 nm emission line (**Figure 105**). It was

found that YAG:Dy has a temperature sensitivity ranging from 1080°C to at least 1500°C. Indeed the lifetime decay measurements were limited by the maximum temperature capabilities of the furnace (1500°C). Extrapolation of the lifetime results to the detection limit of the measurement set-up (0.3-0.4 µs) shows that the YAG:Dy coating could be used to measure temperatures up to around 1700°C compared to 1000°C for the YSZ:Dy phosphor. The calibration curve was fitted to **Equation 8** for an energy gap of 7300 cm^{-1} and phonon energy of 315 cm^{-1}. From this modelling it is calculated that 23 phonons are required to bridge the energy gap. **Figure 105** illustrates the importance of the host material in the high temperature quenching process. For the same rare earth dopant in two different host materials the maximum temperature measurement capability of the phosphor could be increased by more than 700°C.
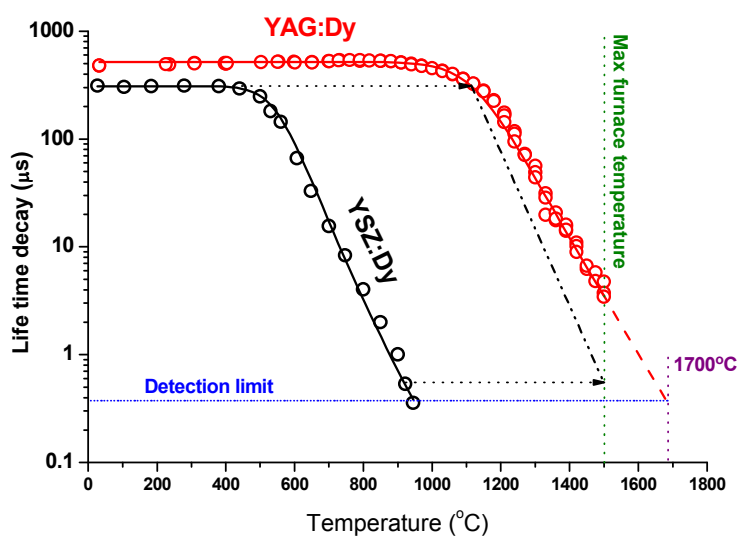
Figure 105: Calibration curves of YSZ:Dy and alumina/YAG:Dy EB-PVD coatings.

The YAG:Dy coating calibration curve was compared with the results obtained by *Allison et al.* [138] at *Oak Ridge National Laboratory* on powder material in **Figure**

106. The plots are very similar, especially the slope of the thermal quenching part of the curve. The excitation wavelength was not specified, but the lifetimes correspond to the emission lines at 480 and 575 nm compared favourably to 585 nm for this study. The XRD results in **Figure 103** showed that a coating containing the YAG phase was successfully deposited by EB-PVD. Furthermore, the graphs in **Figure 104** revealed that, even though the YAG phase is in equilibrium with alumina, all the peaks in the phosphorescence spectrum of the coating correspond to YAG:Dy emissions and have the same position. Most importantly, the EB-PVD YAG:Dy coating was found to have a maximum temperature capability of at least 1500°C, and potentially up to 1700°C. Further, because the slope of the YAG:Dy calibration curve is less steep than that of YSZ:Dy (**Figure 105**), it can be used to measure a broader range of temperatures:

- YSZ:Dy: 500°C → 950°C (450°C)
- YAG:Dy: 1080°C → 1700°C (620°C)
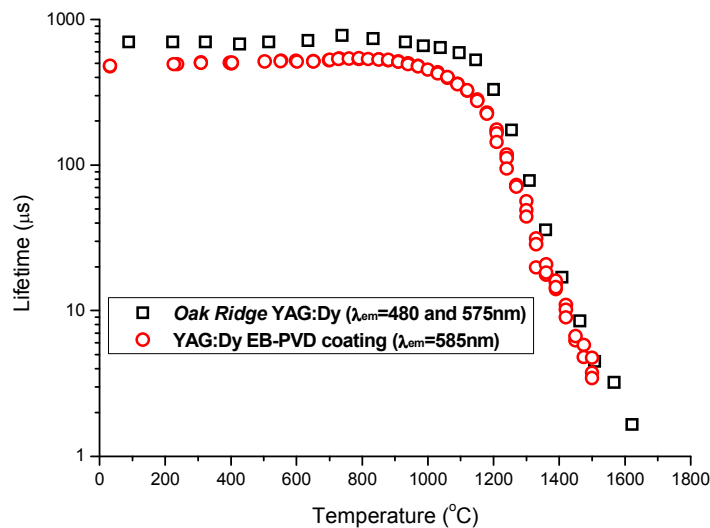
Figure 106: Comparison of the YAG:Dy calibration curves obtained at *STS* on the EB-PVD deposited coating and powder data measured at *Oak Ridge National Laboratory* (redrawn from [138]).

Because the phosphorescence spectra of YSZ:Dy and YAG:Dy overlap, YAG:Dy cannot be used to measure the temperature at the surface of the TBC if the coating already contains a YSZ:Dy inner layer. YAG:Eu and YAG:Tb phosphors also have a temperature sensitivity above 1300°C and therefore are potential candidates to be used as a top layer. However, as shown in **Table 15** if one of these phosphors were to be used, two different laser sources would be required in order to excite the top and inner phosphor layers.

Table 15: Phosphors and their excitation wavelengths.

Phosphor	*Excitation wavelength*
YSZ:Dy	355 nm
YAG:Dy	355 nm
YAG:Tb	266 nm
YAG:Eu	532 nm

Research on powder materials conducted at *STS* showed that the lifetime of YAG doped with thulium oxide (YAG:Tm) can be measured up to at least 1300°C, when excited at 355 nm (same wavelength as for YSZ:Dy). Consequently, in order to test a multilayer sensing EB-PVD coating and to be able to measure the temperature at two different depths in the TBC using one excitation wavelength and the *STS* set-up, the aim was to deposit a multilayer coating comprising a YSZ:Dy (inner layer), a standard 7YSZ and a YAG:Tm layer (top layer).

6.4. *Multilayer sensing EB-PVD TBC*

6.4.1. Coating deposition and characterisation

The multilayer coating was deposited by evaporating a multistage rod similar to the one represented in **Figure 57** with a YSZ:Dy2%, 7YSZ and yttria/YAG:Tm ingot successively (from top to bottom). A dysprosia concentration of 2 mol% was chosen for the YSZ:Dy layer because it represents the worst case scenario in term of luminescence intensity, compared to 0.3 and 1 mol% (**Figure 51**). Moreover, a high dysprosia content makes the positioning of the doped layer using EDX easier to identify. It also facilitates the study of the possible diffusion of dysprosia from the YSZ:Dy to the standard YSZ layer due to high temperature exposure (see **Section 6.4.3.2**). However, for real applications low dysprosia concentration may be preferred, as they give higher luminescence intensities, and the doped layer should be as thin as possible for a more localised temperature measurement.

The yttria/YAG:Tm[♦] rod was manufactured in exactly the same way as the yttria/YAG:Dy ingot in the previous section. As expected, the evaporation of the first two stages (YSZ:Dy2% and 7YSZ) took place without problems. However, since the yttria/YAG:Tm ingot melts at low power and the e-beam is not entirely focused on the top of the rod and has a certain width, the sides of the yttria/YAG:Tm ingot started to melt before the 7YSZ stage was completely evaporated (**Figure 107**).

[♦] YAG:Tm powder supplied by *STS LTD*, UK.
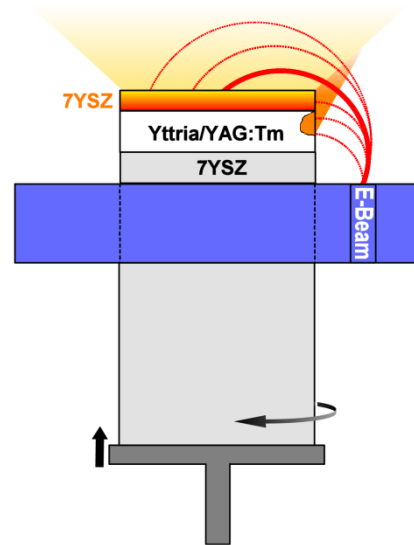
Figure 107: Schematic of the evaporation of the multistage ingot.

Consequently, the boundary between the 7YSZ and the YAG:Tm layers is not very localised (**Figure 108**). EDX analysis showed that the 7YSZ layer contains alumina "stripes" and that there was a gradient of zirconia in what was supposed to be the YAG:Tm layer. The coating has a columnar microstructure with "fibrous" rounded column tips similar to those observed previously in **Figure 90** for YAG:Dy.
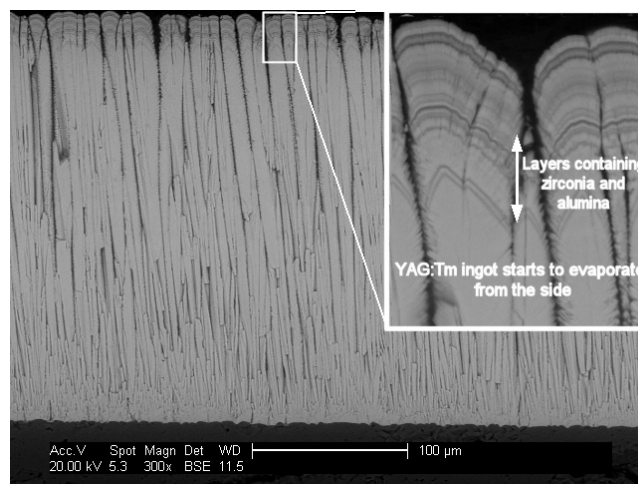
Figure 108: SEM micrograph of the coating deposited from the multistage ingot.

This deposition showed that a multilayer coating comprising a YAG:Tm layer cannot be deposited using a multistage rod due to the low melting point of the yttria/YAG:Tm ingot. Therefore, a repeat deposition was undertaken in two steps. In the first run, the YSZ:Dy2% and YSZ layers were deposited then the chamber was vented, the samples left to cool down and the ingot replaced by the yttria/YAG:Tm ingot which was evaporated during 20 minutes in a second run. The remaining size of the ingot after the deposition was surprisingly large. The evaporation rate was much lower, when compared to the previous depositions, and therefore the coating should be thinner than expected.
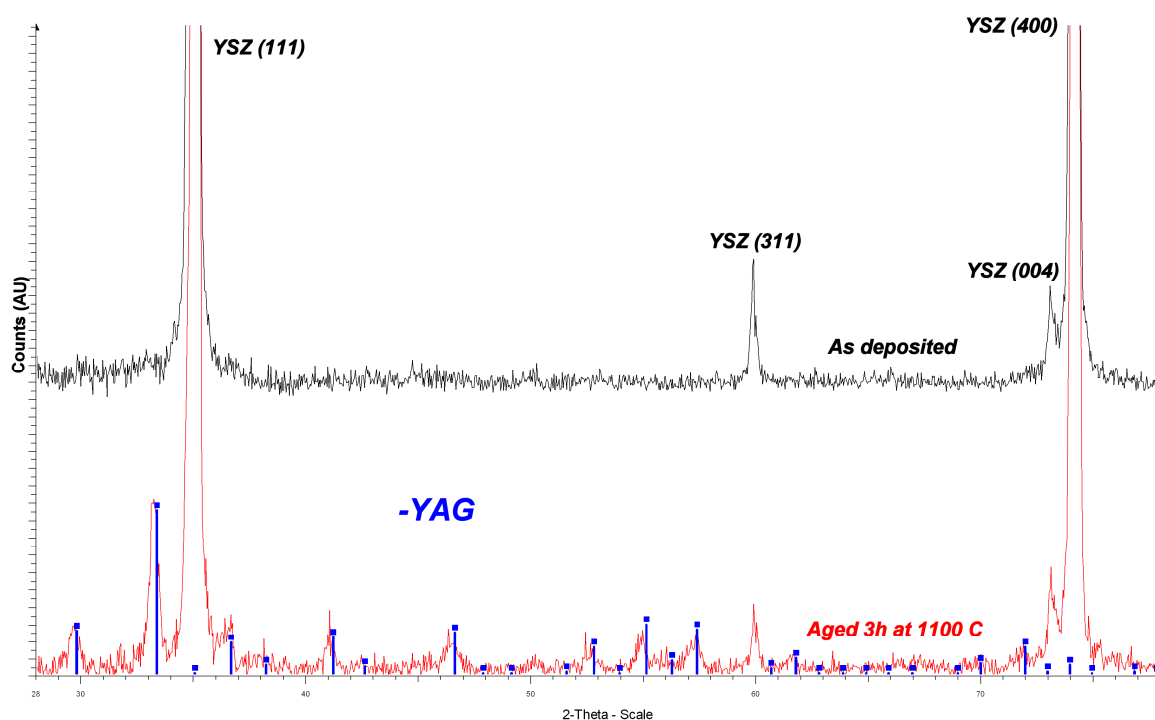
Figure 109: XRD graphs of the multilayer coating before and after heat treatment.

The as deposited YAG:Tm top layer was found to be amorphous however after aging the YAG phase crystallised as shown in the XRD graphs in **Figure 109**. Contrary to the YAG:Dy coating (**Figure 103**), alumina could not be detected in the TBC by XRD

analysis. Intense diffraction peaks characteristic of the *t'* YSZ phase can be observed in the XRD pattern of the multilayer TBC, which confirms that the YAG:Tm top layer must be thin. It was found to be around 4-6 μm thick and, as observed in the SEM micrograph in **Figure 110**, the YAG layer deposited in the second run nucleated and grew from the YSZ column tips hence maintaining the columnar microstructure of the coating.
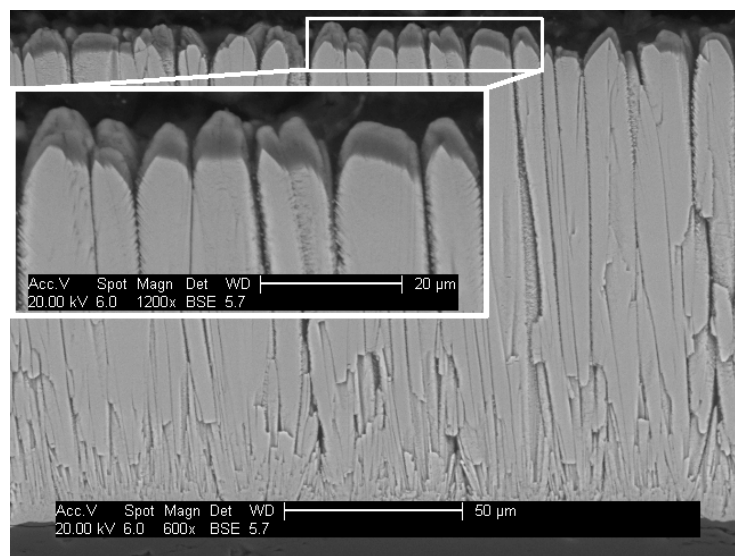
Figure 110: SEM micrograph of the multilayer sensing TBC.

6.4.2. Phosphorescence

The multilayer sensing EB-PVD TBC was isothermally tested in a furnace in order to obtain the luminescence calibration curves of YSZ:Dy and YAG:Tm. For both phosphors the data were recorded during the same experiment using 355nm excitation (**Figure 111**) and switching from the YAG:Tm to the YSZ:Dy emission wavelengths, using the wavelength drive on the spectrometer (**Figure 38 – page 97**). The results, **Figure 111**, show that the inner YSZ:Dy phosphorescent layer has a temperature

sensitivity ranging from about 400°C to 950°C and the YAG:Tm top layer from 1000°C to 1300°C. As highlighted in **Chapter 5.3**, the YSZ:Dy phosphor has an emission line at 458 nm which can also be used for temperature measurements (**Figure 52**). This luminescence peak overlaps with the 455 nm emission of the YAG:Tm phosphor hence the irregular shape of the calibration curve between 400°C and 950°C). However, the decay of the YSZ:Dy 458nm line is very fast at 900°C, and quenches at about 950°C, therefore will not affect the surface temperature measurements at higher temperatures.
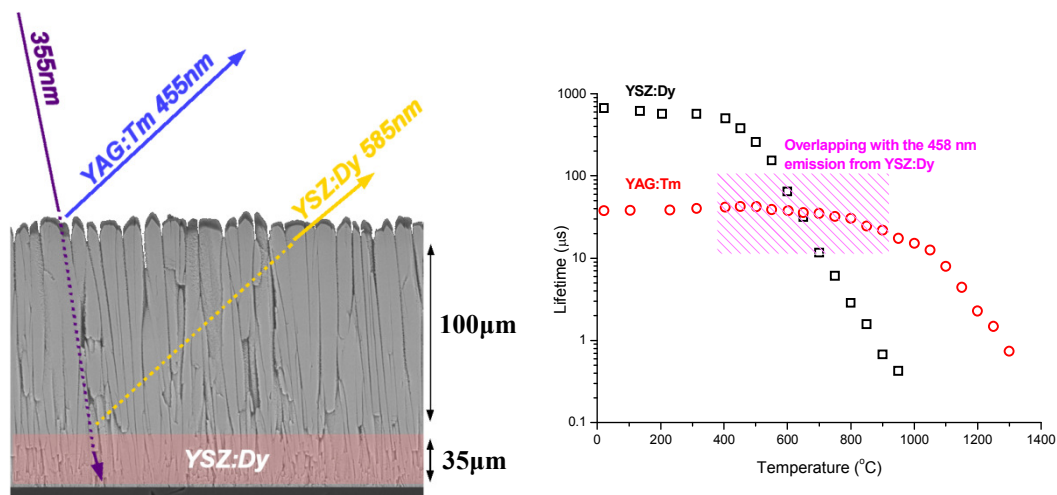
Figure 111: Calibration curves of YSZ:Dy2% and YAG:Tm phosphors and SEM micrograph of the multilayer sensing TBC with the excitation and emission wavelengths.

In **Figure 112**, the lifetime data obtained for the multilayer coating is compared with the calibration curve of the YSZ:Dy2% single layer TBC (**Figure 41**) and the YAG:Tm results found by *Allison et al.* [138] at *Oak Ridge National Laboratory*. First of all, it was found that the lifetime decay measurements using the YSZ:Dy phosphor were not affected by the YAG:Tm top layer and above 400°C both calibration curves are identical. At lower temperatures, the layered coating has slightly longer lifetimes due to the "*saturation effect*" as shown in **Figure 60** (**Page 124**). Secondly, the lifetime measurements of the YAG:Tm phosphor made at *STS*, and deposited in this work as an

EB-PVD topcoat, are in very good agreement with those found at *Oak Ridge National Laboratory*. This confirms that a YAG:Tm top layer was successfully deposited by EB-PVD evaporation from a customised ingot. Moreover, **Figure 112** shows that, by using a detector with a higher sensitivity (0.1 μs), the YAG:Tm phosphor could potentially be used to measure temperatures up to 1400°C.
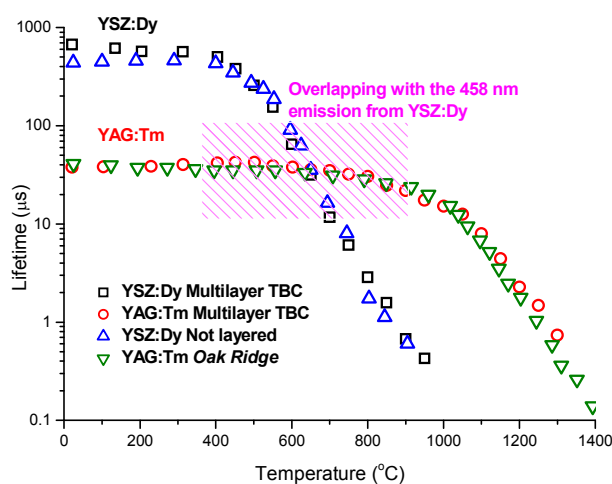
Figure 112: Comparison of the calibration curves obtained with the multilayer coating and the results found at *Oak Ridge National laboratory* [138].

6.4.3. High temperature aging

The multilayer sample was heat treated for 1000 hours at 1200°C and analysed with XRD and EDX in order to determine the high temperature stability of the TBC and, more particularly, how each layer would behave when aged for a long period of time. The top surface of the heat treated samples were impregnated with transparent epoxy resin (cured for two hours at 100°C) prior to sample preparation, in order to prevent any damage to the thin YAG:Tm top layer during the cutting and mounting process. The SEM micrographs are presented in **Figure 113**. The sintering behaviour of the multilayer coating is comparable to that for a standard TBC (**Figure 13 – page 31**). The

top 30 μm of the coating, aged 300 hours at 1200°C, are bent to the left which is probably due to the resin impregnation rather than the heat treatment.

As Deposited   **Aged 300h at 1200°C**

Aged 1000h at 1200°C
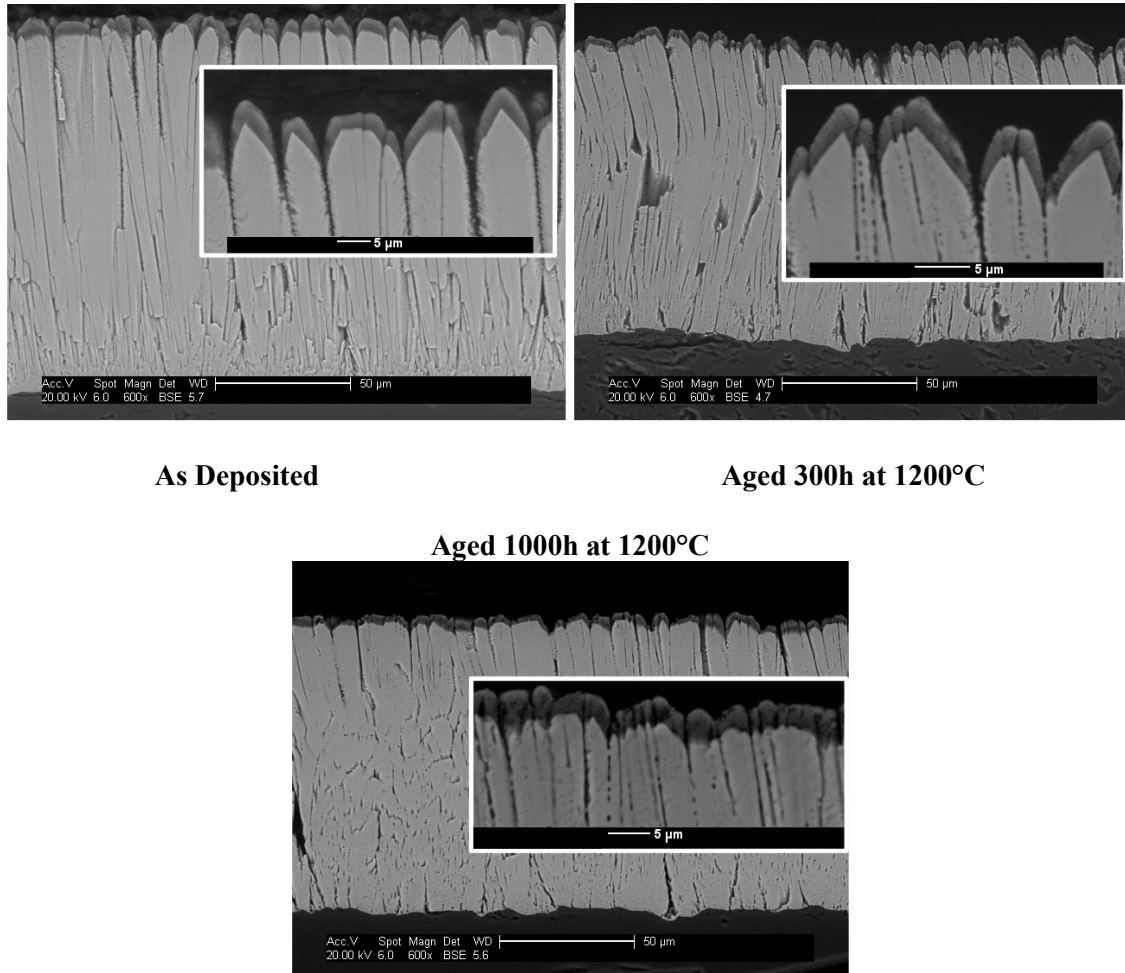
Figure 113: Cross section micrographs of the multilayer sensing TBC, as deposited and after aging.

6.4.3.1. YAG:Tm layer

As shown in **Figure 109**, the as deposited top layer recrystallised when heat treated for three hours at 1100°C. After 300 hours at 1200°C the XRD peaks corresponding to the YAG phase become sharper and have a higher intensity (**Figure 114**). Moreover, the XRD pattern shows that the coating contains alumina. It is believed that the YAG phase in the coating aged three hours at 1100°C was not completely crystalline and the

YAG:Tm layer did not reach its equilibrium phase composition. More importantly, longer heat treatments do not seem to cause any phase transformations in the top layer. The YAG and alumina phases are still in equilibrium after 1000 hours at 1200°C and the corresponding XRD peaks have the same positions and intensities.
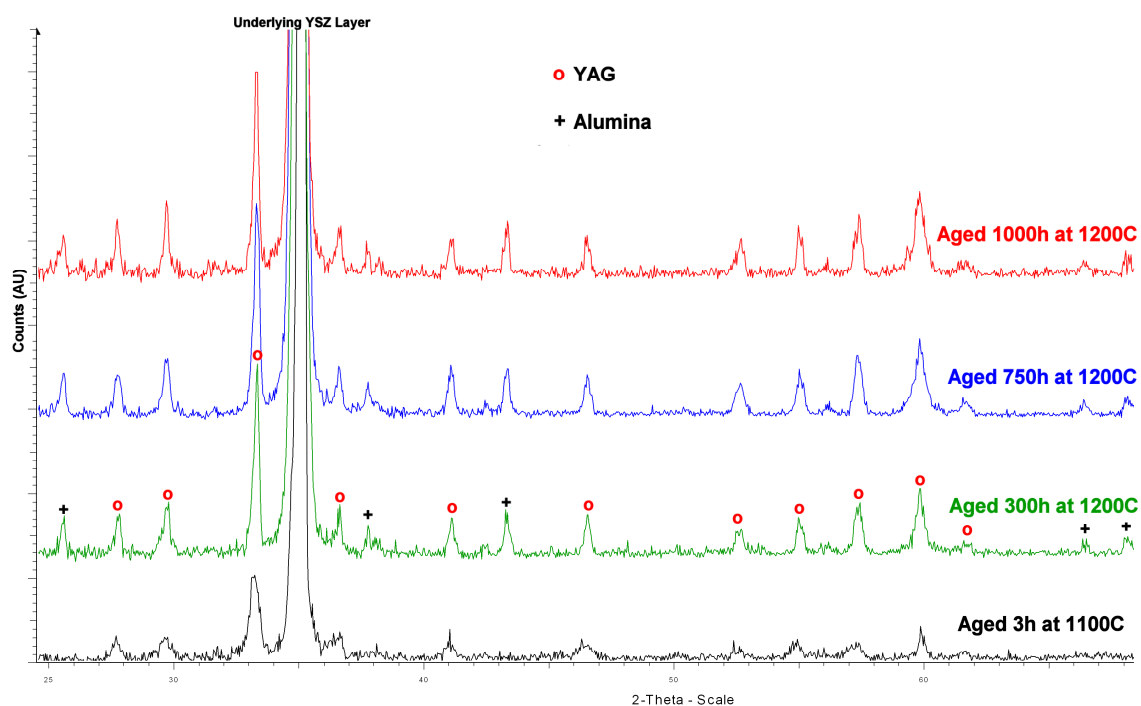
Figure 114: XRD spectra of the multilayer coating aged 3h at 1100°C and 300h, 750h and 1000h at 1200°C.

The intensity and the width of the XRD peaks of the YAG phase do not change significantly after a heat treatment of 1000 hours at 1200°C. Moreover, the relative intensity of the alumina, YSZ and YAG diffraction peaks remains constant between 300 and 1000 hours at 1200°C which suggests a good stability of the various phases present in the multilayer coating.

As shown in the EDX maps in **Figure 115**, there is no significant diffusion of zirconia into the YAG:Tm layer or alumina into the rest of the coating. The EDX analysis also

revealed that the yttria concentration under the YAG:Tm layer remained constant after aging. Moreover, the XRD spectra presented in **Figure 116** showed that the underlying *t'* YSZ still separates into the low yttria *t* phase and the high yttria *c* phase during heat treatment. After 1000 hours at 1200°C the phase composition was found to be 50% *t*, 35% *c* and 15% *t'*. Therefore, it is believed that there was no significant diffusion of yttria from the YAG:Tm layer, which could have further stabilised the underlying *t'* YSZ phase.
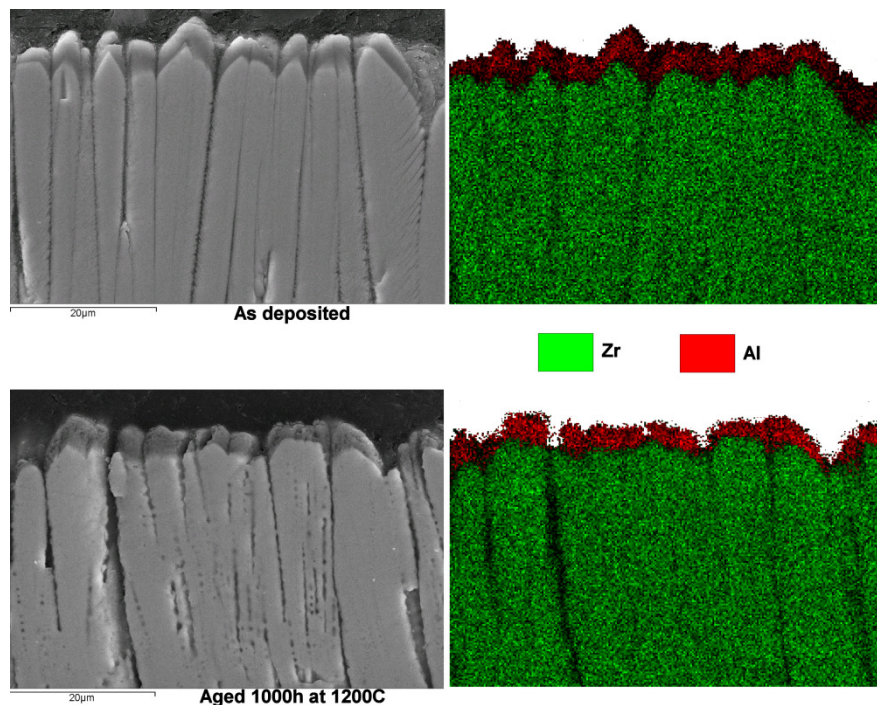
Figure 115: EDX maps of the as deposited multilayer TBC and after aging 1000h at 1200°C.

Because alumina has a higher vapour pressure, compared to yttria, it evaporates faster therefore the very first microns of the YAG:Tm layer should be almost pure alumina. Consequently it is believed that this thin alumina layer acts as a diffusion barrier preventing any diffusion of elements from one layer to another hence the remarkable phase stability.
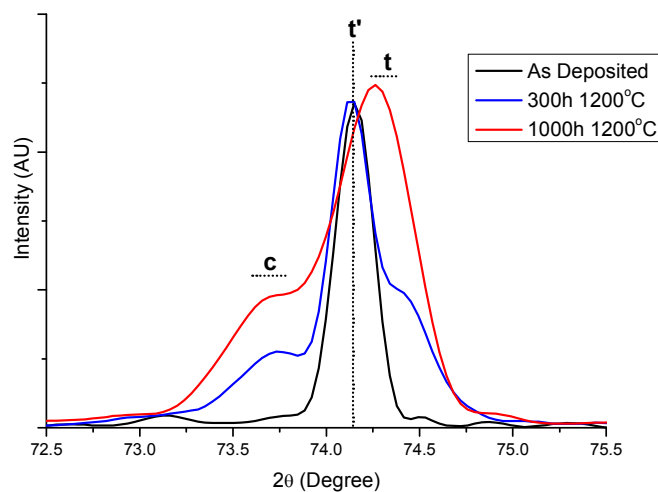
Figure 116: XRD graphs of the YSZ layer (under the YAG:Tm layer) before and after heat treatment.

6.4.3.2. YSZ:Dy layer

The thickness of the YSZ:Dy layer was analysed by EDX in order to determine if dysprosia diffuses into the standard YSZ layer when heat treated (**Figure 117**).
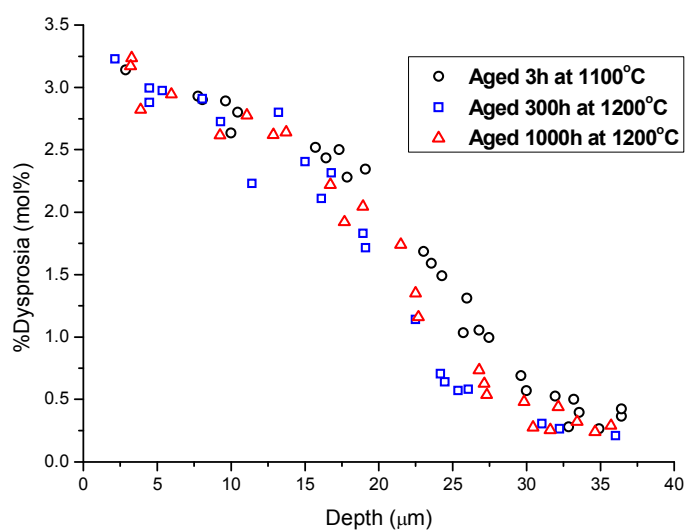
Figure 117: Diffusion of dysprosia after heat treatment.

Contrary to the results presented in **Figure 58** where there was no clear gradient of concentration, the concentration of dysprosia in the sample aged only three hours at 1200°C varies from about 3.2 mol% to 0.4 mol% over 36 μm. The highest concentrations were found at the interface with the alumina substrate. However, it seems that an equilibrium concentration gradient is reached very rapidly. Indeed longer heat treatments (up to 1000 hours at 1200°C) do not seem to further affect the composition profile through the YSZ:Dy layer. More importantly EDX results show that there is no significant diffusion of dysprosia from the YSZ:Dy to the standard YSZ layer over this extended high temperature exposure. Consequently, it seems that the depth where the temperature is measured in the coating will not vary due to high temperature exposure. Furthermore, as shown in **Section 5.1**, the variations in dysprosia concentration within the YSZ:Dy layer should not affect the temperature measurement capability.

6.5. General conclusion on multilayer sensing EB-PVD TBCs

This study successfully illustrates the concept of multilayer sensor coatings. It has been shown that YSZ:RE phosphors can be used to remotely measure the temperature inside a TBC, with YSZ:Dy offering the highest temperature sensitivity. Because of the high temperature that the top surface of the TBC experiences it is believed that YSZ:RE phosphors cannot be used to measure such temperatures. However, for industrial gas turbine where the operating temperatures are lower, these phosphors are still a viable

option. For this type of application YSZ:Dy, YSZ:Eu, YSZ:Sm and YSZ:Tm phosphors could be used in a multilayer system, as they all have a temperature sensitivity of at least 800°C. Such coatings can be easily deposited by EB-PVD using a multistage ingot.

Developing a similar coating for aero gas turbine application requires more effort in terms of phosphor materials and deposition techniques. To further extend the maximum temperature detection limit of sensing TBCs YAG:RE phosphors were investigated. This material is known to have excellent luminescence properties but it dissociates when deposited by EB-PVD, making the deposition of YAG coatings very challenging. A way that has been investigated in this work to overcome the evaporation problems consisted in changing the stoichiometry of the ingot. This technique was only used to demonstrate that temperatures could be measured at two different depths in the coating, simultaneously, using phosphorescence, in the temperature ranges that a TBC would experience during service. The melting and the evaporation of the rods manufactured for this study were not perfectly stable. Consequently, it was difficult to control the evaporation rates and therefore the coating thickness and composition. Moreover, such an ingot cannot be evaporated continuously as the molten pool becomes rapidly saturated with yttria. An alternative would be to use a multisource evaporator with a "jumping" electron beam like the one recently acquired at *Cranfield University* in the *National High Temperature Surface Engineering Centre* (**Figure 118**), where three different ingots can be evaporated. With such deposition equipment an alumina and an yttria rod can be evaporated at different rates using the appropriate beam pattern in order to achieve the desired YAG stoichiometry.

It is not believed that multilayer EB-PVD sensing TBCs will be used in service for online monitoring, as the costs involved in the development and the deposition of such coatings are too high. However, it is seen as a very promising development tool in order to optimise current TBC systems. Sensing coatings would enable one to determine very accurately the temperatures that a TBC experiences during service at different depths in the coating. This would in turn provide useful data for a better understanding of the TBC failure mechanisms, cooling optimisation and therefore the ability to use TBCs at their full potential. Sensing coatings offer many advantages over the techniques currently used to determine TBCs temperature in service. Mainly, it is fast, non intrusive and the temperature readings are not limited to pre-installed points, nor to the top surface of the TBC.
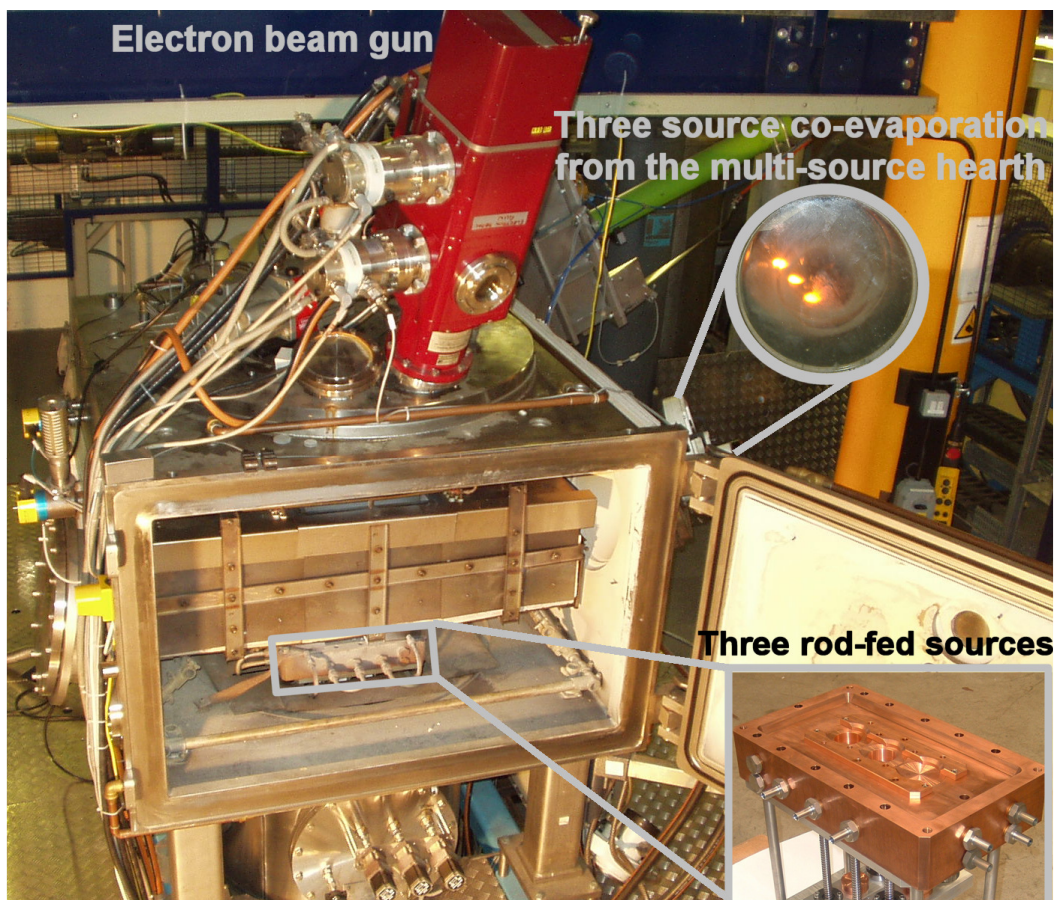
Figure 118: Multi-source EB-PVD evaporator.

Reliable temperature detection in an operating gas turbine has not yet been achieved therefore, due to uncertainties in current temperature measurement systems [88], engines are not run at their maximum potential for safety reasons. Current safety margins are believed to be as high as 200°C giving great potential for an increase in operating temperatures [208]. Sensing TBCs could be used to reduce the safety margins by 50°C or even more and a rule of thumb says a 50°C increase in firing temperature corresponds to 1% efficiency gain [209] which is considerable considering the size of the market. For example, *GE* claimed that a 1% improvement in engine efficiency can save $20 million in fuel over the life of a typical, gas-fired, 400-500 MWatt combined-cycle plant [210], not mentioning the environmental benefits due to the reduction of NO_X and CO_2 emissions.

Finally it was found that the luminescence of YSZ:Dy phosphor is sensitive to phase transformations and can be used to quantitatively determine the extent of monoclinic phase formation in the TBC. Such a technique can be easily implemented in order to monitor the TBC degradation due to high temperature exposure, as it only involves co-doping standard YSZ material with dysprosia. It has been shown that such compositions are easily deposited by EB-PVD, do not deteriorate the high temperature phase stability of the coating and it has already been shown in the literature that dysprosia additions can further reduce the thermal conductivity of the EB-PVD thermal barrier coating [166].

CONCLUSIONS

- YSZ based phosphors, for example YSZ co-doped with europium or dysprosium oxide, present no problem to be deposited by EB-PVD. YSZ:Dy, YSZ:Eu and YSZ:Gd coatings were successfully deposited by EB-PVD in this study.

- Ternary additions of dysprosia, europia and gadolinia change the crystallography of the coating and tend to produce a TBC with a more "cubic like" microstructure. It was also found that doped coatings have finer, closely packed, columns.

- The importance of substrate purity on the phase stability of the coating was highlighted. Impurities such as silica, magnesia or calcia can diffuse from the substrate into the TBC and cause the early formation of the monoclinic phase. These compounds also affect the sintering behaviour of the coating and give rise

to liquid phase sintering, leading to a rapid loss of the TBC columnar microstructure.

- Ternary addition of dysprosia further stabilises the *t'* YSZ phase, hence, limiting the formation of the monoclinic phase, compared to a standard 7YSZ TBC.

- Phosphorescence measurement showed that YSZ:Dy, YSZ:Eu and YSZ:Gd phosphors can be used to measure temperatures up to 950°C, 800°C and 250°C respectively. It was noted that these temperature sensitivities could be further improved by using a detection system with a higher sensitivity and a better fitting routine. With such improved instrumentation, YSZ:Dy phosphor could be used to measure temperatures up to at least 1100°C.

- YSZ:Dy was found to be a good phosphor to be used as an inner layer in a TBC in order to measure the temperature at the TGO/ceramic interface.

- For sensing purposes, low concentrations of dysprosia are preferred as they give higher luminescence intensities. However, the temperature measurements will not be affected when the concentration of dysprosia ranges from 0.3 to 2 mol%.

- Temperature measurements are insensitive to high temperature aging and the associated phase transformations that could occur during service.

- Different emission lines from the YSZ:Dy phosphorescence spectrum can be used for temperature measurements.

- A multilayer EB-PVD TBC, comprising a YSZ:Dy inner layer was successfully deposited and tested. There was no problem to excite and detect the inner layer phosphorescence through a 100μm thick YSZ layer.

- The formation of the monoclinic phase during aging results in the appearance of new YSZ:Dy luminescence peaks. The intensity of those lines varies with the percentage of monoclinic phase in the coating.

- The lifetime of the YSZ:Dy phosphorescence at room temperature is also sensitive to the formation of the monoclinic phase in the TBC.

- Both techniques can be used to quantitatively determine the percentage of the monoclinic phase in the coating providing a non-destructive way of assessing the degradation of the TBC due to high temperature exposure.

- YSZ:RE phosphors were found unsuitable to measure the surface temperature of the TBC, because of their limited sensitivity above 1100°C. Other compositions such as YAG-based phosphors were investigated for that purpose.

- Due to the difference in vapour pressure between alumina and yttria a pure YAG coating cannot be deposited using single source EB-PVD evaporation.

- EB-PVD rods were successfully manufactured from yttria/alumina and yttria/YAG powders and evaporated, but produced gradient structures.

- A luminescent YAG:Dy/alumina coating was deposited by increasing the yttria concentration in the rod material. Such a coating has a temperature sensitivity of at least 1500°C, potentially 1700°C.

- A multilayer phosphorescent TBC comprising an outer YAG:Tm and an inner YSZ:Dy layer was deposited by EB-PVD. The coating was successfully tested and showed that temperature measurements could be performed at two different depths in the TBC with such system.

- The YAG:Tm layer had a temperature sensitivity of at least 1300°C and the luminescence of YSZ:Dy was not affected by the YAG top layer.

- The high temperature stability of the multilayer sensing TBC was investigated. It showed that there was no significant diffusion of elements between the various layers and that the YAG phase remained stable, even when heat treated up to 1000 hours at 1200°C.

FUTURE WORK

The following recommendations for further work are suggested:

- The determination of the minimum dysprosia concentration in YSZ for thermometry applications.

- The determination of the minimum thickness of the inner phosphorescent layer that could be deposited and used for precise temperature measurements.

- Customise the fitting routine for each YSZ:RE phosphors in order to further improve their temperature sensitivity.

- Improve the YAG deposition by EB-PVD for a better control of the coating thickness and composition.

- Deposition of a YAG coating using a multi source EB-PVD evaporation.

- Determine the phase stability of the YAG top layer at higher temperatures (typically at around 1500°C).

- Perform erosion testing of the multilayer sensing coating in order to determine if a layered structure significantly affects the erosion mechanisms of the TBC and to determine the erosion resistance of the YAG top layer.

- Investigate alternative phosphors with different matrixes which could be used for TBC applications at ultra high temperatures or in severe combustion environments.

APPENDIXES

Appendix 1: Drawing used to machine the multistage rod.

Machined from
the 7YSZ rod
9

Machined from
the YSZ:Dy2%
rod
14

10

2

Machined from
the 7YSZ rod
70

14
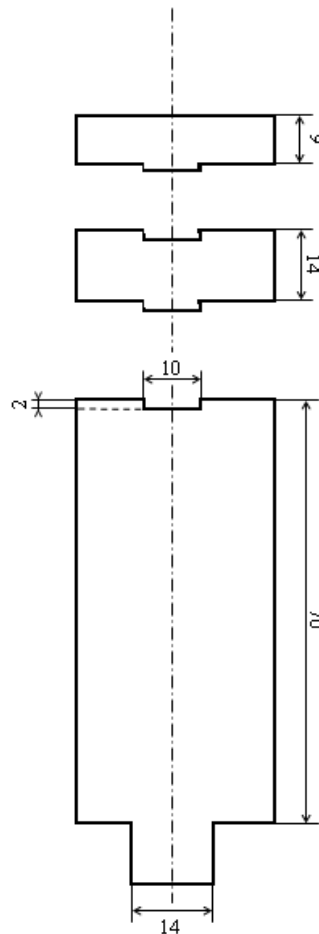
Appendix 2: Drawing used to machine the composite rod for the YSZ 4.9 mol% TBC deposition.

CROSS SECTION   TOP VIEW

17.18

33.3

65

70

65

Ø 17.18

Ø 33.3

14

14
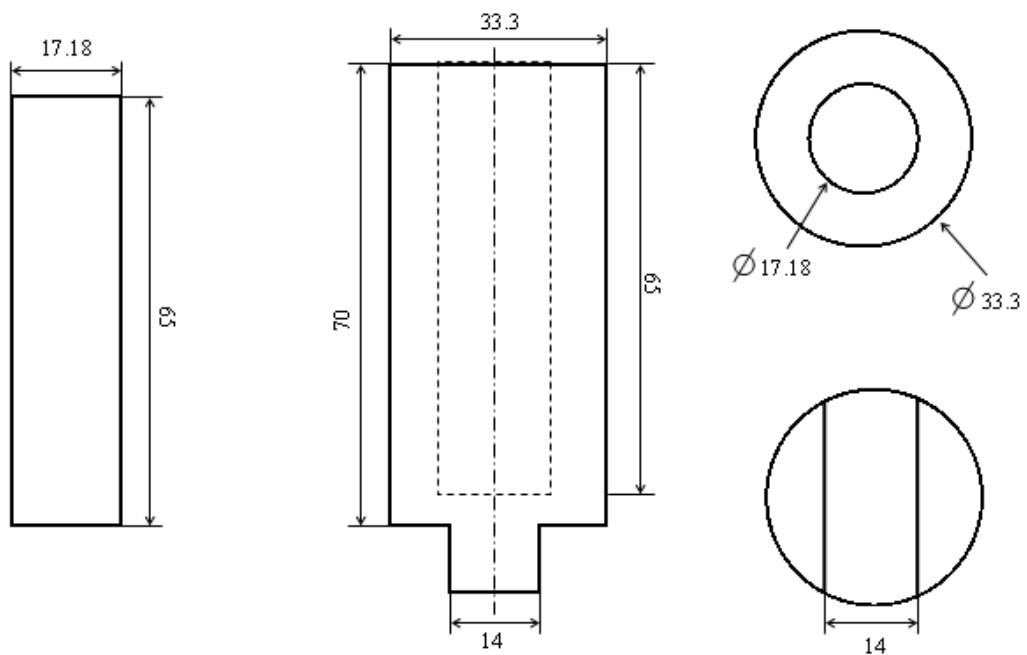
Machined from the
zirconia + 20wt.% yttria rod

Machined from the
zirconia + 7wt.% yttria rod

REFERENCE LIST

[1]   J. R. Nicholls (2003), 'Advances in coating design for high performance gas turbines', *MRS Bulletin,* pp. 659-670.

[2]   U. Schulz, C. Leyens, K. Fritscher, M. Peters, B. Saruhan-Brings, O. Lavigne, J. Dorvaux, M. Poulain, R. Mévrel and M. Caliez (2003), 'Some recent trends in research and technology of advanced thermal barrier coatings', *Aerospace science and technology,* pp. 73-80.

[3]   S. Alperine, V. Arnault, O. Lavigne and R. Mevrel (inventors) (2001), *Heat barrier composition, a mechanical superalloy article provided with a ceramic coating having such a composition, and a method of making the ceramic coating*. US Patent n° 6333118.

[4]   M. Konter and M. Thumann (2001), 'Materials and manufacturing of advanced industrial gas turbine components', *Materials processing technology,* Vol. 117, pp. 386-390.

[5]   M. Cervenka (2000), *The Rolls-Royce Trent Engine,* available at: http://www.msm.cam.ac.uk/phase-trans/mphil/Trent1/sld001.htm   (accessed 2007).

[6]   R. A. Miller (1997), 'Thermal barrier coatings for aircraft engines: History and directions', *Journal of thermal spray technology,* Vol. 6(1), pp. 35-42.

[7]   G. W. Goward (1998), 'Progress in coatings for gas turbine airfoils', *Surface and coatings technology,* Vol. 108-109, pp. 73-79.

[8]   M. Peters, C. Leyens, U. Schulz and W. A. Kaysser (2001), 'EB-PVD thermal barrier coatings for aeroengines and gas turbines', *Advanced engineering materials,* Vol. 4, pp. 193-204.

[9]   R. A. Miller (1987), 'Current status of thermal barrier coatings - An overview', *Surface and coatings technology,* Vol. 30, pp. 1-11.

[10]   J. R. Brandon and R. Taylor (1991), ' Phase stability of zirconia-based thermal barrier coatings Part I. Zirconia-yttria alloys', *Surface and coatings technology,* Vol. 46, pp. 75-90.

[11]   V. Lughi, V. K. Tolpygo and D. R. Clarke (2004), 'Microstructural aspects of the sintering of thermal barrier coatings', *Materials science and engineering,* Vol. A368, pp. 212-221.

[12]   U. Schulz (2000), 'Phase transformation in EB-PVD yttria partially stabilized zirconia thermal barrier coatings during annealing', *Journal of the American Ceramic Society,* Vol. 83(4), pp. 904-910.

[13]   N. R. Rebollo, O. Fabrichnaya and C. Levi (2003), 'Phase stability of Y+Gd co-doped zirconia', *Zeitschrift fur metallkunde,* Vol. 94, No. 3, pp. 163-170.

[14]   C. G. Levi (2004), 'Emerging materials and processes for thermal barrier systems', *Current opinion in solid state and materials science,* Vol. 8, No. 1, pp. 77-91.

[15]   I. T. Spitsberg, D. R. Mumm and A. G. Evans (2005), 'On the failure mechanisms of thermal barrier coatings with diffusion aluminide bond coats', *Materials science and engineering A,* Vol. 394, No. 1-2, pp. 176-191.

[16]   M. J. Pomeroy (2005), 'Coatings for gas turbine materials and long term stability', *Materials and design,* Vol. 26, pp. 223-231.

[17]   C. R. C. Lima and J. M. Guilemany (2007), 'Adhesion improvements of

Thermal Barrier Coatings with HVOF thermally sprayed bond coats', *Surface and Coatings Technology,* Vol. 201, pp. 4694-4701.

[18] U. Schulz and M. Schmucker (2000), 'Microstructure of ZrO_2 thermal barrier coatings applied by EB-PVD', *Materials science and engineering,* pp. 1-8.

[19] O. Unal, T. E. Mitchell and A. H. Heuer (1994), 'Microstructure of Y_2O_3-stabilized ZrO_2 EB-PVD coatings on Ni-base superalloys', *Journal of the American Ceramic Society,* Vol. 77, pp. 984-92.

[20] U. Schultz, B. Saruhan, K. Fritscher and C. Leyens (2004), 'Review on advanced EB-PVD ceramic topcoats for TBC applications', *International journal of applied ceramic technology,* Vol. 1, No. 4, pp. 302-315.

[21] B. D. Kernan, A. He and A. H. Heuer (2003), 'Microstructural evolution and microhardness in zirconia-based EB-PVD TBC', *Journal of the American Ceramic Society,* Vol. 86, pp. 959-968.

[22] B. A. Movchan and A. V. Demchishin (1969), 'Investigations of the structure and properties of thick Ni, Ti, W, Al_2O_3 and ZrO_2 vacuum condensates', *Fizika Metalov i Metalovedenije,* Vol. 28, No. 4, pp. 653.

[23] J. A. Thornton (1977), 'High Rate Thick Film Growth', *Annual Review of Materials Science,* Vol. 7, pp. 239.

[24] Y. H. Sohn, R. R. Biederman and R. D. Sisson Jr (1994), 'Microstructural development in physical vapour-deposited partially stabilized zirconia thermal barrier coatings', *Thin solid films,* Vol. 250, pp. 1-7.

[25] J. S. Bernier, G. Levan, Md. Maniruzzaman, R. D. Sisson Jr and S. Bose (2003), 'Crystallographic texture of EB-PVD TBCs deposited on stationary flat surfaces in a multiple ingot coating chamber as a function of chamber position', *Surface and coatings technology,* Vol. 163-164, pp. 95-99.

[26] U. Schulz, S. G. Terry and C. G. Levi (2003), 'Microstructure and texture of EB-PVD TBCs grown under different rotation modes', *Materials science and engineering,* Vol. A360, pp. 319-329.

[27] K. Wada, M. Yoshiya, N. Yamaguchi and H. Matsubara (Article in press), 'Texture and microstructure of ZrO_2-4mol% Y_2O_3 layers obliquely deposited by EB-PVD', *Surface and coatings technology.*

[28]   K. Wada, N. Yamaguchi and H. Matsubara (2005), 'Effect of substrate rotation on texture evolution in ZrO$_2$-4mol% Y$_2$O$_3$ layers fabricated by EB-PVD', *Surface and coatings technology,* Vol. 191, pp. 367-374.

[29]   U. Schulz, K. Fritscher, C. Leyens, M. Peters and W. A. Kaysser (1997), 'Thermocyclic behavior of differently stabilized and structured EB-PVD TBCs', *Materialwissenschaften und Werkstofftechnik,* Vol. 28, pp. 370-376.

[30]   K. Wada, N. Yamaguchi and H. Matsubara (2004), 'Crystallographic texture evolution in ZrO$_2$-Y$_2$O$_3$ layers produced by electron beam physical vapor deposition', *Surface and coatings technology,* Vol. 184, pp. 55-62.

[31]   J. R. Nicholls, K.J. Lawson, A. Johnstone and D.S Rickerby (2002), 'Methods to reduce the thermal conductivity of EB-PVD TBCs', *Surface and coatings technology,* pp. 383-391.

[32]   J. Singh and D. E. Wolfe (2002), 'Architecture of thermal barrier coatings produced by electron beam-physical vapor deposition', *Journal of materials sciences,* Vol. 37, pp. 3261-3267.

[33]   F. C. Toriz, A. B. Thakker and S. K. Gupta (1989), 'Flight service evaluation of thermal barrier coatings by physical vapor deposition at 5200H', *Surface and coatings technology,* Vol. 39/40, pp. 161-172.

[34]   J. Singh, D. E. Wolfe, and R. Miller 'Low thermal conductivity and high reflectance thermal barrier coatings by EB-PVD for high temperature applications', *Processing and fabrication of advanced materials XII,* 2003, Pittsburgh, Pennsylvania.

[35]   J. R. Nicholls, Y. Jaslier and D. S. Rickerby (1998), 'Erosion of EB-PVD thermal barrier coatings', *Materials at high temperatures,* Vol. 15(1), pp. 15-22.

[36]   J. R. Nicholls, M. J. Deakin and D. S. Rickerby (1999), 'A comparison between the erosion behaviour of thermal spray and electron beam physical vapour deposition thermal barrier coatings', *Wear,* pp. 352-361.

[37]   A. G. Davis, D. H. Boone and A. V. Levy (1986), 'Erosion of ceramic thermal barrier coatings', *Wear,* Vol. 110, pp. 101-116.

[38]   R. G. Wellman and J. R. Nicholls (2000), 'Some observations on erosion mechanisms of EB-PVD TBCs', *Wear,* pp. 89-96.

[39]   R. A. Miller (1987), 'Current status of thermal barrier coatings - An overview', *Surface and coatings technology,* Vol. 30, pp. 1-11.

[40]   A. G. Evans, D. R. Mumm, J. W. Hutchinson, G. H. Meier and F. S. Pettit (2001), 'Mechanisms controlling the durability of thermal barrier coatings', *Progress in materials science ,* Vol. 46, pp. 505-533.

[41]   V. K. Tolpygo, D. R. Clarke and K. S. Murphy (2001), 'Oxidation-induced failure of EB-PVD thermal barrier coatings', *Surface and coatings technology,* Vol. 146-147, pp. 124-131.

[42]   J. W. Hutchinson, M. Y. He and A. G. Evans (2000), 'The influence of imperfections on the nucleation and propagation of buckling driven delaminations', *Journal of the Mechanics and Physics of Solids,* Vol. 48, pp. 709-734.

[43]   M. Gell, K. Vaidyanathan, B. Barber, J. Cheng and E. Jordan (1999), 'Mechanism of spallation in platinum aluminide/electron beam physical vapor-deposited thermal barrier coatings ', *Metallurgical and materials transactions A-Physical metallurgy and materials science,* Vol. 30, No. 2, pp. 427-435.

[44]   Y. H. Sohn, J. H. Kim, E. H. Jordan and M. Gell (2001), 'Thermal cycling of EB-PVD/MCrAlY thermal barrier coatings: I. Microstructural development and spallation mechanisms', *Surface and Coatings Technology,* Vol. 146-147, pp. 70-78.

[45]   M. Gell, E. Jordan, K. Vaidyanathan, K. McCarron, B. Barber, Y-H. Sohn and V. K. Tolpygo (1999), 'Bond strength, bond stress and spallation mechanisms of thermal barrier coatings', *Surface and Coatings Technology,* Vol. 121, pp. 53-60.

[46]   M. Y. He, A. G. Evans and J. W. Hutchinson (2000), 'The ratcheting of compressed thermally grown thin films on ductile substrates', *Acta Materialia,* Vol. 48, pp. 2593-2601.

[47]   V. K. Tolpygo and D. R. Clarke (2000), 'Surface rumpling of a (Ni, Pt)Al bond coat induced by cyclic oxidation', *Acta materialia,* Vol. 48, No. 43, pp. 3283-93.

[48]   M. W. Chen, R. T. Ott, T. C. Hufnagelb, P. K. Wright and K. J. Hemkera (2003), ' Microstructural evolution of platinum modified nickel aluminide bond coat during thermal cycling', *Surface and coatings technology,* Vol. 163-164,

pp. 25-30.

[49]   X. Chen, M.Y. He, I. Spitsberg, N.A. Fleck, J.W. Hutchinson and A.G. Evans (2004), 'Mechanisms governing the high temperature erosion of thermal barrier coatings', *Wear,* Vol. 256, pp. 735-746.

[50]   X. Chen, R. Wang, N. Yao, A. G. Evans, J. W. Hutchinson and R. W. Bruce (2003), 'Foreign object damage in a thermal barrier system: mechanisms and simulations', *Materials Sciences and Engineering,* Vol. A352, pp. 221-231.

[51]   R. G. Wellman and J. R. Nicholls 'Observed Damage Mechanisms In The Erosion And FOD Of EB-PVD TBCs', *Submitted to wear,*

[52]   W. Tabakoff (1989), 'Investigation of coatings at high temperature for use in turbomachinery', *Surface and coatings technology,* Vol. 39/40, pp. 97-115.

[53]   R. G. Wellman and J. R. Nicholls (2004), 'On the effect of ageing on the erosion of EB-PVD TBCs', *Surface and coatings technology,* pp. 80-88.

[54]   R. A. Miller, W. J. Brindley, J. G. Goedjen, R. Tiwari, and D. Mess 'The effect of silica on the cyclic life of a zirconia-yttria thermal barrier coating', *7th National Thermal Spray Conference,* 1994, Boston, Massachusetts, pp. 49-54.

[55]   J. G. Goedjen, W. J. Brindley, and R. A. Miller 'Sintering of plasma-sprayed sol gel zirconia-yttria as a function of silica content', *The 8th National Thermal Spray Conference,* 1995, Houston, Texas, pp. 73-77.

[56]   Y-L. Lin, P. Angelini and M. L. Mecartney (1990), 'Microstructural and chemical influences of silicate grain-boundary phases in yttria-stabilized zirconia', *Journal of the American Ceramic Society,* Vol. 73, No. 9, pp. 2728-35.

[57]   J. L. Smialek, F. A. Archer and R. G. Garlick (1994), 'Turbine airfoil degradation in the Persian Gulf War', *Journal of Metals,* Vol. 46, No. 12, pp. 39-41.

[58]   J. L. Smialek, F. A. Archer, and R. G. Garlick 'The chemistry of Saudi Arabian sand: a deposition problem on helicopter turbine airfoils', *3rd International SAMPE Metals Conference,* 1992, Toronto, Canada, Vol. 3. pp. M63-M77.

[59] F. H. Stott, D. J. de Wet, and R. Taylor 'The effects of molten silicate deposits on the stability of thermal barrier coatings for turbine applications at very high temperatures', *3rd International SAMPE Metals Conference,* 1992, Toronto, Canada, pp. M92-M101.

[60] S. Kraemer, J. Yang and C. G. Levi (2006), 'Thermochemical interaction of thermal barrier coatings with molten $CaO-MgO-Al_2O_3-SiO_2$ (CMAS) deposits', *Journal of the American Ceramic Society,* Vol. 89, No. 10, pp. 3167-3175.

[61] X. Chen (2006), 'Calcium-magnesium-alumina-silicate (CMAS) delamination mechanisms in EB-PVD thermal barrier coatings', *Surface and Coatings Technology,* Vol. 200, pp. 3418-3427.

[62] C. Mercer, S. Faulhaber, A. G. Evans and R. Darolia (2005), 'A delamination mechanism for thermal barrier coatings subject to calcium-magnesium-alumino-silicate (CMAS) infiltration ', *Acta materialia,* Vol. 53, pp. 1029-1039.

[63] P. S. Anderson, X. Wang and P. Xiao (2005), 'Effect of isothermal heat treatment on plasma-sprayed yttria-stabilized zirconia studied by impedance spectroscopy', *Journal of the American Ceramic Society,* Vol. 88, No. 2, pp. 324-330.

[64] A. N. Khan, J. Lu and H. Liao (2003), 'Heat treatment of thermal barrier coatings', *Materials and engineering,* Vol. A359, pp. 129-136.

[65] R. L. Jones and D. Mess (1996), 'Improved tetragonal phase stability at 1400°C with scandia yttria-stabilized zirconia', *Surface and coatings technology,* Vol. 86-87, pp. 94-101.

[66] R. W. Trice, Y. J. Su and al (2002), 'Effect of heat treatment on phase stability, microstructure, and thermal conductivity of plasma-sprayed YSZ', *Journal of materials science,* Vol. 37, pp. 2359-2365.

[67] M. Leoni, R. L. Jones and P. Scardi (1998), 'Phase stability of scandia-yttria-stabilized zirconia TBCs', *Surface and coatings technology,* Vol. 108-109, pp. 107-113.

[68] V. Lughi and D. R. Clarke (2005), 'Transformation of Electron-Beam Physical Vapor-Deposited 8 wt% Yttria-Stabilized Thermal Barrier Coatings', *Journal of the American Ceramic Society,* Vol. 88, No. 9, pp. 2552-2558.

[69]   U. Schultz, K. Fritscher, C. Leyens and M. Peters (2001), 'High temperature aging of EB-PVD thermal barrier coatings', *Ceramic engineering and science proceedings,* Vol. 22, No. 4, pp. 347-355.

[70]   M. Matsumoto, K. Aoyama, H. Matsubara, K. Takayama, T. Banno, Y. Kagiya and Y. Sugita (2005), 'Thermal conductivity and phase stability of plasma sprayed ZrO_2-Y_2O_3-La_2O_3 coatings', *Surface and coatings technology,* Vol. 194, pp. 31-35.

[71]   A. Azzopardi, R. Mévrel, B. Saint-Raymond, E. Olson and K. Stiller (2004), 'Influence of aging on structure and thermal conductivity of Y-PSZ and Y-FSZ EB-PVD coatings', *Surface and coatings technology,* Vol. 177-178, pp. 131-139.

[72]   K. Fritscher, F. Szucs, U. Schultz and B. Saruhan (2002), 'Impact of thermal exposure of EB-PVD TBCs on Young's modulus and sintering', *Ceramic engineering and science proceedings,* Vol. 23, No. 4, pp. 341-352.

[73]   R. G. Wellman, J. R. Nicholls and A. Dyer   (2004),   'Nano and micro indentation studies of bulk zirconia and EB PVD TBCs', *Surface and coatings technology,* pp. 253-260.

[74]   R. G. Wellman, H. Tourmente, S. Impey and J. R. Nicholls (2004), 'Nano and micro hardness testing of aged EB-PVD TBCs', *Surface and coatings technology,* Vol. 188-189, pp. 79-84.

[75]   P. G. Klemens and M. Gell (1998), 'Thermal conductivity of thermal barrier coatings', *Materials science and engineering,* Vol. A245, pp. 143-149.

[76]   J. R. Nicholls, K. J. Lawson, D. S. Rickerby, and P. Morrell. Advanced processing of TBC's for reduced thermal conductivity. AGARD Structures and materials panel. 823, 6-1/6-9. 97.

[77]   D. E. Wolfe, J. Singh, R. A. Miller, J. I. Eldridge and D. M. Zhu (2005), 'Tailored microstructure of EB-PVD 8YSZ thermal barrier coatings with low thermal conductivity and high thermal reflectivity for turbine applications', *Surface and coatings technology,* Vol. 190, No. 1, pp. 132-149.

[78]   J. R. Brandon and R. Taylor (1991), ' Phase stability of zirconia-based thermal barrier coatings Part II. Zirconia-ceria alloys', *Surface and coatings technology,* Vol. 46, pp. 91-101.

[79]   U. Schultz, K. Fritscher and C. Leyens (2000), 'Two-source jumping beam evaporation for advanced EB-PVD TBC systems', *Surface and coatings technology,* Vol. 133-134, pp. 40-48.

[80]   D. Zhu, Y. L. Chen and A. Miller (2003), 'Defect clustering and nano-phase structure characterization of multi-component rare earth oxide doped zirconia-yttria thermal barrier coatings', *Ceramic engineering and science proceedings,* Vol. 24, No. 3, pp. 525-534.

[81]   D. Zhu and R. A. Miller (2004), 'Development of advanced low conductivity thermal barrier coatings', *International journal of applied ceramic technology,* Vol. 1, No. 1, pp. 86-94.

[82]   R. J. L. Steenbakker, R. G. Wellman and J. R. Nicholls (2006), 'Erosion of gadolinia doped EB-PVD TBCs', *Surface and coatings technology,* Vol. 201, pp. 2140-2146.

[83]   H. Lehman, D. Pitzer, G. Pracht, R. Vassen and D. Stoever (2003), 'Thermal conductivity and thermal expansion coefficients of the lanthanum rare-earth zirconate system', *Journal of the American Ceramic Society,* Vol. 86, No. 8, pp. 1338-44.

[84]   Q. Xu, W. Pan, J. Wang, C. Wan, L. Qi and H. Miao (2006), 'Rare-earth zirconate ceramics with fluorite structure for thermal barrier coatings', *Journal of the American Ceramic Society,* Vol. 89, No. 1, pp. 340-342.

[85]   B. Saruhan, P. Francois, K. Fritscher and U. Schulz (2004), 'EB-PVD processing of pyrochlore-structured $La_2Zr_2O_7$-based TBCs ', *Surface and Coatings technology,* Vol. 182, pp. 175-183.

[86]   G. E. Aniolek and O. J. Gregory (1994), 'Thin film thermocouples for advanced ceramic gas turbine engines', *Surface and coatings technology,* Vol. 68/69, pp. 70-75.

[87]   G. Fralick and D. Ng 'Pyrometric gas and surface temperature measurements', *44th international gas turbine and aerospace technical congress,* 1999, Indianapolis, Indiana, pp. 11.

[88]   C. Kerr and P. Ivey (2002), 'An overview of the measurement errors associated with gas turbine aeroengine pyrometer systems.', *Measurement Science and Technology,* Vol. 13, pp. 873-881.

[89] K. W. Tobin, S. W. Allison, M. R. Cates, G. J. Capps, D. L. Beshears, M. Cyr and B. W. Noel (1990), 'High-temperature phosphor thermometry of rotating turbine blades', *AIAA journal,* Vol. 28, No. 8, pp. 1485-1490.

[90] J. Douglas, C. A. Smith, and S. J. R. Taylor 'An integrated approach to the application of high bandwidth optical pyrometry to turbine blade surface temperature mapping', *18th international congress on instrumentation in aerospace simulation facilities,* 1999, Vol. Iss. pp. 4.1-4.6.

[91] N. K. Bhardwaj, B. Glezer, K. H. Maden and S. Smilo (inventors) (1996), *Method and apparatus for producing a surface temperature map.* Patent n° 5580172.

[92] *Thermal paint technology-surface temperature measurement,* available at: www.rolls-royce.com/deutschland/en/technical/thermal.htm (accessed 2007).

[93] P. Neubert (inventor) (1937), *Device for indicating the temperature distribution of hot bodies.* Patent n° 2071471.

[94] M. J. Dyer and D. R. Crosley (1982), 'Two-dimensional imaging of OH laser-induced fluorescence in a flame', *Optics letters,* Vol. 7, No. 8, pp. 382-384.

[95] L. J. Dowell (1992), 'Fluorescence thermometry', *Applied Mechanics Reviews,* Vol. 45, No. 7, pp. 253-260.

[96] P. Baumann (1993), 'Phosphor thermography technique in hypersonic blowdown wind tunnel: feasibility study with pinpoint measurement', *La Recherche Aérospaciale,* Vol. 5, pp. 29-42.

[97] S. W. Allison and G. T. Gillies (1997), 'Remote thermometry with thermographic phosphors: instrumentation and applications', *Review of scientific instruments,* Vol. 68, No. 7, pp. 2615-2650.

[98] B. W. Noel, H. M. Borella, W. Lewis, W. D. Turley, D. L. Beshears, G. J. Capps, M. R. Cates and K. W. Tobin (1991), 'Evaluating thermographic phosphors in an operating turbine engine', *Transactions of the ASME,* Vol. 113, pp. 242-245.

[99] B. W. Noel, H. M. Borella, L. A. Franks, B. R. Marshall, S. W. Allison, W. A. Stange and M. R. Cates (1986), 'Proposed laser-induced fluorescence method for remote thermometry in turbine engines', *Journal of Propulsion,* Vol. 2, No.

6, pp. 565-568.

[100] B. W. Noel, W. D. Turley, and W. Lewis 'Non-intrusive temperature measurements on advanced turbomachinery components', *II Latin American Conference on Turbomachinery,* 1992, Guernavaca, Mexico, pp. 23.

[101] J. E. Goodwin, W. Sage and G. P. Tilly (1969-1970), 'Study of erosion by solid particles', *Proceedings of the Institution of Mechanical Engineers,* Vol. 184, No. 15 , pp. 279-289.

[102] L. P. Goss, A. A. Smith and M. E. Post (1989), 'Surface thermometry by laser-induced fluorescence', *Review of scientific instruments,* Vol. 60(12), pp. 3702-3706.

[103] S. Alaruri, D. McFarland, A. Brewington, M. Thomas and N. Sallee (1995), 'Development of fiber-optic probe for thermographic phosphor measurements in turbine engines', *Optics and lasers in engineering,* Vol. 22, pp. 17-31.

[104] S. Alaruri, T. Bonsett, A. Brewington, E. McPheeters and M. Wilson (1999), 'Mapping the surface temperature of ceramic and superalloy turbine engine components using laser-induced fluorescence of thermographic phosphor', *Optics and lasers in engineering,* Vol. 31, pp. 345-351.

[105] S. D. Alaruri, A. J. Brewington, M. A. Thomas and J. A. Miller (1993), 'High-temperature remote thermometry using laser-induced fluorescence decay lifetime measurements of Y_2O_3:EU and YAG:Tb thermographic phosphors', *Transactions on instrumentation and measurement,* Vol. 42, No. 3, pp. 735-739.

[106] S. W. Allison, G. T. Gillies, A. J. Rondinone and M. R. Cates (2003), 'Nanoscale thermometry via the fluorescence of YAG:Ce phosphor particles: measurements from 7 to 77^oC', *Nanotechnology,* Vol. 14, pp. 859-863.

[107] S. W. Allison, D. L. Beshears, M. R. Cates, S. M. Goedeke, W. A. Hollerman, R. F. Guidry, F. N. Womack, N. P. Bergeron, T. J. Bensic, C. R. Mercer, and J. I. Eldridge 'Advances in high temperature phosphor thermometry for aerospace applications', *39th AIAA/ASME/SAE/ASEE joint propulsion conference and exhibit,* 2003, Huntsville, Alabama, Vol. AIAA-2003-4585.

[108] S. W. Allison, L. A. Boatner and G. T. Gillies (1995), 'Characterization of high-temperature thermographic phosphors: spectral properties of $LuPO_4$:Dy(1%),Eu(2%)', *Applied optics,* Vol. 34, No. 25, pp. 5624-5627.

[109]   J. P. Feist, A. L. Heyes, and S. Seefeldt 'Thermographic phosphors for gas turbines: instrumentation development and measurement uncertainties', 2002, Lisbon, Portugal.

[110]   J. P. Feist, A. L. Heyes and J. R. Nicholls (2001), 'Phosphor thermometry in an electron beam physical vapour deposition produced thermal barrier coating doped with dysprosium', *Proceedings of Institution of Mechanical Engineers,* Vol. 215 Part G, pp. 333-340.

[111]   J. P. Feist and A. L. Heyes (2000), 'Europium-doped yttria-stabilized zirconia for high-temperature phosphor thermometry', *Proceedings of the Institution of Mechanical Engineers,* Vol. 214 Part L, pp. 7-11.

[112]   K-L. Choy, J. Mei, J. P. Feist and A. L. Heyes (2000), 'Microstructure and thermoluminescent properties of ESAVD produced Eu doped Y_2O_3-ZrO_2 coatings', *Surface engineering,* Vol. 16, No. 6, pp. 469-472.

[113]   J. P. Feist and A. L. Heyes (2000), 'The characterization of Y_2O_2S:Sm powder as a thermographic phosphor for high temperature applications', *Measurement Science and Technology,* Vol. 11, pp. 942-947.

[114]   K-L. Choy, A. L. Heyes and J. Feist (inventors) (1998), *Thermal barrier coating with thermoluminescent indicator material embedded therein.* Patent n° 6974641.

[115]   J. P. Feist, J. R. Nicholls, M. J. Fraser and A. L. Heyes (inventors) (2006), *Luminescent material compositions and structures incorporating the same.* Patent n° PCT: WO 2007/023293.

[116]   J. P. Feist (2001), *Development of phosphor thermometry for gas turbines* (Ph.D Thesis), Imperial College, University of London.

[117]   J. P. Feist, A. L. Heyes and S. Seefeldt (2003), 'Thermographic phosphor thermometry for film cooling studies in gas turbine combustors', *Proceedings of Institution of Mechanical Engineers: Part a: Journal of Power and Energy,* Vol. 217, pp. 193-200.

[118]   X. Chen, Z. Mutasim, J. Price, J. P. Feist, A. L. Heyes and S. Seefeldt (2005), 'Industrial sensor TBCs: Studies on temperature detection and durability', *International Journal of Applied Ceramic Technology,* Vol. 2, No. 5, pp. 414-421.

[119] J. P. Feist, A. L. Heyes, K. L. Choy, and B. Su 'Phosphor thermometry for high temperature gas turbine applications', *18th International Congress on Instrumentation in Aerospace Simulation Facilities,* 1999, Toulouse, France, pp. 6.1-6.7.

[120] K-L. Choy, J. P. Feist, A. L. Heyes and B. Su (1999), 'Eu-doped Y_2O_3 phosphor films produced by electrostatic-assisted chemical vapor deposition', *Journal of Materials Research,* Vol. 14, No. 7, pp. 3111-3114.

[121] M. M. Gentleman, V. Lughi, J. A. Nychka and D. R. Clarke (2006), 'Noncontact methods for measuring thermal barrier coating temperatures', *International Journal of Applied Ceramic Technology,* Vol. 3, No. 2, pp. 105-112.

[122] M. M. Gentleman, J. I. Eldridge, D. M. Zhu, K. S. Murphy and D. R. Clarke (2006), 'Non-contact sensing of TBC/BC interface temperature in a thermal gradient', *Surface and Coatings Technology,* Vol. 201, pp. 3937-3941.

[123] M. M. Gentleman and D. R. Clarke (2005), 'Luminescence sensing of temperature in pyrochlore zirconate materials for thermal barrier coatings', *Surface and Coatings Technology,* Vol. 200, pp. 1264-1269.

[124] M. M. Gentleman and D. R. Clarke (2004), 'Concepts for luminescence sensing of thermal barrier coatings', *Surface and coatings technology,* Vol. 188-189, pp. 93-100.

[125] J. I. Eldridge, J. Singh and D. E. Wolfe (2006), 'Erosion-indicating thermal barrier coating using luminescent sublayers', *Journal of the American Ceramic Society,* Vol. 89, No. 10, pp. 3252-3254.

[126] J. I. Eldridge, T. J. Bensic, W. Allison and D. Beshears (2004), 'Depth-penetrating temperature measurements of thermal barrier coatings incorporating thermographic phosphors', *Journal of thermal spray technology,* Vol. 13(1), pp. 44-50.

[127] J. I. Eldridge, T. J. Bensic, C. M. Spuckler, J. Singh and D. E. Wolfe (2006), 'Delamination-indicating thermal barrier coatings using YSZ:Eu sublayer', *Journal of the American Ceramic Society,* Vol. 89, No. 10, pp. 3246-3251.

[128] K. W. Jr. Tobin, D. L. Beshears, B. W. Noel, W. D. Turley, and W. III. Lewis 'Fiber sensor design for turbine engines', *5th Annual Fiber Optics Review Conference,* 1991, Blacksburg, USA, Proceedings of SPIE-International Society

for Optical Engineering, Vol. 1584. pp. 23-31.

[129] R. M. Ranson, C. B. Thomas and M. R. Craven (1998), 'A thin coating for phosphor thermography', *Measurement Science and Technology,* Vol. 9, pp. 1947-1950.

[130] L. Mannik, S. K. Brown and S. R. Campbell (1987), 'Phosphor-based thermometry of rotating surfaces', *Applied optics,* Vol. 26, No. 18, pp. 4014-4017.

[131] C. Bird, J. E. Mutton, R. Shepherd, M. D. W. Smith, and H. M. L. Watson 'Surface temperature measurement in turbines', *Advanced non-intrusive instrumentation for propulsion engines ,* 1997, Brussels, Belgium, AGARD conference proceedings, Vol. 598. pp. 21.4-21.10.

[132] A. C. Edge, G. Laufer and R. H. Krauss (2000), 'Surface temperature-field imaging with laser-induced thermographic phosphorescence', *Applied Optics,* Vol. 39, No. 4, pp. 546-553.

[133] J. Brübach, J. Zetterberg, A. Omrane, Z. S. Li, M. Aldén and A. Dreizler (2006), 'Determination of surface normal temperature gradients using thermographic phosphors and filtered Rayleigh scattering', *Applied Physics,* Vol. B 84, pp. 537-541.

[134] A. Omrane, F. Ossler and M. Aldén (2004), 'Temperature measurements of combustible and non-combustible surfaces using laser induced phosphorescence', *Experimental Thermal and Fluid Science ,* Vol. 28, No. 7, pp. 669-676.

[135] M. K. Chyu and D. J. Bizzak (1994), 'Surface temperature measurement using a laser-induced fluorescence thermal imaging system', *Journal of heat transfer,* Vol. 116, pp. 263-266.

[136] M. R. Cates, A. J. Sanders, and J. Newby 'Ultra high precision phosphor thermometry near 1100 K', *TEMPERATURE: Its Measurement and Control in Science and Industry; Volume VII; Eighth Temperature Symposium. AIP Conference Proceedings,* 2003, Vol. 684. pp. 1039-1044.

[137] M. D. Chambers and D. R. Clarke (2007), 'Terbium as an alternative for luminescence sensing of temperature of thermal barrier coating materials', *Surface and Coatings Technology,* Vol. 207, pp. 688-692.

[138] M. Cates and S. Allison (2002), *Phosphor thermometry tutorial,* available at: http://www.ornl.gov/sci/phosphors/Pdfs/tutorial.pdf (accessed 2007).

[139] E. Wiedemann (1888), 'Uber Flurescenz und Phosphorescenz ', *Annalen der Physik und Chemie,* Vol. 34, pp. 446-463.

[140] G. F. J. Garlick (1949), *Luminescent materials*, Oxford at the Clarendon press, Monographs on the physic and chemistry of materials.

[141] J. Becquerel and H. Kamerlingh Onnes (1908), 'The absorption spectra of the compounds of the rare earths at temperatures obtainable with liquid hydrogen and their change by the magnetic field', *Proceedings of the Academy of Amsterdam,* Vol. 10, pp. 592-603.

[142] H. A. Bethe (1929), 'Splitting of Terms in Crystals', *Annalen fur Physik,* Vol. 3, pp. 133-206.

[143] H. A. Kramers (1930), 'General theory of paramagnetic rotation in crystals', *Proceedings Koninklijke Akademie van Wetenschappen Amsterdam,* Vol. 32, pp. 959 .

[144] J. Becquerel (1929), 'Theory of magneto-optical phenomena in crystals', *Zeitschrift fur Physik,* Vol. 58, pp. 205.

[145] S. Hüfner (1978), *Optical spectra of transparent rare earth compounds*, Academic press, New York, San Francisco, London.

[146] G. Blasse (1979), 'Chemistry and physics of R-activated phosphors', *Handbook on the physics and chemistry of rare earths* (K. A. Gschneidner, Jr. and L. Eyring edition), North-Holland, Amsterdam, pp. 237-255.

[147] B. G. Wybourne (1965), *Spectroscopic properties of rare earths*, Interscience publishers, New York, London, Sydney.

[148] J-C. G. Bunzli (1989), 'Luminescent probes', in J-C. G. Bunzli and G. R. Choppin *Lanthanide Probes in Life, Chemical and Earth Sciences - Theory and Practice*, Elsevier, Amsterdam, Oxford, New York, Tokyo, pp. 219.

[149] H. N. Russell and F. A. Saunders (1925), 'New regularities in the spectra of the alkaline earths', *Ap. J.,* Vol. 61, pp. 38-69.

[150] G. H. Dieke (1968), *Spectra and energy levels of rare earth ions in crystal* (John Wiley and Sons edition)New York, London, Sydney, Toronto.

[151] J. H. Van Vleck (1937), 'The puzzle of rare earth spectra in solids', *Journal of physical chemistry,* Vol. 41, pp. 67-80.

[152] F. Seitz (1939), 'An interpretation of crystal luminescence', *Transactions of the Faraday Society,* Vol. 35, pp. 74-8.

[153] E. Condon (1926), 'A theory of intensity distribution in band systems', *Physical review,* Vol. 28, pp. 1182-1201.

[154] C. W. Struck and W. H. Fonger (1976), 'Quantum mechanical treatment of Eu^{+3} 4f^{-}> 4f and 4f charge-transfer-state transitions in $Y_2 O_2S$ and La_2O_2S', *The Journal of Chemical Physics,* Vol. 64, pp. 1784.

[155] C. W. Struck and W. H. Fonger (1970), 'Role of the charge-transfer states in feeding and thermally emptying the ^5D states of Eu^{+3} in yttrium and lanthanum oxysulfides', *Journal of Luminescence,* Vol. 1-2, pp. 456-469.

[156] M. J. Weber (1968), 'Radiative and multiphonon relaxation of rare-earth ions in Y_2O_3', *The Physical Review,* Vol. 171, No. 2, pp. 283-291.

[157] R. Orbach (1975), *Optical properties of ions in solids* (B. Di Batolo edition), Plenum Press, New York.

[158] T. Miyakawa and D.L. Dexter (1970), 'Phonon sidebands, multi-phonon relaxation of excited states, and phonon-assisted energy transfer between ions in solids', *Physical Review ,* Vol. B1, pp. 2961-2969.

[159] B. Henderson and G. F. Imbusch (1989), *Optical spectroscopy of inorganic solids*, Oxford University Press, New York.

[160] L. A. Riseberg and H. W. Moos (1968), 'Multiphonon orbit-lattice relaxation of excited states of rare-earth ions in crystals', *The Physical Review,* Vol. 174, No. 2, pp. 429-438.

[161] S. Imanaga, S. Yokono and T. Hoshima (1980), 'Luminescence saturation effects in Y_2O_2S: Eu phosphor', *Japanese Journal of Applied Physics,* Vol. 19, No. 1, pp. 41.

[162] M. J. Weber (1979), *Handbook on the physics and chemistry of rare earths* (K. A. Gschneidner, Jr. and L. Eyring edition), North-Holland, Amsterdam, pp. 275-315.

[163] P. Dorenbos (2005), 'Influence of Lanthanide Level Locations on the Performance of Phosphors', *SID Symposium Digest of Technical Papers,* Vol. 36, No. 1, pp. 1416-1419.

[164] A. M. Srivastava , A. A. Setlur, H. A. Comanzo, J. W. Devitt, J. A. Ruud and L. N. Brewer (inventors) (2001), *Apparatus for determining past-service conditions and remaining life of thermal barrier coatings and components having such coatings.* Patent n° 6730918B2.

[165] J. P. Feist and A. L. Heyes (inventors) (2003), *Coatings and an optical method for detecting corrosion process in coatings'.* GB. Patent n° 0318929.7 .

[166] J. R. Nicholls, K. J. Lawson, A. Johnstone and D. S. Rickerby (2000), 'Low thermal conductivity EB-PVD thermal barrier coatings', *Materials science forum,* Vol. 369-372, pp. 595-606.

[167] K. Amano, H. Takeda, T. Suzuki, M. Tamatani, M. Itoh and Y. Takahashi (inventors) (1987), *Thermal barrier coating.* Patent n° 4774150.

[168] Rolls-Royce (1923), *Trent 900 Facts,* available at: http://www.rolls-royce.com/media/showPR.jsp?PR_ID=40445 (accessed 2007).

[169] J. C. Wurst and J. A. Nelson (1972), 'Lineal intercept technique for measuring grain size in two-phase polycrystalline ceramics', *Journal of the American ceramic society,* pp. 109.

[170] D-J. Kim (1990), 'Effect of Ta_2O_5, Nb_2O_5, and HfO_2 alloying on the transformability of Y_2O_3-stabilized tetragonal ZrO_2', *Journal of the American Ceramic Society,* Vol. 73, No. 1, pp. 115-20.

[171] R. D. Shannon (1976), 'Revised effective ionic radii and systematic studies of interatomic distances in halides and chalcogenides', *Acta Crystallographica,* Vol. A32, pp. 751-767.

[172] M. Yoshimura, M. ashima, T. Noma and S. Somiya (1990), 'Formation of diffusionlessly transformed tetragonal phases by rapid quenching of melts in ZrO_2-$RO_{1.5}$ systems (R=rare earths)', *Journal of materials science,* Vol. 25, pp.

2011-2016.

[173]   T-S Sheu, T-Y Tien and I-W Chen   (1992),   'Cubic-to-tetragonal (t')
         transformation in zirconia-containing systems',   *Journal of the American
         Ceramic Society,* Vol. 75, No. 5, pp. 1108-16.

[174]   J. R. Vanvalzah and H. E. Eaton (1991), 'Cooling rate effects on the tetragonal
         to monoclinic phase transformation in aged plasma-sprayed yttria partially
         stabilized zirconia', *Surface and coatings technology,* Vol. 46, pp. 289-300.

[175]   M. Peng, Z. Pei, G. Hong and Q. Su   (2003), 'Study on the reduction of Eu^{3+}–
         Eu^{2+} in $Sr_4Al_{14}O_{25}$: Eu prepared in air atmosphere', *Chemical Physic Letters,*
         Vol. 371, No. 1-2, pp. 1-6.

[176]   Z. Pei and Q. Su (1993), 'The valence change from RE^{3+} to RE^{2+} (RE=Eu, Sm,
         Yb) in SrB_4O_7: RE prepared in air and the spectral properties of RE^{2+}', *Journal
         of Alloys and Compounds,* Vol. 198, No. 1-2, pp. 51-53.

[177]   A. Rouanet (1971), 'Contribution a l'etude des systemes zircone-oxides des
         lanthanides au voisinage de la fusion',   *Revue internationale des hautes
         températures et des réfractaires,* Vol. 8, No. 2, pp. 161-180.

[178]   U. Schulz, K. Fritscher and M. Peters (1996), 'EB-PVD Y_2O_3-and CeO_2/Y_2O_3-
         stabilized zirconia thermal barrier coatings - crystal habit and phase composition
         ', *Surface and Coatings Technology,* Vol. 82, pp. 259-269.

[179]   I. Spitsberg and B. A. Boutwell (inventors) (2003), *Thermal barrier coatings
         with improved impact and erosion resistance.* US. Patent n° 6869703 B1.

[180]   M.D. Chambers and D. R. Clarke   (2006),   'Effect of long term, high
         temperature aging on luminescence from Eu-doped YSZ thermal barrier
         coatings', *Surface and coatings technology,* Vol. 201, pp. 3942-46.

[181]   D. J. Robbins, B. Cockayne, J. L. Glasper and B. Lent (1979), 'The temperature
         dependence of rare-earth activated garnet phosphors',   *Journal of the
         Electrochemical Society: Solid-State Science and Technology,* Vol. 126, No. 7.

[182]   US Geological Survey (USGS) (2006), *2005 mineral year book: Zirconium and
         hafnium,* available at: http://minerals.usgs.gov/minerals/pubs (accessed 2007).

[183] US Geological Survey (USGS) (2006), *2005 mineral year book: Rare Earths,* available at: http://minerals.usgs.gov/minerals/pubs (accessed 2007).

[184] STS *Sub-surface temperature measurement in an APS TBC,* available at: www.stsscience.com/technol/subsurface-temperature.pdf (accessed 2007).

[185] H. K. Schmid (1987), 'Quantitative analysis of polymorphic mixes of zirconia by X-ray Diffraction', *Journal of the American Ceramic Society,* Vol. 70, No. 5, pp. 367-376.

[186] H. Toraya, M. Yoshimura and S. Somiya (1984), 'Quantitative analysis of monoclinic-stabilized cubic ZrO_2 systems by X-Ray diffraction', *Communications of the American Ceramic Society,* Vol. 67, No. 6, pp. C-183-184.

[187] H. Toraya, M. Yoshimura and S. Somiya (1984), 'Calibration curve for quantitative analysis of the monoclinic-tetragonal system by X-Ray diffraction', *Communications of the American Ceramic Society,* Vol. 67, No. 6, pp. C-119-121.

[188] P. A. Evans, R. Stevens and J. G. P. Binner (1984), 'Quantitative X-ray diffraction analysis of polymorphic mixes of pure zirconia', *British Ceramic Transactions Journal,* Vol. 83, pp. 39-43.

[189] B-K. Kim, J-W Hahn and K. R. Han (1997), 'Quantitative phase analysis in tetragonal-rich tetragonal/monoclinic two phase zirconia by Raman spectroscopy', *Journal of materials science letters,* Vol. 16, pp. 669-671.

[190] D. R. Clarke and F. Adar (1982), 'Measurement of the crystallographically transformed zone produced by fracture in ceramics containing tetragonal zirconia', *Journal of the American Ceramic Society,* Vol. 65, No. 6, pp. 284-288.

[191] V. Lughi and D. R. Clarke (2005), 'High temperature aging of YSZ coatings and subsequent transformation at low temperature', *Surface and coatings technology,* Vol. 200, pp. 1287-1291.

[192] M. P. Borom, C. A. Johnson and L. A. Peluso (1996), 'Role of environmental deposits and operating surface temperature in spallation of air plasma sprayed thermal barrier coatings', *Surface and coatings technology,* Vol. 86-87, pp. 116-126.

[193] K. Lesniak (1990), 'Crystal fields and dopant-ligand separations in cubic centres of rare-earth ions in fluorites', *J. Phys.: Condens. Matter,* Vol. 2, pp. 5563-5574.

[194] K. Lesniak (1991), 'Crystal field and local lattice distortions in some tetragonal symmetry centers in fluorite crystals doped with trivalent rare-earth ions', *J. Chem. Phys.,* Vol. 94, No. 5, pp. 3919-3927.

[195] R. I. Merino, V. M. Orera, O. Povill, W. Assmus and E. E. Lomonova (1997), 'Optical and electron paramagnetic resonance characterization of Dy^{3+} in YSZ single crystal', *J. Phys. Chem Solids,* Vol. 58, No. 10, pp. 1579-1585.

[196] J. L. Sommerdijk , A. C. Van Amstel and F.M.J.H. Hoex-Strik (1976), 'On the luminescence of ß-Ga_2O_3:Dy^{3+}', *Journal of Luminescence,* Vol. 11, pp. 433-436.

[197] N. P. Padture, M. Gell and P. G. Klemens (inventors) (2000), *Ceramic Materials for Thermal Barrier Coatings.* Patent n° 6015630.

[198] Y. J. Su, R. W. Trice, K. T. Faber, H. Wang and W. D. Porter (2004), 'Thermal conductivity, phase stability and oxidation resistance of $Y_3Al_5O_{12}$ (YAG)/Y_2O_3-ZrO_2 (YSZ) thermal-barrier coatings', *Oxidation of metals,* Vol. 61, No. 3/4, pp. 253-271.

[199] T-I. Mah, T. A. Parthasarathy and H. D. Lee (2004), 'Polycrystalline YAG; structural or functional', *Journal of Ceramic Processing Research,* Vol. 5, No. 4, pp. 369-379.

[200] A. Ikesue and I. Furusato (1995), 'Fabrication of polycrystalline, transparent YAG ceramics by a solid-state reaction method', *Journal of American Ceramic Society,* Vol. 78, No. 1, pp. 225-228.

[201] M. Nyman, J. Caruso and M. J. Hampden-Smith (1997), 'Comparison of solid-state and spray-pyrolysis synthesis of yttrium aluminate powders ', *Journal of American Ceramic Society,* Vol. 80, No. 5, pp. 1231-1238.

[202] R. A. Rodrigez-Rojas, E. De la Rosa-Cruz, L. A. Diaz-Torres, P. Salas, R. Melendrez, M. Barboza-Flores, M. A. Menses-Nava and O. Barbosa-Garcia (2004), 'Preparation, photo- and thermo-luminescence characterization of Tb^{3+} and Ce^{3+} doped nanocrystalline $Y_3Al_5O_{12}$ exposed to UV-irradiation', *Optical Materials,* Vol. 25, pp. 285-293.

[203] Y. Deng, J. D. Fowlkes, J. M. Fitz-gerald and P. D. Rack (2005), 'Combinatorial thin film synthesis of Gd-doped $Y_3Al_5O_{12}$ Ultraviolet emitting materials', *Applied Physics A,* Vol. A80, pp. 787-789.

[204] K. R. Han, H. J. Koo and C.S. Lim (1999), 'A simple way to synthesize yttrium aluminum garnet by dissolving yttria powder in alumina sol', *Journal of the American Ceramic Society,* Vol. 82, No. 6, pp. 1598-600.

[205] T. Tachiwaki, M. Yoshinaka and al (2001), 'Novel synthesis of YAG leading to transparent ceramics', *Solid state communications,* Vol. 119, pp. 603-606.

[206] Balzers, (Ed.) Coating materials, sputtering targets, evaporation sources, quartz crystals.

[207] R. W. Bruce, D. W. Skelly, W. P. Minnear, R. A. Nardi, D. J. Wortman, A. F. Maricocchi, R. Viguie and D. V. Rigney (inventors) (1993), *Vapor deposition of ceramic materials*. US. Patent n° 5418003.

[208] R. Singh 'Civil aero gas turbines: technology & strategy', *Aero India,* 2003, Bangalore, India.

[209] M. P. Boyce (2001), *Gas turbine engineering handbook (2nd Ed.)*, Gulf Professional Publishing.

[210] J. Ruud, Y. C. Lau, and V. Kwasniewski (2003), *Increased fuel efficiency and decreased emissions through TBCs,* available at: http://statusreports.atp.nist.gov/reports/95-07-0018TEXT.html (accessed 2007).